



TECHNISCHE  
UNIVERSITÄT  
WIEN  
  
VIENNA  
UNIVERSITY OF  
TECHNOLOGY

# DISSERTATION

## Development of a combined positron emission mammograph and ultrasound scanner

ausgeführt zum Zwecke der Erlangung des akademischen Grades eines Doktors der  
Technischen Wissenschaften unter der Leitung von

**Univ. Prof. D.I. Dr. Hannes Aiginger**  
Atominstitut der Österreichischen Fakultäten (E141)

eingereicht an der Technischen Universität Wien  
Fakultät für Physik von

**Dipl.-Ing. Benjamin Armand FRISCH**

Matr.Nr. 0125046  
Gersthoferstrasse 156/3/ 5  
A – 1180 Wien

Diese Arbeit wurde unterstützt vom  
Österreichischen Bundesministerium für Wissenschaft und Forschung

Genf, am 31. Oktober 2012



# Kurzfassung

Brustkrebs gehört zu den häufigsten frühzeitigen Todesursachen von Frauen. Da eine frühzeitige Erkennung zu hohen Genesungsraten führt, haben zahlreiche Länder vorsorgliche Brustkrebsuntersuchungen in ihre Gesundheitsagenden aufgenommen. Allerdings fehlt klassischen Methoden wie der Röntgen-, der Ultraschallmammographie und der Magnetresonanztomographie Spezifität während Ganzkörper-PET zu gering ortsauflöst. Es ist deshalb notwendig die zu Verfügung stehenden diagnostischen Möglichkeiten zu verbessern und zu ergänzen.

Die Crystal Clear Collaboration hat ClearPEM, einen für die Mammographie bestimmten Positronenemissionstomographen (PEM), als Ergänzung klassischer Methoden der Vorsorgeuntersuchung entwickelt. Der Nachteil eines PEM ist die geringe Ortsauflösung anatomischer Merkmale. Die Diagnose kann verbessert werden, indem man die metabolische Information des PEM, welche die exakte Position krebsartiger Geschwüre zeigt, mit anatomischer Information eines anderen Verfahrens verbindet.

ClearPEM-Sonic verbindet ClearPEM mit dem SuperSonic Aixplorer, einem 3D Ultraschall- und Elastographiegerät. Der Aixplorer bietet, zusätzlich zur anatomischen Information des konventionellen 3D B-Mode Ultraschalls, eine objektive Messung der Elastizität des Gewebes, welche die Spezifität weiter verbessert.

Im Rahmen dieser Dissertation wurden die Vorbereitung der Kristalle des ClearPEM-Detektors vereinfacht und die Kristalleigenschaften verbessert. Die Lichtausbeute ist nun 30 % höher, die Energieauflösung zwei Prozentpunkte besser während die Tiefenauflösung beibehalten wurde.

Das Hauptergebnis dieser Dissertation ist die Entwicklung praktischer Lösungen zur Integration des Ultraschallgeräts in ClearPEM. Alle durch die Anatomie, das klinische Umfeld und die verschiedenen Technologien gestellten Bedingungen wurden im Rahmen einer vertiefenden Studie ausgewertet. Dadurch konnte die Integration optimiert werden ohne die Leistung der verschiedenen Modalitäten zu schmälern. Einige Lösungen wurden im Labor ausgewertet, darunter Systeme zur Brusthalterung oder zur räumlichen Standortverfolgung der US-Sonde.

Der endgültige Entwurf benötigt nur wenige Änderungen des ClearPEM, welches als unabhängige Partnermodalität des US-Systems arbeitet. Die Brust wird mit einem konischen Haltesystem stabilisiert. Ein entfernbarer 3D-Arm bringt den Ultraschallkopf in jede beliebige Position. Er ist die einzige mechanische Schnittstelle zwischen den beiden Geräten. Die Position des US-Bildes kann ausgehend von der Messung der Position des Ultraschallkopfs mit einem Standortverfolgungssystem berechnet werden. Die Information aller teilnehmenden Geräte wird an eine dedizierte Software zur Bildverarbeitung übertragen.

Schließlich wurde die Leistung von ClearPEM-Sonic bewertet. Die Ortsauflösung rekonstruierter Bilder beträgt 1,3 mm. Der erfolgreiche Bildabgleich eines mit beiden Modalitäten aufgenommenen Phantoms bestätigt die Machbarkeit multimodaler Bildgebung mit ClearPEM-Sonic. Die Ergebnisse des ersten klinischen Versuchs zeigen, dass ClearPEM-Sonic mehr Läsionen findet als ein Ganzkörper-PET und die Spezifität der Diagnose verbessert.



# Abstract

Breast cancer is one of the most frequent causes of premature death amongst women. Considering early detection leads to a very high cure rate, breast cancer screening is now part of healthcare policies in many countries. However, conventional methods like X-ray mammography, ultrasound or MRI lack specificity while whole-body PET lacks resolution. It is thus of highest importance to improve and provide additional diagnostic means with high sensitivity, specificity and good spatial resolution.

The Crystal Clear Collaboration developed a dedicated positron emission tomograph for mammography (PEM), the ClearPEM, to be used alongside standard screening techniques. Yet, a major disadvantage of PEM is its low resolution with regards to anatomical features. A way to improve diagnosis is to combine metabolic information from PEM, highlighting the exact position of cancerous lesions, with anatomic and morphologic information from another modality, localizing the lesion in the surrounding tissue.

ClearPEM-Sonic couples ClearPEM to a 3D ultrasound (US) elastography system, the SuperSonic Imagine Aixplorer. In addition to the anatomical information given by conventional 3D B-mode ultrasound imaging, the Aixplorer improves the specificity by providing true 3D tissue elasticity obtained with 3D Shear Wave elastography.

In the frame of this thesis, the crystal preparation process for the ClearPEM detector is simplified and the crystal properties improved. The light yield increases by 30 %, the energy resolution improves by 2 percentage points whilst the depth of interaction resolution remains unchanged.

The major result of the thesis is the development of practical solutions to integrate the US modality into the ClearPEM machine. All constraints imposed by the anatomy and the clinical environment on one side and different technologies on the other side are evaluated in the frame of an in-depth study that optimizes the integration without compromising the performance of any modality. Some practical solutions are evaluated in the laboratory, including different breast holding systems or spatial tracking systems for the US transducer.

The final design induces only minimal changes to ClearPEM as it works as an independent partner modality with the US system. The breast is immobilized with a conical stabilization system integrated in the patient bed. A removable arm used to bring the US transducer in any required position is the only mechanical interface between both devices. The position of the US image can be calculated by recording the transducer position with a tracking system. The information from all modalities is transferred to dedicated software for image treatment.

Finally, the performance of ClearPEM-Sonic is evaluated. The resolution in a reconstructed image is 1.3 mm. The co-registration of a dedicated phantom acquired with both modalities proves the concept of multimodality imaging with ClearPEM-Sonic. Preliminary results from the first clinical trial show that ClearPEM detects more cancerous lesions than whole-body PET and contributes to an increase of the specificity in the diagnostic process.



*In fond memory of my father,*  
*Dr. Armand Kurt Frisch,*  
אהרנ בן אברהם חיימ  
ת.נ.צ.ב.ה.

“O fim duma viagem é apenas o começo doutra. É preciso ver o que não foi visto, ver outra vez o que se viu já, ver na Primavera o que se vira no Verão, ver de dia o que se viu de noite, com sol onde primeiramente a chuva caía, ver a seara verde, o fruto maduro, a pedra que mudou de lugar, a sombra que aqui não estava. É preciso voltar aos passos que foram dados, para os repetir, e traçar caminhos novos ao lado deles. É preciso recomeçar a viagem. Sempre. O viajante volta já.”

in José Saramago, *Viajem a Portugal*





# Acknowledgements

Giving acknowledgements at the beginning of one's thesis is a custom I will certainly not evade although, I believe, finding the best order for mentioning people is amongst the main challenges one faces during the compilation of his thesis. The easiest solution would of course be to simply thank everybody who contributed with their support, such support being not only of academic or financial nature but also friendship and, ultimately, love.

The preceding five lines could be all of my acknowledgements and allow you, my dear reader, to immediately jump – willingly or not, it depends on the reasons you have for opening this thesis – into the core of this work. Wouldn't this be the best solution, the one recommended by the duties of scientific enthusiasm? No. It would do wrong to all those who shall be personally named in the following paragraphs because of their immense contribution to my scientific development and, well, mental sanity.

Some four years before I moved to Geneva, all I knew about CERN was its role in particle physics and its excellence in science. I was still an undergraduate student, Prof. Hannes Aiginger and Karin Poljanc from the Technische Universität Wien my mentors. And then, some day in February 2006, Karin called to tell me about an open position as a Technical Student at CERN. Not knowing at that moment what exactly I was committing to, I accepted and applied. It was only in summer that I moved to Geneva and first set foot on Friday, the 1<sup>st</sup> of September 2006, in building 27. Here, I was met by Etienne Auffray and Paul Lecoq who quickly introduced what, at that moment, should only be a short assignment lasting ten months and lead to my master thesis.

Six years later I can say that I never regretted any decision I took, neither of moving to Geneva nor accepting the extension as a Doctoral Student. I am more than very grateful to Prof. Aiginger and Karin who, during all those years, were my Viennese supervisors and gave me more than just academic support by following as close as possibly, despite the distance, my work and personal development. I need to express the same gratitude to Etienne and Paul for having been my CERN supervisors and following almost every step I did in their laboratory, giving me every academic but also financial support I needed to successfully fulfil my tasks. I also thank the CERN Technology Transfer Group for their support.

A thesis like this one is everything but the work of just one person. Without the help and collaboration of my colleagues at CERN and other institutes it would not exist. There is the need of daily scientific exchanges with colleagues at the office. Daniel Abler, Ahmad Ali, Stefan Brunner, Stefan Gundacker, Arno Knapitsch, Matthias Kronberger, Michel Lebeau, Julien Lollierou, Gaetan Martin, Georgios Mavromanolakis, Yuri Musienko, Nils Nedfors, Kristof Pauwels, Oliver Poppe, Alessandro Thea, Pier Paolo Trapani and Julia Trummer all patiently endured my questions and sometimes monologues about whatever crossed my mind and helped whenever they could. They and those whom I forgot mentioning really merit an immense thank-you for everything they helped with.

It is not like such a thesis could be done without the practical help of those who know to transform into reality the most absurd wishes of a physicist: Antonio Conde Garcia, Hervé

Cornet, Jérôme Daguin, Dominique Deyrail and Alain Machard. Dominique, the guardian of the sacred Nespresso machine in his office, became through numerous oenological conversations a good friend.

I need to thank all my collaborators from partner institutes and companies. This project would simply not have been possible without them and now that it is over, many of them are my personal friends. There are Prof. Stefaan Tavernier from Vrije Universiteit Brussel, who is so kind to support this work as a reviewer, and his student Dang Jun, whom I remember not only as a great cook when it came to gelatine-based creations but mostly as a friend and companion on our culinary explorations of the South of France, Portugal and Milos.

I absolutely need to mention my Portuguese colleagues, Prof. Joao Varela, Pedro Almeida, Ricardo Bugalho, Sofia Ferreira, Catarina Ortigao and Andreia Trindade from LIP in Lisboa on one side and of course Joaquim Santos from INEGI in Porto, without whom many technical modification to ClearPEM-Sonic would not have been possible. Being in an international collaboration calls for English as a main language for correspondence. However, having a certain affinity to foreign languages, I could not refrain from using Portuguese whenever possible. It is in this sense that I express my highest gratitude for having supported my ambitions and thus thoroughly contributed to my learning curve. I must admit I expected to learn many things during my PhD albeit not Portuguese.

The next destination on my acknowledgment tour of Europe is Milano. The help of Giacomo Cucciati, Nicolas Di Vara, Alessio Ghezzi and Marco Pizzichemi, under the auspices of Marco Paganoni, were essential to the completion and commissioning of ClearPEM-Sonic. We will never forget the many days and nights spent in the windowless room at Hôpital Nord in Marseille, trying to improve the qualities of our machine.

I will finish my travel through Europe in the South of France by stopping first at the LMA in Marseille where I need to thank Stefan Devic, Philippe Lasaygues and Serge Mensah for their help on ultrasound studies and mechanical designs and then of course at SuperSonic Imagine in Aix-en-Provence where I have to express my highest gratitude to Nicolas Felix. Finally, the staff of the nuclear medicine and radiology departments at Hôpital Nord was essential to the evaluation of this machine. I particularly thank the physicians, Valérie Juhan, Olivier Mundler, Pascale Silès and Laurent Tessonier for their availability.

Friends add zest to life. I cannot remember whether I heard this saying somewhere or whether it just relies on my personal experience. In any case, my friends are amongst the most precious beings in this world. They are who keep me happy, accompany me through my numerous adventures and leave many lasting memories.

Vienna was the city where I grew up and studied, it still is the place where many of my close friends live. They are friends including Oliver Majcher, the architect, Thomas Zika, my favourite Amstettner, and Immanuel Kalcher.

When I moved to Geneva, it did not take too long before meeting some very nice people. Naming them all would take the long: these are acknowledgments, not a thesis about the merits of friendship although, thinking of it, I might be tempted to write one later. I should start with the Austrians, Gerhard Burghart, Gerhard Bruckner, Stefan Brunner, Lukas Gruber, Florian

Hinterschuster, Arno Knapitsch, Matthias Kronberger, Christian Patauner, Stefan Rossegger, Elisabeth Vinek and all the other ones with their better halves! Being in Geneva gave me the opportunity to meet many more great people of whom I shall mention Nathaniel Powell who kept my interest in international relations awake and contributed to incredible memories from Tunisia.

Aurelien Marsili merits a category of his own because of all the time we spent together, discussing about everything and advising the other if necessary, just as one should with an extraordinary friend.

Can love be expressed with words? I doubt it. These feelings are the most intimate and complex a human can ever have. Yet, without me having to say a word, She will undoubtedly understand!

I have kept the most important for the end of these acknowledgments. I could have started with this part yet it seemed more important to save it as the persons concerned are those I keep in the heart of my hearts: my father, Dr. Armand Kurt Frisch and my mother, Maria Frisch. The time I spent in Geneva has not been easy for us. Although we got used to the physical separation over the weeks, months and years I spent here, such separation is a burden to bear. My parents supported whatever decision I took, patiently waited for me to visit them and always had an ear for my countless calls.

Much as I rejoice about finishing my thesis, the sadness my father could not live to see it cannot be erased. He passed away on 14<sup>th</sup> of September 2009.

Dear reader, I am sad to say you have now reached the end of my acknowledgments. You are now at the edge of this cliff that is the last obstacle before jumping into the vast sea of medical imaging. I, the author, feel guilt because if you keep on reading I was the one pushing you over this cliff. There probably just is no way you could avoid it so you shall, just like Baudelaire in his *Les Fleurs Du Mal*: “Au fond de l’inconnu trouver du *nouveau*!”, find in the Depths of the Unknown the New!



# Table of Content

List of Figures.....	xvi
List of Tables.....	xx
Abbreviations .....	xxi
1 Introduction.....	1
1.1 Thesis Overview .....	2
1.2 CERN .....	2
1.3 Crystal Clear Collaboration .....	4
1.4 Technology Transfer .....	5
2 Positron Emission Tomography .....	7
2.1 Principle.....	7
2.2 Medical Interest .....	8
2.3 Radiopharmaceuticals .....	9
2.4 Physical Background.....	10
2.5 Technology .....	11
2.5.1 Scintillating Detectors.....	11
2.5.2 Localisation of the Interaction within the Detector System .....	13
2.5.3 Image Reconstruction.....	15
2.5.4 Image Quality .....	17
2.5.4.1 Attenuation .....	17
2.5.4.2 Unwanted Coincidences .....	17
2.5.4.3 Parallax Error.....	18
2.6 State of the art .....	19
2.6.1 Human Whole-body PET .....	19
2.6.2 Small Animal PET .....	20
2.6.2.1 ClearPET .....	21
2.6.3 Dedicated Human PET.....	23
3 The ClearPEM-Sonic Project .....	25
3.1 Breast Cancer .....	25
3.1.1 Epidemiology.....	26
3.1.2 Pathology.....	27
3.1.3 Prognosis .....	29
3.1.4 Screening.....	30
3.1.5 Diagnostic Techniques .....	31
3.1.6 Therapy .....	33
3.2 ClearPEM .....	33
3.2.1 Detector Design .....	35
3.2.2 Detector Performance.....	36
3.2.3 Image Reconstruction.....	38
3.2.4 Image Quality of the first ClearPEM .....	39
3.3 The Ultrasound System .....	41
3.3.1 Theory of Ultrasound .....	41

3.3.2	Theory of Elastography .....	43
3.3.3	SuperSonic Imagine Aixplorer .....	45
3.3.4	Trial Results.....	46
3.4	ClearPEM-Sonic .....	48
3.4.1	Objectives .....	48
3.4.2	Challenges .....	49
4	Scintillator Performance .....	51
4.1	Inorganic Scintillators .....	51
4.1.1	Scintillation Process .....	52
4.1.1.1	The Band Theory .....	52
4.1.1.2	Mechanism of Scintillation.....	53
4.1.1.3	Cerium-activated crystals .....	55
4.1.2	Energy and light loss in the crystal .....	55
4.1.2.1	Thermal quenching .....	56
4.1.2.2	Concentration Quenching .....	57
4.1.2.3	Selfabsorption .....	57
4.2	General Characteristics.....	58
4.2.1	Light Output .....	58
4.2.1.1	Theory .....	58
4.2.1.2	Single-Crystal Characterisation .....	60
4.2.1.3	Large-Scale Characterisation.....	62
4.2.2	Energy Resolution.....	63
4.2.3	Depth Of Interaction .....	65
4.2.3.1	Theory .....	65
4.2.3.2	Characterisation .....	67
4.3	Results .....	71
4.3.1	Depolishing Study.....	71
4.3.2	Mechanical Depolishing.....	75
4.3.3	Large-Scale Quality Control.....	76
4.4	Detector Matrices .....	77
4.4.1	Production Process Selection.....	77
4.4.2	Comparison with APD measurements .....	78
5	Multimodality Integration .....	79
5.1	Development of a Breast Stabilization System.....	79
5.1.1	Stabilization Plates .....	80
5.1.1.1	Measurement of the speed of sound and US attenuation coefficient .....	81
5.1.1.2	Creation of transversal US modes.....	84
5.1.1.3	Evaluation of Candidate Materials under Nuclear Aspects .....	85
5.1.1.4	Possible Mechanical Integration .....	86
5.1.1.5	Conclusion.....	87
5.1.2	Stabilization Cone .....	87
5.1.2.1	Design .....	87
5.1.2.2	Cone Production.....	89

5.1.2.3	Conclusion.....	90
5.2	Image Co-registration.....	91
5.2.1	Fiducial Markers .....	91
5.2.1.1	Visibility of fiducial markers with US .....	91
5.2.1.2	Visibility of fiducial markers with PEM .....	94
5.2.1.3	Discussion.....	94
5.2.2	Position Tracking Systems .....	95
5.2.2.1	Survey of Different Approaches .....	95
5.2.2.2	Magnetic Positioning System .....	96
5.2.2.3	Tests in ClearPEM .....	99
5.2.2.4	Discussion.....	102
5.2.3	Image Co-registration Software.....	102
5.3	Mechanical Integration of both Modalities into a Single Machine .....	105
5.3.1	Conical Stabilization .....	105
5.3.2	Ultrasonic Transducer .....	106
5.3.3	Overall Design .....	108
6	System Evaluation .....	109
6.1	ClearPEM Detector Performance.....	109
6.2	ClearPEM Image Resolution .....	110
6.3	Image Co-registration.....	113
6.4	Patient Imaging Trial.....	115
6.4.1	Case 1: infiltrating ductal carcinoma .....	117
6.4.2	Case 2: bilateral breast cancer .....	118
6.4.3	Case 3: multifocal breast cancer .....	119
7	Summary and Outlook.....	121
	Literature .....	125

# List of Figures

Figure 1 : The LHC layout [21] .....	3
Figure 2 : The CMS layout [25] .....	4
Figure 3 : Scintillating Crystal Detector Technology Transfer .....	5
Figure 4 : Phases in the development of technology transfer projects and their financing [40]....	6
Figure 5 : Basic principle of a full body PET .....	8
Figure 6 : Chemical Formula of FDG [51].....	9
Figure 7 : Scintillation detector. The figure shows which events are selected in a full energy spectrum. ....	13
Figure 8 : Light distribution in a multi-PMT setup.....	14
Figure 9 : CTI-type multi-crystal configuration .....	14
Figure 10 : Sinogram formation and image reconstruction [59].....	15
Figure 11 : 1-dimensional backprojection a) without use of filters, b) with filters, c) with time-of-flight information .....	16
Figure 12 : Illustration of the possible coincidences: true, scattered and random .....	18
Figure 13 : Illustration of the parallax error (a) without information about the depth of interaction and (b) with information about the depth of interaction .....	19
Figure 14 : ClearPET: a) detector module, b) ClearPET Neuro at FZ Jülich, c) Raytest ClearPET, d) image of a rat brain with FDG from FZ Jülich [84].....	22
Figure 15 : a) The female breast, b) Lobular Carcinoma In Situ and c) stages of Ductal Carcinoma In Situ [102].....	28
Figure 16 : ClearPEM: the first prototype [110].....	34
Figure 17 : ClearPEM module with 32 crystals and back-to-back APD readout [110] .....	35
Figure 18 : Front-End ASIC performance: a) ASIC response to an input test signal, b) noise as a function of the channel number [112].....	36
Figure 19 : Detector Resolution: a) typical 511keV photopeak, b) mean energy resolution, c) mean time coincidence resolution, d) depth of interaction resolution for different photon interaction points [113]–[115] .....	37
Figure 20 : Scanner Performance: a) DCC rate, b) scanner detection sensitivity [16], [113]–[115].....	37
Figure 21 : Influence of the DOI measurement on image quality: a) reconstruction without DOI information, b) reconstruction with DOI information [119] .....	39
Figure 22 : Reconstructed images that have been obtained with 1) 3D OSEM, 2) list-mode ML-EM and 3) 2D-OSEM of a) a breast phantom, b) a mouse and c) a mini-Derenzo phantom [114] .....	40
Figure 23 : Derenzo phantom [16].....	40
Figure 24 : SuperSonic Aixplorer [17].....	41
Figure 25 : Refraction of an ultrasonic wave on a planar surface.....	42
Figure 26 : Propagation of the focal point in tissue and creation of a lateral shearwave .....	45
Figure 27 : Propagation and deformation of the shear wave as a function of time [126] .....	45
Figure 28 : SuperSonic Imagine Aixplorer 3D Transducer [126] .....	46



Figure 29 : 3D elastography image of a phantom with a hard lesion surrounded by soft tissue. The images have been converted to grayscale images with non-standard colour schemes to be shown in a document printed in black and white. [126] .....	47
Figure 30 : B-mode and elastographic image superposed on the B-mode image of a female breast. A millimetric lesion is visible on the elastography. The images have been converted to grayscale images with non-standard colour schemes to be shown in a document printed in black and white. [126] .....	47
Figure 31 : Energy bands of a) an insulating and b) an impurity-activated crystal .....	53
Figure 32 : Configurational coordinate diagram showing a) the scintillation process and b) the overlap of the absorption and emission region .....	57
Figure 33 : Light yield bench .....	61
Figure 34 : Typical Light Output Spectrum .....	62
Figure 35 : Photo of MiniACCOS [138].....	63
Figure 36 : Crystal of length L, readout out at both ends with a photodetector .....	66
Figure 37 : Geometry of the DOI bench .....	67
Figure 38 : DOI bench data acquisition setup .....	68
Figure 39 : DOI sample spectra .....	69
Figure 40 : Correlation between the quantities of light measured by each PMT and the position of the gamma interaction in a) a fully polished crystal and b) a crystal with one depolished lateral side. ....	70
Figure 41 : Correlation between the average asymmetry $\langle \alpha \rangle$ and the position of the interaction in a) a fully polished crystal and b) a crystal with one depolished lateral side. The error bars represent the FWHM of the asymmetry distribution in each point. ....	70
Figure 42 : Energy resolution as a function of the crystal polishing.....	72
Figure 43 : Light Output as a function of the crystal polishing.....	72
Figure 44 : DOI resolution $\alpha_{DOI}$ as a function of the crystal polishing .....	73
Figure 45 : Roughness of compared crystal batches.....	73
Figure 46 : Energy Resolution of compared crystal batches .....	74
Figure 47 : Light output of compared crystal batches.....	74
Figure 48 : DOI resolution $\alpha_{DOI}$ of compared crystal batches .....	74
Figure 49 : Schematic cross-section of the depolishing device .....	75
Figure 50 : Photo of the depolishing device, fully loaded with crystals, without the brass weight .....	75
Figure 51 : a) Average roughness and b) spread in percent between the lowest and the highest Ra on a single crystal face. ....	76
Figure 52 : Normalized light output measured on MiniACCOS for a) 965 fully polished CPI crystals and b) 880 PML crystals depolished on 4 lateral faces .....	77
Figure 53 : Initially proposed setups: a) with stabilization plates and b) with a stabilization cone .....	80
Figure 54 : Photo of the US transmission setup, placed in a filled water tank .....	81
Figure 55 : Scheme of the US transmission setup and measurements .....	82
Figure 56 : Example of a) recorded temporal signals and b) the Fourier transformations for a reference measurement and subsequent sample measurement with a 2 mm thick PVC plate.....	82

Figure 57 : Influence of a rotation of the plate on the sound propagation .....	85
Figure 58 : Evolution of the signal for a) a 50 $\mu$ m Mylar foil and b) a 3 mm RenShape plate ...	85
Figure 59 : Possible stabilization plate integration: a) fixed to the PET arm, b) fixed to the table .....	86
Figure 60 : CAD drawing of a typical cone.....	88
Figure 61 : Practical tests with cones: a) cone fits, b) there is an air gap, c) the cone is too big.	88
Figure 62 : Compatibility tests of the cone with the US transducer. a) shows an exam of a breast phantom in the cone. b) shows the imaging cone of the transducer .....	89
Figure 63 : SuperSonic Imagine Aixplorer image of a 1.5 cm lesion in the phantom. The elastography image is superposed with the ultrasound image.....	89
Figure 64 : Cone Production Setup.....	90
Figure 65 : a) Plate with different potential fiducial markers used for tests.....	92
Figure 66 : Example for a US test with a) the fiducial markers facing towards and b) away from the transducer. A Mylar 50 $\mu$ m foil is used as the transmitting plate.....	93
Figure 67 : a) Geant4 simulation of the visibility of 3 mm and 5 mm point sources with background radiation at varying source to background activity ratios [154] and b) measurement at 16 positions of a 1 mm point source without background radiation with ClearPEM [119] ....	94
Figure 68 : Influence of a fiducial marker placed in front of the cone window on the ultrasound image quality .....	95
Figure 69 : Ascension trakSTAR, definition of the axes and coordinate system of the emitter and sensor [155].....	97
Figure 70 : Setup used to test the theoretical performance of the magnetic tracking system.....	98
Figure 71 : Measured and theoretical position on the reference grid.....	98
Figure 72 : Angular Precision under ideal conditions for a) roll, b) azimuth and c) elevation measurement.....	99
Figure 73 : Measured deviation under ideal conditions for a) the position and b) the angular measurement.....	99
Figure 74 : Setup used to test the tracking performance in ClearPEM (Porto, PT).....	100
Figure 75 : Measured position on the reference grid in ClearPEM .....	101
Figure 76 : Data storage structure.....	103
Figure 77 : The Image Loader module of the ClearPEM-Sonic software [156].....	104
Figure 78 : Cutaway CAD model of the table with the breast cone.....	106
Figure 79 : Proposal for the US Integration, 12/2010.....	106
Figure 80 : Detail of the PEM platform. The transducer and its arm are highlighted in dark grey. ....	107
Figure 81 : Detail of the PEM platform as installed in Marseille, showing a mock-up of the US transducer on its arm and the bridge holding the magnetic emitter .....	107
Figure 82 : Final Design of ClearPEM-Sonic: the new ClearPEM design is .....	108
Figure 83 : ClearPEM-Sonic as it is installed at Hopital Nord, Marseille. The SuperSonic Imagine Aixplorer is in the foreground, ClearPEM in the background. ....	108
Figure 84 : a) Photospectrum measured over all events in the detector plates, b) coincidence time spectrum of the same events. Black crosses are real data points, the grey line represents the Gaussian fit.....	110

Figure 85 : a) Photography and b) CT image of the empty Ultra Micro Hotspot Phantom. The numbers are the rod diameters in millimetres.....	111
Figure 86 : a) ClearPEM image of the Ultra Micro Hotspot Phantom, filled with $^{18}\text{F}$ FDG. The numbers are the rod diameters in millimetres. b) the same image with enhanced contrast.....	111
Figure 87 : a) Photography and b) CT image of the Bioscan mini-Jaszczak Phantom. The numbers are the rod diameters in millimetres.....	112
Figure 88 : a) Reconstructed ClearPEM image of the Bioscan mini-Jaszczak Phantom. The numbers are the rod diameters in millimetres. b) the same image with enhanced contrast.....	112
Figure 89 : Contrast according to Michelson of both phantoms .....	113
Figure 90 : A gelatine-Agar phantom being imaged.....	113
Figure 91 : a) US image, b) elastography image and c) ClearPEM image of a gelatine/Agar phantom.....	114
Figure 92 : a) Coronal, b) sagittal, c) transverse and d) 3D images of the co-registered US and ClearPEM acquisition .....	114
Figure 93 : a) Coronal, b) sagittal, c) transverse and d) 3D images of the co-registered elastography and ClearPEM acquisition .....	115
Figure 94 : a) Whole-body PET/CT of case 1 .....	117
Figure 95 : a) coronal and b) sagittal ClearPEM images of case 1 .....	117
Figure 96 : a) whole-body PET, b) CT, c) MRI of and d) ClearPEM of the right breast of case 2 .....	118
Figure 97 : a) whole-body PET, b) CT, c) MRI and d) ClearPEM of the left breast of case 2 ..	119
Figure 98 : a) Whole-body PET/CT of the left breast and b) MRI of case 3 .....	119
Figure 99 : a) coronal and b) sagittal ClearPEM images of case 3 .....	120

## List of Tables

Table 1 : Common Radiopharmaceuticals for PET, their production process and possible applications [44], [53], [54].....	10
Table 2 : Typical inorganic crystal scintillator materials in PET [56] .....	12
Table 3 : Isolated breast cancer risk factors [97]–[100].....	27
Table 4 : Breast Cancer Survival Prognosis [47].....	29
Table 5 : The BIRADS lexicon [96] .....	30
Table 6 : Density and stiffness of some types of human breast tissue [122].....	43
Table 7 : Results of a study on 192 lesions [127] .....	48
Table 8 : Properties of LYSO, at room temperature, under excitation by a 511 keV photon [56] .....	58
Table 9 : Results from the production process selection.....	78
Table 10 : Measurements performed at LIP [145].....	78
Table 11 : Attenuation measurements at LMA, at 2.5 MHz ultrasound centre frequency (measured values with a precision of 5 %).....	83
Table 12 : Speed of sound measurements at LMA (measured values with a precision of 5 %).....	84
Table 13 : 511 keV attenuation with different materials (calculated values with a precision of 1 %).....	86
Table 14 : Fiducial marker visibility under ultrasound .....	93
Table 15 : Testing the correction procedure for the magnetic tracking system (values in millimeters) .....	101

# Abbreviations

ALICE	A Large Ion Collider Experiment
APD	Avalanche PhotoDiode
ATLAS	A Toroidal LHC ApparatuS
BGO	Bismuth-Germanate-Oxide
CeF <sub>3</sub>	Cerium Fluoride
CERN	European Organization for Nuclear Research
CCC	Crystal Clear Collaboration
CMS	Compact Muon Solenoid
CT	Computed Tomography
DOI	Depth Of Interaction
FDG	<sup>18</sup> F-FluoroDesoxyGlucose
FOV	Field Of View
FWHM	Full Width at Half Maximum
ICNAS	Instituto de Ciências Nucleares Aplicadas á Saúde, Coimbra, Portugal
INEGI	Instituto de Engenharia Mecânica e Gestão Industrial, Porto, Portugal
IPO	Instituto Português de Oncologia, Porto, Portugal
LEP	Large Electron-Positron Collider
LIP	Laboratório de Instrumentação e Física Experimental de Partículas, Lisbon, PT
LHC	Large Hadron Collider
LHCb	Large Hadron Collider beauty
LO	Light Output
LOR	Line Of Response
L(Y)SO	Lutetium (Yttrium) Oxyorthosilicate
Lu(Y)AP	Lutetium (Yttrium) Aluminium Perovskite
FWHM	Full Width Half Maximum
MRI	Magnetic Resonance Imaging
NaI	Sodium Iodide
OSEM	Ordered Subset Expectation Maximization
PEM	Positron Emission Mammography
PET	Positron Emission Tomography
PMT	PhotoMultiplier Tube
PWO	Lead Tungsten Oxide
SPECT	Single Photon Emission Computer Tomography
SSI	SuperSonic Imagine
US	Ultrasound



Para qué escribe uno, si no es para juntar sus pedazos?  
Desde que entramos en la escuela o la iglesia, la  
educación nos descuartiza: nos enseña a divorciar el alma  
del cuerpo y la razón del corazón.

Sabios doctores de Ética y Moral han de ser los  
pescadores de la costa colombiana, que inventaron la  
palabra sentipensante para definir al lenguaje que dice la  
verdad.

in Julio Cortazar, *El libro de los abrazos*

## 1 Introduction

The concept of using positrons for medical imaging arose at the end of the 1940s [1] and was for the first time applied by Sweet and Brownell at Massachusetts General Hospital in 1951 [2]. Although they were still far from using complex multiple detectors and reconstruction algorithms, the use of two sodium iodide (NaI) detectors facing each other to detect brain tumours heralded over two decennia of development until PETT II was presented by Ter-Pogossian and Phelps [3]. PETT II, the Positron Emission Transversal Tomograph, was the first positron emission scanner based on coincidence detection with proper attenuation correction and used filtered back projection for image reconstruction [4].

Since then, a series of rapid technological advancements in various fields led to the use of more efficient scintillators like BGO [5], [6] and later LSO [7], the synthetisation of  $^{18}\text{F}$ -desoxyglucose (FDG) as a standard tracer molecule [8], the development of dedicated cyclotrons for medical tracer production as well as more efficient projective or iterative reconstruction algorithms. These advances led to a wider propagation of PET in major hospitals whilst offering increasingly better image resolution and wider applications such as the combination with computed tomography (CT) [9] or, more recently, magnetic resonance imaging (MRI) [10].

In parallel, more specialised systems have been developed in order to address more specific problems with higher image resolution. These include the development of dedicated systems for small animal imaging and the imaging of certain body parts like the brain, the breast or the prostate [11]–[13].

This thesis presents such a dedicated system, the multimodal breast imaging system ClearPEM-Sonic [14]. It combines the positron emission mammograph ClearPEM [15], [16], developed by

the Crystal Clear Collaboration hosted by CERN, with an elastography ultrasound system developed by SuperSonic Imagine, a company from Aix-en-Provence, France [17].

## 1.1 Thesis Overview

The present introduction places the thesis into its historical and current organisational background. It explains how this project came into existence and how it is embedded into the CERN framework. The second chapter introduces positron emission tomography: starting with its medical interest, an explanation of the principle behind it and concluding with a survey of the contemporary state of the art.

ClearPEM-Sonic will be introduced in the third chapter. It will assess the medical importance of mammography and then detail the two components of this machine: the positron emission mammograph ClearPEM and the ultrasound elastography system SuperSonic Imagine Aixplorer. The fourth chapter addresses one main topic of the thesis, the positron detectors used in ClearPEM. Beginning with a theoretical introduction on scintillating crystals and the importance of some of their characteristics for PET, it then describes the technological advances and their impact on the ClearPEM detector performance. The second main topic of this thesis, the combination of the PET and US modalities into a single machine, is treated in the fifth chapter. Both challenges from the mechanical integration and image co-registration along with their respective resolutions are explained. The sixth chapter surveys the performance of the machine installed at Hôpital Nord, Marseille, FR with different phantoms and presents first patient images. The last chapter concludes the thesis and gives an overview of further developments.

## 1.2 CERN

The present work was hosted by CERN, the European Organisation of Nuclear Research, based in Geneva, Switzerland. CERN was established by a formal act in Paris, on 1<sup>st</sup> of July 1953, as an organisation that “shall provide for collaboration among European States in nuclear research of a pure scientific and fundamental character, and in research essentially related thereto” [18]. The declaration was initially supported by Belgium, Denmark, France, the German Federal Republic, Greece, Italy, the Netherlands, Norway, Sweden, Switzerland, the UK and Yugoslavia. Except Yugoslavia, all founding members are still part of CERN and have been joined by Austria, Bulgaria, the Czech Republic, Finland, Hungary, Poland, Portugal, Slovakia and Spain. Additionally, eight countries and international organizations have observer status and 28 more countries participate in experiments as non-member states.

During its history, CERN continuously provided the international particle physics community with tools to study the fundamental elements and forces governing our universe whilst always keeping an eye on developments and discoveries that might lead to a new understanding of elementary physics.



The Large Hadron Collider (LHC), which entered operation in fall 2008, stands in the line with decades of technological achievements since the first accelerator, the Synchrocyclotron, entered operation in 1957 [19]. Being the most powerful particle accelerator ever built, it is expected to accelerate proton beams to energies of up to 7 TeV whilst maintaining a rather high luminosity of  $10^{34} \text{ cm}^{-2}\text{s}^{-1}$  [20]. However, such parameters are very demanding for detectors. It was therefore necessary to develop technologies able to withstand high energetic particle fluxes. The four experiments attached to the LHC: ATLAS, CMS, ALICE and LHCb have been designed with this constraint in mind.

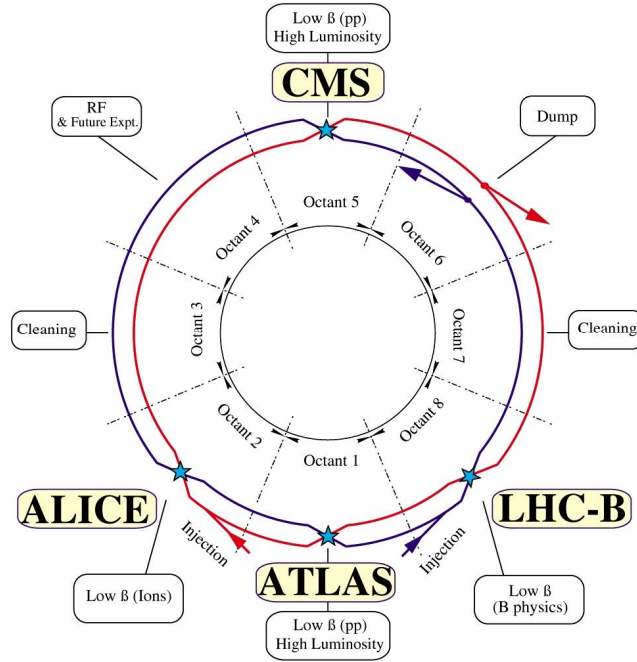


Figure 1 : The LHC layout [21]

CMS, the Compact Muon Solenoid, is, with ATLAS, one of two multipurpose detectors used at LHC. It is divided into a 4 T solenoid magnet and several concentric subdetectors that include a tracker, an electromagnetic, a hadronic calorimeter as well as muon detectors in its outermost layer. This setup, combined with its geometry that allows measurements in all directions, should lead to the identification of new particles or evidence of physics beyond that of the Standard Model. An example of such achievements is the observation of a boson at a mass of 125 GeV, in the frame of searches for the standard model Higgs boson [22], [23].

The present thesis was hosted by the CERN section responsible for the development and construction of the electromagnetic calorimeter. The latter is based on fast scintillating crystal detectors that were developed to handle the high constraints of LHC operation. The crystals shall withstand radiation doses of several kGy per year whilst the electronics needs to operate flawlessly in a magnetic field of around 4 T, at a rate of up to 40 MHz [24]. The knowledge gained during this development was transferred to medical applications, for example by the Crystal Clear Collaboration.

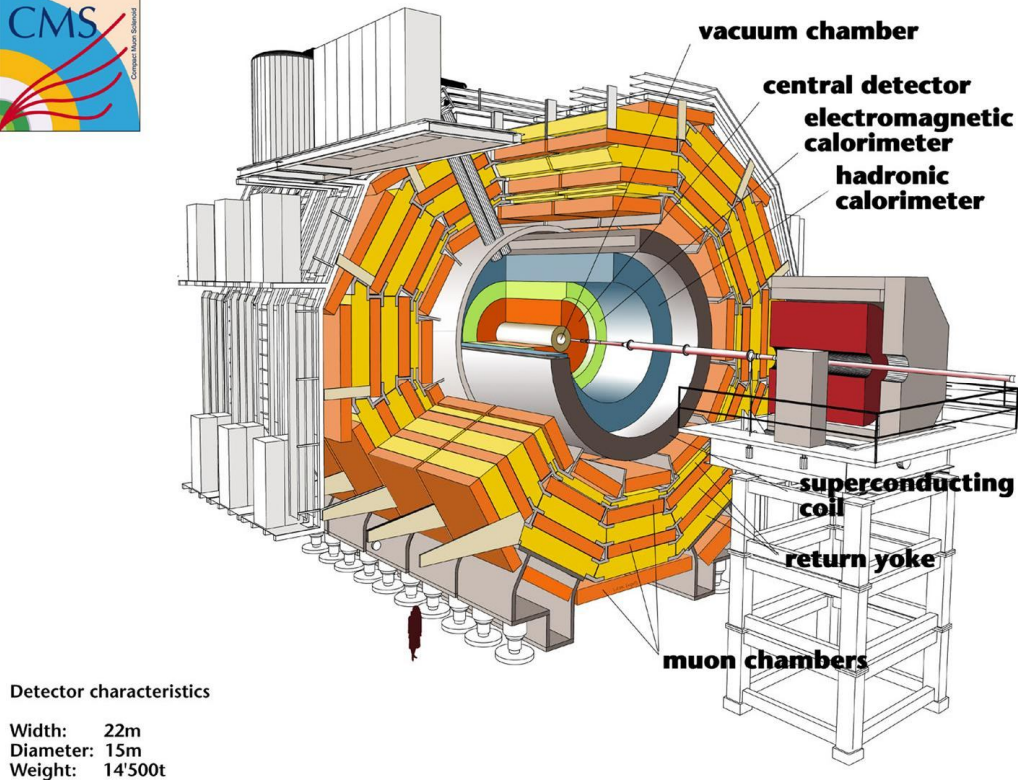


Figure 2 : The CMS layout [25]

### 1.3 Crystal Clear Collaboration

The Crystal Clear Collaboration was founded in 1990 as an international academic network of laboratories and industrial partners for the development of scintillating crystal detectors as well as their applications. It comprises of experts in crystallography and solid state physics as well as in radiation detection and instrumentation from the following laboratories: CERN, Forschungszentrum Jülich and German Cancer Research Centre DKFZ Heidelberg (Germany), Institute for Nuclear Problems Minsk (Belorussia), Institute for Physical Research Ashtarak (Armenia), Laboratório de Instrumentação e Física Experimental de Partículas in Lisbon (Portugal), CIEMAT in Madrid (Spain), the Sungkyunkwan University School of Medicine in Seoul (South Korea), Universiteit Gent and Vrije Universiteit Brussels (Belgium) as well as Centre de Physique des Particules de Marseille, UCB Lyon I and CNRS (France) [26].

The primary goal of the CCC was the development of a radiation-hard crystal that perfectly withstands LHC radiation conditions. This led to the development of  $\text{PbWO}_4$  (PWO) and  $\text{CeF}_3$  as potential candidates for LHC [27]–[29]. PWO was selected in 1994 for the construction of the electromagnetic calorimeter of CMS. Since, several materials for future applications have been identified whilst the current focus lies on scintillating crystal fibres for a potential electromagnetic calorimeter at CLIC.

In parallel, the collaboration decided to transfer the knowledge gained through the development of scintillating detectors for high energy physics to other domains. Medicine is one of the main fields of application. As shown in figure 3, requirements for medical imaging are very similar to those for high energy physics, with the exception of radiation resistance. Research is now focused on crystals for medical imaging applications. This has led to the development of Lutetium and Yttrium Perovskite Crystals LuAP and LuYAP [30]–[35]. The findings were first applied in a dedicated small-animal PET demonstrator. This machine, the ClearPET, is used for clinical and pharmaceutical research on rodents and the heads of small primates and is now commercialized by the German company Raytest GmbH [36]–[38].

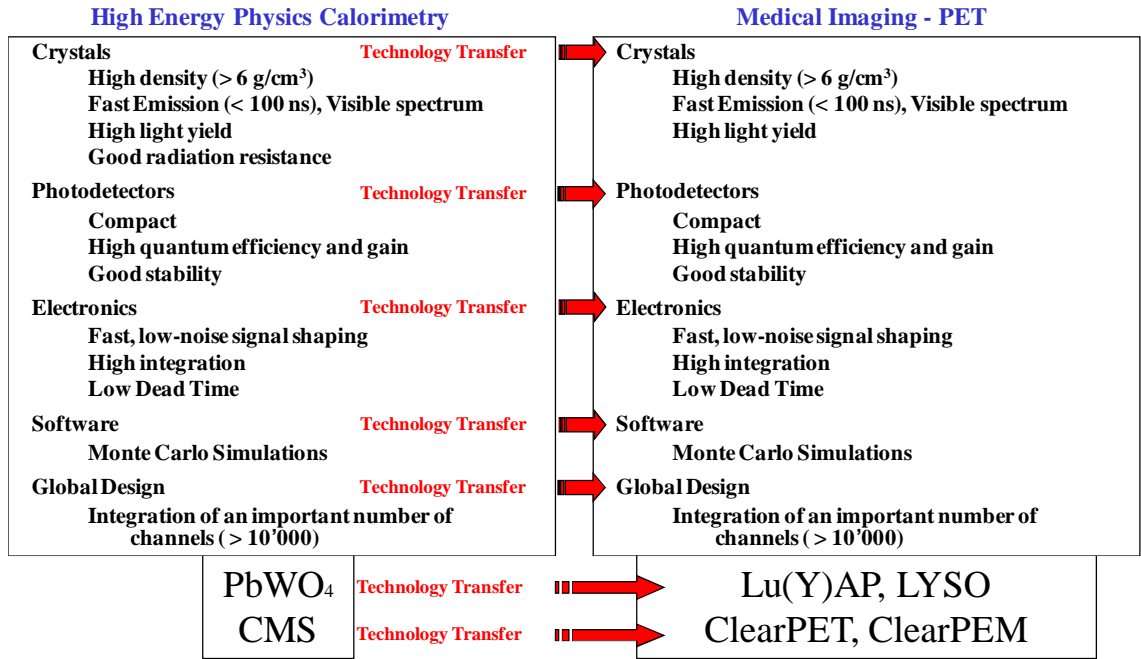


Figure 3 : Scintillating Crystal Detector Technology Transfer

The next step was to apply the technology of dedicated PET to the clinical domain by developing a solution for mammography, the ClearPEM [15], [39]. This machine underwent first clinical trials at IPO - Instituto Português de Oncologia in Porto and then moved to ICNAS – Instituto de Ciências Nucleares Aplicadas à Saúde in Coimbra. The next step in this development is the integration of an ultrasonic elastography system into the ClearPEM in order the combine metabolic information from PET with morphologic information from ultrasound. This development, ClearPEM-Sonic, is the aim of this thesis.

## 1.4 Technology Transfer

In the year 2000, CERN decided to introduce an active technology transfer policy in order to identify, protect, promote, transfer and disseminate technologies developed at CERN in the frame of, or in parallel with, particle physics [40].

The adopted process first requires proper evaluation of technologies that have been proposed, either by the inventor or by other experts in the field, for transfer. Once such a technology has been properly identified, it will be assessed by experts at CERN with focus on intellectual property. Then, the necessary steps are taken to protect the technology by appropriate means in order to later promote it actively. During this final step the technology transfer group looks for potential transferees, these being in general industrial partners willing to carry the risk of, and doing the necessary adaptations for, a commercialisation of the technology developed at CERN.

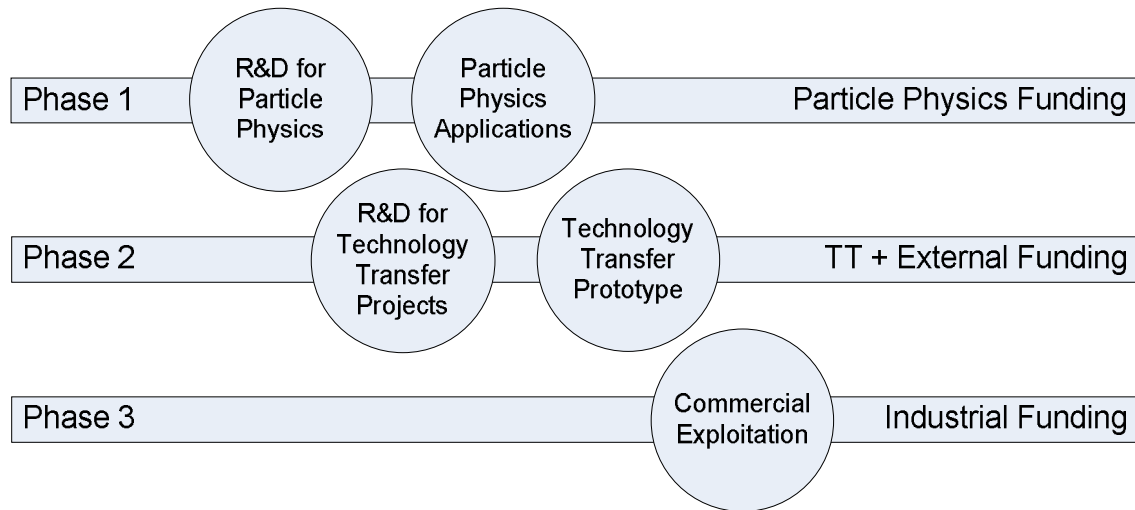


Figure 4 : Phases in the development of technology transfer projects and their financing [40]

Technology transfer can take place in any domain CERN is involved in. The most famous example of a successfully transferred technology, although this occurred some 10 years before technology transfer started to be actively promoted, is the release of the World Wide Web protocol into the public domain. It initiated the development of internet into an essential tool that is now integrated into our daily private and working lives.

CERN has successfully transferred other technologies in a wide range of domains, including: communications and information technology, vacuum technology, electronics, mechanical engineering and medicine. In the medical domain, transfer has been for therapeutic and diagnostic applications. An example for therapeutic applications is the PIMMS study for cancer particle therapy that led to the development of several particle therapy centres in Europe including TERA in Italy and MedAustron in Austria [41]–[43].

Finally, several detector technologies developed over the past years have found diagnostic applications. The work of the Crystal Clear Collaboration is a prime example when scintillating crystal detector technology was applied to small animal PET imaging with the ClearPET and followed by its use in to human breast imaging with the ClearPEM project. ClearPEM-Sonic is the next step in this succession that shall prove the benefits of ongoing crystal research and multimodality integration know-how at CERN.

I have a friend who's an artist, and he sometimes takes a view which I don't agree with. He'll hold up a flower and say, "Look how beautiful it is," and I'll agree. But then he'll say, "I, as an artist, can see how beautiful a flower is. But you, as a scientist, take it all apart and it becomes dull."

[...] Although I might not be quite as refined aesthetically as he is, I can appreciate the beauty of a flower. But at the same time, I see much more in the flower than he sees. I can imagine the cells inside, which also have a beauty. There's beauty not just at the dimension of one centimeter; there's also beauty at a smaller dimension.

in Richard Feynman, *What do you care what other people think?*

## 2 Positron Emission Tomography

Nuclear medicine is a discipline which relies on the decay of radioactive isotopes for diagnostic or therapeutic purposes. It involves the oral or intravenous incorporation by the patient of radiopharmaceuticals that combine a radionuclide attached to a carrier molecule. The carrier molecules are designed to match characteristic properties of the targeted cells, specific to an organ or modified due to an illness. This makes nuclear medicine fundamentally different from most other medical disciplines as it relies on physiological processes on the microscopic level instead of anatomical features on the macroscopic level.

Diagnostic processes imply the use of a radioactive tracer molecule to detect a disease by exploiting changes in the physiological behaviour of a cell or organ. The resulting distribution of radioactivity in the patient's body is then charted with imaging systems based on radiation detectors like gamma cameras, Single Photon Emission Computed Tomography or Positron Emission Tomography [44]–[46].

If an illness can be cured by the local application of radiation, highly targeted radiopharmaceuticals are an option. Standard applications include  $^{131}\text{I}$ -Sodium Iodide therapy for hyperthyroidism and thyroid cancer,  $^{131}\text{I}$ -MIBG for neuroendocrine tumours or palliative bone pain treatment with  $^{153}\text{Sm}$  or  $^{89}\text{Sr}$  [47].

### 2.1 Principle

The basic idea of PET is to measure the distribution of a positron-emitting molecule in the body of the patient or in the part of the body that needs to be imaged. As the positron rapidly annihilates with an electron into two gamma photons emitted in almost opposing directions,

detectors around the body measure simultaneous events within a short coincidence time window. The line that joins the two detectors that have detected simultaneous events is called line of response (LOR). The point where the radiation was emitted is expected to be somewhere along this line.

Most scanners in clinical use are so-called whole-body scanners. As shown in figure 5, the patient lies on a bed in the centre of the field of view (FOV) of a detector ring. As the bed is passed through the PET, an image of the entire patient can be acquired.

The information from the LORs that are acquired during this process is summarized in sinograms that are later used to reconstruct the image. Details of the different components that lead to a PET image and the difficulties to be overcome are discussed in the following sections.

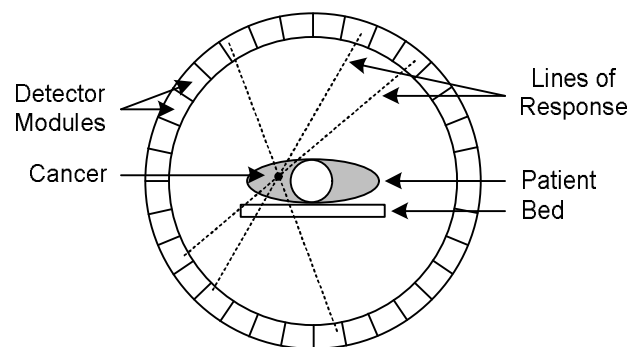


Figure 5 : Basic principle of a full body PET

## 2.2 Medical Interest

Medical imaging modalities can be categorized in several ways, for example by the underlying physical process of image formation, the possibility of 3D imaging or the examination of metabolic processes. According to the diagnostic goal, the clinician will choose the most adapted modality.

Positron Emission Tomography is amongst the preferred applications for 3D imaging of the metabolism in several clinical routines. Some examples from oncology, cardiology and neurology shall be cited.

PET has proven its high sensitivity and specificity in cancer detection [48]. This led to its acceptance for a wide range of oncologic applications and the use of  $^{18}\text{F}$ -FluoroDesoxyGlucose (FDG) as it is the most available tracer molecule used in PET. In the United States of America for example, FDG PET is now fully supported by the public health system for diagnosis, staging, restaging and monitoring response of all tumours with the exception of the initial staging of breast, cervical and prostate cancers or melanomas [49].

The mechanism that makes FDG suitable for oncology is the glucose metabolism of cancer cells as – for many cancer types – they consume a higher amount of glucose than healthy cells without being able to differentiate between normal glucose and FDG. However, some cancer types including certain kinds of lymphoma and well-differentiated neuroendocrine tumours may

not exhibit higher FDG uptake than healthy cells and lead to false negatives. In parallel, the adverse effect of high FDG uptake by non-cancerous cells in the case of a local inflammation can lead to false positives [50]. Therefore, more specific tracer molecules are being developed and used. For example,  $^{11}\text{C}$  marked molecules can image the amino acid transport that is increased in most malignant tumour cells.

In the field of cardiology, the use of PET focuses on myocardial viability studies with FDG or myocardial perfusion along with  $^{13}\text{NH}_3$  and cardiac perfusion with  $^{82}\text{Rb}$  to detect coronary artery diseases.

As around 20 % of the administered FDG accumulates in the patient's brain, FDG PET can be used alongside more specific tracer molecules to detect abnormal uptake for neurologic examinations. This allows the diagnosis and treatment follow-up of dementing neurodegenerative diseases or the differential diagnosis of different types of dementia [49].

## 2.3 Radiopharmaceuticals

The production of radiopharmaceutical tracer molecules requires the proper identification of  $\beta^+$ -decaying radionuclides and of ways to produce those radionuclides. Most are produced through bombardment of a mother target with, for instance, a high energy proton beam from a cyclotron.  $^{18}\text{F}$ , the most common radionuclide, is produced this way:



Table 1 gives an overview of some radionuclides commonly used in PET as well as their production processes. It should be highlighted that most isotopes have rather short half-lives. This requires onsite production and therefore the installation of a cyclotron at the hospital. If such an installation is not available, PET exams are reduced to the use of comparatively long-lived isotopes and therefore, in general,  $^{18}\text{F}$ .

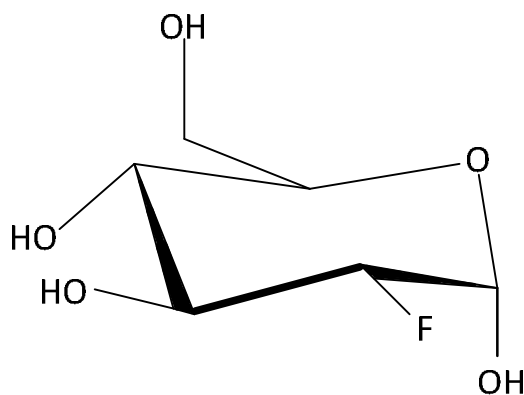


Figure 6 : Chemical Formula of FDG [51]

The radionuclide then needs to be attached to a tracer molecule that is targeted at the physiological process it exploits. A very common approach is the chemical substitution of an atom of a natural or synthetic molecule. In the case of FDG (Figure 6), the hydroxyl group on the 2-carbon of a glucose molecule is replaced by  $^{18}\text{F}$  in order to create 2-Deoxy-2- $(^{18}\text{F})$ fluoro-D-glucose [52]. Such synthesis is done in the hot cell of a chemical laboratory shortly before the radiopharmaceutical is given to the patient through an intravenous injection or inhalation.

Isotope	Half-life (minutes)	Production Process	Tracer Molecule	Clinical Application	Medical Discipline
$^{11}\text{C}$	20.4	Cyclotron	$^{11}\text{C}$ -acetate	Myocardial Perfusion Prostate Cancer	Cardiology Oncology
$^{13}\text{N}$	9.96	Cyclotron	$^{13}\text{N}$ - $\text{NH}_3$	Myocardial Perfusion	Cardiology
$^{15}\text{O}$	2.05	Cyclotron	$\text{H}_2^{15}\text{O}$	Cardiac Perfusion	Cardiology
$^{18}\text{F}$	110	Cyclotron	$^{18}\text{F}$ -FDG	Glucose Metabolism Central Nervous System Disorders	Oncology Neurology
$^{82}\text{Rb}$	1.3	$^{82}\text{Sr}$ generator		Cardiac Perfusion	Cardiology

Table 1 : Common Radiopharmaceuticals for PET, their production process and possible applications [44], [53], [54]

After the exam, the patient has to be kept under surveillance until the radionuclide decayed to a level sufficiently low to prevent radiological exposition of the environment. The effective decay time  $T_e$  of the radionuclide elimination from the patient's body is a function of the physical decay time  $T_p$  and the biological decay time  $T_b$ :

$$\frac{1}{T_e} = \frac{1}{T_p} + \frac{1}{T_b} \quad (2.2)$$

## 2.4 Physical Background

Positron Emission Tomography relies on the physical process of the  $\beta^+$ -decay of a radionuclide. This implies that a proton of the radionuclide will decay into a neutron and emit a positron and a neutrino:

$$^Z_X \rightarrow ^{Z-1}_Y + e^+ + \nu \quad (2.3)$$

Whilst the neutrino is a neutral particle with a very small mass that is usually not detected, the positron is a positively charged particle with properties otherwise similar to an electron. It has sufficient kinetic energy to travel a few millimetres from the emission point. However, the positron will soon combine with an electron of the surrounding tissue. They will annihilate and their combined kinetic and potential energies resulting from their movement and mass ( $E=mc^2$ )



will be converted into photons or kinetic energy. This interaction generally leads to two gamma photons that are emitted in opposing directions:

$$e^+ + e^- \rightarrow 2\gamma \quad (2.4)$$

Due to the conservation of energy and momentum, both gamma photons will have an energy that equals half of the rest energy of the electron-positron pair, i.e. 511 keV. As the momentum of the electron-positron pair is not exactly zero at the moment of the decay, the gamma rays are likely not to be emitted at an angle of exactly 180 degrees. This angular variation has a Gaussian distribution with a full width half maximum (FWHM) of about 0.5 degrees [55].

The first step that leads to the creation of an image is the proper detection of the radioactivity, in the case of PET with scintillating crystals. By definition, scintillation is the emission of visible or ultraviolet light as a response to an external excitation of the material by ionizing radiation. This excitation corresponds to an energy transfer, in the case of medical imaging application, from 511 keV photons.

If a flow of particles penetrates the scintillator, the transmitted intensity  $I(x)$  after a distance  $x$  in the material is:

$$I(x) = I_0 e^{-\mu x}, \mu = \frac{n_e \sigma_e}{Z} \quad (2.5)$$

with  $I_0$  the intensity before entering the material and  $\mu$  the linear attenuation coefficient.  $\mu$  is a function of the electron density  $n_e$ , the atomic number  $Z$  as well as the total absorption cross section  $\sigma_e$ .  $\sigma_e$  itself is the sum of the cross sections for the photoelectric effect, the Compton effect and the pair production. In the case of the photoelectric effect, the incident gamma photon transfers all its energy to an electron in the crystal. The Compton effect is an inelastic scattering process between the gamma photon and an electron where part of the photon energy is transferred to the electron and the photon deflected from its original trajectory. Whilst the photoelectric effect is dominant for lower energies, the Compton effect gains in importance for energies between 0.5 and 1 MeV. Pair production leads to the creation of an electron-positron pair. It occurs only at energies above 1.02 MeV and can be neglected in PET.

## 2.5 Technology

### 2.5.1 Scintillating Detectors

Scintillating detectors combine a scintillating crystal that emits visible or near-UV light and a photodetector that converts the light emitted in the scintillator into an electrical signal. This signal can later be treated by the electronics and ultimately be recorded.

Inorganic crystals are the scintillating material of choice for PET due to the heaviness of their atomic constituents, their high density and therefore high gamma ray stopping power. Out of the available crystals, the most suitable exhibit the best combinations of high and fast light emission as well as cost-efficiency. Table 2 lists the most common in commercial applications. The principle of inorganic scintillating crystals is explained in section 4.1 of this thesis.

	<b>NaI:Tl</b>	<b>L(Y)SO</b>	<b>BGO</b>	<b>GSO</b>	<b>LuAP</b>
<b>Density</b> [g/cm <sup>3</sup> ]	3.67	7.4	7.13	6.71	8.34
<b>Z<sub>eff</sub></b>	50.8	66	75.2	59.4	64.9
<b>Photo Absorption Coefficient</b> @511keV [cm <sup>-1</sup> ]	0.058	0.28	0.336	0.175	0.29
<b>Decay Time [ns]</b>	10	40	300	60, 600	18, 200
<b>Light Output</b> [ph/MeV <sup>1</sup> ]	43000	27000	8200	12500	11400

Table 2 : Typical inorganic crystal scintillator materials in PET [56]

The light emitted by the crystal is collected by a photodetector. This can either be a classical photomultiplier (PMT), like in most commercial full-body PETs, or a more advanced technology like avalanche photodiodes (APD) or Geiger-mode APDs, which are also called silicon photomultipliers (SiPM). In a PMT, the light that strikes the cathode window produces electrons by the photoelectric effect. An electrical field accelerates them towards an electron multiplier that consists of a succession of dynodes: electrodes that allow the production of further electrons as a result of secondary electron emission. The signal is thereby amplified and remains proportional to the initial current created by the light reaching the cathode window and therefore to the energy deposited by the gamma photon in the crystal.

Amongst the main disadvantages of a PMT are its sensitivity to magnetic fields and its size. Thus, APDs are of increasing interest for PET applications. Their smaller size allows their integration into dedicated machines and their insensitivity to magnetic fields makes them interesting for PET-MRI (Magnet Resonance Imaging) applications. However, their gain and noise statistics are worse than for PMTs. An alternative to both PMTs and classic APDs are SiPMs. A SiPM is made of thousands of microscopic APD pixels that operate in Geiger-mode and are read in parallel. Assuming that each microscopic pixel is fired by only one photon of the impinging light, it is thereby possible to achieve dynamic ranges between one and several thousand photons. This technology is under investigation by several laboratories worldwide. They combine the advantage from APDs, which are insensitive to magnetic fields, with the high gain and much lower noise from a PMT [57].

The signal generated by the photodetector is then amplified by appropriate electronics. Energy-dispersive discriminators reject events that are of unwanted energies. This is particularly important because if a gamma photon deposits energy lower than 511 keV, it is either not related to a  $\beta^+$ -decay or has lost energy during its flight and thus been scattered by Compton

interaction. Photons that deposit energy above 511 keV should also be rejected as they belong either to background noise or multiple events in the scintillator. The energy window should thus be kept as narrow as possible around the 511 keV photopeak. This contributes to the overall signal quality as it rejects both noise and scattered gamma photons. The signal is finally analysed and stored for later evaluation.

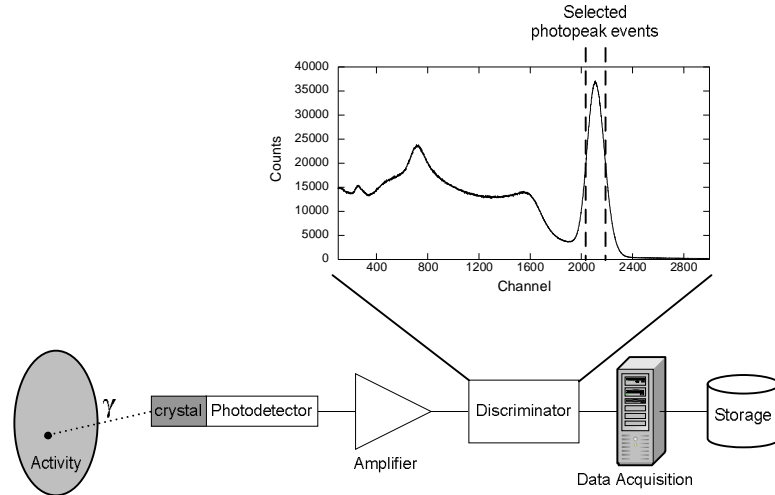


Figure 7 : Scintillation detector. The figure shows which events are selected in a full energy spectrum.

### 2.5.2 Localisation of the Interaction within the Detector System

In most PET systems, the detectors are arranged around the patient in such way that the crystals face him whilst the photodetectors face away. This avoids that gamma rays interact in the photodetector before they reach the crystal. It increases the signal-to-noise ratio (SNR):

$$SNR = \frac{I_{signal}}{I_{noise}} \quad (2.6)$$

If every crystal is connected to a single photodetector, it is easy to know where in the detector system the interaction took place. This technique, combined with sufficiently small crystals, is used in most dedicated PET applications including small-animal PETs.

However, there are configurations where either one crystal is connected to many photodetectors or where, on the other hand, many crystals are connected to fewer photodetectors.

In the first case, a centre of gravity algorithm can be used to determine the exact point of interaction [54]. As shown in figure 8, several PMTs will record light from the interaction. However, the amount of light recorded by each PMT varies according to the proximity of the PMT to the interaction point in the crystal. By weighting the light quantities  $S_i$  in the different PMTs with the relative distances  $x_i$  of the PMTs from the centre of the crystal, it is possible to reconstruct the interaction point of the gamma photon in the crystal:

$$\bar{x} \propto \sum_i x_i S_i \quad (2.7)$$

With increasing computing power, centre of gravity algorithms have been replaced by maximum likelihood estimators or trained neural networks.

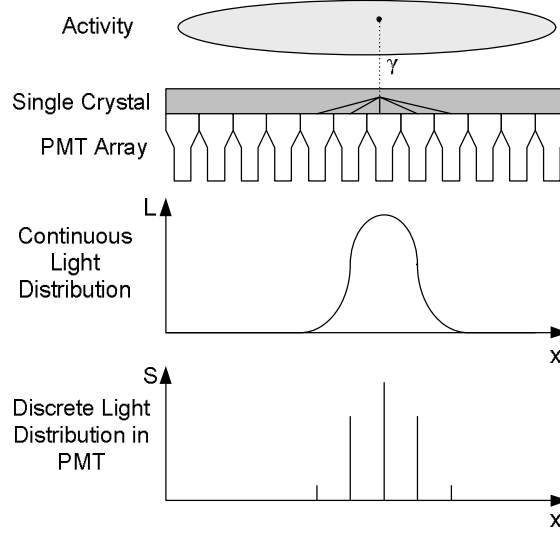


Figure 8 : Light distribution in a multi-PMT setup

Another common approach, introduced by CTI (Computer Technology and Imaging) in 1986 [58], is to reduce the number of photodetectors by using more crystals than photodetectors. Therefore, good crystal segmentation can be kept without putting too many constraints on the miniaturisation of the photodetectors. It requires a light guide between the crystal and the photodetector. This guide distributes the light between the photodetectors in a way which allows proper identification of the crystal which absorbed the gamma photon (Figure 9).

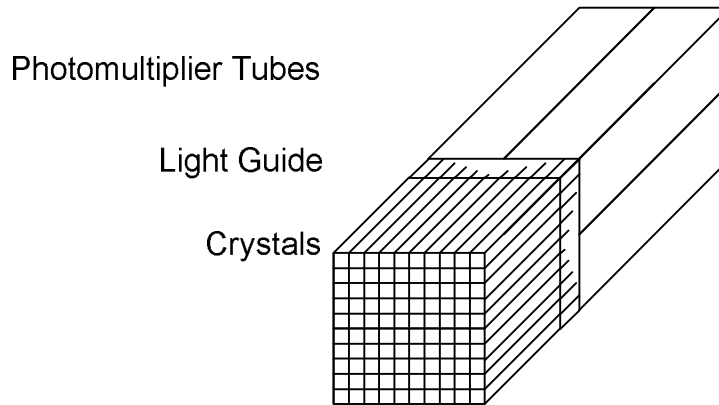


Figure 9 : CTI-type multi-crystal configuration

### 2.5.3 Image Reconstruction

Each LOR acquired during an exam is characterized by its angle of orientation with respect to the horizontal plane and its shortest distance to the centre of the gantry. It is therefore possible to create a two-dimensional graph that plots the angular orientation as a function of the displacement. Figure 10B illustrates how such a plot is created with the information from the LORs from figure 10A. For instance, LOR A has an angle of 0 degrees from the horizontal plane and is at a distance  $x_A$  from the centre of the gantry. This leads to the creation of a point of coordinates  $(x_A, 0)$ .

If a large number of LORs that pass through the same point are plotted this way, the result is half of a sine wave. This graph is called a sinogram. The superposition of LORs emanating from different points leads to a complex sinogram with overlapping sine waves (Figure 10C).

Each 2-dimensional acquisition plane that is defined by detectors facing each other produces a dedicated sinogram. Each horizontal row in such a sinogram represents all parallel LORs from this plane with varying distances from the centre of the gantry. Each point in the sinogram represents the number of events measured along one LOR [59].

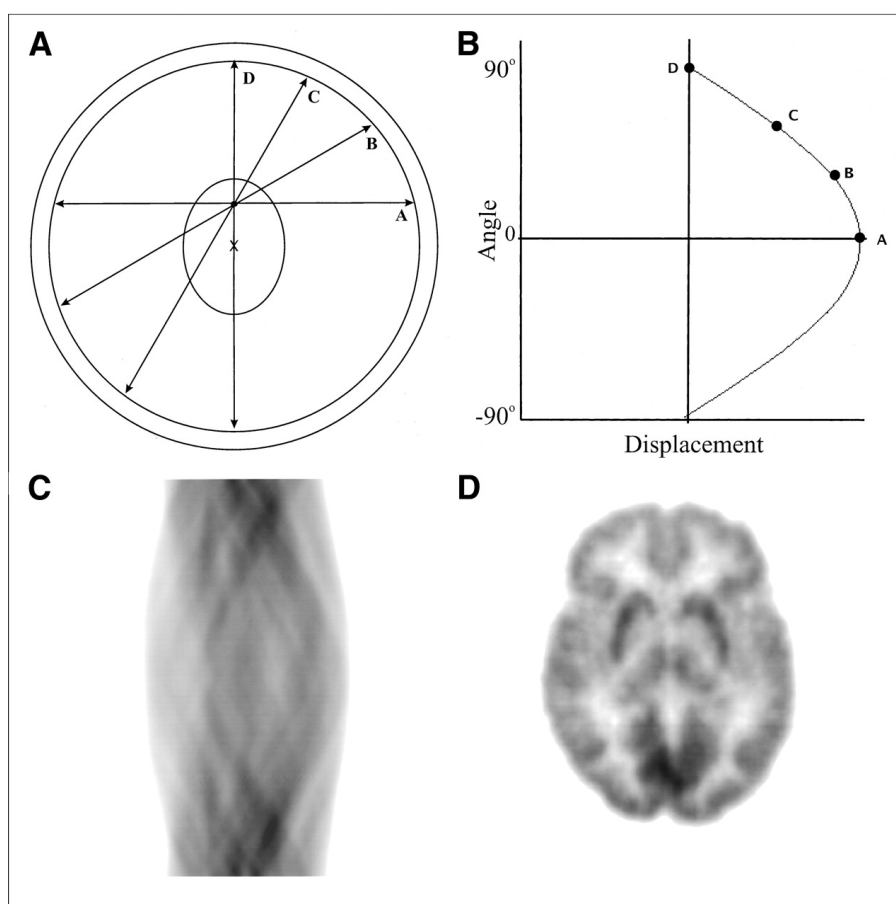


Figure 10 : Sinogram formation and image reconstruction [59]

The information from the sinograms is used for image reconstruction. The two possible approaches are either back-projections or iterative solutions.

The classical method that consumes less computing power is back-projection. In this case, each point in the sinogram is projected on the plane as a line with uniform intensity. Large, bright spots appear at points where many such lines intersect. Due to the uniform back-projection, such an image is quite blurred. By using appropriate filters, the region where such a line is back-projected can be restricted and the image noise reduced. Filtered back-projection (FBP) has been the method of choice for PET image reconstruction for many years. As more powerful computers became available for routine clinical use, iterative algorithms began replacing filtered back-projection. Indeed, they provide better lesion detectability [60]–[63].

Yet, if the detector system is sufficiently fast to register time-of-flight information, the region where the information is back-projected can be reduced to the one defined by the coincidence time resolution. This approach is now being implemented by several research groups and industrial companies and leads to a return of FBP as a method of reconstruction [64].

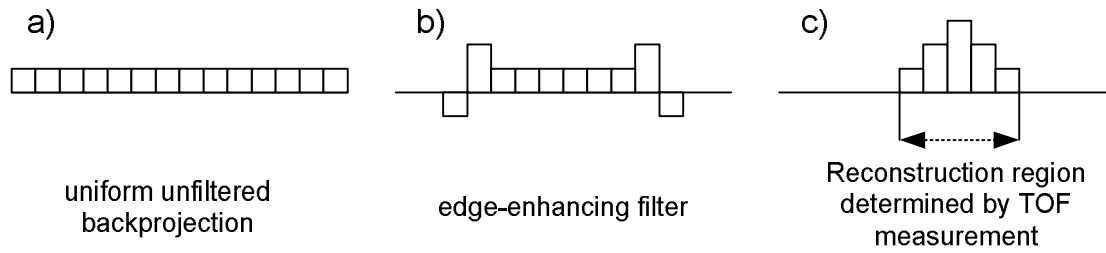


Figure 11 : 1-dimensional backprojection a) without use of filters, b) with filters, c) with time-of-flight information

Iterative algorithms rely on statistical models for the distribution of image information [60]. The basic idea is to divide the plane that will be reconstructed into a finite number of pixels and to assign them an initial brightness. This brightness can be a random value or given by a preliminary FBP. The next step is to calculate the sinograms for this initial distribution and to compare them to the measured sinograms. If the initial brightness values were correct, the two would match. As it is not the case, the initial data is modified according to the differences between the datasets. This process can be repeated until the reconstruction is judged acceptable.

With PET, it is possible to either acquire LORs from dedicated planes that are parallel to each other or to also include LORs from events triggering detectors on different planes. In the first case, all data is 2-dimensional and the planes to be reconstructed to form a 3-dimensional sliced image are well defined. In the second case, it is possible to use complex and time-consuming algorithms that handle 3D reconstruction. The general, faster approach is to rebin the 3D data into 2D planar datasets. This process involves loss of information yet yields, combined with iterative reconstruction algorithms, results that are comparable to the complicated 3D reconstruction [65].

## 2.5.4 Image Quality

### 2.5.4.1 Attenuation

The intensity of an electromagnetic wave transmitted through a layer of material with thickness  $x$  and attenuation coefficient  $\mu$  is related to its initial energy via the Beer-Lambert law:

$$I(x) = I_0 e^{-\mu x} \quad (2.8)$$

This property also applies to the passage of gamma photons through the body of a patient that are attenuated, either due to absorption or scattering. The measured signal will therefore be attenuated and lead to an underestimate of the radioactivity from the edge to the centre of the body.

If PET is used as a stand-alone modality, a transmission scan with a small radioactive source gives the  $\mu(x,y)$  values needed to correct the image. In the case of PET/CT, the CT image information is used.

### 2.5.4.2 Unwanted Coincidences

Three types of coincidences are recorded during a PET scan:

- true coincidences of gamma photons from the same annihilation that reached the detector without scattering. They contribute to the signal.
- scattered coincidences of gamma photons from the same annihilation that were scattered in the tissue. They contribute to the noise.
- random coincidences of gammas from different annihilations that also contribute to the noise.

The signal-to-noise ratio can be expressed as a function of true  $T$ , scattered  $Sc$  and random  $R$  coincidence rate [66]:

$$SNR \propto \sqrt{\frac{T^2}{T + R + Sc}} \quad (2.9)$$

The optimization of the signal-to-noise ratio therefore implies minimization of the scattered and random coincidences. If only 2-dimensional planes are acquired, septa can be used to reduce the amount of scattered and random coincidences. Septa of lead or tungsten act as a retractable collimator and separate each crystal ring from its neighbours. Therefore, only coincidences between detectors on the same ring are recorded. Events that would contribute to oblique LORs are absorbed by the septa.

In the case of 3-dimensional event acquisition, septa cannot be used. In this case, scatter can be reduced by discriminating events where at least one of the photons had energy substantially lower than 511 keV and therefore lost energy during previous scattering. This puts constraints on the energy resolution of the crystal, requiring noise-free subsequent signal shaping and

suitable discrimination algorithms. A possible approach is to weight the contribution of LORs according to the energies of the events. In this case, the importance accorded to each LOR would diminish with diminishing energies of the photons [67].

The random coincidence rate  $R$  is the product of the coincidence window  $\tau$ , defined as the maximum time difference between two events, and the individual count rates  $S^+$  and  $S^-$  from opposing detectors in coincidence [60]:

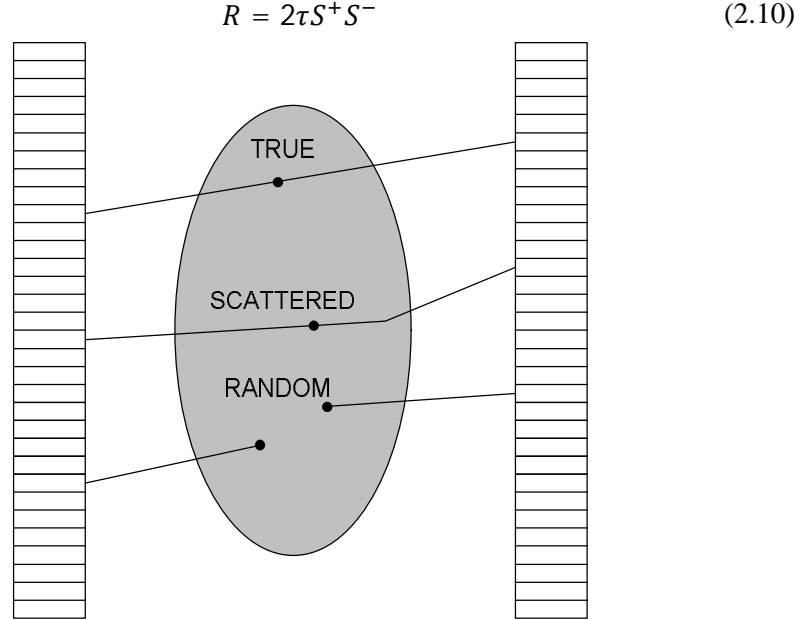


Figure 12 : Illustration of the possible coincidences: true, scattered and random

If the activity increases, the true detection rate increases linearly while the random coincidence rate increases squared. The coincidence time therefore plays a crucial role in random coincidence reduction. The coincidence window needs to be sufficient to allow all true coincidences to be detected. It increases therefore with the distance between the detectors. It shall also be kept small enough to not include too many random events. The major constraint in this balance thus lies on the speed of the detector, which is determined by the decay time of the scintillator as well as the speed of the front-end electronics. Time-of-flight measurement also influence this as it allows more precise determination of the position of the emission point and therefore excludes random emissions from regions known not to have any activity.

#### 2.5.4.3 Parallax Error

In the case of events at the margin of the field of view of a full-body PET, the photons penetrate the crystals at an oblique angle. The same happens in parallel-plate configuration PETs, such as the ClearPET, for events whose photon emission is not perpendicular to the PET plates. As shown in figure 13a), this leads to the computation of false LORs that do not pass through the spot of annihilation.



The parallax error is reduced if the depth of interaction (DOI) information is available. This implies that it is possible to determine with sufficient precision where along the crystal axis the interaction takes place. Two common techniques are the phoswich detector and light readout at both ends of the crystals. In the case of a phoswich detector, crystals with different light emission properties are combined and read out by a single photodetector. The characteristics of the emitted light indicate which crystal emitted the light. The main limitation of this technique is that the precision depends on the number of different crystals used to make the phoswich.

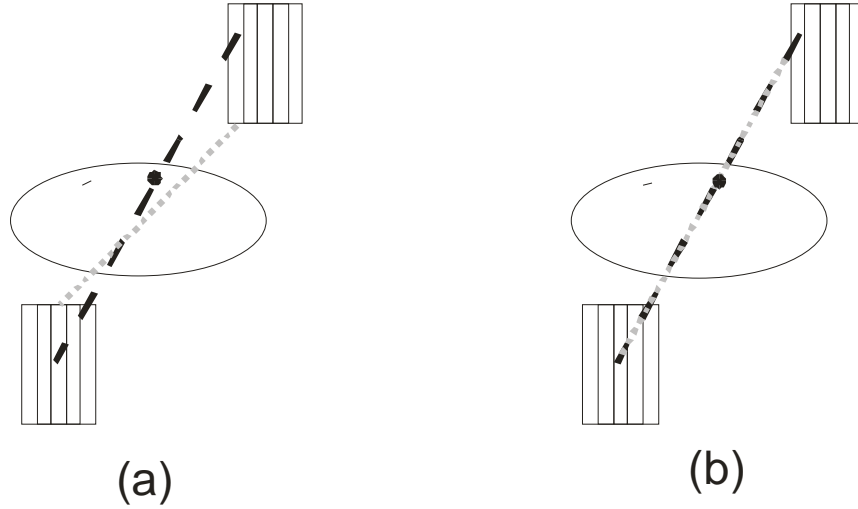


Figure 13 : Illustration of the parallax error (a) without information about the depth of interaction and (b) with information about the depth of interaction

The second technique relies on light absorption in the crystal. The light is collected with two photodetectors, one at each extraction surface. As the absorbed amount increases with the path of the light until it reaches an extraction surface, the photodetector closer to the photoelectric event will measure a higher amount of light than the one that is farther away. Analysis and comparison of the measured light quantities at each extraction surface allow determination of the interaction point. This technique is explained in further details in section 4.2.3.

## 2.6 State of the art

### 2.6.1 Human Whole-body PET

Most clinical routine and research installation are whole-body PETs supplied by one of the major multinational companies: General Electrics, Philips or Siemens. Having incorporated the smaller companies that initially developed PET during the last decade, they share the market of new installations. When PET/CT was introduced in 2000 [9], the obvious advantages of combining metabolic information from PET with anatomical information from the CT soon established this multimodality device as a new standard.

Siemens established itself as distributor in 1986 and later partner of CTI PET System Inc. before buying the company in 2005 [4], [68]. The company now sells the Biograph TruePoint PET-CT and Biograph mCT so-called molecular CT series. Both feature PMT-readout LSO crystals and HD-PET technology, a commercial name for the use of measured point-spread-functions to reduce the parallax error during iterative image reconstruction [69]. With the Biograph mCT, Siemens created a compact PET-CT and introduced time-of-flight measurement [70]. In clinical routine, the coincidence time resolution is measured to be 527 ps FWHM while the spatial resolution can be expected to be around 4 mm FWHM [71].

General Electrics entered the market after purchasing Scanditronix in 1990. Their current product line of Optima and Discovery PET/CT uses BGO or LYSO crystals that are readout by PMTs [72]. The most recent LYSO-based model, Discovery 690, incorporates time-of-flight measurements. The coincidence time resolution is around 550 ps FWHM, with an image resolution of 5 mm FWHM [73].

Philips' current line of products includes the Gemini LXL, Ingenuity and TF PET/CT scanners. Gemini TF is based on LYSO crystals that are coupled to PMTs. It integrates time-of-flight measurement with a coincidence time resolution of 585 ps FWHM. The spatial resolution is measured to be 4.8 mm FWHM at the centre of the FOV with a NEMA phantom [74].

Asides the technological improvements of the PET part, all companies provide their latest CT developments and image treatment and analysis workstations in their PET/CT products. There is also an important effort in providing systems with bigger gantry diameters to easier accommodate overweight patients.

The research amongst industrial providers therefore focuses more on software improvements and faster electronics that allows time-of-flight acquisition than detector technology. However, cost-efficient use of faster crystals and electronics can be expected in future PET/CT scanners, where research will focus more on increasing the overall system sensitivity rather than improving the image resolution to a greater extent. This will allow shorter examination times with similar tracer concentrations or lower tracer concentrations and therefore radiation exposure if the total examination time is kept constant. Another development is the fusion of PET and MRI made possible by APD-based radiation detectors reaching the stage of commercialisation [10].

## 2.6.2 Small Animal PET

Pre-clinical research involves small animal studies, mostly on rodents but also on small primates, due to the need for trials in living beings for pharmacology as well as genetic and pathologic investigations. In the last years, the interest in in-vivo studies on the molecular level leads to the development of dedicated imaging systems including PET, SPECT and CT. Indeed, human PETs are often not available for animal studies. Additionally, image resolution for small animal images should be better than for humans as the imaged organs are much smaller.

The use of nuclear medicine has the clear advantage of performing studies on the animal without needing to sacrifice it. This of course allows substantial savings as the number of animals needed can be drastically reduced. Its main value however is of scientific interest. It is

for example possible to observe metabolic processes in-vivo during the image acquisition, information quite valuable to study the distribution of a drug in the body. Sparing the animal also has the advantage of studying its evolution over a longer period of time. It is then possible to assess the animal's response to a treatment, for example against cancer.

Several competing systems have been developed over the past years, which are now being commercialised. Siemens offers the Inveon system. It is a modular small animal imaging platform that allows the combination of dedicated PET, SPECT and CT in a single machine. This LYSO crystal-based PET is an evolution of the microPET and provides an image resolution of 1.9 mm in the centre of the FOV and 2.2 mm at 40 cm offset with sensitivities of up to 9.3 % [75], [76].

General Electric's Triumph is also a multimodality PET/SPECT/CT system, designed in collaboration with Gamma Medica-Ideas. The machine integrates the X-PET design that is based on a BGO scintillator ring with spatial resolution of 1.6 mm and sensitivity of 10 % at the centre of FOV [77]. Gamma Medica-Ideas also offers the LabPET, whose design is based on LYSO/LGSO phoswich detectors with APD readout. It features 1.4 mm image resolution in the centre of FOV and 2.1 mm at the edge of the FOV and sensitivities around 2.1 % [78].

Mediso Medical Imaging Systems offers the nanoScan family of small animal imaging systems. It includes PET, SPECT, MRI and CT in various combinations. The PET features an image resolution of 700  $\mu\text{m}$  and a global system sensitivity of 9 % [79].

Philips finally has the MOSAIC small animal PET. It is based on GSO crystals read out by PMTs and features an 18 cm wide FOV that allows rapid scanning of rodents and bigger animals. It features image resolution of 2.7 mm at the centre of the FOV and 3.2 mm at a radial offset of 45 mm. The global system sensitivity is around 1.2 % [80].

Many other research groups have developed small animal PETs that should be seen as technology demonstrators, although some of them are commercialised in very small units.

The HIDAC-PET developed by Oxford Positron Systems is amongst the rather exotic designs, as it uses gas multiwire proportional chambers [81]. This allows excellent spatial resolution in the domain of 1 mm at the centre of FOV, the drawback being lower sensitivity which is less than 1 % [82]. Another system is the YAP-(s)PET that uses two times two opposing detector heads that rotate around the animal. This reduces the overall cost of the system yet keeps satisfying image resolution of 1.5-2.0 mm at acceptable sensitivity between 1 and 2 % [83].

The Crystal Clear Collaboration also developed a small animal scanner: the ClearPET [36]–[38]. It is now being commercialized by the German company Raytest GmbH.

#### 2.6.2.1 *ClearPET*

Since 1995, in the frame of technology transfer from high energy physics towards life sciences, one of the main focuses of the Crystal Clear Collaboration was the development of novel scintillators for medical imaging. This research led to the development of Cerium-doped Lutetium Oxyorthosilicate (LuAP) and Lutetium Yttrium Oxyorthosilicate (LuYAP) crystals.

This knowledge was then used for the development of a technology-demonstrator small animal PET, the ClearPET.

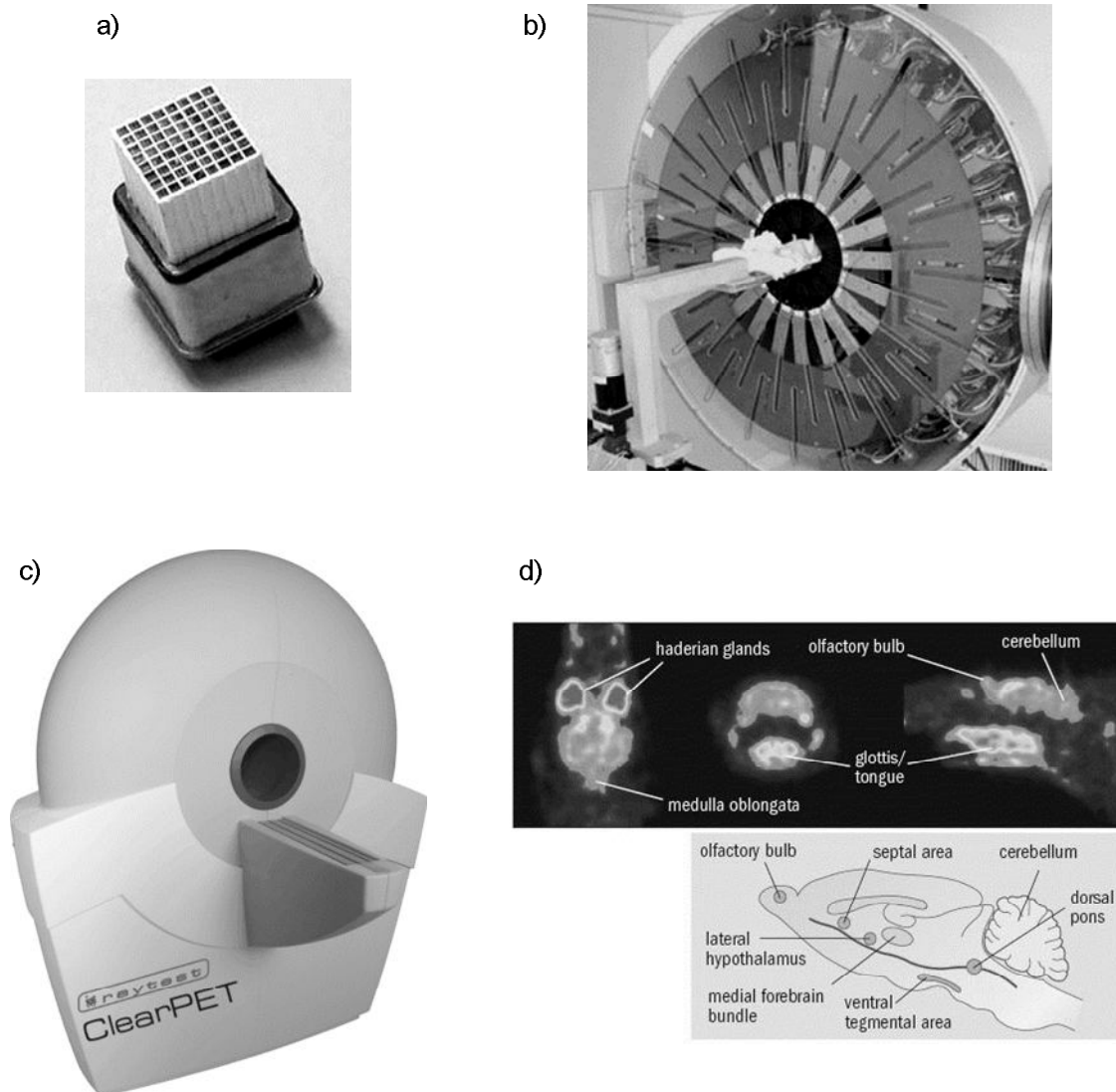


Figure 14 : ClearPET: a) detector module, b) ClearPET Neuro at FZ Jülich, c) Raytest ClearPET, d) image of a rat brain with FDG from FZ Jülich [84]

ClearPET is based on multichannel PMTs produced by Hamamatsu. The R7600-M64 PMT incorporates 8x8 individual channels with a detector window size of  $2 \times 2 \text{ mm}^2$  into a single housing. This improves the resolution as each detector pixel can be readout individually. In order to reduce the parallax effect whilst having sufficiently long pixels that have enough stopping power for 511 keV gamma photons, a phoswich arrangement of LSO and LuYAP was chosen. Each pixel is made of a  $2 \times 2 \times 10 \text{ mm}^3$  LSO pixel coupled to a  $2 \times 2 \times 10 \text{ mm}^3$  LuYAP pixel that is itself coupled to the PMT. The individual pixels are separated by a matrix of reflecting material. Four detector heads are fit with front-end readout electronics and assembled into a cassette. 20 such cassettes are placed on a circular gantry. They are laterally shifted by 7 mm to each other and rotate on the gantry around the animal. This allows best coverage of the FOV.

The FOV diameter can be varied between 135 mm and 285 mm to allow both small and medium size animals to be imaged. Free-running ADCs sample the signal at a rate of 40 MHz. Data is stored in list-mode format.

The current generation of the commercial ClearPET has a maximum sensitivity of 3.8 % and spatial resolution of 1.25 mm at the centre of the FOV.

### 2.6.3 Dedicated Human PET

Besides small animal PET, human PET designs dedicated to certain body parts are the other application of PET detector research. Most groups developing new or improved detectors and electronic designs look for human applications, generally dedicated to breast or brain imaging, with prostate imaging emerging as a new field of interest.

The idea is to develop machines with a much smaller FOV adapted to the organ. As the imaged volume is much smaller than in a whole-body PET and the detectors much closer to it, the general sensitivity can be increased. Second, new technologies can easier be implemented as fewer detectors are needed and therefore reduce the global price compared to the amount needed for whole-body application.

Due to the ease of access, most developments focussed on breast cancer detection. Such Positron Emission Mammography (PEM) prototypes generally rely on one or two pairs of parallel detector plates. There are currently two commercial models: the PEM Flex by Naviscan Inc and the Mammi BreastPET by Oncovision.

The Naviscan PEM Flex features LYSO crystals coupled to position-sensitive PMTs in two parallel paddles that are used to compress the breast [12]. This prevents plate rotation around the breast. Naviscan Flex thus provides only limited-angle, focal-plane tomography and not full 3D tomography. The PEM flex has been installed in several oncology institutions around the world and clinical studies were performed. On the technical side, the machine features FWHM spatial resolution of 2 - 2.4 mm for images parallel to the detectors plates and FWHM spatial resolution of 6.5 - 8 mm for images perpendicular to the detector plates. The total system normalized sensitivity has been characterized to be about 0.15 % [85], [86]. First clinical results published by Berg et al. in a preliminary multicentre trial on 77 patients with a total of 92 lesions showed the Naviscan Flex has a sensitivity of 91 % and a specificity of 93 % for breast cancer [87]. These rather promising values can be compared with sensitivities between 60 % and 80 % and specificities between 74 % and 95 % obtained with standard screening techniques [88].

The Mammi BreastPET is based on continuous LYSO crystals coupled to position-sensitive PMTs [89]. It features twelve modules that are arranged in a circular geometry, around the breast. The woman lies in prone position on a special bed and inserts the breast into the ring. The ring moves along the breast to scan the whole region of interest. The spatial resolution is 1.90, 1.82 and 1.63 mm in the radial, tangential and axial profiles, respectively. The system's average global detection sensitivity is 0.77 %. First clinical studies are ongoing.

Alternative designs include the LBNL PEM camera that features two pairs of parallel detector plates and includes DOI readout, the CYBPET cylindrical PEM as well as the ClearPEM

developed by the Crystal Clear Collaboration [15], [90], [91]. The latter will be described in detail in section 3.2.

The next step in the development of dedicated PET is research on endoscopic systems. Both the endoTOFPET-US project [92] and the high resolution fast stereotactic PET Imager designed at West Virginia University (WVU) [13] work on the design of a miniature PET probe that can be inserted into the patient's body and detects radioactive decays in coincidence with an external detector. While the WVU project aims at prostate exams, endoTOFPET-US will develop systems for both prostate and pancreas exams. The main difficulties to overcome are the miniaturization of the whole acquisition chain in the endoscopic probe and the low sensitivity due to this miniaturization. Technical innovations include the use of highly efficient SiPMs, crystals fibres, time-of-flight and depth-of-interaction measurement as well as dedicated reconstruction algorithms that take the limited angle of view into account [93].

Paresseuse odalisque, arrière!  
Voici le tableau dans son jour,  
Le diamant dans sa lumière ;  
Voici la beauté dans l'amour!

Sa tête penche et se renverse ;  
Haletante, dressant les seins,  
Aux bras du rêve qui la berce,  
Elle tombe sur ses coussins.

Ses paupières battent des ailes  
Sur leurs globes d'argent bruni,  
Et l'on voit monter ses prunelles  
Dans la nacre de l'infini.

in Théophile Gautier, *Le poème de la femme*

### 3 The ClearPEM-Sonic Project

ClearPEM-Sonic is a multimodal breast imaging device that combines the dedicated positron emission mammograph ClearPEM [15], [16] developed by the Crystal Clear Collaboration with the ultrasound elastography system Aixplorer developed by the French company SuperSonic Imagine [17]. It is developed in the frame of CERIMED, the European centre for research in medical imaging.

ClearPEM-Sonic shall combine the advantage of metabolic PET imaging with the morphologic and structural information provided by ultrasound and elastography. After an introduction about breast cancer, the involved techniques will be discussed in detail. Finally, the objectives of this project will be detailed.

#### 3.1 Breast Cancer

“If thou examinest a man having bulging tumors on his breast, and if thou puttst thy hand upon his breast upon these tumors, and thou findest them very cool, there being no fever at all when thy hand touches him, they have no granulation, they form no fluid, they do not generate secretions of fluid, and they are bulging to thy hand. Thou shouldst say concerning him: One having bulging tumors. An ailment with which I will not contend”.

This description of a breast disease is taken from an ancient Egyptian medical papyrus dating back to the 16<sup>th</sup> century before our era, discovered by Edwin Smith in 1862 and translated into English by James Breasted at the beginning of the 20<sup>th</sup> century [94], [95]. Although it is not known whether the condition that is described in this excerpt is breast cancer, it is widely

recognized as the first written mention of breast diseases with symptoms similar to breast cancer and cited by some scholars as the first ever mention of breast cancer in the history of medicine. The three and a half thousand years following the aforementioned description led to the medical discoveries and understanding of the human body that today allow proper identification of cancerous diseases and their therapy. It is now known that, after lung and gastric cancers, breast cancer is the most frequent cancer amongst human. Due to its relative ease of diagnosis and treatment, it is part of standard health policies in most developed countries to perform routine examinations of the female breast with the goal of detecting tumours as early as possible to provide optimum treatment.

This section provides some fundamental medical information about breast cancer. If not stated otherwise, the information is taken from *Breast Cancer – a practical guide* by Orlando Silva et al. [96].

### 3.1.1 Epidemiology

Epidemiology is, according to Webster's New Encyclopedic Dictionary, the "branch of medical science that deals with the rate of occurrence, distribution, and control of disease in a population". This definition implies that it is based on statistical findings that vary not only in function of objective criteria including the geographic delimitation, age or previous medical history of the population that was studied but also according to the interpretation one makes of it. The following data can therefore not be seen as an absolute truth but give an idea of the prevalence of breast cancer and its cure rates in today's developed countries [97]–[100].

Breast cancer is not only the third most frequent cancer amongst human, it is also the most frequent cancer amongst women and accounts for up to 23 % of all cancer cases in female patients. Indeed, although men can also contract breast cancer, a woman is around 135 times likelier to contract the disease. The surveys presented in [97]–[100] estimate the risk of a female patient in contracting it during her lifetime between 8 % and 11 %, based on life expectancies between 70 and 90 years. The probability to develop a malignant tumour in the breast region increases with the age of the patient.

Although there is no absolute correlation between anterior lifestyle, diseases or genetic predispositions and the incidence of breast cancer, a number of risk factors can be outlined. For instance, the risk increases with early menarche and late menopause, however decreases if the patient was young when giving birth to her first child.

There also might be a correlation between the use of postmenopausal hormone replacement therapy (HRT) and the risk for breast cancer. Indeed, several studies summarized by Hindle et al. in [100] or Silva et al. in [97] indicate there could be a higher relative risk, evaluated to be between 1.4 and up to 11.3 times greater. However, both also cite concurrent studies that came to the conclusion of no correlation between the use of postmenopausal HRT and breast cancer.

The use of contraceptives, coffee, alcohol, cigarette consumption or specific diets has no proven influence on the probability to develop breast cancer.



<b>Risk Factor</b>	<b>Control Group</b>	<b>Relative Risk increased by a factor of:</b>
<b>Early Menarche: 11 yrs</b>	16 yrs	1.3 – 1.5
<b>Age at First Birth : &gt; 30 yrs</b>	< 20 yrs	2-3
<b>Late Menopause: &gt; 55 yrs</b>	45-55 yrs	1.5
	< 45 yrs	2
<b>Premenopausal Oophorectomy</b>	No Oophorectomy	0.3 – 0.4
<b>Postmenopausal HRT</b>	No HRT	1 – 11.3
<b>Irradiation &gt; 1Gy</b>	No irradiation	3 – 4
<b>Family History: 1 relative affected</b>	No relatives affected	1.4 – 3
<b>&gt; 1 relative affected</b>		4 – 6
<b>Anterior Breast Cancer</b>	No Anterior Breast Cancer	5
<b>Anterior Proliferating Breast Diseases</b>	Healthy Breast	2 – 4
<b>Age Group: 30-39</b>	20-29	7.8
<b>40-49</b>		24
<b>50-59</b>		36
<b>60-69</b>		48
<b>70-79</b>		55

Table 3 : Isolated breast cancer risk factors [97]–[100]

Family histories of breast cancer patients increase a woman's risk of developing breast cancer. Although the relative risk varies according to the studied population, the number of affected parents, the degrees of relation with the affected parents and the severity of the affections, it can be situated between a factor of 2 and 6. Genetic studies in the 1990s allowed the identification of BRCA1 and BRCA2, two tumour suppressor genes associated to higher breast cancer risk if mutated. They allow scientific confirmation of the abovementioned statistical findings, confirming hereditary breast cancer.

Finally, female patients with some anterior breast diseases, especially atypical hyperplasia or other proliferative diseases, have an up to 4 times higher risk of developing breast cancer. In the case of previous breast carcinoma, the risk is 5 times higher.

### 3.1.2 Pathology

The female breast is the only human gland dedicated to the survival of the species rather than of the individual. Indeed, it is responsible for producing milk that is adapted to the diet of a newborn. Figure 15a) shows an image of a healthy breast. The breast rests on the surface of the pectoralis major muscle (F) and is lodged against the rib cage (G). Its main components are fatty tissue (E) as well as lobules (B) that produce milk. This milk is then carried via lactiferous ducts

(A) to the nipple (D). Dilated sections of the ducts (C), in front of the nipple, hold the milk during the breastfeeding period [101].

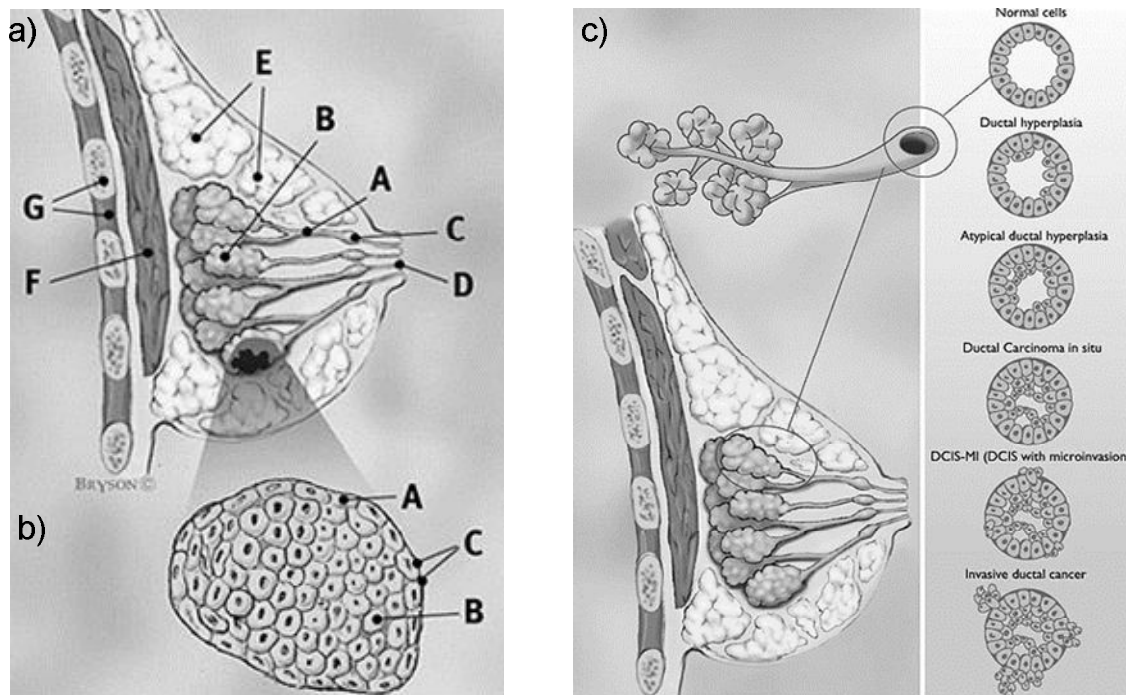


Figure 15 : a) The female breast, b) Lobular Carcinoma In Situ and c) stages of Ductal Carcinoma In Situ [102]

Breast cancer can be divided into non invasive, so-called “in situ” carcinoma as well as invasive carcinoma.

Figure 15b) shows a case of Lobular Carcinoma in Situ (LCIS), the development of cancerous cells in the lobules that produce milk. LCIS involves malignant cell proliferation in the intralobular ductules. This carcinoma has a tendency to multicentricity, which means it appears at several distinct positions at the same time. In 37% of the patients it later leads to an invasive carcinoma. A carcinoma is not invasive if the malignant cells (Figure 15b), item B) do not leave their place of origin close to normal cells (Figure 15b), item A) and do not cross the basement membrane (Figure 15b), item C), a membrane that prevents the spread of malignant cells from the epithelium to neighbouring organs or blood vessels.

Figure 15c) shows a case of Ductal Carcinoma In Situ (DCIS). DCIS is the growth of malignant epithelial cells in the epithel of the lactiferous ducts. It is considered a malignant evolution of atypical hyperplasia and increases the risk for more aggressive, invasive carcinoma by a factor of 8 to 10. It is easiest detected by mammography due to local calcium depositions.

Invasive carcinomas are carcinoma that will spread from their place of origin and eventually affect the lymphatic system and finally create metastases at other places in the body. The most frequent, with a likelihood of about 75 %, is invasive ductal carcinoma. It typically metastasises in bones, the liver and the lungs. Other invasive mammary carcinomas are of invasive lobular, mucinous, medullary, papillary or tubular types [97].

### 3.1.3 Prognosis

The prognosis of long-term breast cancer disease-free survival depends on a number of factors. However, the stage of the tumour, its size and the number of affected lymph nodes or even metastases have a direct influence on it. Additionally, younger age, poorly differentiated tumours or a modification of the BRCA1 gene also worsen the prognosis.

Stage	Tumour Size	Affected Regional Lymph Nodes	10-yr Disease-Free Survival (%)	
			No Treatment	Optimal Treatment
<b>no cancer</b>	no tumour	none	94	98
<b>very early</b>	< 2 cm	none	92	96
<b>early</b>	In situ	N1	80	90
	< 2 cm	N1	75	87
	> 2 but < 5 cm	none	83	90
	> 2 but < 5 cm	N1	60	80
	> 5 cm	none	50	75
<b>Locally advanced</b>	In situ	N2	50	75
	< 2 cm	N2	60	80
	> 2 but < 5 cm	N2	55	75
	> 5 cm	N1	45	70
	> 5 cm	N2	30	65
	Any size	N3	5	10
<b>Locally advanced</b>	any size with extension to chest wall or inflammatory cancer	none	25	40
		N1	10	30
		N2	5	10
<b>Metastatic</b>	Any size	Any	5	10

N1 = spread to 1–3 axillary nodes, tiny amounts of cancer in internal mammary lymph nodes (near the sternum) detected during sentinel lymph node biopsy, or both; N2 = spread to 4–9 axillary nodes or enlargement of the internal mammary nodes; N3 = Spread to  $\geq 10$  axillary nodes, spread to infra- or supraclavicular nodes or spread to  $\geq 4$  axillary nodes plus tiny amounts of cancer in internal mammary nodes detected during sentinel node biopsy

Table 4 : Breast Cancer Survival Prognosis [47]

Table 4, taken from the 18<sup>th</sup> edition of the Merck Manual of Diagnosis and Therapy [47], gives an idea of the prognosis for a 10 year disease-free survival in function of the size of the tumour and the number of affected regional lymph nodes as well as under the assumption of optimal treatment or no treatment. It clearly shows that the chances for survival are directly related to the stage of the tumour and therefore its size and number of affected lymph nodes. Indeed, if the cancer is smaller than 2 centimetres and had only limited effect on regional lymph nodes, survival rates are only a few percentage points lower than if the patient had not had breast cancer.

This leads to the direct conclusion that breast cancer shall be detected at an as early stage as possible to allow optimum treatment and justifies, combined with the breast cancer incidence amongst the female population, the importance of breast cancer screening.

### 3.1.4 Screening

The pathologic evolution of breast cancer shows that breast cancer always starts with a local, small malign neoplasm that grows with time and eventually spreads to the lymphatic system to create metastases. It is therefore necessary to detect malign tumours as soon as possible to remove them and therefore prevent their evolution and spread to other organs. Breast cancer screening in the form of breast x-ray was introduced in the 1960s and is now part of standard health policies in most industrialized countries. Although the criteria for selecting patients for screening may vary from country to country, first long-term studies show a significant decrease of breast cancer mortality amongst the screened population. In [96], Silva et al. report 7 studies from 4 countries with 678.883 subjects. The cancer mortality rate in the screened group versus the group that was not screened was between 20 and 45 percent lower except for one Canadian study where no significant decrease could be observed. However, the last study is thought to be contaminated as randomization flawed and over a quarter of the unscreened control group had mammograms done privately.

Screening mammography is different from diagnostic mammography in the sense that it is performed on asymptomatic patients and does not necessarily require the presence of a physician. Indeed, it is a routine exam that should be as cost-efficient as possible. It generally involves recording two routine films X-rays of each breast, one in the craniocaudal and one in the medial lateral oblique direction. They are evaluated with a focus on detecting breast cancer in its early stages, i.e. with a size smaller than 1.5 cm and thus before it metastasizes. The findings are rated according to the Breast Imaging Reporting and Data System BIRADS (Table 5).

Category	Assessment	Recommendation
0	Incomplete Study	Need additional imaging
1	Negative	Routine Screening
2	Benign Findings	Routine Screening
3	Probable Benign Finding	Initial short-interval follow-up
4	Suspicious Anomaly	Biopsy should be considered
5	Highly suggestive of malignancy	Appropriate action should be taken
6	Known, biopsy-proven malignancy	Appropriate action should be taken

Table 5 : The BIRADS lexicon [96]

Recommendations for screening mammography vary from country to country, however the following summary is given by Silva et al.:

- by age 40: baseline mammogram
- after age 40: yearly mammogram, accompanied by a physical examination
- in high-risk patients, incl. BRCA1 and BRCA2 mutation carriers, screening should start at age 25, or 5-10 years earlier than the earliest age in which breast cancer presented in a family member.

Additional physical examination by palpation and/or an ultrasound given by a physician is necessary as up to 15 % of palpable breast cancers are not visible on mammography. In women with dense breasts, this percentage might be even higher due to mammography relaying on density differences between cancerous masses and the surrounding, healthy tissue.

However, no studies prove the value of breast palpation in reducing cancer mortality if used as the only screening method. Therefore, clinical breast palpation – and therefore also the less accurate breast self-examination on a monthly basis recommended to most patients – can only be seen as complementary to X-ray mammography and should not substitute them [96], [101].

### 3.1.5 Diagnostic Techniques

Before discussing different diagnostic techniques, the two main quality indicators for medical diagnostic techniques shall be introduced: the sensitivity and the specificity. Sensitivity indicates the rate of true positives and therefore the number of cancers detected out of a total number of cancers that were present. Ideal sensitivity of 100 % implies that all cancers present in a population could be found. Specificity indicates the rate of true negatives, i.e. the number of healthy patients diagnosed as being healthy. Ideal specificity of 100 % indicates that all healthy patients have been diagnosed as healthy.

Film mammography has already been mentioned as the screening technique of choice in section 3.1.3. It is indeed the most common imaging technology used for both screening, but also diagnostic mammography. It relies on the assumption that cancerous masses are of higher density compared to healthy tissue. This leads to sensitivities between 98 % for patients with fatty breasts and 55 % for patients with very dense breasts, incl. most young patients as well as patients with postmenopausal hormone therapy. The specificity is between 70 % and 90 %. Digital mammography has been introduced as a complement to film mammography. It has the advantages of better contrast resolution, requires less radiation dose and allows digital storage. It can be used as an alternative to film mammography as the sensitivities and specificities are similar. However, its higher cost prevents recommending digital mammography as a replacement for film mammography.

A new technique that has recently been presented is digital breast tomosynthesis (DBTS). This technique acquires individual planes of interest by rotation an x-ray source on an arc above the stationary compressed breast and the detector. It is a technique similar to x-ray computer tomography. Initial clinical studies suggest better sensitivity than classic mammography although further trials are necessary to prove its value [103]–[105].

Classic ultrasound evaluates sound waves reflected at the interface between layers of different densities and forms an image that represents these layers. Being the most operator-dependent modality, ultrasound may increase the sensitivity for patients with dense breasts. Otherwise, ultrasound is widely used to refine the diagnosis and differentiate between cystic or solid lesions. It is also the method of choice for guiding the aspiration and biopsy needles.

Magnetic resonance imaging (MRI) is increasingly used in breast imaging, up to the point of having been proposed as an additional screening method [106]. MRI is based on varying spin relaxation times between different types of tissues. In general, dedicated breast coils are used. MRI is highly sensitive for the detection of breast cancer, with sensitivities around 93 % observed for invasive carcinoma, including for patients where echography and x-ray showed low sensitivities [101]. However, MRI has the major disadvantage of rather low specificity and thus leads to an important number of unnecessary biopsies. The cost of performing an MRI exam compared to the low costs of x-ray mammography and echography also prevent the use of MRI as a screening tool.

MRI is thus mostly seen as an additional imaging device to refine unclear prior screening diagnosis, typically BI-RADS 3 or 4, to refine a diagnosis in the case of known malignancy or as a method of choice if the patient has breast implants.

The previously mentioned imaging procedures all image the morphology of the breast. Another approach to breast cancer imaging is the use of metabolic processes, for example in the frame of scintimammography and PET.

Scintimammography uses  $^{99m}\text{Tc}$ -Sestamibi that distributes in the body in function of the blood flow and concentrates in cancerous tissue in higher proportion than in healthy tissue. The scan itself is performed with a classic gamma camera that measures the radioactivity distribution. Scintimammography has proven to increase the specificity of screening or diagnostic exams in breasts that have lesions greater than 1 cm in diameter and unclear malignancy.

Finally, whole-body PET has been studied as a mammographic technique. Most studies used FDG as a tracer to locate malignant lesions. Both [107] and [108] report sensitivities between 80 and 90 % and specificity values up to 95 % if the cancerous lesion is sufficiently big, typically above one centimetre. Otherwise, sensitivity can rapidly decrease to 50 %. Due to its high cost and low sensitivities for small cancers, as well as due to the lack of dedicated tracers for breast cancer, whole-body PET cannot be used as a screening modality and encounters some difficulties as a diagnostic technique. In breast cancer diagnosis, PET is mainly used to detect metastases in the patient's body. Dedicated breast PET, so-called Positron Emission Mammography (PEM) is now being developed. It combines the main advantage of PET, i.e. imaging metabolic processes, with high resolution and, in further studies, dedicated tracers. First clinical results, provided for instance by Berg et al. in [87] or Levine et al. in [109] indicate PEM sensitivities and specificities around 90 %, measured on first prototypes of the Naviscan PEMFlex with reported image resolutions between 1.5 and 3 mm FWHM parallel to the detectors plates and spatial resolution of 6.5 - 8 mm FWHM for images perpendicular to the detector plates. Further development should provide 1.5 mm image resolution in the full field of view and thereby even improve the cancer sensitivity. One such prototype, the ClearPEM, will be presented in section 3.2.

Independent of the probable accuracy of an imaging modality, any suspicious lesion and the sentinel lymph node – the very first lymph node that would be reached by metastasizing cancer cells – should be biopsied. This gives histological certitude about the malignancy so as to schedule proper actions.

### 3.1.6 Therapy

If the malignancy of a lesion has been confirmed, different therapeutic actions can be taken. These will always depend on the type, size and multifocality of breast cancer. The paradigm of any intervention is to fully remove every malignant lesion yet inflict as few damage as possible to the surrounding healthy tissue. The following paragraphs describe possible techniques without attributing them to specific diagnostic findings.

Surgical removal of malignant lesions is the standard for breast cancer treatment. It requires the removal of all lesions including a minimum safety margin around the tumour. If the lesion is small enough, minimal invasive surgery can be sufficient. Otherwise, according to size, multifocality or spread of the lesion to the surrounding tissue and lymph nodes, invasive surgery is necessary. If the chosen method is sufficient to remove all cancerous tissue, survival rates do not change whether breast-conserving surgery or partial to full mastectomy are performed. The advantage of breast-conserving surgery is mainly cosmetic. It has an important positive psychological impact on the patient and should be the method of choice. However, cosmetic considerations are overridden by the medical necessity of completely removing the cancer [47].

Radiotherapy is generally used as post-operative treatment to reduce the probability for local recurrence of the cancer, for example in the surrounding tissue for breast-conserving surgery or in the adjacent chest wall and lymph nodes for mastectomy. Indeed, Brettes et al. conclude in [101] that post-operative radiotherapy reduces the risk for a local recurrence by 60-70 %.

Chemotherapy is used both for pre- and post-operative treatment. In the pre-operative phase, it helps to reduce the size of the cancer and therefore the amount of tissue to be removed. This allows breast-conserving surgery in some cases where mastectomy would otherwise have been necessary.

In post-operative treatment, both chemo- and hormone therapies are used to reduce the rate of recurrence of cancer. According to [47], adjuvant chemotherapy reduces the relative risk of recurrence by 25 to 35 % for pre-menopausal patients and by 10 to 20 % for postmenopausal patients.

## 3.2 ClearPEM

ClearPEM, the Crystal Clear Positron Emission Mammograph, is a dedicated mammography PET developed by the Crystal Clear Collaboration. The rationale of developing such a machine is based on the epidemiologic breast cancer incidence amongst female patients, the excellent prognosis if detected early enough and the ensuing need of powerful diagnostic modalities. Considering whole-body PET as being insufficient for early-stage diagnosis, the development of a dedicated metabolic imaging system should provide physicians with an accurate nuclear medical tool to complement their diagnostic means.

Based on these thoughts, Lecoq and Varela lay the fundament for this project in 2001 [15]. The ulterior motive is to include the knowledge gained during the development of ClearPET, i.e. the possibility to reach image resolution at around 1.5 mm as well as high global detection efficiencies, in a modality designed for human patient imaging. This would lead to the development of a system that could, if its value is proven in clinical trials, have a real impact on healthcare.

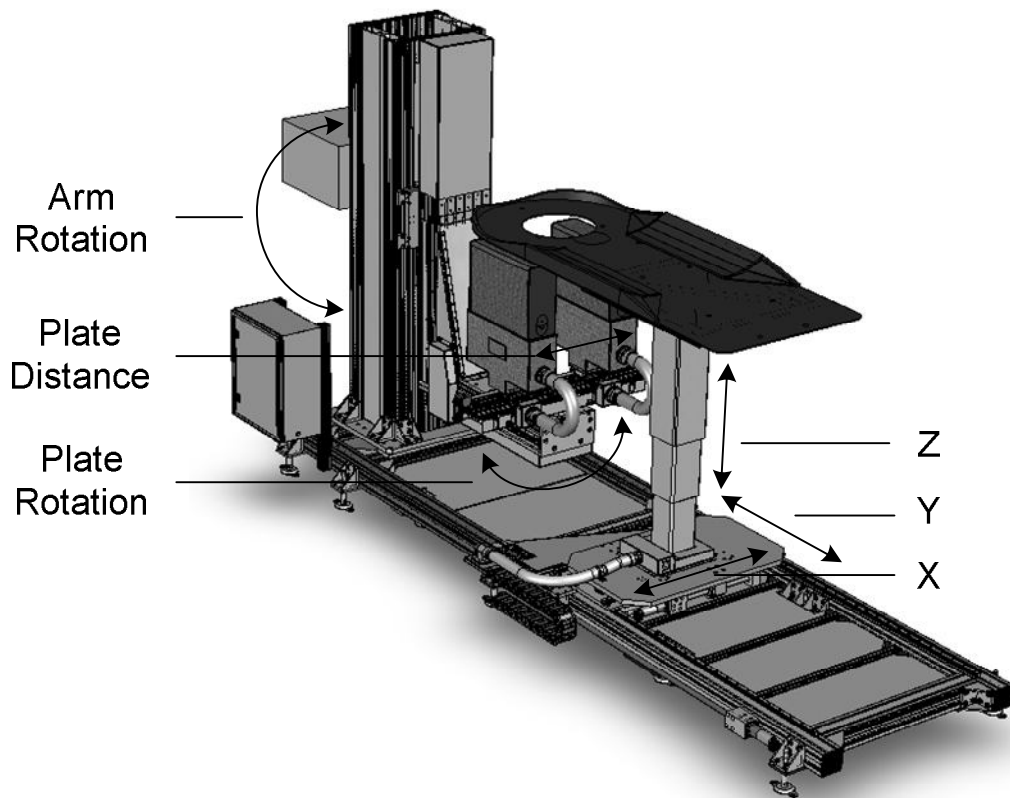


Figure 16 : ClearPEM: the first prototype [110]

ClearPEM is based on a horizontal patient bed with a hole for the breast and two parallel detector plates that revolve around the breast to register a 3-dimensional PET image. Figure 16 shows a CAD image of the first prototype as it has been installed at ICNAS – Instituto de Ciências Nucleares Aplicadas à Saúde in Coimbra, PT. The robot is designed to bring the bed into any required position above the plates by moving it along the X, Y or Z axis. The distance between the plates can be adjusted as required in order to keep it as low as possible and therefore increase the global detection efficiency. The plates rotate around the breast to complete the acquired sinograms with information from all angles.

Finally, it is also possible to rotate the complete detector arm by 90 degrees. Then, one plate is above the patient and another under the patient bed. This allows axillary exams to detect lesions close to the chest wall as well as lymph node metastases.



The first ClearPEM has been built by LIP and installed at ICNAS Coimbra. The second, improved, ClearPEM has been built by LIP and installed at Hôpital Nord, Marseille, in the frame of the ClearPEM-Sonic project.

### 3.2.1 Detector Design

The ClearPEM detector is based on 6144  $2 \times 2 \times 20$  mm<sup>3</sup> LYSO crystals. These crystals are grouped in BaSO<sub>4</sub> matrices of 4x8 crystals. BaSO<sub>4</sub> acts both as a cladding material that procures rigidity to the matrix and as a reflector that increases the light yield of the individual crystals. Each crystal matrix is coupled to two Hamamatsu S8550 4x8 APD matrices (Figure 17). Thus, each  $2 \times 2$  mm<sup>2</sup> light readout face is coupled to a dedicated APD. This configuration allows precise determination of the depth of interaction, as explained in section 2.5.4.3.

24 such modules are combined into a so-called supermodule, each detector plate holding 4 supermodules. The complete detector heads cover a field of view of  $17.2 \times 15.2$  cm<sup>2</sup> with a packing fraction of about 47 %.

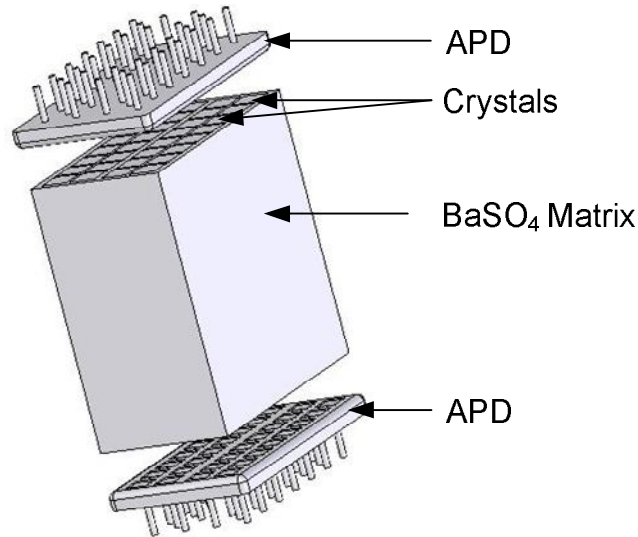


Figure 17 : ClearPEM module with 32 crystals and back-to-back APD readout [110]

Each signal channel is coupled to one input of a dedicated 192-channel ASIC that performs the signal readout, amplification, sampling and storage in analog memories. It also selects two active channels above a common threshold at a working rate of 50-100 MHz. The ASIC thus combines the front-end signal treatment of one side of six modules and acts as a multiplexer with 192 inputs and two outputs. The amplified signal is then digitized in the front-end by 10-bit sampling ADCs running at a maximum frequency of 100 MHz before being transmitted to the off-detector data acquisition (DAQ) system.

The DAQ system is made of two types of boards. The DAQ boards themselves are responsible for the initial phase of data reduction and pipeline data storage. The trigger and data concentrator (TRG/DCC) boards select relevant events in coincidence and transmit them to the acquisition PC. There, the data is analyzed with regards to energy and timing. The energy values

allow calculating the DOI component in the crystals, based on the energy asymmetry between the bottom and top APDs. The position, energy and timing information is then stored in a list-mode format on the server and can be retrieved for image reconstruction [39], [111].

### 3.2.2 Detector Performance

The above-mentioned design is used in both ClearPEM prototypes. Both the detectors as well as the readout electronics of the first ClearPEM have undergone extensive tests in the frame of their development, in the laboratory as well as onsite, including source and phantom acquisitions. The present section summarizes the results of these tests [112]–[115].

The front end electronics can be tested with dedicated test boards that include all functions of the final front-end boards, can be connected to six detector modules and have some additional testing features. As shown in figure 18 a), the amplifier has a risetime of 30 ns, a shaping time of 60 ns and very low baseline variation. The ASIC also has excellent low-noise properties with noise levels around 2.2 ADC counts that, if compared to the ADC counts generated by a 511 keV photopeak, correspond to around 7 keV and therefore less than two percent. Additionally, the interchannel noise dispersion is relatively low, around 8 %.

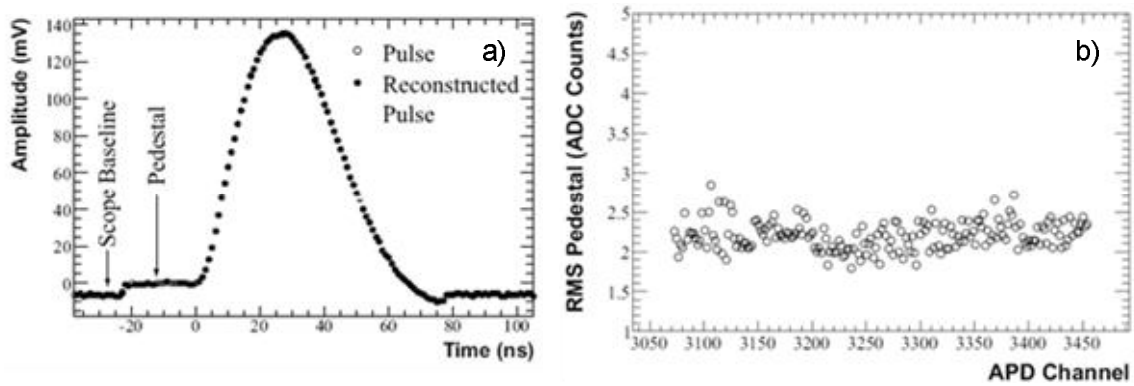


Figure 18 : Front-End ASIC performance: a) ASIC response to an input test signal, b) noise as a function of the channel number [112]

Figure 19 shows some results of detector tests in the laboratory at LIP that assess the energy, time and depth of interaction resolution of the detector matrix in laboratory conditions. A  $^{22}\text{Na}$  radioactive source was used to produce 511 keV photons, simulating the 511 keV photons from a  $\beta^+$ -tracer. If the setup is properly calibrated, it generates the photopeak visible in figure 19a). One of the key figures of merit of the detector is its energy resolution, as it determines the limit narrowness of the acceptance window for true coincidences. Figure 19b) shows the mean energy resolution over several thousand events registered with a test setup of 6 production matrices. It is, on average, 15.9 % with an FWHM of 1.9 percentage points and corresponds to the energy resolution determined by Trummer et al. [116] for single LYSO crystals with PMT readout. In order to test the depth of interaction resolution, the figure of merit that is important to reduce the parallax error during image reconstruction, a point source was moved to different positions

along the crystal. Figure 19d) shows the evolution of the energy asymmetry between the bottom and top matrix during such an experiment. Roughly, the measured asymmetry per unit length is over 4 %/mm. Finally, the coincidence time resolution of the whole scanner, including all detector matrices, was determined to be 5.2 ns FWHM (Figure 19c). This is sufficiently short to efficiently reduce random interaction generated by single photons from independent beta annihilations. These results were further refined after the installation of the first ClearPEM prototype and presented in [16]: the measured energy resolution at 511 keV is 13.3 %, the time resolution 4.5 ns FWHM.

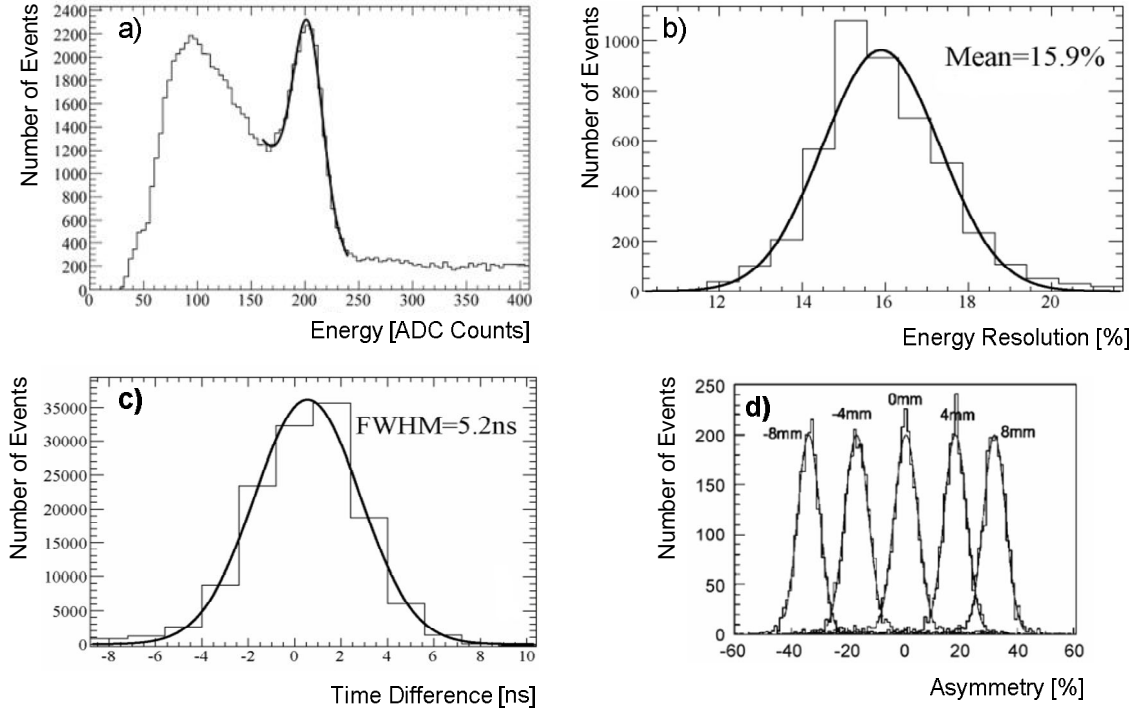


Figure 19 : Detector Resolution: a) typical 511keV photopeak, b) mean energy resolution, c) mean time coincidence resolution, d) depth of interaction resolution for different photon interaction points [113]–[115]

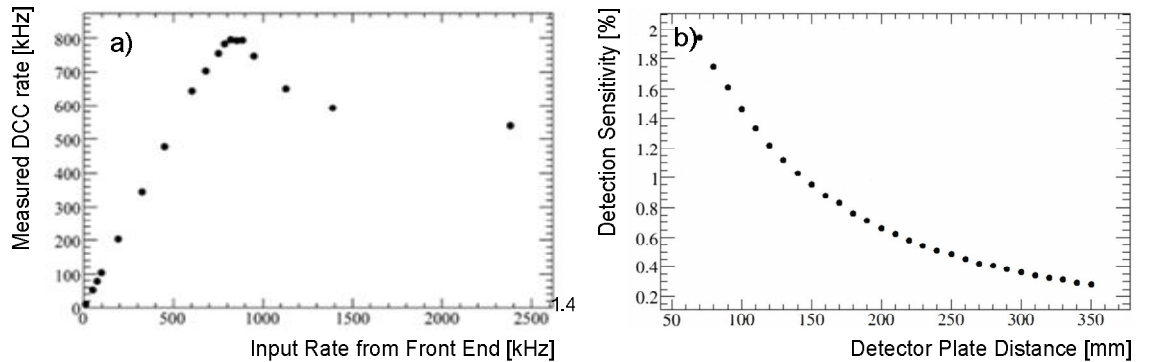


Figure 20 : Scanner Performance: a) DCC rate, b) scanner detection sensitivity [16], [113]–[115]

The DAQ needs to be sufficiently fast to acquire as many events as possible and thereby increase the global detection efficiency of the whole scanner. While the trigger is able to follow the input signal with a rate up to 2.5 MHz, figure 20a) shows that the final limiting factor, the DCC, has its acquisition rate limited to around 0.8 MHz.

Finally, the global detection efficiency of the scanner was assessed. Figure 20b) shows measurements presented in [16] that indicate a global detection efficiency of 1.5 % at a plate distance of 100 mm.

### 3.2.3 Image Reconstruction

The data acquired by the DAQ system is stored on a main server in a listmode format, including information about the position of the interaction in the scanner plate, information about the event's energy and a timestamp. There are several image reconstruction algorithms that can be used with ClearPEM [117], [118].

The first approach is the use of 2-dimensional ordered subsets expectation maximization (2D-OSEM) that was specifically developed for ClearPEM. As the listmode data acquired by the scanner contains the coincidence interactions in all three dimensions, this data first needs to be transformed, i.e. rebinned, into 2-dimensional datasets with single-slice rebinning (SSRB). These datasets are then rebinned into linograms and each linogram reconstructed separately. This method is quite fast but the rebinning processes loose information: the system sensitivity is lowered.

Alternatively, 3D-OSEM from STIR - Software for Tomographic Image Reconstruction has been adapted to the ClearPEM geometry, the necessary sinograms being calculated directly from the list-mode data before the image reconstruction starts. This method requires, additionally to planar sinograms for opposing detector elements, oblique sinograms for each possible detector combination. Then, rebinning does not lose any information but the calculation gets quite expensive due to the important amount of sinogram data that needs to be processed.

In both cases, the DOI information is used by defining the line of reconstruction as the line that joins the two photon absorption points registered in the list-mode data.

Finally, a list-mode maximum likelihood expectation maximization (ML-EM) algorithm has been tested. This has the advantage of directly reconstructing the image from the list-mode data, thereby preventing any rebinning processes that either loose information or are quite expensive. All three algorithms are available on the prototypes to adapt the reconstruction algorithm to the specific situation in which data needs to be reconstructed. For example, fast 2D-OSEM could be used for quick image assessment while the slower algorithms could be used to calculate the final image.

### 3.2.4 Image Quality of the first ClearPEM

Figure 21 shows the influence of the depth of interaction measurement on the reconstructed image quality. The data was acquired by moving a 1 mm  $^{22}\text{Na}$  source on a grid with 5 mm pitch. All 16 source positions were then simultaneously reconstructed, first without including the DOI information (Figure 21a) and then with the DOI information (Figure 21b). The images show clearly that without DOI, the parallax effect increases and creates a blurred image. However, the properly reconstructed image with DOI information is clear. The measured image resolution in this trial was of 1.3 mm FWHM in the horizontal and 1.2 mm FWHM in the vertical direction.

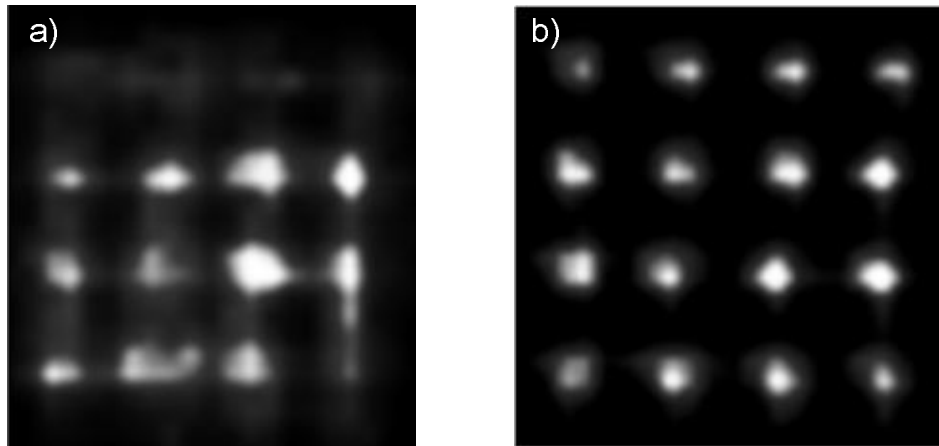


Figure 21 : Influence of the DOI measurement on image quality: a) reconstruction without DOI information, b) reconstruction with DOI information [119]

The quality of the scanner and the influence of different reconstruction algorithms was further assessed at ICNAS by acquiring phantom and small animal images [114].

Figure 22a) shows a breast phantom. The breast phantom has been developed by Jun Dang et al. [120]. It emulates both the properties of healthy breast tissue and malign lesions for PET, ultrasound and elastography. It is similar to the one used for ClearPEM-Sonic tests. In the image, both a major lesion of about 15 mm in diameter as well as the background noise are clearly visible. Figure 22b) was acquired with a mouse that had a small tumour implanted in one of its legs. This tumour is visible on the images. Finally, figure 22c) shows a mini-Derenzo phantom. It is suited to determine the resolution of the reconstructed image because it is divided into regions that contain small radioactive sources of different diameters: 1.2 mm, 1.5 mm, 2.0 mm, 2.5 mm and 3 mm. It also provides a good overview of the influence of the reconstruction algorithm on the image quality. 2D-OSEM, being subject to loss of information, provides the most blurred image. List mode ML-EM however shows good results that are quite comparable with 3D-OSEM: the 2.0 mm rods are still clearly distinguishable with 3D-OSEM. Figure 23, published in [16], confirms that the 3D-OSEM algorithm allows reconstructing ClearPEM images with a resolution better than 1.5 mm.

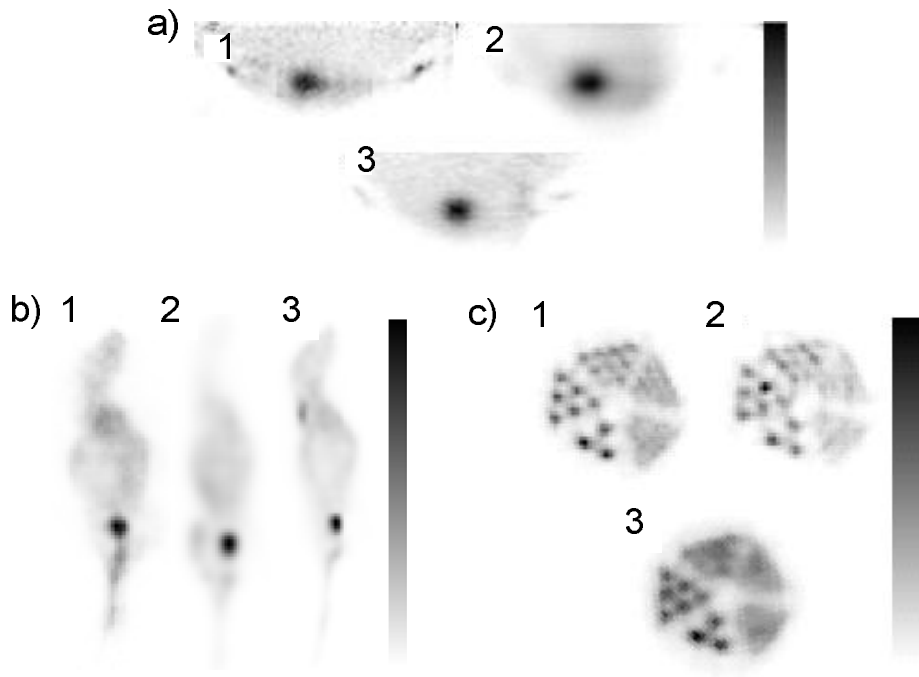


Figure 22 : Reconstructed images that have been obtained with 1) 3D OSEM, 2) list-mode ML-EM and 3) 2D-OSEM of a) a breast phantom, b) a mouse and c) a mini-Derenzo phantom [114]

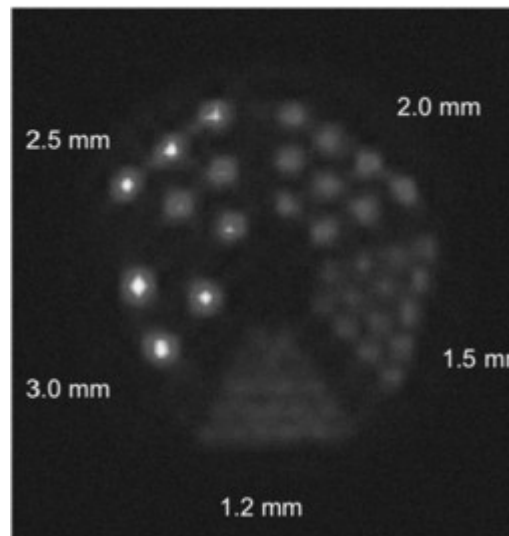


Figure 23 : Derenzo phantom [16]

### 3.3 The Ultrasound System

The ultrasound platform that is integrated into ClearPEM-Sonic is provided by the French company SuperSonic Imagine, based in Aix-en-Provence, France. The so-called Aixplorer system (Figure 24) combines classic B-mode ultrasound, which images density differences, with supersonic elastography, which quantifies the elastic properties of tissue. It provides important information for breast tumour diagnosis and follow-up including the morphology, the local and global elasticity, the vascularisation as well as the acoustic signature of the tissue [17].



Figure 24 : SuperSonic Aixplorer [17]

#### 3.3.1 Theory of Ultrasound

Ultrasonography is an imaging technology that relies on the properties of sound waves - with a frequency between 1 and 15 MHz - in a solid. The imaging process is performed by a transducer that is in direct contact with the body to be imaged. It is connected to a central unit that controls the complete acquisition process, pilots the transducer and constructs the image [54].

In the transducer, a piezoelectric array is excited by electrical pulses from the central unit and produces the ultrasonic wave. It is focussed on the region of interest by beamforming techniques that include the shape of the transducer, lenses or complex control pulses. In the body, the wave propagates at a velocity  $c$  that can be defined as follows:

$$c = \sqrt{\frac{K}{\rho}} \quad (3.1)$$

where  $K$  is the compression module and  $\rho$  the mass density. If it reaches a boundary between two regions of different densities, part of the wave will be reflected according to the laws of refraction:

$$\alpha_3 = -\alpha_1, \quad \frac{\sin \alpha_1}{\sin \alpha_2} = \frac{c_1}{c_2} \quad (3.2)$$

where  $c_1$  and  $c_2$  are the speed of sound in medium 1 and medium 2 and the angles  $\alpha_i$  defined according to figure 25.

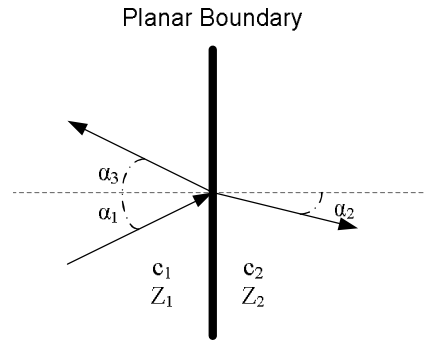


Figure 25 : Refraction of an ultrasonic wave on a planar surface

The reflected wave travels back to the transducer, which switched into the receiving mode immediately after emitting the original wave, where it vibrates the piezoelectric element. This generates an electric signal that is transmitted to the central unit that transforms it into an image, based on the amplitude of the reflected signal and the time delay between the emission and reception.

The acoustic refraction at boundaries has the unwanted side-effect that there are strong reflections at the transducer/air or air/body boundary if the transducer and body are not in perfect contact. In order to reduce this reflection, a high-viscosity water-soluble gel with a density similar to the one of the body is applied and couples the transducer to the patient.

The ultrasound wave  $J(z)$  will be exponentially attenuated with increasing depth, the absorption coefficient  $\mu$  being roughly proportional to the acoustic frequency  $\nu$ :

$$J(z) = J(0)e^{-\mu z}, \quad \mu \propto \nu \quad (3.3)$$

Considering the axial and transversal resolutions  $\Delta r$  and  $\Delta x$  are inversely proportional to the frequency:

$$\Delta r \propto \frac{1}{\nu}, \quad \Delta x \propto \frac{1}{\nu} \quad (3.4)$$



the chosen frequency for an exam always needs to be a compromise between the depth at which an image shall be obtained and the maximum achievable resolution at this depth.

According to complexity of the ultrasound system, several acquisition modes can be distinguished. Amongst the most common are:

- 1) A-mode ultrasound is the simplest approach. In this case a single US transducer produces a 1D wave and displays the amplitude of the echoes as a function of the depth on a line.
- 2) B-mode ultrasound uses a linear array of transducers that simultaneously scan parallel lines, i.e. a plane through the body, and display the acquired information as a 2D image.
- 3) M-mode ultrasound acquires a sequence of B-mode images in time that can then be analysed with regards to the motion of an organ.
- 4) 3D-ultrasound uses a moving linear transducer array that creates a series of parallel, 2-dimensional B-mode images that can then be assembled into a 3D image.
- 5) Doppler-ultrasound uses the Doppler Effect to assess the direction and velocity of a structure or liquid in the body.

### 3.3.2 Theory of Elastography

Elastography is a method to assess and ideally quantify the elastic properties of tissue [121], measured by a physical quantity called the Young's modulus  $E$ , expressed in Pascals:

$$E \stackrel{\text{def}}{=} \frac{\sigma}{\varepsilon} \quad (3.5)$$

Tissue stiffness is characterized by the tissue's deformation  $\varepsilon$  as a response to an external, uniform compression  $\sigma$ . With elastography, it is possible to estimate the tissue's stiffness by applying a mechanical force to the tissue and measuring its deformation. This information has important diagnostic value because, although the density of different tissues only varies within very small boundaries, the stiffness of the same tissues can vary by several orders of magnitude (Table 6).

Tissue type	Young's Modulus [kPa]	Density [g/cm <sup>3</sup> ]
Normal Fat	18-24	1000 +/- 8 % ( ~ water)
Normal Glandular	28-66	
Fibrous Tissue	96-244	
Carcinoma	22-560	

Table 6 : Density and stiffness of some types of human breast tissue [122]

The two main technologies are magnetic resonance (MR) and ultrasound (US) elastography. In MR elastography, an external vibrator induces a continuous vibration whose effect is measured with conventional MR technologies. This technology has proven its value since its introduction

in 1995 [123]. However, it has the disadvantage of requiring an expensive and not easily available MR tomograph.

A possible US elastography approach, as commercialised by Hitachi, is the qualitative measure of artificial strain in the tissue with a conventional US transducer [124]. In this case, the clinician is required to induce local physical compression by manually increasing and decreasing the pressure of the transducer on the body. As it requires only additional software, this method has the advantage of being rather easily implemented on many existing US platforms. On the other hand, due to the fact the compression is induced by the user, it has the disadvantage of being heavily user-dependent. This user-dependency also prevents quantitative measurements and limits the system to qualitative measurement of the tissue stiffness.

The other US elastography approach that has been developed by Bercoff, Tanter and Fink [122] and implemented in a commercial solution by SuperSonic Imagine [125], is so-called supersonic shear imaging (SSI). SSI relies on creating mechanical shear waves whose wave front is deformed by regions of varying stiffness, the information contained in this process being readout with ultrafast imaging and converted into a quantitative assessment of the elastic properties of the sample. The following is based on the fundamental publication by Bercoff et al. [122], where a more detailed explanation can be found.

SSI uses a standard ultrasound array driven by special electronics that focus the US beam at a certain depth in the tissue. This focalization creates acoustic radiation force that acts as a dipolar source of shear waves. It mainly radiates in transverse directions. The shear source is then successively focussed at increasing depths. The displacement of the focal point has to be faster than the lateral movement of the shear waves, i.e. it occurs at supersonic speed. The resulting, successive and independent shear waves interfere constructively along a Mach cone, creating two quasiplane shear wave fronts that propagate in opposite directions. Figure 26 illustrates this process.

Immediately after the creation of the shear waves, the transducer switches into the imaging mode. It uses planar US waves, similar to standard B-mode imaging, to follow the progression of the shear wave. In order to collect sufficient information, the sequence has to be quite fast, generally at least 3 kHz. This process is called Ultrafast<sup>TM</sup> imaging and quite different from classic B-mode US that has an image acquisition rate around 50-60 Hz. As the shear wave will be deformed by regions of varying stiffness, the transducer will register this deformation during the imaging phase. Finally, the registered information is used to calculate an exact elasticity map of the tissue and assigns each voxel a stiffness value expressed in kPa. The total sequence of creating and imaging the progression of the shear wave takes around 20 ms (Figure 27).

This technology is completely user-independent and allows fast and user-friendly acquisition of objective information about the stiffness of the tissue.

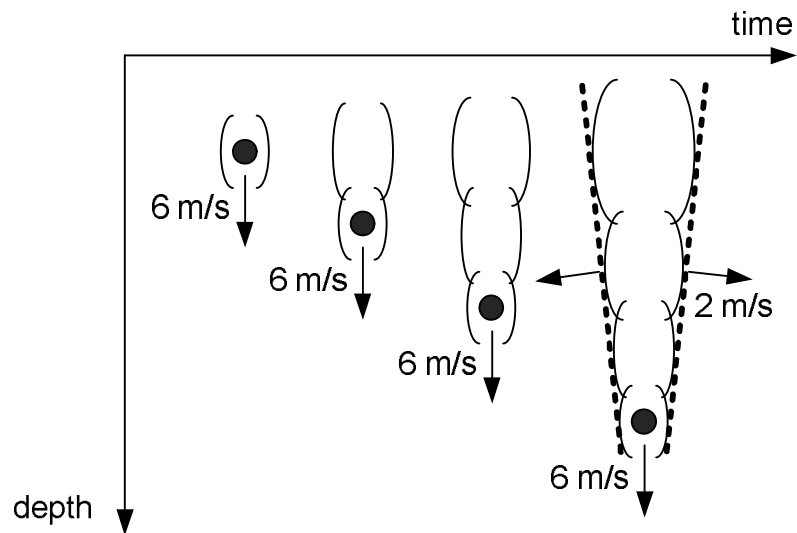


Figure 26 : Propagation of the focal point in tissue and creation of a lateral shearwave

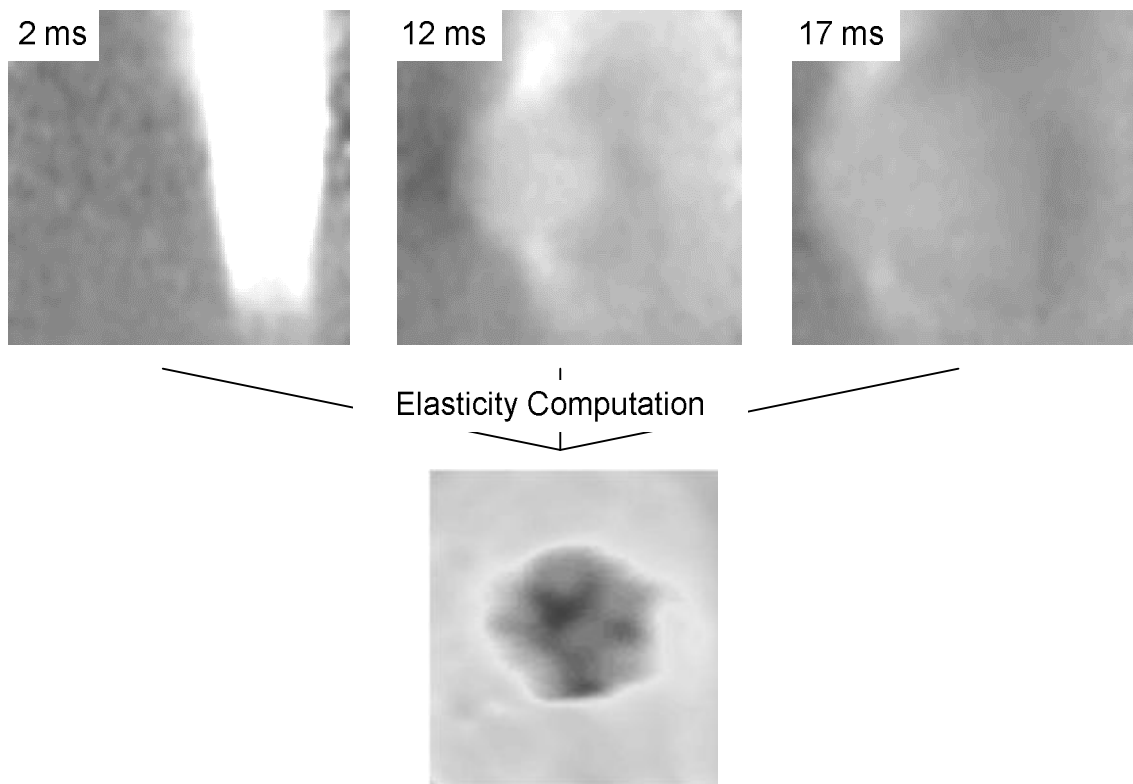


Figure 27 : Propagation and deformation of the shear wave as a function of time [126]

### 3.3.3 SuperSonic Imagine Aixplorer

SuperSonic Imagine Aixplorer is the first commercial system that provides supersonic shear imaging in a clinically tested system [17]. Aixplorer is available both with 2D and 3D transducers. In ClearPEM-Sonic, the 3D transducer depicted in figure 28 will be used.

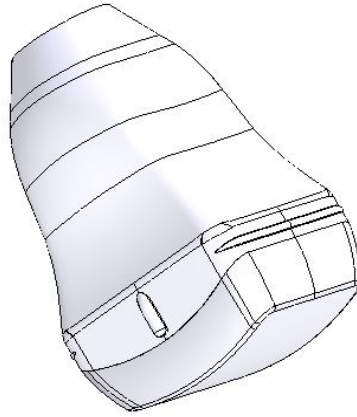


Figure 28 : SuperSonic Imagine Aixplorer 3D Transducer [126]

This conventional high frequency probe acquires a sequence of 2D images with a linear array that is mechanically moved in order to gather the information needed to reconstruct a 3D volume. For each plane, the probe completes a full B-mode and elastography sequence. It first acquires a conventional B-mode image. This image also serves as a reference image for the calculation of the displacements induced by the shear-wave. It then switches to the elastographic mode and creates the shear wave within 2 ms. Finally, the shear wave is imaged during 18 ms, at an acquisition frequency of up to 20 kHz.

The probe ideally operates at an ultrasound frequency of 8 MHz in order to acquire a volume of  $40 \times 40 \times 40 \text{ mm}^3$  with a voxel size of  $100 \times 100 \times 75 \text{ }\mu\text{m}^3$ . It is possible to use lower frequencies in order to reach deeper regions, although this is not advisable because the resolution decreases too much. The complete acquisition of 3D high-resolution B-mode and elastography information takes around 20 seconds.

### 3.3.4 Trial Results

SuperSonic Imagine Aixplorer has been tested both in the laboratory and in a clinical environment. Figures 29 and 30 are two samples acquired during the tests that demonstrate the capacity of the system. In real operation, Aixplorer displays the B-mode information in black and white and superposes the elastographic information in colour, the most common being a rainbow colour map where blue indicates region of low stiffness and red indicates regions with high stiffness values.

Figure 29 shows an x-, y-, and z-plane cut of a 3D elastographic image. It is a test image registered to present the 3D imaging modus and shows a hard lesion – the dark region in the centre of the images – surrounded by soft tissue. Figure 30, on the contrary, is an image acquired during clinical tests. It shows the same part of a female breast, once only in B-mode and once with elastography superposed on the B-mode image. Although the B-mode does not show any abnormality, the elastography clearly exhibits a spot of hard tissue. A biopsy confirmed this to be a malignant lesion.

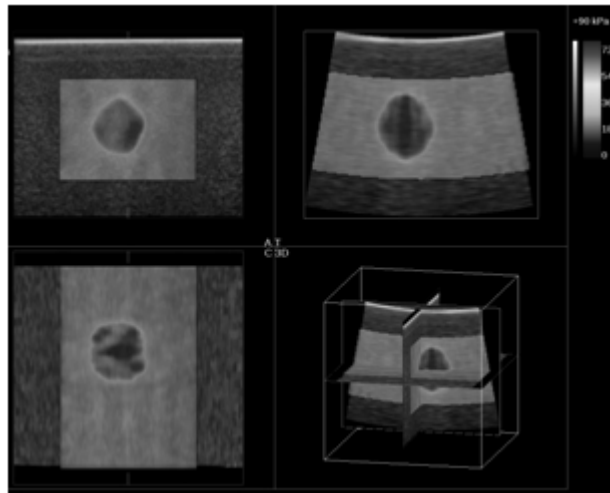


Figure 29 : 3D elastography image of a phantom with a hard lesion surrounded by soft tissue. The images have been converted to grayscale images with non-standard colour schemes to be shown in a document printed in black and white. [126]

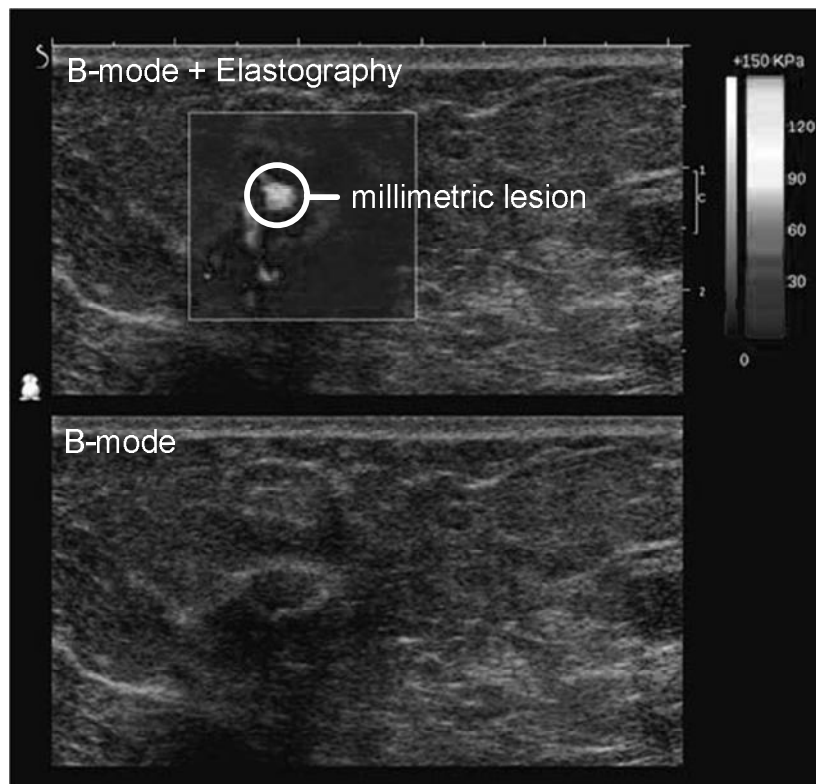


Figure 30 : B-mode and elastographic image superposed on the B-mode image of a female breast. A millimetric lesion is visible on the elastography. The images have been converted to grayscale images with non-standard colour schemes to be shown in a document printed in black and white. [126]

Since 2008, several multinational clinical studies assess the value of elastography for breast imaging. Table 7 summarizes results on a subset of 192 female breast lesions that were presented by Cohen-Bacrie et al. [127]. The increase of the specificity shows that the number of

false positives is considerably reduced. This is directly related to an increase of the total number of correctly classified lesions by over 12 percentage points. However, as shown by the sensitivity values, the rate of false negatives increased slightly. These results are confirmed by Berg et al. [128]. This study on 958 patients shows that the evaluation of elastographic information in addition to B-mode information improves the specificity of an ultrasound exam from 61.1 % to 78.5 %. The sensitivity is reported to be the same. A further study by Cosgrove et al. [129] concludes that shear wave elastography is highly reproducible for assessing elastographic features of breast masses both within and across observers. Elastography thus can be seen as a valuable addition to B-mode ultrasound.

<b>Criterion</b>	<b>BI-RADS test on B-mode US</b>	<b>BI-RADS + elasticity shape + maximum elasticity</b>
<b>Sensitivity</b>	92.7 %	87.8 %
<b>Specificity</b>	61.8 %	87.3 %
<b>Correctly Classified Lesions</b>	75 %	87.5 %

Table 7 : Results of a study on 192 lesions [127]

## 3.4 ClearPEM-Sonic

### 3.4.1 Objectives

ClearPEM-Sonic is designed with the explicit goal of combining the advantages from PET with those from ultrasound and elastography. It provides metabolic information from ClearPEM as well as morphologic and structural information from Aixplorer, maximizing the information available and allowing refined assessment of lesions under all aspects. This improves the screening, diagnosis, staging, re-staging as well as follow-up exams for patients with breast lesions.

The design of this multimodal system is based on the assumption that PET allows precise identification of metabolically hyperactive regions in the breast which, assuming that cancer cells are hyperactive, should be malignant lesions. ClearPEM creates a 3D image of the complete breast and, if needed, of the axillary lymph nodes. However, ClearPEM is subject to the main disadvantage of PET: being targeted at metabolic processes, it does not provide sufficiently accurate information about the anatomy in general. Such information is quite valuable for biopsies as well as for follow-up exams. In full-body PET, this problem is solved by coupling PET to CT. In the case of the breast, the installation of a dedicated CT would have been too complicated and expensive. Standard X-ray would have had the disadvantage of generating only 2-dimensional images, preventing the co-registration with the PET image to display all information in one final image. This leads to the choice of 3D ultrasound to obtain anatomic information.

If any suspicious regions have been identified during the ClearPEM exam, they will be imaged with Aixplorer. This provides necessary high-resolution 3D anatomic information to locate the lesions with reference to the surrounding anatomy.

Aixplorer was chosen because it also provides elastography information that further improves the specificity of the exam. As an example, some inflammatory diseases of the breast are benign yet exhibit higher glucose uptake, just like cancer [130]. However, they do not necessarily have the same elastic properties and should be elastographically well differentiated from breast cancer [131]. The false positive rate and thus the number of necessary biopsies will be reduced. Finally, the high spatial resolution of both the B-mode and elastography allow for a precise delimitation of the cancer from surrounding healthy tissue.

ClearPEM-Sonic is particularly suited for exams of patients where no clear diagnosis has been possible based on conventional X-ray and US B-mode exams. They typically fall into BI-RADS categories 3 or 4, requiring either a follow-up exam within a short amount of time or a biopsy. In both cases, the additional information from ClearPEM-Sonic should allow sufficient refinement of the initial diagnosis and, if there are no malignant findings, prevent a biopsy. This would reduce both the stress on the patient as well as the overall costs.

### 3.4.2 Challenges

The subject of this thesis is the development, commissioning and trial of ClearPEM-Sonic. It summarizes the challenges we had to overcome to develop this multimodal imaging platform. Most technical developments were developed as part of this thesis or supervised in the frame of the thesis.

The first challenge of this project is the improvement of ClearPEM itself. A certain number of lessons were made during the development of the first ClearPEM prototype and are now implemented. This includes an upgrade of the robot, the data acquisition system, the front-end electronics as well as the detector crystals themselves.

The upgrade of the robot is the duty of INEGI, the Institute of Mechanical Engineering and Industrial Management in Porto. The first ClearPEM prototype still had a very rudimentary design that was optimized towards easy assembling. ClearPEM-Sonic has a more marketable look, including easier operation as well as full casing that hides the mechanical parts from the user.

The upgrade of the data acquisition system and front-end electronics is under the responsibility of LIP, the Laboratory of Instrumentation and Experimental Particles Physics in Lisbon. It aims at reducing the noise level and power consumption, has a faster data link and improved temperature monitoring.

Finally, we develop scintillating detectors compatible with ClearPEM in the frame of this thesis. The basic detector configuration, consisting of LYSO crystals of dimensions  $2 \times 2 \times 20 \text{ cm}^3$  in a  $\text{BaSO}_4$  matrix and coupled to dedicated APD arrays on both light extraction faces, is kept for ClearPEM-Sonic. However, the crystal manufacturer of the first prototype, Photonic Materials Ltd. (PML) from Scotland, is not available to produce all crystals for the development of

ClearPEM-Sonic. The first step of this work is to find another company. We then aim at simplifying the processes that optimize the crystal properties for ClearPEM.

Second, two fundamentally different modalities need to be combined into a single machine. This creates a certain number of technological challenges that we have to overcome.

One major constraint is the image co-registration. It implies that the breast should not move and keep the same shape during the PEM and US acquisitions to simplify the software combination of both images. If the breast was in a different position or changed its shape, it would be necessary to always use intelligent correction algorithms that reduce the effect of geometrical differences between both images. Therefore, a breast stabilization system that deforms the breast the least possible is designed. At the same time, this system must not prevent the access to any ROI with any of the modalities and should be as comfortable as possible for the patient.

Then, both Aixplorer itself as well as the breast stabilization system are mechanically integrated into ClearPEM. This implies that there are no interferences with the respective other modality. ClearPEM-Sonic is assembled in a way to allow imaging any ROI with both modalities and, finally, is as user-friendly as possible.

ClearPEM-Sonic also provides all additional information necessary for image co-registration. The first step to image co-registration is to know how the images are located in space. The position of the ClearPEM image is known with reference to the PEM plates. The ultrasound images can be referenced to the transducer. The transducer itself however moves freely in space. ClearPEM-Sonic thus needs some system to accurately track the position of Aixplorer in space with help of a dedicated tracking system and relate this position to the position of the PEM plates.

Then, we develop software. This includes retrieving the image data from Aixplorer and ClearPEM as well as auxiliary information from the tracking system. Image co-registration requires, in the ideal case, only geometric transformations to superpose both images. If deformations are introduced in only one of the modalities, more intelligent correction algorithms have to be implemented. The images also have to be displayed in a user-friendly user interface. Ideally, this software is compatible with existing medical picture archiving and communication systems (PACS).

Finally, ClearPEM-Sonic is installed at Hôpital Nord, commissioned and evaluated. We assess the detector performance by measuring the energy resolution and coincidence time resolution of the detector modules. We evaluate the objective performance of the ClearPEM with dedicated phantoms. The clinical performance is tested by imaging patients and comparing the results with other modalities such as full-body PET, ultrasound or MRI. We assess the feasibility of combined ClearPEM and ultrasound acquisition, the final goal of ClearPEM-Sonic, by imaging multimodality phantoms with both modalities and co-registering both images.



Si le Sage, faisant peu de cas de l'albâtre, vénère le pur  
Jade onctueux, ce n'est point que l'albâtre soit commun  
et l'autre rare : Sachez plutôt que le Jade est bon,

Parce qu'il est doux au toucher – mais inflexible, qu'il est  
prudent : ses veines sont fines, compactes et solides.

in Victor Segalen, *Stèles*

## 4 Scintillator Performance

The performance of any PET is directly related to the performance of its detectors and thus to both its scintillating crystals and photodetectors. For ClearPEM-Sonic, scintillating detectors compatible to the ClearPEM design need to be developed.

This chapter gives a theoretical introduction to inorganic scintillating crystals and the experimental processes used to measure their quality. It describes the work necessary to obtain the crystal matrices implemented into ClearPEM-Sonic.

### 4.1 Inorganic Scintillators

In its broadest definition, a scintillating material is any substance that emits visible or ultraviolet light at well-defined wavelengths after it has been excited by an ionizing charged particle or high energy photon. It absorbs the energy of the incident photon and emits a number of lower-energetic photons that is proportional to the incident energy. The light emission process is called radioluminescence.

Scintillators can be divided into two major categories: organic and inorganic scintillators. These two groups differ both in their chemical composition as well as in the physical principles leading to light emission. In organic scintillators, the luminescence process is a consequence of transitions made by free valence electrons that occupy so-called molecular orbitals. It is thus a property of the molecular structure. On the contrary, the luminescence of inorganic scintillators is due to the electronic band structure of the crystal and thus a consequence of the crystalline structure [132].

In PET, one of the major requirements for the scintillator is good radiation stopping power in order to fully detect an incoming gamma photon. As inorganic scintillators are produced by combining much heavier elements than organic scintillators, they are used for this application. They will be treated in the following sections.

The theoretical explanation limits to a phenomenological description of the processes. It is based on the works by Birks [133], Rodnyi [134] and Lecoq et al. [56].

#### 4.1.1 Scintillation Process

##### 4.1.1.1 *The Band Theory*

The collective electron or band theory of crystalline solids developed by Felix Bloch and applied to crystalline structures provides a suitable model for the discussion of inorganic crystals [133]. In isolated atoms, the solution of the Schroedinger equation yields discrete energy levels. In an inorganic crystal lattice, the discrete energy levels are replaced by so-called energy bands with closely spaced energy levels. The different sublevels in these bands are distinguished by the value of the wave number  $k$ . These energy bands are separated by forbidden regions. The innermost energy levels remain virtually unperturbed. The valence band, which is the highest filled band, is separated from the conduction band, the lowest empty band, by an energy gap  $E_g$  of a few eV (Figure 31a).

This model changes if additional energy levels, either intrinsic or extrinsic, are introduced in the band gap (Figure 31b). If they are unoccupied, they can be filled by electrons, holes or excitons, which are bound states of electrons and holes. Several types of energy levels can be distinguished: luminescence centres, quenching centres and traps.

Luminescence centres are responsible for scintillation in an inorganic crystal. They undergo radiative disexcitation by emitting a photon during the transition from the excited to the ground state. The emission process is called intrinsic scintillation if the centre is of intrinsic nature, i.e. a consequence of the crystal structure. Centres of extrinsic nature are induced by voluntary doping or involuntary defects and impurities in the crystal and induce so-called extrinsic luminescence.

Quenching centres have the same origins as luminescence centres, however the transition from the excited to the ground state is radiationless with the exchange of one or more phonons.

Finally, metastable traps retain electrons or excitons for prolonged periods of time compared to that of other types of centres. Electrons can escape to either the conduction band by acquiring additional energy or the valence band by radiationless transition.

Quenching centres and metastable traps reduce the efficiency of the scintillator because they trap charge carriers thereby lost for scintillation.

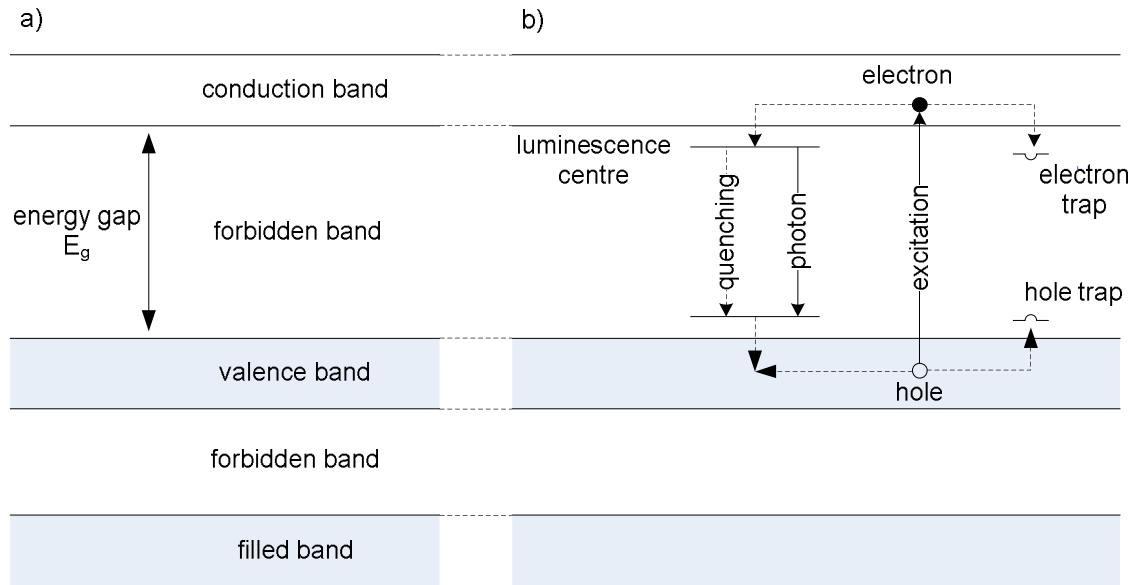


Figure 31 : Energy bands of a) an insulating and b) an impurity-activated crystal

#### 4.1.1.2 Mechanism of Scintillation

Starting with the absorption of energy from an incident particle by the crystal, several successive processes distribute the energy of the primary holes and electrons to other charge carriers and finally lead to the emission of scintillation light. The commonly proposed sequence is [134]:

##### a) Absorption of energy in the crystal and creation of primary holes and electrons

The energetic photon that impacts on the crystal transfers all or part of its energy to an electron of the inner shell, producing a hole in the inner shell of an atom and a free electron. The energy of the primary electron is equal to the energy transferred by the gamma photon minus the energy of the level it has been kicked out.

##### b) Relaxation of the primary electrons and holes that leads to the creation of secondary electrons and holes, photons, plasmons and other excitations

The highly energetic, so-called primary electron and hole relax in a variety of processes. The atom from which the electron has been emitted relaxes by either radiative or non-radiative processes by emitting an X-ray photon that can be reabsorbed by the crystal and an Auger electron. This leads to the production of additional energetic e-h pairs. The Auger as well as the primary electron will lose energy by inelastic electron-electron scattering or phonon emission. In parallel, by moving through the crystal, the primary electron produces a cascade of additional free electrons and holes. These processes continue until the energy of the particles is too low to produce further ionizations.

The fast electron can also interact with valence electrons and produce collective oscillations of the electron continuum, so-called plasmons. They will eventually decay into e-h pairs.

c) *Thermalization of the secondary electrons and holes. This creates a number of electron-hole (e-h) pairs whose energy is proportional to the band-gap energy  $E_g$*

At the beginning of the thermalization, the electrons and holes begin to interact with vibrations of the environment and enter electron-phonon relaxation. In these interactions, the electrons and holes will lose energy and move to the lower boundary of the conduction band or, respectively, the upper border of the valence band. This e-h pair has energy proportional to the band gap energy  $E_g$ . The resulting number  $N_{e-h}$  of thermalized e-h pairs is directly proportional to the absorbed energy  $E_\gamma$ . A factor  $b$ , determined by the crystal structure and type of chemical bonds in the material, needs to be considered. It is between 1.5-2 for ionic crystals and 3-4 for crystals with covalent bounding:

$$N_{e-h} = \frac{E_\gamma}{bE_g} \quad (4.1)$$

d) *Migration of the e-h pairs and energy transfer to luminescent centres*  
and

e) *Relaxation of excited luminescent centres and emission of scintillation light*

After their thermalization, electrons and holes close to the band edges enter a migration phase where they lead to scintillation in several ways, described by Lecoq et al. [56]:

1.  $e + h \rightarrow h\nu$
2.  $e + h \rightarrow ex \rightarrow h\nu$
3.  $e + h + A \rightarrow ex + A \rightarrow A^* \rightarrow A + h\nu$
4.  $e + h + A \rightarrow A^{1+} + e \rightarrow A^* \rightarrow h\nu$
5.  $e + h + A \rightarrow (A^{1-})^* + h \rightarrow A + h\nu$
6.  $A \rightarrow A^* \rightarrow A + h\nu$

where  $e$  and  $h$  are an electron and a hole,  $ex$  an exciton,  $A$  an activator ion and  $h\nu$  a photon.

The first emission process (1.) is a result of the direct radiative recombination of free thermalized electrons in the conduction band with holes from the valence band or from deeper electronic shells. Usually, as explained earlier in this section, the highly energetic primary electrons and holes produced by ionizing radiation are converted into electrons and holes of smaller energy. The recombination would only take place once the energies of the electron and the hole have sufficiently decreased so they can bind together and create an exciton. However, for certain configurations of the valence and core atomic electron bands, the relaxation cannot take place and the electron recombines with a deep hole. This process, called cross-luminescence, gives rise to fast UV emission.

Process 2. shows that thermalized carriers can be bound in some places of the lattice, for instance in the vicinity of a specific atom or a structural defect. They are then called autolocalized excitons ( $ex$ ). The luminescence of free excitons or bound excitons is generally absent in complex compounds. It has been observed in simple oxides.

In the presence of impurity centres or activator ions (A), the exciton luminescence is quenched, causing a sensitization of the luminescence of the activating ions A (process 3.). The radiative centres are thus excited by an energy transfer from excited matrix states.

Processes 4. and 5., where free thermalized electrons (4.) or holes (5.) are directly captured by an activator ion, compete with the formation of excitons. The ion A is activated and enters an excited state  $A^*$ . The excitation of radiative centres is now a consequence of a charge transfer mechanism from excited matrix states.

Finally, activating centres can be directly excited by ionizing radiation (6.).

In processes 3. to 6., the light photon is emitted when the excited activator ion returns to its ground state.

#### 4.1.1.3 Cerium-activated crystals

ClearPEM-Sonic uses Cerium(Ce)-activated LYSO crystals. They are the material of choice for PET applications due to their high light output, fast decay characteristics and ease of handling.

Rare-earth ions are commonly used as activator ions due to their parity-allowed 5d-4f transition. This transition generates a fast light emission component in the range of 20 to 100 ns in Ce-doped inorganic scintillators. In L(Y)SO crystals, the Ce 4f lies just above the valence band and the excited levels just below the conduction band. This increases the hole and electron capture probabilities and leads to very efficient scintillators.

The commonly accepted scintillation mechanism in crystals doped with Ce is radiative recombination. In a purely phenomenological description, this can be modelled by a  $Ce^{3+}$  that captures a hole. It then catches an electron and enters an excited  $Ce^{3+}$  state. This excited  $Ce^{3+}$  returns to the ground state under emission of a light photon. This process is in competition with the recombination of e-h pairs via deep trap centres.

$Ce^{4+}$  ions can also be present in the crystal. They can capture an electron from the valence band. The resulting charge transfer state ( $Ce^{3+}$ +hole) relaxes non-radiatively to the ground state. This process is in concurrence with the excitation of  $Ce^{3+}$  5d-states.

#### 4.1.2 Energy and light loss in the crystal

Several different processes lead to energy and light loss in the crystal. As indicated in equation (4.1), only a part of the energy deposited in the scintillator will be converted into thermalized e-h pairs. Further energy losses in the crystal also reduce the number of emitted photons, for example the capture of free electrons and holes in traps or the non-radiative relaxation of luminescence centres under emission of phonons. Finally, the number of detected photons is reduced by photon self-absorption processes in the crystal.

The loss mechanisms explained in the following are relevant for crystals used in PET as they have a direct influence on the crystal performance.

#### 4.1.2.1 Thermal quenching

Quenching corresponds to the disexcitation of an excited centre without emission of photons. It can best be explained by using a configurational coordinate diagram like in figure 32a). It summarizes the scintillation mechanism in an inorganic scintillator. The diagram shows parabolic curves that represent the potential energies of the ground and excited states versus the mean inter atomic distance between the luminescent centre and neighbouring atoms. Horizontal lines correspond to vibrational states of the nearby ions or phonons.

Figure 32a) shows a luminescent centre in its ground state A. If it absorbs energy, it is excited, a process represented by the line [AB]. This line is vertical because, according to the Franck-Condon principle, the process is fast compared to atomic or ionic movements. However, B is not the equilibrium position of the excited state. The equilibrium position C of the excited state is vertically separated by an amount  $\Delta Q$  from the equilibrium position of the ground state: this is called the Stokes shift. It depends on the electron-phonon coupling in the crystal. The luminescence centre will thermally dissipate its excess energy and oscillate around its equilibrium position C. The time spent in this position depends on the probability for an optical transition [CD] to the ground state. In the ground state, the centre returns to oscillate around the equilibrium position A by thermal dissipation.

However, the potential energy curves often intersect at a certain point. If the excited state gains sufficient thermal energy  $E_q$  to reach this crossing point, it can disexcite non-radiatively by creating a cascade of phonons: this is called thermal quenching. The process is in direct competition with photon emission. Considering a probability for photon emission  $k_{hv}$  and for thermal quenching  $k_{th}$ , the luminescence quantum efficiency  $q$  is:

$$q = \frac{k_{hv}}{k_{hv} + k_{th}} \quad (4.2)$$

where:

$$k_{th} = A e^{-\frac{E_q}{k_B T}} \quad (4.3)$$

and thus:

$$q(T) = \frac{1}{1 + C e^{-\frac{E_q}{k_B T}}} \quad (4.4)$$

This directly implies that the probability for non-radiative disexcitation increases with the temperature, thereby reducing the light yield as well as the decay time. This effect has to be considered in PET applications as they are carried out at room temperature. It is summarized in

a parameter  $\tau$  that corresponds to the ratio of  $q(T)$  at certain temperature and  $q(T_0)$  at a reference temperature:

$$\tau = \frac{q(T)}{q(T_0)} = \frac{1 + C e^{-\frac{E_q}{k_B T_0}}}{1 + C e^{-\frac{E_q}{k_B T}}} \quad (4.5)$$

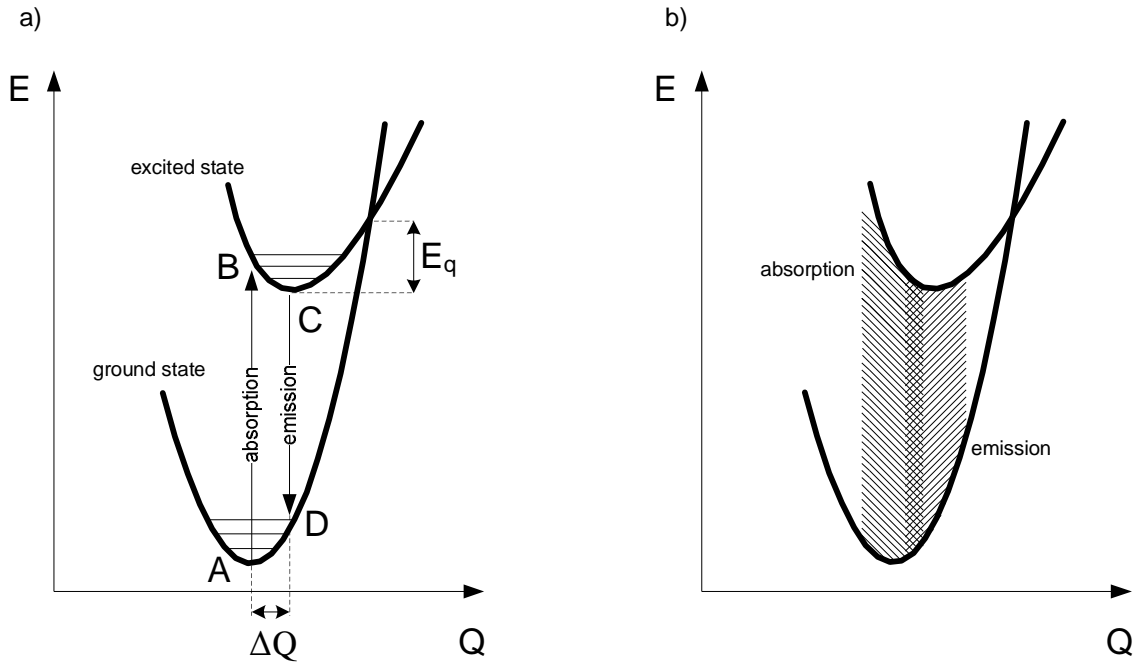


Figure 32 : Configurational coordinate diagram showing a) the scintillation process and b) the overlap of the absorption and emission region

#### 4.1.2.2 Concentration Quenching

In doped crystals, increasing dopant concentration increases the probability of an interaction between individual luminescence centres. Energy can then be transferred from centre to centre until it reaches a quenching site where it is lost nonradiatively. The critical concentration where concentration quenching gets noticeable is a few atomic percent of dopant in the crystal.

#### 4.1.2.3 Selfabsorption

Ideally, all light photons would propagate in the crystal without being absorbed in the scintillator material. In the real crystal, this is prevented by impurity- or defect-induced background absorption as well as reabsorption by luminescence centres.

Background absorption is a direct consequence of the presence of unwanted elements in the crystal. It can be reduced by carefully controlling the crystal growth process by the proper choice of high-purity raw materials, an appropriate crucible as well as stable growth conditions including pressure and temperature.

Reabsorption by luminescence centres does not so much decrease the light yield as most of the radiation is reemitted but increases the decay time. Figure 32b) shows the origin of reabsorption: if the separation  $\Delta Q$  between the equilibrium positions is sufficiently small, the emission and absorption bands overlap.

In addition, some photons are lost due to Fresnel losses. These photons reach the extraction surface at an angle equal or greater than the angle of total reflection. They cannot exit the crystal, increase their path length within it and have a higher probability of reabsorption.

## 4.2 General Characteristics

The suitability of a scintillating crystal for different applications is defined by a set of measurable properties. These include physical properties like its density, radiation stopping power and ease of growth as well as optical properties including the light output, energy resolution, depth of interaction resolution, decay time, light absorption and its fluorescence spectra. Most crystal properties are a direct consequence of its chemical composition.

ClearPEM-Sonic uses LYSO:Ce crystals, whose main characteristics are summarized in Table 8. As the scintillator used for ClearPEM had been chosen in a previous project – the development of the first ClearPEM prototype – the present study focuses on the optimization of the parameters that depend on the crystals' production process as well as on its surface state: the light output, the energy resolution and the DOI resolution. These values are also particularly important for PET because high light output leads to better energy resolution (see section 4.2.2) which in turn has a direct impact on the quality of the Compton event discrimination (see section 2.5.1). Good DOI resolution reduces the parallax effect (see 2.5.4.3).

The following, theoretical, introduction is therefore limited to these properties.

Property	Average Value
Density [g/cm <sup>3</sup> ]	7.4
$Z_{\text{eff}}$	66
Photo. absorb. coeff [cm <sup>-1</sup> ]	0.28
Light Output [ph/MeV <sup>1</sup> ]	27 000
Decay Time [ns]	40
Maximum Emission Wavelength [nm]	420

Table 8 : Properties of LYSO, at room temperature, under excitation by a 511 keV photon [56]

### 4.2.1 Light Output

#### 4.2.1.1 Theory

The amount of light produced by a crystal can be defined as either the intrinsic or absolute light yield, which is the absolute number of light photons generated in the crystal per energy



deposited by the incident particle, or as the efficient or collected light output which corresponds to the number of light photons collected by the photodetector per energy deposited.

The number of light photons intrinsically emitted by a crystal is a function of the number  $n_{e-h}$  of electron-hole pairs created by the incident gamma photon, the energy transfer efficiency  $S$  from the e-h pairs to luminescence centres and the quantum yield for intracentre luminescence  $Q$  [135]:

$$n_{ph} = n_{e-h} \cdot S \cdot Q ; 0 < S, Q < 1 \quad (4.6)$$

If equation (4.1) for the number of e-h pairs per deposited energy is considered, this leads to:

$$n_{ph} = \frac{E_\gamma}{bE_g} \cdot S \cdot Q \quad (4.7)$$

The intrinsic light yield  $LY_{in}$  of a crystal therefore is:

$$LY_{in} = \frac{n_{ph}}{E_\gamma} = \frac{1}{bE_g} \cdot S \cdot Q \quad (4.8)$$

Both  $E_g$  and  $Q$  can directly be measured by optical spectroscopy of solids.  $b$  can be estimated with Monte-Carlo simulations of the energy dissipation in crystals.

The efficient light output  $LO_{eff}$  measured by the photodetector is always inferior to the generated  $LY_{in}$ . This is due to a series of light loss mechanisms including self-absorption and quenching processes described in section 4.1.2. Part of the photons will also escape from the crystal on the lateral surfaces. This rate can be influenced and, generally, reduced by changing the surface state of the crystal itself, using reflecting materials or both. However, these materials have the disadvantage of absorbing part of the photons. Then, due to the mismatch in the refractive indices of the crystal and the photodetector, not all photons that leave the crystal on the surface coupled to the photodetector will enter the latter. This effect can be reduced by the use of optical glue with an adapted refractive index. The influence of these effects is summarized in the light collection efficiency  $\eta_L$ . It is defined as the ratio of the efficient light output and the intrinsic light yield:

$$\eta_L = \frac{LO_{eff}}{LY_{in}} \quad (4.9)$$

Thus:

$$LO_{eff} \left[ \frac{ph}{MeV} \right] = \eta_L \cdot LY_{in} \quad (4.10)$$

and, under consideration of the temperature dependence according to (4.5):

$$LO_{eff}(T) \left[ \frac{ph}{MeV} \right] = \tau \cdot \eta_L \cdot LY_{in} \quad (4.11)$$

Finally, due to the quantum detection efficiency  $q$  of the photodetector, only some of the light photons will create photoelectrons. The number of photoelectrons  $N_e$  is thus:

$$N_e \left[ \frac{pe}{MeV} \right] = q \cdot LO \quad (4.12)$$

#### 4.2.1.2 Single-Crystal Characterisation

A light output measurement allows the determination of the effective light output and energy resolution of a crystal. Such a measurement depends on many factors inherent to the crystal and described in the previous sections [136]. This includes the size of the crystal, different light loss mechanisms, the surface state of the crystal, the possible use of a reflecting material as well as the coupling of the crystal to the photodetector. The stability of the photodetector itself with regards to temperature and high voltage fluctuations also influences the measurement.

Considering these dependencies and fluctuations they are subject to, the comparison of light output values in photons per MeV from different measurement runs, using different setups, is very difficult and out of the scope of this thesis. These factors and different techniques for measuring the light output also explain the important spread of values found in the literature.

The method used to determine the light output of crystals in this thesis is the single-electron method. The number of photoelectrons per incident energy  $N_e$  is calculated by forming the ratio of the position of the photoelectron peak and the position of the single electron peak in a so-called light output spectrum:

$$N_e \left[ \frac{pe}{MeV} \right] = \frac{\text{position of the photopeak}}{\text{position of the single electron peak}} \cdot \frac{1}{E_\gamma [MeV]} \quad (4.13)$$

If the electronic readout chain has a pedestal that is different from zero, it must be subtracted from the respective positions of the peaks. If the ratio of the gains of the electronics for the photopeak and the single electron measurements  $R_{gain}$  is taken into account, we get:

$$N_e \left[ \frac{pe}{MeV} \right] = \frac{\text{position of the photopeak} - \text{pedestal}}{\text{position of the single electron peak} - \text{pedestal}} \cdot \frac{R_{gain}}{E_\gamma} \quad (4.14)$$

and the effective light output under consideration of an appropriate quantum efficiency  $q$ :

$$LO_{eff} \left[ \frac{ph}{MeV} \right] = \frac{1}{q} \cdot \frac{\text{position of the photopeak} - \text{pedestal}}{\text{position of the single electron peak} - \text{pedestal}} \cdot \frac{gain}{E_\gamma} \quad (4.15)$$

For all measurements presented in this thesis, Photonics XP2020Q photomultipliers were used. Their quantum efficiency for LYSO crystals is 22 % [136].

The measurement setup used is shown in Figure 33. The crystals that are measured generally have a quadratic shape, for example in the dimensions  $2 \times 2 \times 20 \text{ mm}^3$ , and can be measured with one of the  $2 \times 20 \text{ mm}^2$  or one of the  $2 \times 2 \text{ mm}^2$  sides connected to the photomultiplier (PMT). In the first, so-called horizontal setup, the crystal is lying flat on the PMT. Several layers of Teflon are put on top of it and act as a reflector. In the other, so-called vertical setup, the crystal stands on the PMT. It has previously been wrapped into several layers of Teflon that cover all lateral sides as well as the small side parallel to the one coupled to the PMT. In both setups, silicon grease is used to optically couple the crystal to the PMT. A  $^{137}\text{Cs}$  source is used to excite the crystals with monoenergetic gamma photons at 662 keV.

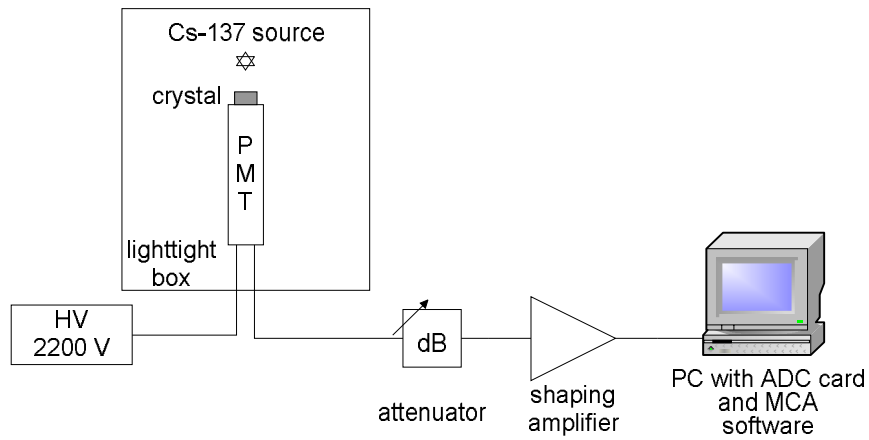


Figure 33 : Light yield bench

The PMT is powered by a high voltage source that delivers a tension of 2.2 kV. If the signal produced by the PMT exceeds the maximum admissible signal of the subsequent electronics, it is attenuated to an acceptable level. Then, a shaping amplifier converts the incoming, exponentially decaying pulse into a Gaussian shaped curve whose area is directly proportional to the area of the incoming pulse. This Gaussian signal is finally integrated by an analog-to-digital converter (ADC) Peripheral Component Interconnect (PCI) card from Ortec. The multi channel analyser software MAESTRO-32, also provided by Ortec, creates a histogram of the integrated pulses. This histogram corresponds to the light spectrum of the crystal (Figure 34).

The thereby recorded signal can then be fitted with a simple Gaussian curve in the case of a single electron measurement. In the case of a full energy spectrum, a combination of a Fermi and a Gaussian distribution are used (4.16): they take, respectively, the Compton edge and the full energy photopeak into account.

$$y(x) = \frac{p}{e^{\frac{x-c}{r}} + 1} + a \cdot e^{-\frac{(x-\mu)^2}{2\sigma^2}} \quad (4.16)$$

where  $p$ ,  $c$  and  $1/r$  are respectively the height, position and slope of the Compton edge and  $a$ ,  $\mu$  and  $\sigma$  respectively the height, position and the standard deviation of the photopeak.

The photopeak's full width at half maximum (FWHM) is calculated as:

$$FWHM = 2\sqrt{2\ln 2} \sigma \sim 2.36 \sigma \quad (4.17)$$

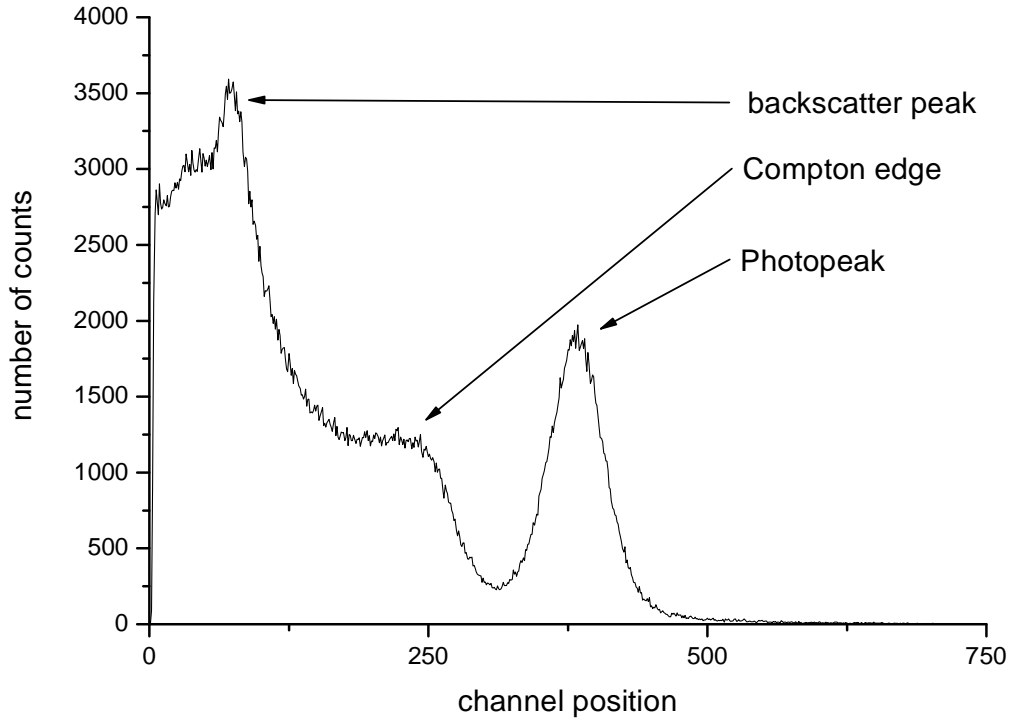


Figure 34 : Typical Light Output Spectrum

The measurement error is calculated according to the considerations proposed by Moszynski et al. in [137]. Considering experimental reproducibility errors induced by the reflective wrapping of the crystal or minor temperature fluctuations, the uncertainty in determining the exact position of the photoelectric peak and the uncertainty in the determination of the quantum efficiency, the precision of a light output measurement is around 5 %.

#### 4.2.1.3 Large-Scale Characterisation

Crystals used for the production of detector matrices have to comply with certain specifications. In order to test the compliance of a representative sample of crystals, we use an automatic machine. MiniACCOS is a computer-controlled machine designed to assess within about 8 hours the homogeneity of the quantity of light emitted by 100 scintillating crystals [116], [138]. As shown in figure 35, a  $^{137}\text{Cs}$  source excites the crystals and a Photonics XP2020Q photomultiplier is used to collect the scintillation light. Whilst the PMT and source are fixed,

the Teflon tray is moved by two linear motors. The whole setup is installed in a light-tight box and kept at constant temperature.

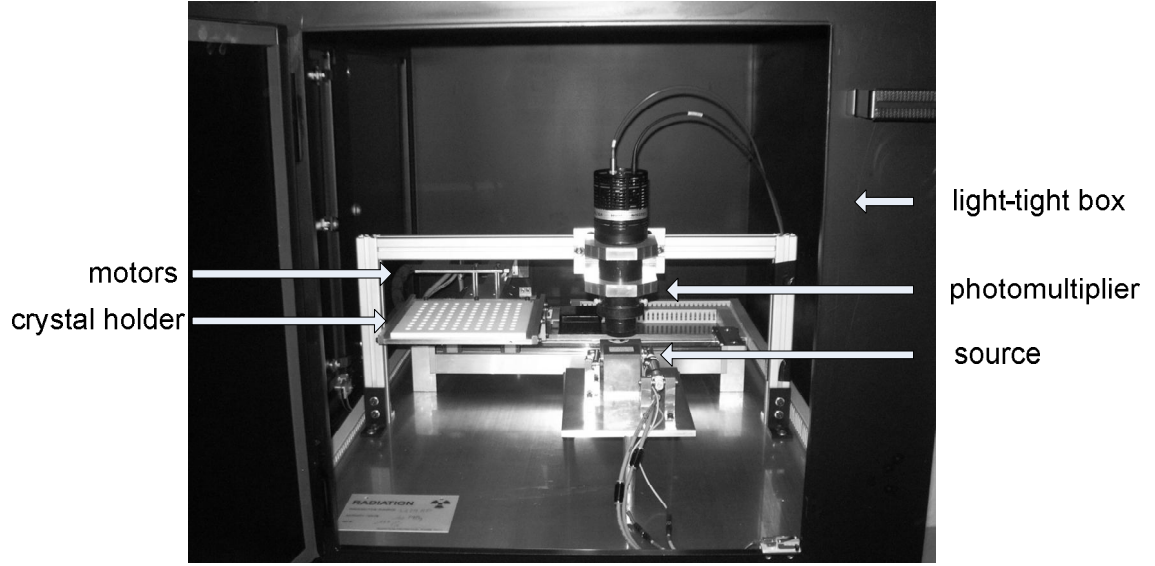


Figure 35 : Photo of MiniACCOS [138]

The spectrum is recorded by an oscilloscope and evaluated with regards to the position of the photopeak in the spectrum. A number of calibration factors are applied to account for high voltage and temperature fluctuations. By measuring a few crystals on both MiniACCOS and the single-crystal characterisation setup explained in chapter 4.2.1.2, it is possible to correlate the position of the photopeak to a number of emitted photons per MeV.

#### 4.2.2 Energy Resolution

The ability of a crystal to exhibit well defined and distinguishable peaks for neighbouring incident photon energies is called the energy resolution. It is most generally defined as the FWHM of the photopeak over its position:

$$\text{Energy Resolution } [\%] = R = \frac{FWHM}{\text{peak position}} \quad (4.18)$$

In order to be able to discriminate gamma photons with slightly different energies, the energy resolution should be as small as possible. Considering its relation to the photopeak position given in (4.18) and thus also the light output, shown in equation (4.15), the latter should be as high as possible.

Some theoretical considerations based on Birks [133] summarize the factors influencing the energy resolution. The mean output pulse  $\bar{Q}$  at the anode of a photomultiplier is:

$$\bar{Q} = \bar{n}_{ph} \cdot \bar{p} \cdot \bar{M} \quad (4.19)$$

where  $\overline{n_{ph}}$  is the mean number of photons created in the scintillator crystal,  $\overline{M}$  the overall gain of the PMT and  $\overline{p}$  the mean photon transfer efficiency defined as:

$$\overline{p} = g_c q \eta_L \quad (4.20)$$

where  $g_c$  is the collection efficiency at the first dynode,  $q$  the quantum efficiency of the photocathode and  $\eta_L$  the fraction of photons produced in the crystal that reach the photocathode, according to the considerations in section 4.2.1.1.

The fractional variance  $v(Q)$  of  $Q$  is defined as the variance  $\text{var}(Q)$  divided by the average of  $Q$  squared:

$$v(Q) = \frac{\text{var}(Q)}{\overline{Q}^2} \quad (4.21)$$

The global energy resolution  $R$  of a detector system can directly be related to the fractional variance  $v(Q)$  of  $Q$ :

$$R = 2.36 \sqrt{v(Q)} \quad (4.22)$$

Following the considerations in Breitenberger [139] and Birks [133],  $v(Q)$  can be approximated to:

$$v(Q) \sim \left[ v(n_{ph}) - \frac{1}{\overline{n_{ph}}} \right] + v(p) + \frac{1 + v(M)}{\overline{n_{ph}} \overline{p}} \quad (4.23)$$

The bracketed term in (4.23) represents the variance in the number of photons due to other effects than Poisson statistics,  $v(p)$  represents the transfer resolution for the photons from the scintillator to the photomultiplier and the last term represents the resolution of the photomultiplier.

One can now introduce the terms intrinsic resolution  $R_i$ , transfer resolution  $R_p$  and photomultiplier resolution  $R_M$ . By defining them directly proportional to the respective square root of the three terms in (4.23), this leads to:

$$R^2 = R_i^2 + R_p^2 + R_M^2 \quad (4.24)$$

The intrinsic resolution can be split into the non proportional response  $R_{np}$  of the scintillator to different photon energies and the influence  $R_{inh}$  of local inhomogeneities on the light output:

$$R_i^2 = R_{np}^2 + R_{inh}^2 \quad (4.25)$$

The transfer resolution is dependent on a combination of factors including the wavelength of the photons, the optical properties of the scintillator, the incidence angle of the photon on the photocathode and the properties of the photocathode itself. In a modern scintillation counter, one can assume that each light photon has an equal probability of generating an electron in the photomultiplier. Therefore,  $v(p)$  can be neglected.

This approximates the energy resolution to:

$$R^2 = R_i^2 + R_M^2 \quad (4.26)$$

where:

$$R_M = 2.36 \sqrt{\frac{1 + v(M)}{n_{ph}\bar{p}}} \quad (4.27)$$

While (4.27) represents the fundamental limit for the energy resolution of a scintillation counter under the assumption that  $R_i$  can be neglected, (4.26) shows that the measured energy resolution in a real system is a function of the intrinsic resolution of the crystal, the number of photons emitted, the photon transfer efficiency and the variance of the PMT gain.

### 4.2.3 Depth Of Interaction

#### 4.2.3.1 Theory

Light propagation in a crystal is directly linked to its intrinsic optical properties, the presence of defects as well as the behaviour of photons at the boundary of the crystal with the surrounding medium. The quality of a crystal with respect to the light propagation is best expressed by the effective light attenuation length  $\lambda$  that corresponds to the distance in the crystal where the chance that a photon has not been absorbed drops to  $1/e$ .

In a real crystal of length  $L$ , with a finite  $\lambda$ , it is possible to determine the position  $x$  of the gamma photon interaction with an uncertainty, the depth of interaction (DOI) resolution  $\Delta x$ . Figure 36 shows such a crystal split in two equal portions, the origin of the  $x$  axis being in the centre of the crystal. If  $2N_0$  is the number of photons produced following an interaction and  $P$  the probability that a light photon extracted from the crystal will generate a photoelectron, the signals  $S_A$  and  $S_B$  read out at each end of the crystal are:

$$S_A = N_0 P e^{-\frac{1}{\lambda}(\frac{L}{2} + x)} \quad (4.28)$$

$$S_B = N_0 P e^{-\frac{1}{\lambda}(\frac{L}{2} - x)} \quad (4.29)$$

The ratio of the two signals is:

$$\frac{S_A}{S_B} = e^{-\frac{2}{\lambda}x} \quad (4.30)$$

which gives:

$$x = \frac{\lambda}{2} \ln \frac{S_B}{S_A} \quad (4.31)$$

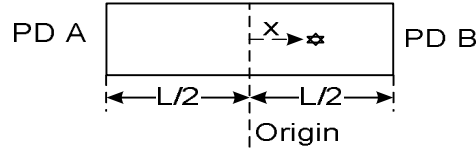


Figure 36 : Crystal of length L, readout out at both ends with a photodetector

Considering that:

$$\frac{\Delta E}{E} \propto \frac{1}{\sqrt{E}} \quad (4.32)$$

the Gaussian law of error propagation applied to (4.31) gives:

$$\Delta x = \left| \frac{\partial X}{\partial S_A} \right| \cdot \Delta S_A + \left| \frac{\partial X}{\partial S_B} \right| \cdot \Delta S_B \quad (4.33)$$

$$\Delta x \propto \frac{\lambda}{2\sqrt{N_0 P}} e^{\frac{L}{4\lambda}} \left( \sqrt{e^{-\frac{x}{\lambda}}} + \sqrt{e^{\frac{x}{\lambda}}} \right) \quad (4.34)$$

Equation (4.33) shows that the DOI resolution depends on the number of generated photons, the position of the interaction along the crystal as well as the attenuation length. The best DOI resolution can be achieved at the centre of the crystal ( $x = 0$ ).

Provided the number of photons generated is independent of the position of the event in the crystal and assuming a stable probability for the generation of a photoelectron P, the only variable that can be tuned is the effective attenuation length.

In an ideal crystal, no light that is produced is lost by absorption, scattering or total reflection. If one supposes that the light is emitted isotropic, the amount of light collected at each extraction end of a quadratic crystal would be the same. In such a crystal, the light absorption coefficient is zero while the effective attenuation length is infinite. It would therefore be impossible to determine the exact position of the light source within the crystal by comparing the number of photons measured on each side.



However, in a real crystal, light is lost by the processes explained in section 4.1.2. They all have an influence on the effective absorption length and can, for some of them, be tuned to a level where the DOI resolution is sufficient for PET applications, as shown in section 2.5.4.3. The most accessible parameter is the surface finishing of the crystal that can be altered by either changing the coating of the crystal or by influencing the crystal itself, for example by having polished or unpolished faces. If, for example, the lateral side of a crystal is polished, light reflection will be specular and photons will reach the extraction surface on the most direct way possible. If however that lateral face is not polished, the rough structure induces diffuse reflection, thereby reducing the chance of a photon to remain on the fastest way to the extraction surface, increasing the transit time in the crystal as well as the chance for absorption. If the photon is not emitted in the centre of the crystal, the photodetector closer to the interaction will collect more light than the photodetector farther away. This ratio allows precise determination of the position of the photopeak within the crystal.

#### 4.2.3.2 Characterisation

In order to determine the DOI resolution, we develop in the frame of this thesis the setup presented in figure 37, based on the work by Trummer et al. [140], [141] and Vilardi et al [142]. The crystal that is assessed is wrapped in Teflon to reduce light losses and increase the light collection efficiency. It is then placed between two PMTs that readout the light at each extraction surface. The PMT window surface that is not occupied by the crystal is also covered with reflective Teflon. A third PMT is equipped with a BGO crystal wrapped in Teflon. It is placed at a sufficient distance of the first crystal and works as a tagging detector. A  $^{22}\text{Na}$  source that is located between the studied crystal and the tagging crystal produces two collinear gamma rays. By only accepting events that are simultaneously detected in all three PMTs, it is possible to collimate the source on a sufficiently small area on the crystal and exclude all events that hit the crystal outside of this area. The crystal under investigation as well as the two readout PMTs are on a common mechanical structure that is moved by a LabView-controlled motor to successively irradiate different portions of the crystal.

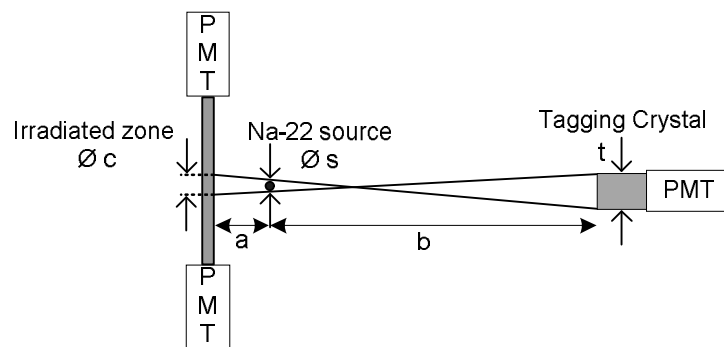


Figure 37 : Geometry of the DOI bench

The diameter  $c$  of the irradiated zone can be calculated under consideration of the source diameter  $s$ , the diameter  $t$  of the irradiated zone as well as the distances  $a$  and  $b$  between respectively the studied crystal and the source as well as the source and the tagging crystal:

$$c = s + \frac{a}{b} (s + t) \quad (4.35)$$

The source has an active diameter of  $s = 1$  mm. The tagging crystal has a square surface whose edges measure  $d = 63$  mm. The source was placed at a distance  $a = 35$  mm from the crystal. The tagging crystal was at a distance of  $b = 750$  mm from the source. This diameter of the irradiated zone therefore is  $c = 1.3$  mm.

Figure 38 shows the electronic setup used for data acquisition. In order to comply with the maximum signal accepted by the subsequent electronics, the signals from the PMTs connected to the crystal are first attenuated to a maximum amplitude of 2 V. Fan-In/Fan-Out modules duplicate the incoming pulse: one is used to verify whether the signal is valid and in coincidence with the signals from the other channels whilst the other one is delayed and then sent to a gate.

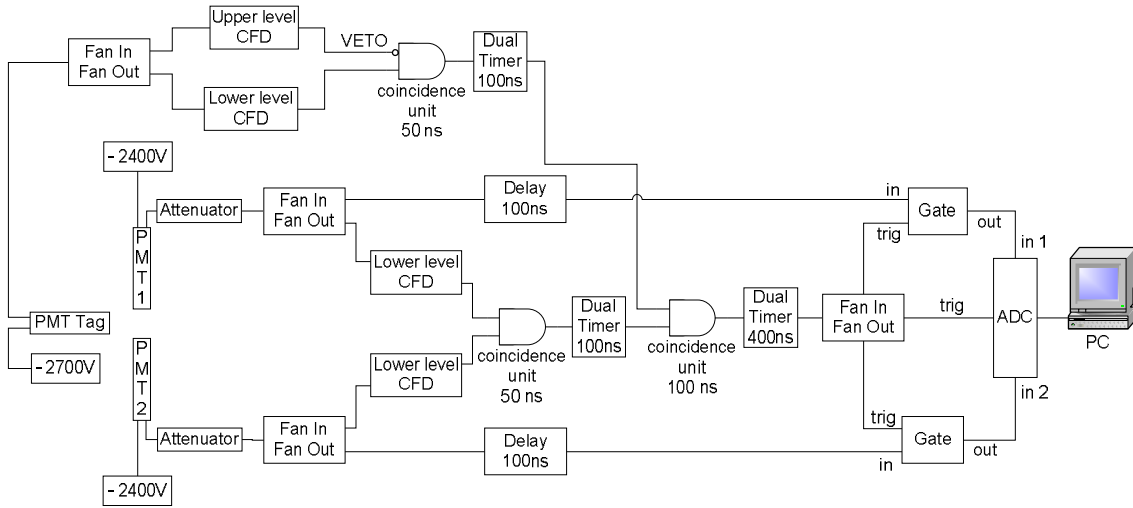


Figure 38 : DOI bench data acquisition setup

In the branch that verifies the coincidence's validity, each signal first transits a lower level constant fraction discriminator (CFD) that rejects low amplitude noise signals. The signals from PMT1 and PMT2 then enter a coincidence unit that emits a logic pulse if there are simultaneous events. In parallel, the signal from the tagging PMT is filtered to select only events that are part of the photopeak. Indeed, the signal is split by a Fan-In/Fan-Out and enters two separate CFD channels set to a lower level and an upper level. If the signal from the tagging PMT lies within these boundaries, the subsequent coincidence unit will emit a logic pulse. If the signal lies under the lower limit or above the upper limit, a veto prevents the emission of a pulse. The signals from the tagging and verification branches enter a final coincidence unit that emits a logic pulse if it gets simultaneous inputs. The logic pulse from the final coincidence unit is then split by another FanIn/Fan-Out and simultaneously opens the two gate modules for the original signals from PMT1 and PMT2 and triggers a LeCroy 2259B ADC. This 11-bit voltage-sensitive ADC generates a value proportional to the peak voltage of the incoming signal and therefore also proportional to the amount of light recorded by the respective PMT.

The ADC is connected via USB to a computer that runs a LabView software for automatic data acquisition and evaluation. It creates three histograms with the recorded information. Two histograms are generated with the pulses recorded at each PMT: they are dedicated light yield spectra for each PMT. The third histogram considers, for each event, the sum of the ADC counts for both PMTs. It represents the global light yield spectrum for the crystal. Once enough information about a position has been collected – in general between 500 and 1000 simultaneous events – the computer changes the position of the crystal by actuating the motor.

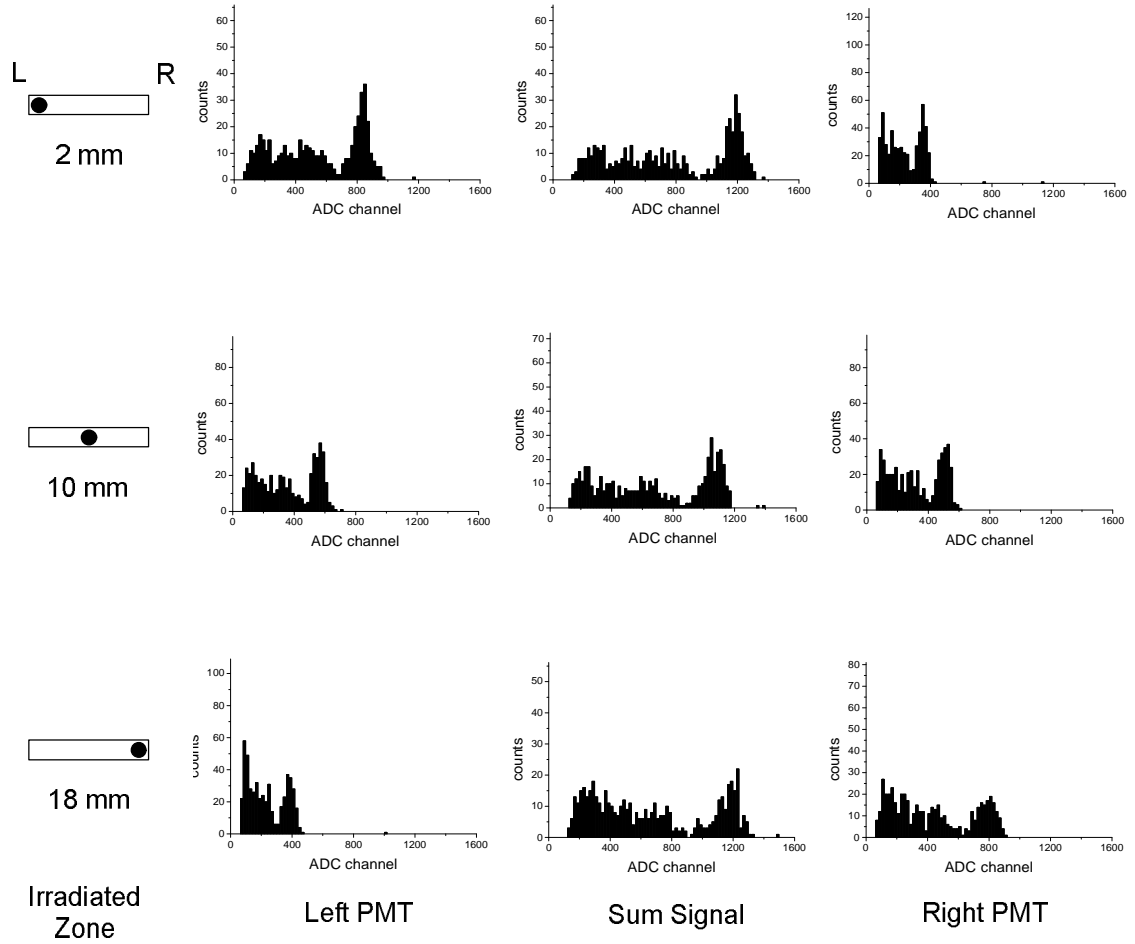


Figure 39 : DOI sample spectra

Figure 39 shows an example of individual spectra recorded at each one of the PMTs for three different irradiated zones  $c$ , as well as the combined spectrum. Figure 40 shows the evolution of the quantities of light measured by each PMT as a function of the position of the gamma interaction for an LYSO crystal produced by CPI, before and after depolishing of one lateral side.

The precision of the DOI information is determined with the data evaluation routine of the LabView controlling software. At each measurement position, the position of the photopeak is determined within the combined spectrum. A Gaussian fit provides the exact position of the centroid  $\mu$  as well as the standard deviation  $\sigma$ . For all events that are considered part of the

photopeak, i.e. whose sum pulse area lies within the interval  $\mu \pm \sigma$ , the asymmetry  $\alpha$  between the pulse areas  $A_1$  and  $A_2$  on the individual PMTs is computed:

$$\alpha = \frac{A_1 - A_2}{A_1 + A_2} \quad (1.1)$$

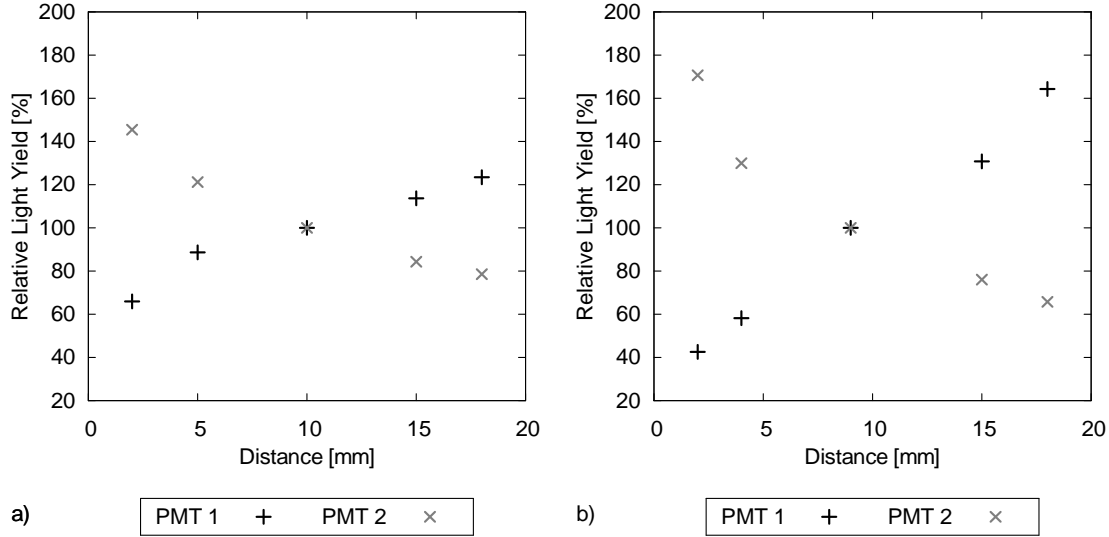


Figure 40 : Correlation between the quantities of light measured by each PMT and the position of the gamma interaction in a) a fully polished crystal and b) a crystal with one depolished lateral side.

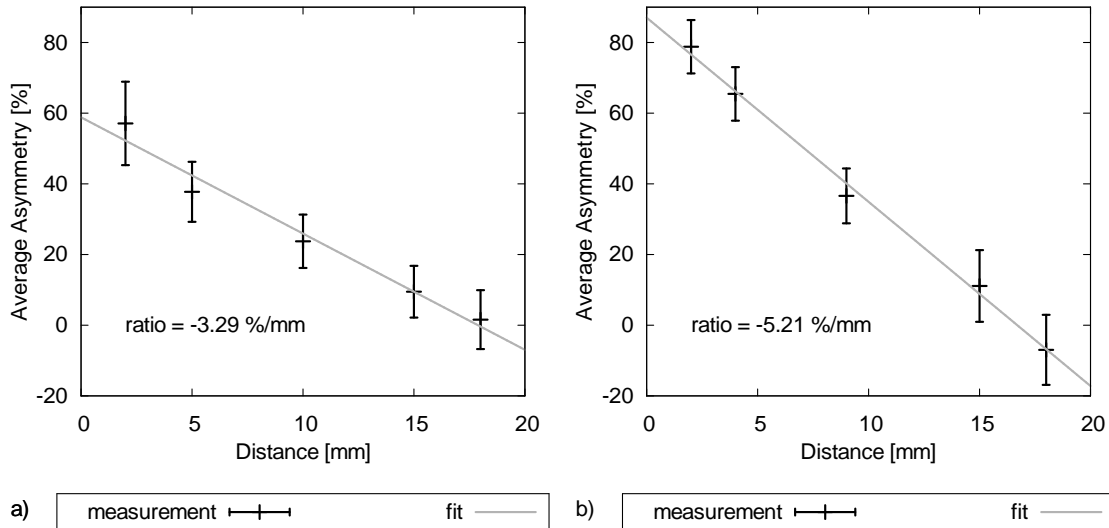


Figure 41 : Correlation between the average asymmetry  $\langle \alpha \rangle$  and the position of the interaction in a) a fully polished crystal and b) a crystal with one depolished lateral side. The error bars represent the FWHM of the asymmetry distribution in each point.

This yields a Gaussian distribution for the asymmetries that is properly fitted in order to provide a mean  $\langle \alpha \rangle$  and the full width at half maximum  $\text{FWHM}_\alpha$  for the position of the asymmetry

curve. The mean asymmetry  $\langle \alpha \rangle$  is then plotted against the measurement position in the experimental setup. This line can be fitted in a good approximation with a straight line. This slope is the light output asymmetry per unit length  $\alpha_{\text{DOI}}$  in %/mm that characterizes the DOI resolution of a crystal.

Figure 41 shows the evolution of the average asymmetry as well as the fit applied for the crystals given as an example in figure 40. Since the two acquisition channels had not been calibrated to have the exact same gain, the zero crossing is not in the centre of the crystal.  $\alpha_{\text{DOI}}$  is -3.29 %/mm before and -5.21 %/mm after the mechanical depolishing.

It is possible to estimate the precision of the DOI by dividing  $\alpha_{\text{DOI}}$  by the average FWHM of the asymmetry peaks  $\langle \text{FWHM}_{\alpha} \rangle$ . For the given example, this would indicate a DOI precision of 2.7 mm before and 1.6 mm after the depolishing. However, the width of the asymmetry peak is directly related to the size of the irradiated zone on the crystal and thus the quality of the measurement setup. It is therefore not used in the further evaluation of crystal properties.

## 4.3 Results

The production of a ClearPEM requires 6144 crystals. We already had 800 crystals available from Photonic Materials Ltd (*PML*), Glasgow, UK, a surplus from the production of the first ClearPEM prototype. These crystals had been depolished on all four lateral sides by the manufacturer. We needed to provide 5344 additional crystals for the completion of ClearPEM-Sonic. They were bought from Crystal Photonics Inc. (*CPI*), Sanford, Florida, USA. We ordered those crystals polished on all faces to study the influence of different surface states on the crystal properties, optimize them in order to correspond to ClearPEM requirements and, ideally, exceed the properties of crystals used for the production of the first prototype. At the start of this study, laboratory tests performed on the first ClearPEM prototype, made with PML crystal depolished on four lateral faces, indicated an energy resolution around 13 % and a DOI resolution  $\alpha_{\text{DOI}}$  better than 4 %/mm [39].

The surface state of a crystal has a direct influence on the light output, energy resolution and depth of interaction resolution of the crystal [141]. We thus study crystals from both manufacturers, with different surface polishing.

### 4.3.1 Depolishing Study

A first study is conducted on a set of six fully polished crystals. We measure the effect of depolishing one side to an average roughness of 280 nm on the crystal properties, comparing light output, energy resolution and DOI resolution before and after the depolishing. On selected crystals, we depolish additional sides to evaluate whether this could further improve the crystal properties.

Figures 42 to 44 summarize the measurements. In their fully polished status, the crystals show an energy resolution of  $13 \pm 1.5$  %. The DOI resolution  $\alpha_{\text{DOI}}$  is  $3.5 \pm 0.24$  %/mm, at the limit of what is acceptable for ClearPEM. The depolishing of a single lateral face substantially alters the DOI resolution. All crystals now exhibit DOI resolution close to  $5.3 \pm 0.3$  %/mm and therefore comply with the project requirements. Although the light output diminishes by 10 % for most of the crystals, the energy resolution is unaltered. Further depolishing of two more lateral sides does not change much to these results. The depolishing of the fourth lateral face however further improves the DOI resolution to 7.5 %/mm. However, the energy resolution also deteriorates. These results are in agreement with previous studies by J. Trummer [141], who also notices an improvement of the DOI resolution as a function of the number of depolished sides.

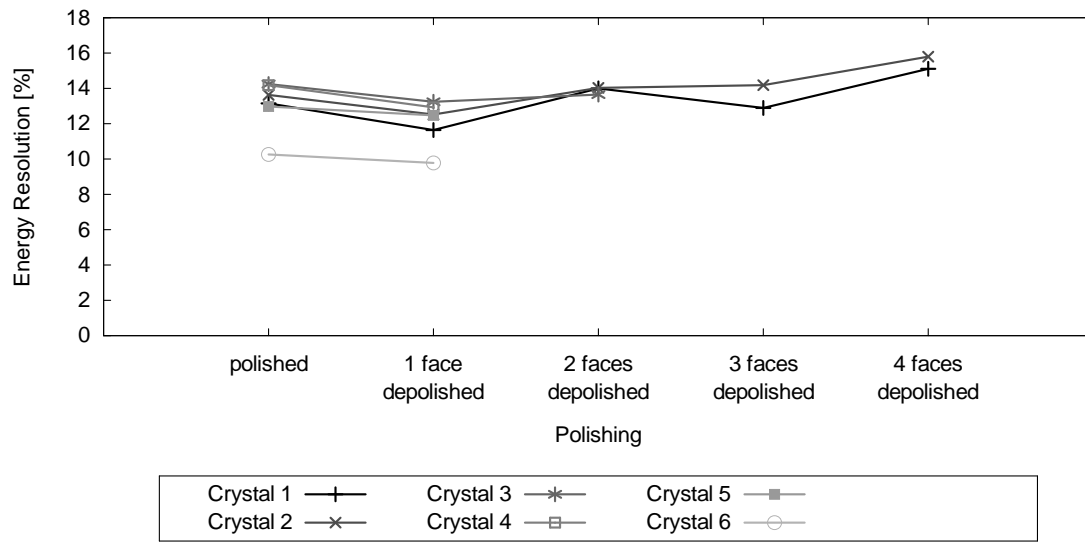


Figure 42 : Energy resolution as a function of the crystal polishing

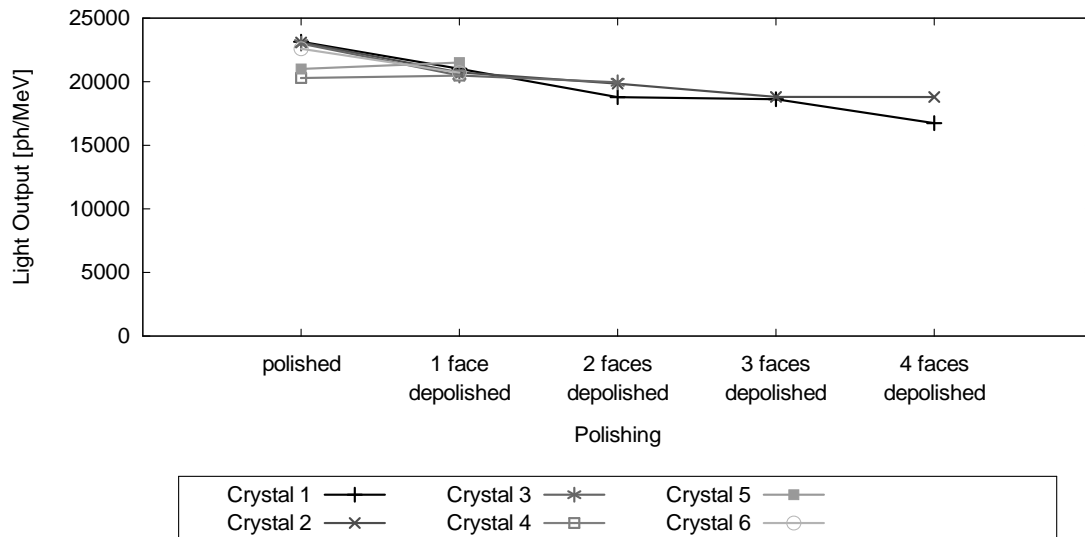


Figure 43 : Light Output as a function of the crystal polishing

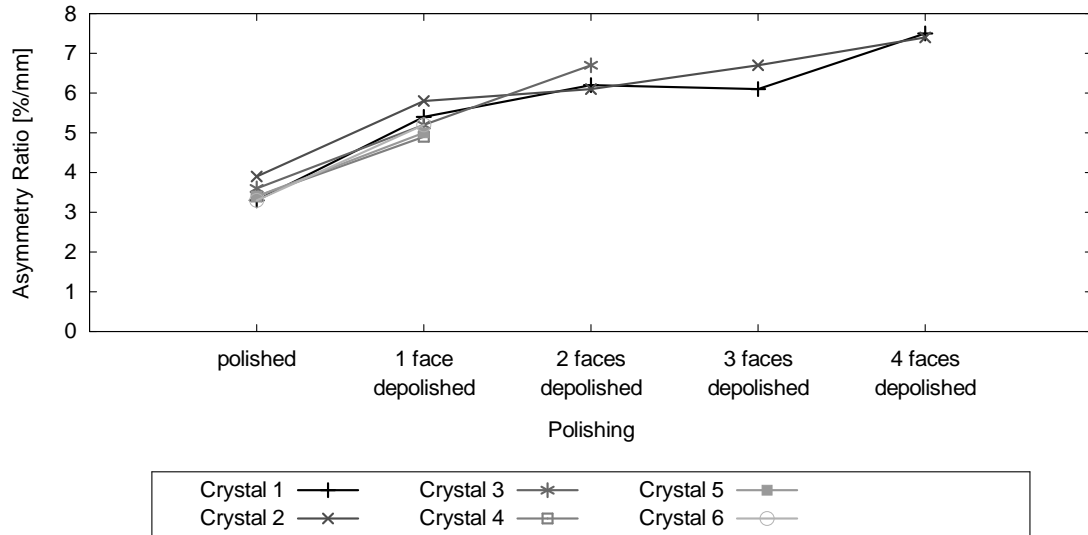


Figure 44 : DOI resolution  $\alpha_{DOI}$  as a function of the crystal polishing

In a subsequent study, we evaluate how these crystals compare to crystals used during the production of the first ClearPEM prototype. We compare the performance of 4 CPI crystals depolished on one face with 6 standard PML crystals depolished on 4 lateral faces, used in the production of ClearPEM. We also assess 4 PML crystals depolished on only one lateral face with the same method as CPI crystals. Figure 45 compares the average roughness of these crystals.

The DOI resolution (Figure 48) is similar around 5 %/mm for both crystals depolished on one lateral face. PML crystals depolished on all 4 lateral faces have better DOI resolution. Figures 46 and 47 show a gain of 2 percentage points in energy resolution and 30 % in light output with CPI crystals depolished on one side – used in ClearPEM-Sonic – with respect to PML crystals depolished on 4 sides – used in the first ClearPEM and, in small numbers, also ClearPEM-Sonic. The comparison with PML crystals depolished in a similar way than CPI crystals also shows that the better performance of CPI crystals is not only due to the different depolishing. Indeed, PML crystals depolished on one face have light output and energy resolution similar to PML crystals depolished on four lateral faces.

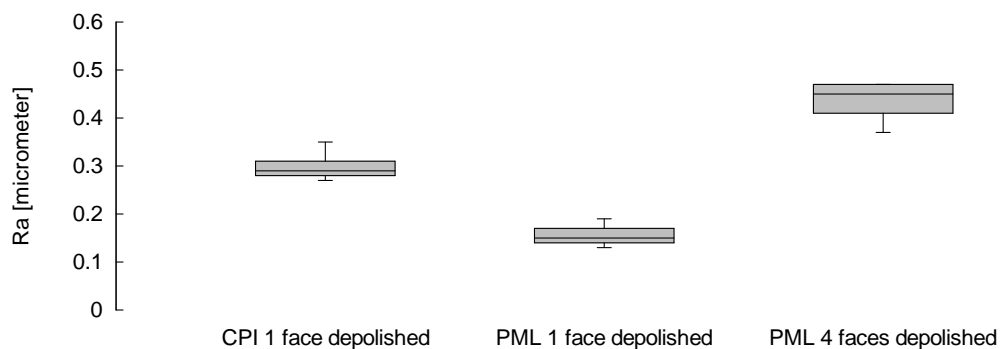


Figure 45 : Roughness of compared crystal batches

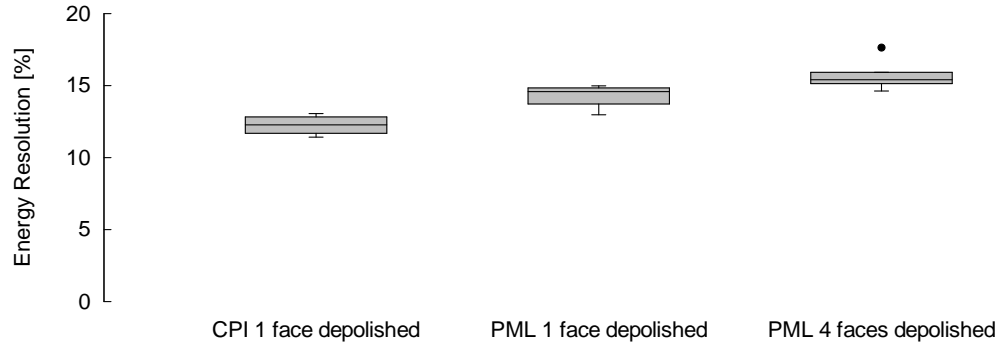


Figure 46 : Energy Resolution of compared crystal batches

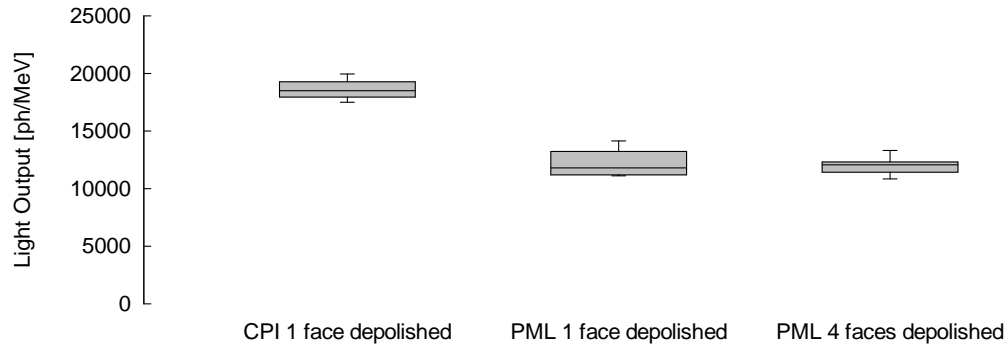


Figure 47 : Light output of compared crystal batches

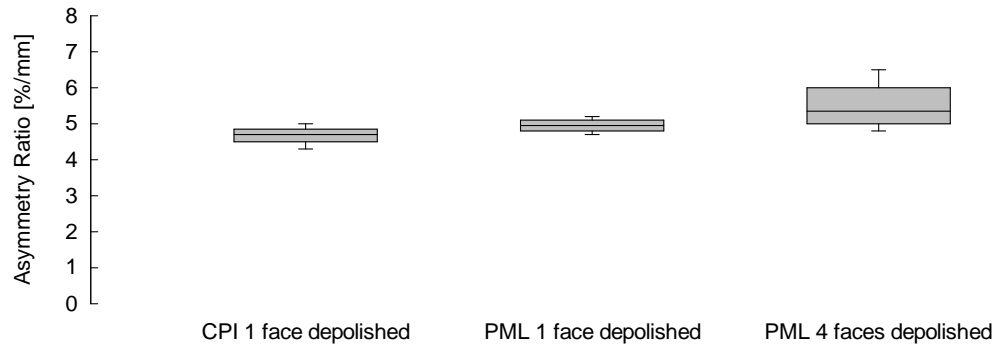


Figure 48 : DOI resolution  $\alpha_{DOI}$  of compared crystal batches

We conclude that CPI crystals depolished on one side have a comparable DOI resolution, higher light output and better energy resolution than crystals used in the first ClearPEM prototype. They thus comply with the project requirements. We further notice that the depolishing of more than one lateral side does not yield a substantial improvements as long as at least one lateral face remains polished. Considering the additional amount of work such depolishing would be, and given the relatively small impact it would have, we decided to depolish only one lateral side of all crystals used in the production process. This will also minimize the impact on the light loss in the crystal.



### 4.3.2 Mechanical Depolishing

The depolishing study and the comparison with crystals from PML confirm that we are able to produce crystals with properties that comply with the requirements for ClearPEM. We thus develop a depolishing procedure that allows depolishing up to 20 crystals at once, based on previous work in the frame of the construction of the electromagnetic calorimeter of CMS [143].

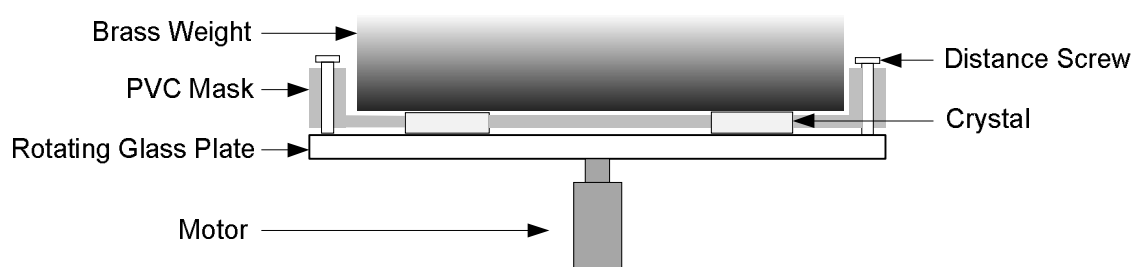


Figure 49 : Schematic cross-section of the depolishing device

The procedure consists in roughing up one lateral face of the crystals on a LAM PLAN MM8027 lapping machine. Figures 49 and 50 show a drawing and a photo of the depolishing device. The crystals are immobilized in a PVC holder. A brass weight applies a constant and uniform pressure of  $200 \text{ g/cm}^2$  on the crystals. The crystals are pressed against a rotating glass plate that is covered with the LAM PLAN diamond abrasive BioDiamant MM142 with a grain size of  $6 \mu\text{m}$ . The depolishing of 20 crystals with this system takes about half an hour. All crystals produced by CPI, used for the construction of ClearPEM-Sonic were depolished by Dominique Deyrail on this machine.

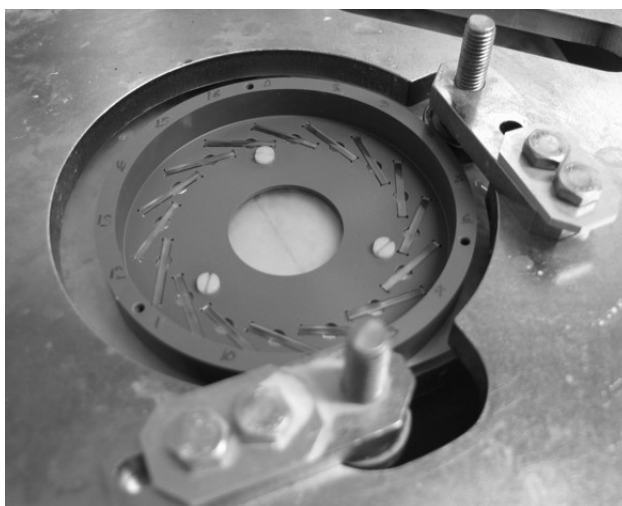


Figure 50 : Photo of the depolishing device, fully loaded with crystals, without the brass weight

The homogeneity of the depolishing is verified on a few samples with a surface roughness measurement. We use a Taylor-Hobson Surtronic 3+ surface profiler. We record the  $R_a$ , which corresponds to arithmetic mean of the departures of the profile from the mean line, on the

depolished faces. According to the manufacturers notice, in ideal conditions, the Ra is measured with a precision of  $0.02\ \mu\text{m}$  [144].

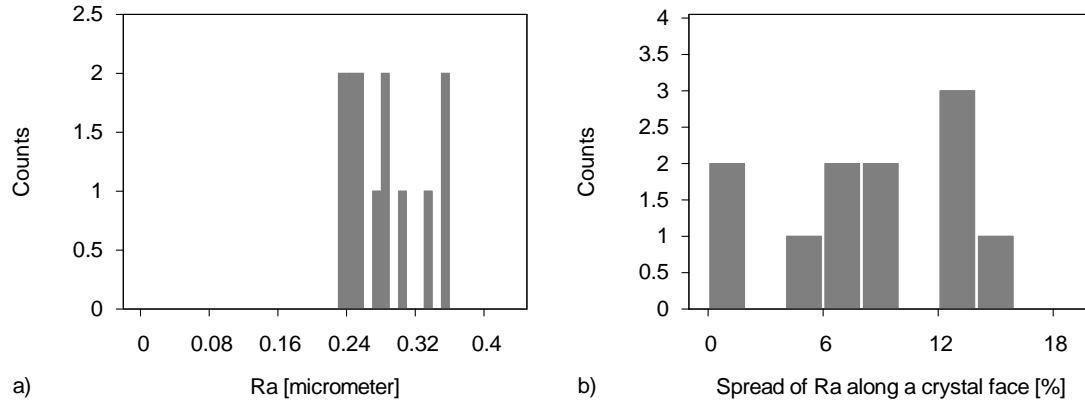


Figure 51 : a) Average roughness and b) spread in percent between the lowest and the highest Ra on a single crystal face.

We measure the Ra at three positions on the crystals: at both ends and at the centre of the crystal, on a length of 2 mm each. Each measurement is repeated three times. Figure 51 summarizes these measurements. It shows that the depolishing of different crystals is homogeneous around  $0.28 \pm 0.05\ \mu\text{m}$ . It is also sufficiently homogeneous along the crystal, with average variations of  $8 \pm 5\%$  along a single crystal side.

#### 4.3.3 Large-Scale Quality Control

ClearPEM-Sonic uses 800 crystals delivered by PML, prepared to the same specifications than crystals used in the first ClearPEM prototype. All other 5344 crystals are produced by CPI and delivered to CERN in a fully polished state. At CERN, a representative sample of all delivered crystals undergoes initial quality control, before further processing. This includes both a visual quality control to ensure broken or splintered crystals are removed as well as a scan with MiniACCOS, explained in chapter 4.2.1.3, to verify the homogeneity in the amount of light emitted by the crystals.

The results are summarized in figure 52. The crystals delivered by CPI have an average light output of 18615 photons per MeV with a spread of 4.8 percent while the crystals delivered by PML have an average light output of 13997 photons per MeV with a spread of 9.4 percent. The light output of both crystals batches is sufficiently homogeneous for the production of crystal matrices. The light output of CPI crystals is expected to decrease by around 10 % after the depolishing of one lateral side.

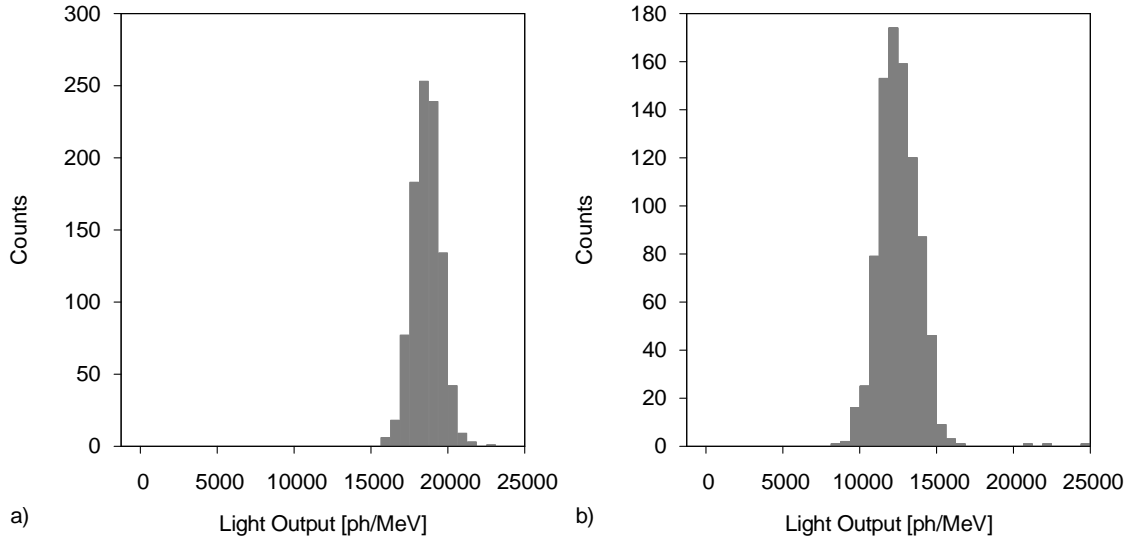


Figure 52 : Normalized light output measured on MiniACCOS for a) 965 fully polished CPI crystals and b) 880 PML crystals depolished on 4 lateral faces

## 4.4 Detector Matrices

After their initial quality control, CPI crystals are depolished at CERN according to the method described in chapter 4.3.1. All crystals are then shipped to the matrix manufacturer for crystal matrix production. There, the crystals are aligned in matrices of 4x8 crystals, with BaSO<sub>4</sub> being used as the cladding material that serves both as a diffusing reflector and gives rigidity to the matrix. The matrices are then shipped to the Laboratório de Instrumentação e Física Experimental de Partículas (LIP) in Lisbon, Portugal, where they undergo a quality test using APDs to individually check all matrix channels. They are then glued to APDs and mounted on ClearPEM modules, as described in chapter 3.2.1.

### 4.4.1 Production Process Selection

Before launching the large-scale production for ClearPEM-Sonic, we test two production processes for the crystal matrices. The details of the processes were not communicated by the crystal manufacturer. Both processes are supposed to produce matrices to the ClearPEM specifications. We order two matrices made with each process:

- the first is made with PML crystals depolished on all four lateral sides
- the second is made with fully polished CPI crystals.

We base this selection on fully polished CPI crystals to perform it in parallel with the development of the above-mentioned depolishing procedure. This decision is taken to reduce the delay this would have on the global schedule of the project.

The matrices are measured by coupling the whole matrix with silicone grease to the window of a Photonis XP2020Q photomultiplier, similar to the method used to evaluate individual crystals.

The measured light output therefore is the mean light output of all crystals contained in the respective matrix. The energy resolution is the energy resolution measured on events of all crystals in the matrix. It therefore combines the energy resolution of individual crystals with the spread in absolute light output between crystals.

Table 9 shows that due to differences in the processes, matrices produced by process 1 have a substantially lower light output than matrices produced with process 2. Based on these results, we select production process 2 for the production of crystal matrices used in ClearPEM-Sonic.

Crystal Producer	Production Process	Light Output [ph/MeV]	Energy Resolution [%]
PML	Production Process 1	4579	30.5
	Production Process 2	11169	30.5
CPI	Production Process 1	5454	28.5
	Production Process 2	16474	25.7

Table 9 : Results from the production process selection

#### 4.4.2 Comparison with APD measurements

The measurements made at CERN in the frame of this thesis are complemented by a series of measurements made on complete matrices at the Laboratório de Instrumentação e Física Experimental de Partículas (LIP) and the Instituto Superior Técnico of the Universidade Técnica de Lisboa, both located in Lisbon, Portugal, presented by Inês Rolo in [145].

In this work, 12 crystal matrices with PML crystals depolished on 4 faces and 12 crystal matrices with CPI crystals depolished on one face are compared with regards to light output, energy resolution and depth of interaction resolution. For the light yield and energy resolution measurement, each matrix is coupled to a Hamamatsu S8850 APD. Each channel of this APD matrix is read out individually by dedicated electronics. The depth of interaction performance is measured by coupling each light extraction face of the matrix to a S8550 APD, using dedicated electronics similar to the electronics used in the production ClearPEM.

The results are summarized in table 10. The light output measurements confirm findings from this thesis: the energy resolution of CPI crystals is an average of 2 percentage points, the light output an average 21 % better than for PML crystals. The DOI measurements confirm that CPI crystals depolished on one side have a  $\alpha_{DOI}$  around 5 %/mm and thus comply with the specifications of a depth of interaction capability better than 4 %/mm. They also confirm that PML crystals depolished on four faces have better DOI resolution.

Crystal	Light Output [ADC channels]	Energy Resolution [%]	$\alpha_{DOI}$ [%/mm]
PML	1738	$15.6 \pm 1.3$	5.8
CPI	2095	$13.7 \pm 1.3$	5.2

Table 10 : Measurements performed at LIP [145]

Zum Werke, das wir ernst bereiten,  
Geziemt sich wohl ein ernstes Wort,  
Wenn gute Reden sie begleiten,  
Dann fließt die Arbeit munter fort.  
So laßt uns jetzt mit Fleiß betrachten,  
Was durch die schwache Kraft entspringt,  
Den schlechten Mann muß man verachten,  
Der nie bedacht, was er vollbringt.  
Das ist's ja, was den Menschen zieret,  
Und dazu ward ihm der Verstand,  
Daß er im innern Herzen spüret,  
Was er erschafft mit seiner Hand.

in Friedrich Schiller, *Das Lied von der Glocke*

## 5 Multimodality Integration

ClearPEM-Sonic is an evolution of breast imaging based on dedicated PEM. The latter offers the possibility of detecting metabolically hyperactive regions in the breast. These can be associated with cancerous tissue although, as explained in section 2.2, not all regions with a higher glucose metabolism are cancerous. A second, different imaging modality could help refining this diagnosis.

The main drawback of PEM is inherent to its principle: it does not show anatomy in sufficient detail and delivers only insufficient information about the surrounding anatomy. The SuperSonic Imagine Aixplorer ultrasound system has been chosen to be the modality that provides complimentary information: it combines standard 3D ultrasound, which provides information about the anatomy, with 3D elastography, which provides additional specificity during the diagnosis.

In order to provide a final system in which both modalities are completely integrated and that provides a co-registered image at the end of the exam, a number of difficulties addressed in section 3.4.2 have to be overcome.

The solutions developed in the frame of the thesis are presented in this chapter.

### 5.1 Development of a Breast Stabilization System

The workflow for acquiring images with ClearPEM-Sonic requires the patient to remain in the same position for both exams. If movement of the breast is prevented, this will ease the superposition of the images to display a final, combined image. We therefore develop methods

for stabilizing the breast without impeding on the proper function of the other modality or preventing the access to any region of interest.

The two initially proposed designs are breast compression paddles or a conical stabilization system. Figure 53 shows respective schematics as proposed during initial discussions in June 2008. Both possible designs are evaluated under all aspects to find the best one for ClearPEM-Sonic.

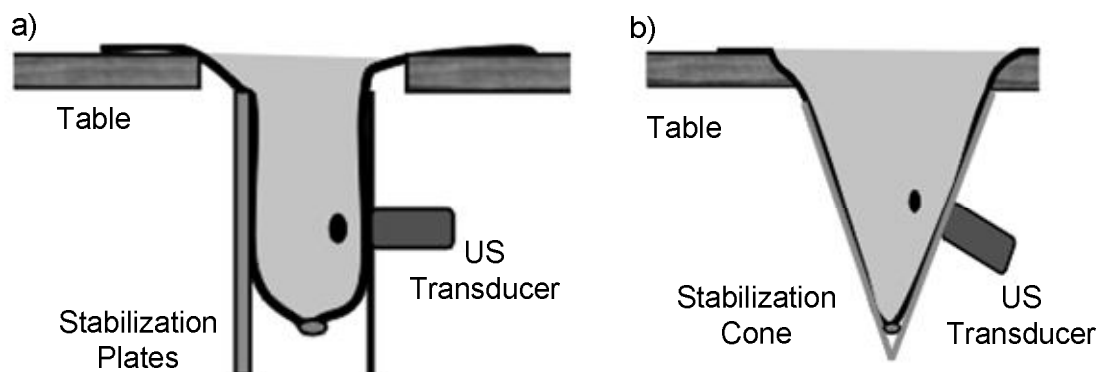


Figure 53 : Initially proposed setups: a) with stabilization plates and b) with a stabilization cone

### 5.1.1 Stabilization Plates

Stabilization plates can be used to retain the breast in its position by applying pressure to prevent any movement. This flattens the breast. The position of the stabilization system thus cannot be changed during the exam as this would change the deformation of the breast, which is a serious disadvantage during image co-registration. Therefore, the paddles remain in the same position and the US transducer must be able to image any region of interest under this circumstances. It can only be brought into contact with one of the stabilization plates. The breast must therefore be sufficiently flattened to have homogeneous contact with the stabilization plates. This prevents air gaps that would impede on the US examination. The applied pressure would however be lower than during an X-ray mammography exam where the breast has to be flattened as much as possible to spread it, thereby separating superposed structures, increasing the level of detail and globally reducing the radiation dose.

This solution implies that the US transducer will not be in direct contact with the breast. The compression paddle on the US transducer's side should ideally not absorb US energy and not produce any reflections of the US wave at either the transducer/plate or plate/tissue interfaces. It should absorb or scatter radiation the least possible as it is in the flight path of emitted positrons. This plate, called front plate, should thus have low  $Z$  to prevent photon absorption and scattering, be thin and have density similar to organic tissue to reduce US absorption and reflection. Thin organic plates or stretched foils should fulfil those requirements.

The plate on the opposite side of the breast, called rear plate, should equally prevent photon absorption and scattering. It should again have organic tissue density to reduce reflections at the

tissue/plate interface but be a good ultrasound absorber to prevent artefacts from reflections at the plate/air interface.

In all cases, the materials must be suited for use in a clinical environment, being biocompatible and easy to disinfect.

#### 5.1.1.1 Measurement of the speed of sound and US attenuation coefficient

We evaluate different candidate materials in the ultrasound laboratory of the Laboratoire de Mécanique et d'Acoustique of the Centre National de la Recherche Scientifique (LMA-CNRS) in Marseille.

The first series of tests on all materials shall determine the US attenuation coefficient as well as the speed of sound in the material, which has a direct influence on the ultrasound reflection (3.3.1). The tests are made with an ultrasound transmitter/receiver setup placed in a water tank (Figure 54). The water ensures optimal US coupling. A frame holding the sample plate can be inserted between the transmitter and the receiver. Motors allow changing the distance between the US probes and the sample. The probes can also be rotated around the sample to record information under different angles.

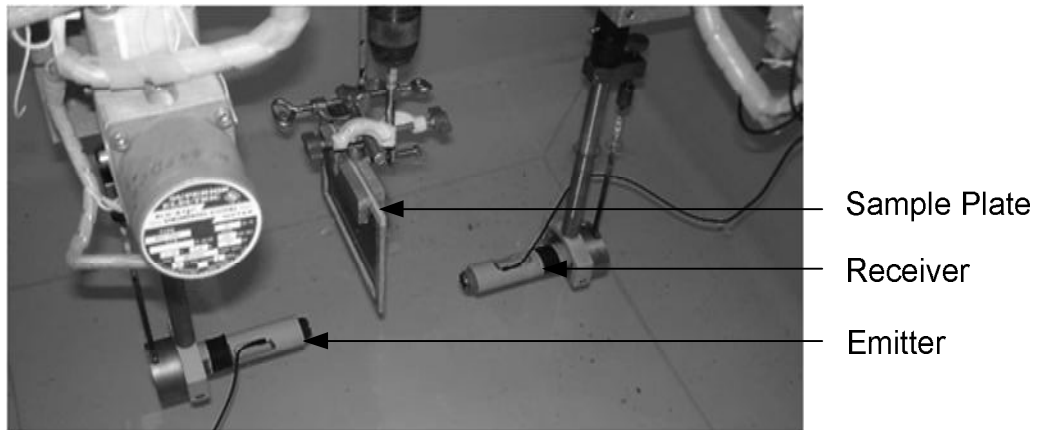


Figure 54 : Photo of the US transmission setup, placed in a filled water tank

For each material, two successive transmission measurements are made: first, a reference measurement where no sample disturbs the US wave and then, a measurement with the sample (Figure 55). During each measurement, the temporal signal is measured by the receiver and the Fourier transformation calculated (Figure 56).

The speed of sound in the material  $C_b$  can be calculated according to:

$$C_b = \frac{C_0}{1 - \frac{\Delta t \cdot C_0}{e}} \quad (5.1)$$

where  $C_0$  is the known speed of sound in water,  $e$  the measured thickness of the plate and  $\Delta t$  the measured time difference between the arrival of the US wave in the reference and sample scans.

The US attenuation at a certain frequency can be calculated knowing the difference in amplitude between the reference and the sample scans.

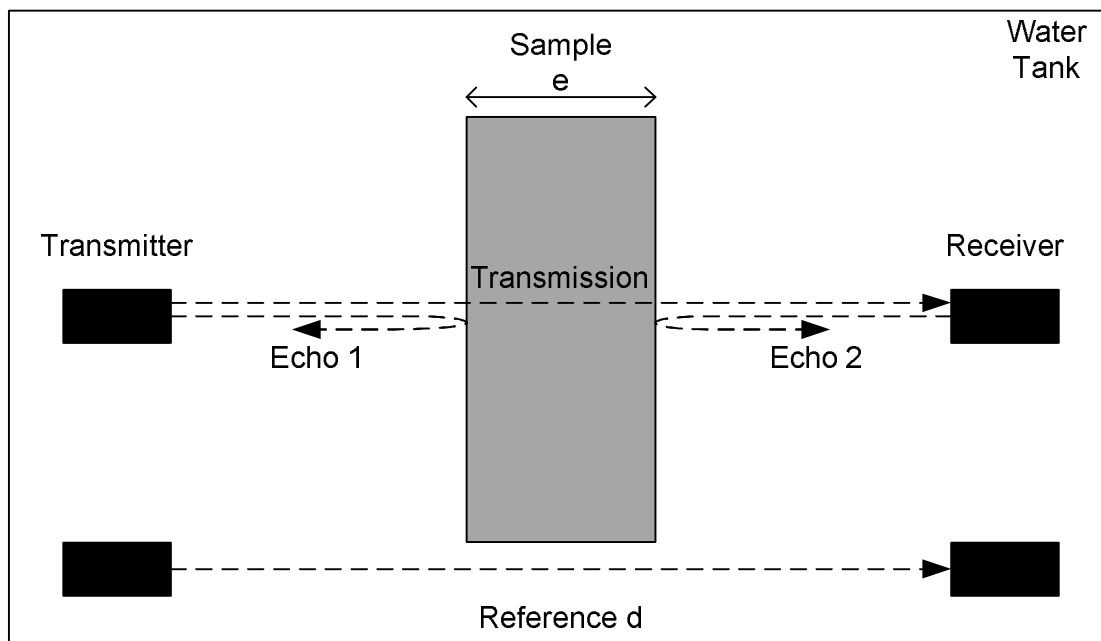


Figure 55 : Scheme of the US transmission setup and measurements

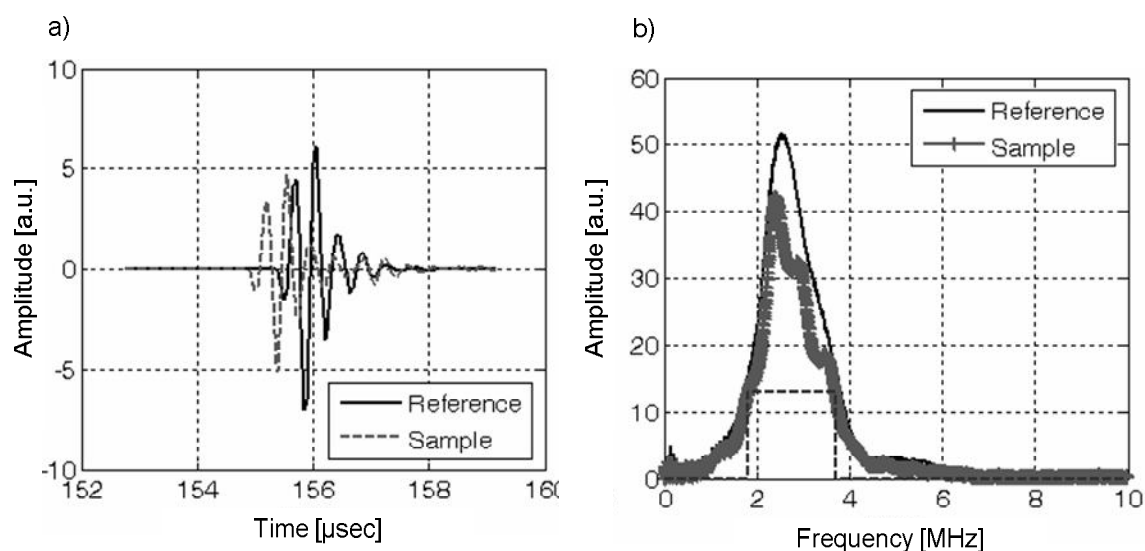


Figure 56 : Example of a) recorded temporal signals and b) the Fourier transformations for a reference measurement and subsequent sample measurement with a 2 mm thick PVC plate

For the front plate, we test both stretched thin films and rigid plates. Stretched thin films are expected to be thin enough to have only minimal impact on the US signal. Plates should have low attenuation to reduce the absorption of the US wave and speed of sound similar to human tissue to avoid parasitic reflections. We test stretched films of biaxially-oriented polyethylene terephthalate (boPET, commercial name Mylar) and Kapton and rigid plates made out of polymethyl acrylate (PMMA, commercial name Plexiglas), polyvinyl chloride (PVC),



polyethylene terephthalate (PET) and polymethylpentene (PMP, commercial name TPX RT-18). For the rear plate, we test RenShape BM5066, a polyurethane with a density of  $1.1 \text{ g/cm}^3$  produced by Huntsman Advanced Materials [146]. It is expected to have excellent US absorption properties and should help reduce reflections.

We are able to determine the attenuation of all materials. However, the comparatively high attenuation per millimetre measured for the foils indicates that the experimental system is not reliable in this range. The amplitude of the signal recorded with the receiver is mainly reduced by reflections at the interface, not attenuation in the foil. We can measure the speed of sound of the plates. The low thickness of the tested foils does not allow measuring their speed of sound. The results from all measurements, as well as a comparison with values found in literature, are summarized in tables 11 and 12.

	Material	Density [g/cm <sup>2</sup> ]	Thickness [cm]	US Attenuation [dB]	US attenuation [dB/mm]	
					Measured	Literature
FOILS	Mylar	1.37	0.05	0	n.a.	n.a.
			0.0125	0.12	9.6	
			0.0175	0.19	10.85	
	Kapton	1.43	0.0125	0.78	62.4	n.a.
PLATES	PMMA	1.19	0.1	0.34	0.34	0.49 [147]
	PVC	1.38	0.2	1.85	0.92	1.12 [148]
	Polyethylene	0.94	0.2	1.25	0.63	0.86 [147]
	TPX	0.83	0.3	0.51	0.17	n.a.
	RenShape BM 5066	1	0.3	10.9	3.63	n.a.

Table 11 : Attenuation measurements at LMA, at 2.5 MHz ultrasound centre frequency (measured values with a precision of 5 %)

The values found in literature may deviate from measured values because the acoustic properties of plastic are strongly dependent on the exact chemical composition, the presence of additives as well as antecedent treatment or exposure including varying temperatures, mechanical stress or radiation. The most noticeable difference is found for TPX, whose measured speed of sound is quite slower than values found in literature. This is not surprising considering TPX is a brand name used by Mitsui for a wide series of polymethylpentenes. The type of TPX referenced in [149] is different from the one measured in Marseille.

The speed of sound in TPX is closest to the speed of sound in breast tissue, which is around 1500 m/s. TPX also has the lowest attenuation coefficient of all tested plates. It thus seems to be the most adapted material for the front plate. Thin, stretched foils can be considered as an alternative. Their negligible thickness leads to vanishing attenuation: in the case of 50  $\mu\text{m}$ , none

is measureable. However, their rather high speed of sound quoted in literature might lead to reflection artefacts in the final image.

RenShape BM5066 is confirmed as a good rear plate. Its sufficiently low speed of sound limits reflections at the interface of the breast and the plate. Its high attenuation coefficient absorbs the US wave at a satisfactory level that reduces or excludes artefacts at the plate/air border.

	Material	Density [g/cm <sup>2</sup> ]	Thickness [cm]	Speed of sound Measured [m/s]	Speed of sound Literature [m/s]
FOILS	Mylar	1.37	0.05	n.a.	2400 [147]
			0.0125		
			0.0175		
	Kapton	1.43	0.0125	n.a.	2500 [150]
PLATES	PMMA	1.19	0.1	2642	2700 [147]
	PVC	1.38	0.2	2204	2270 [149]
	Polyethylene	0.94	0.2	2333	2431 [149]
	TPX	0.83	0.3	1780	2170 [149][148]
	RenShape BM 5066	1	0.3	1950	1700 – 2000 [149]

Table 12 : Speed of sound measurements at LMA (measured values with a precision of 5 %)

#### 5.1.1.2 Creation of transversal US modes

If the US wave enters the material at an incident angle  $\theta_{\text{incident}}$  different from  $90^\circ$ , lateral shear waves (S-waves) can be created in addition to the longitudinal compression waves (P-waves). If this phenomenon, called mode-conversion, occurs, both waves will propagate through the solid. The waves have different speeds: the S-wave is proportional to the material's shear modulus while the P-wave is proportional to the elastic modulus.

Waves at different speeds are likely to create artefacts in the final image because echoes reach the transducer at different moments. Figure 57 shows the setup used to measure the influence of this mode conversion on the measured signal. It is identical to the setup used in section 5.1.1.1 with the difference that the plate is rotated in steps of 1 degree until a maximum angle of up to 50 degrees.

Figure 58 shows typical plots: the 50  $\mu\text{m}$  Mylar foil that does not alter the signal while the 3mm RenShape plate clearly creates shear waves. These induce artefacts visible as shadow measurements in the image, arriving some microseconds after the main, compression wave. If the plates were selected for the stabilization system, the question of shearwave induction and their influence on the registered image would need to be studied on a phantom or patient with a medical US transducer similar to the one used in the final system.

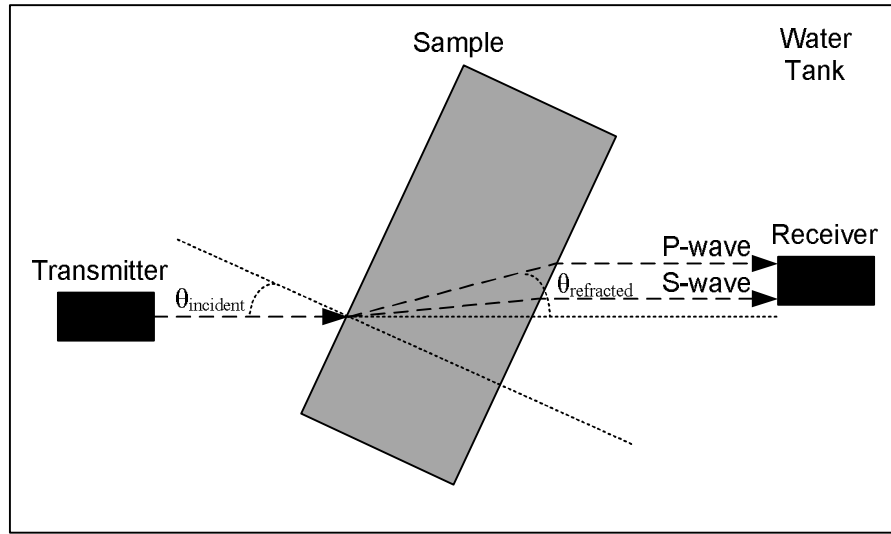


Figure 57 : Influence of a rotation of the plate on the sound propagation

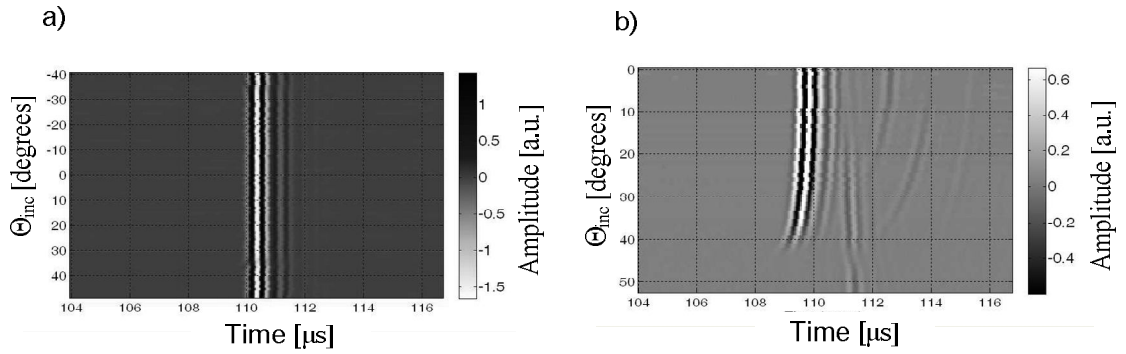


Figure 58 : Evolution of the signal for a) a 50 μm Mylar foil and b) a 3 mm RenShape plate

#### 5.1.1.3 Evaluation of Candidate Materials under Nuclear Aspects

The stabilization system used in ClearPEM-Sonic has to be adjusted once the patient is installed. Its position cannot be not altered throughout the complete exam, including the acquisition of the PEM image. It is therefore necessary to estimate whether the presence of the paddles could have a negative influence on this exam.

The total photon attenuation coefficient can be computed using the NIST Photon Cross Section Database [151], knowing the exact chemical formula of the material. The density and thickness provide the additional information required to calculate the total photon absorption in the plate. Table 13 shows the results.

The use of thin films has practically no influence on the emitted radiation. Plates absorb between one and two percent of the emitted radiation, which is considered acceptable. The influence of the RenShape plate on the PEM image quality would however have to be studied more closely in simulations.

	Material	Density [g/ccm]	Thickness [cm]	Chemical Formula	Mass Attenuation Coefficient [cm <sup>2</sup> /g]	Total photon Attenuation [%]
FOILS	Mylar	1.37	0.005	C <sub>10</sub> H <sub>8</sub> O <sub>4</sub>	9.00E-02	0.06
			0.0125			0.15
			0.0175			0.22
	Kapton	1.43	0.0125	C <sub>22</sub> H <sub>10</sub> N <sub>2</sub> O <sub>5</sub>	8.86E-02	0.16
PLATES	Plexiglas	1.19	0.1	C <sub>5</sub> O <sub>2</sub> H <sub>8</sub>	9.32E-02	1.10
	PVC	1.38	0.2	C <sub>2</sub> H <sub>3</sub> Cl	8.90E-02	2.43
	Polyethylene	0.94	0.2	C <sub>2</sub> H <sub>4</sub>	9.86E-02	1.84
	TPX	0.83	0.2	C <sub>6</sub> H <sub>12</sub>	9.86E-02	1.62
	RenShape	1	0.3	exact formula	8E-02	2.5 - 3.5
	(polyurethane)		1	unknown	- 1.2E-01	7.5 - 11

Table 13 : 511 keV attenuation with different materials (calculated values with a precision of 1 %)

#### 5.1.1.4 Possible Mechanical Integration

There are two options for mechanically integrating stabilization paddles into ClearPEM-Sonic. Figure 59 shows that they can either be fixed to the PET arm or to the table.

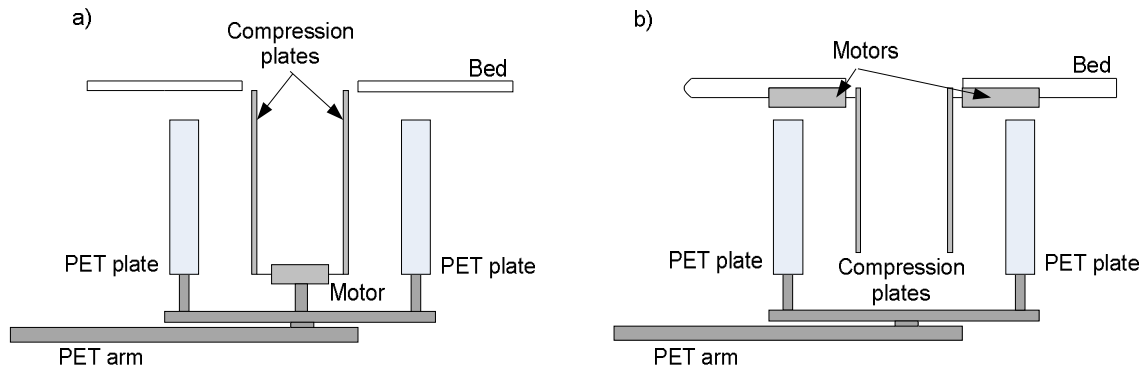


Figure 59 : Possible stabilization plate integration: a) fixed to the PET arm, b) fixed to the table

Fixing the plates to the PEM arm has the advantage of not requiring any alterations of the bed. The PEM plates could therefore still be approached to the bed as much as without the presence of any stabilization system. The stabilization plates need to be positioned on a holder that is between the PEM plates and mechanically independent from them. This would require complex changes to the PEM arm.

If the plates are fixed on the bed, the complex design of the PEM arm does not need to be altered. However, the bed would increase in thickness and increase the distance between the patient torso and the PEM plates.

In both setups a completely manual, semi-manual or entirely motorised system can be used to setup the plate separation and rotation around the breast.

#### *5.1.1.5 Conclusion*

Considering all constraints, experiments and tentative configurations, if the compression paddles were chosen, the best solution would be two paddles attached to the bed. For the plate in contact with the US transducer, ultrasound measurements show that it would be preferable to use either a TPX plate, as its properties are closest to those of human tissue, or a thin stretched foil of Mylar, because it is too thin to have a major influence on the ultrasound image. On the opposite side, the RenShape plate could be used as an absorbing plate.

However, such a stabilization system has inconveniences. Indeed, even the most adapted materials for the compression paddles do not guarantee they will not induce any artefacts to the final image. The major drawback of this solution however is the geometrical deformation of the breast by the compression that needs to be applied. Not only does it prevent anatomically correct imaging, it also deforms the breast in a different way each time the position of the paddles changes. This presents major obstacles for the final image evaluation.

It is therefore necessary to study another solution more in depth: a conical stabilization system that stabilises the breast without deforming it during both the PEM and US acquisitions, does not present an obstacle during any of them and allows access to every region of interest.

### **5.1.2 Stabilization Cone**

#### *5.1.2.1 Design*

The conical stabilization system is an alternative to usual compression paddle systems used for most mammographic applications. Its first advantage is that no mechanical parts and rails – like for the plates – are needed to adjust its position: the mechanical integration into the existing machine is simpler and needs less modifications of existing components. The stabilization cone also keeps the natural form of the breast: besides improved patient comfort due to the lack of compression it allows anatomical correct imaging. Such a cone was used by Shipley and Duck in [152].

The convex shape of the cone however poses a problem in combination with the Aixplorer US transducer that also has a convex shape: if both are brought into contact, only a tangent line remains as direct contact. If a hole is cut into the cone, the transducer can be in direct contact with the breast. This window will be left open during the exam, thereby preventing any artefacts in the US image that would otherwise arise from a plastic film. The cone will be included in ClearPEM-Sonic in a way that it can be rotated to position the window in front of every region of interest. Figure 60 shows a CAD drawing of such a cone.

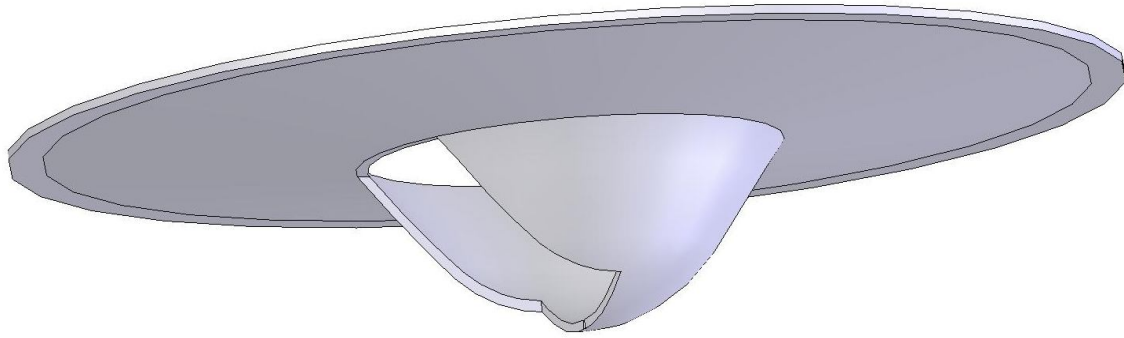


Figure 60 : CAD drawing of a typical cone

We produce prototype cones at CERN – the procedure is explained in section 5.1.2.2 – to perform tests that verify their ease of use in a clinical environment as well as with different modalities. Figure 61 shows experiments at Hôpital La Timone in Marseille. We test a set of 5 different sized cones on 15 patients. In the ideal case, for example in figure 61a), the cone fits. In some cases, like in figure 61b), the cone fits in principle but, due to for example a malformation or scars, an air gap is left. This can be filled with US gel during the exam. In the final case, figure 61c), the cone is too big for the breast.

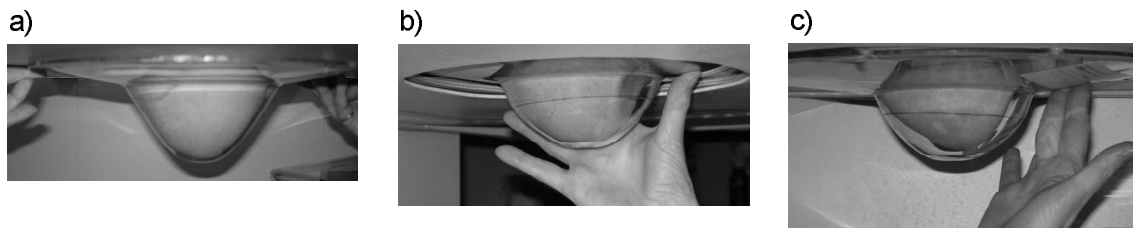


Figure 61 : Practical tests with cones: a) cone fits, b) there is an air gap, c) the cone is too big

In parallel, we test the compatibility of the cone with the US modality at SuperSonic Imagine in Aix-en-Provence. Figure 62a) shows an exam made with a dedicated breast phantom produced by Dang Jun (VUB) and presented in [120]. The images recorded in this work (Figure 63) prove the cone to be useable with the US transducer. We also address the problem of potential artefacts coming from reflections of the US wave at the cone. Figure 62b) shows that due to the position of the window on the cone, the inclination of the US transducer is such that the wave is always directed towards the patient's chest. It should therefore not reach the opposite cone wall.

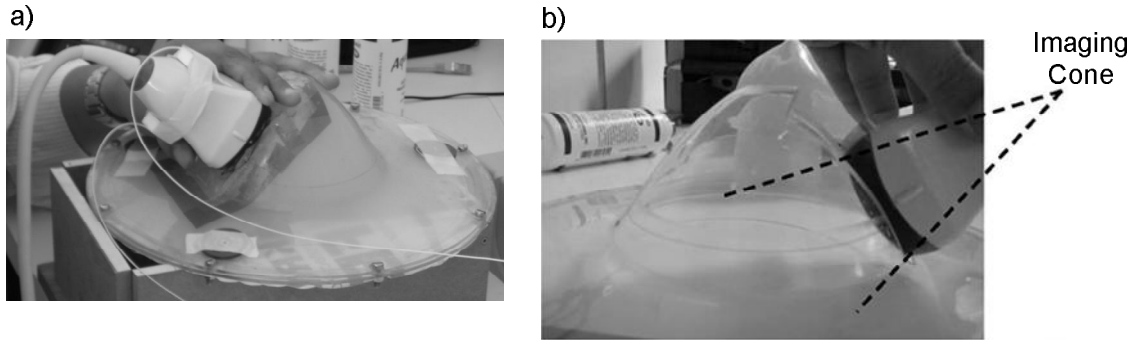


Figure 62 : Compatibility tests of the cone with the US transducer. a) shows an exam of a breast phantom in the cone. b) shows the imaging cone of the transducer

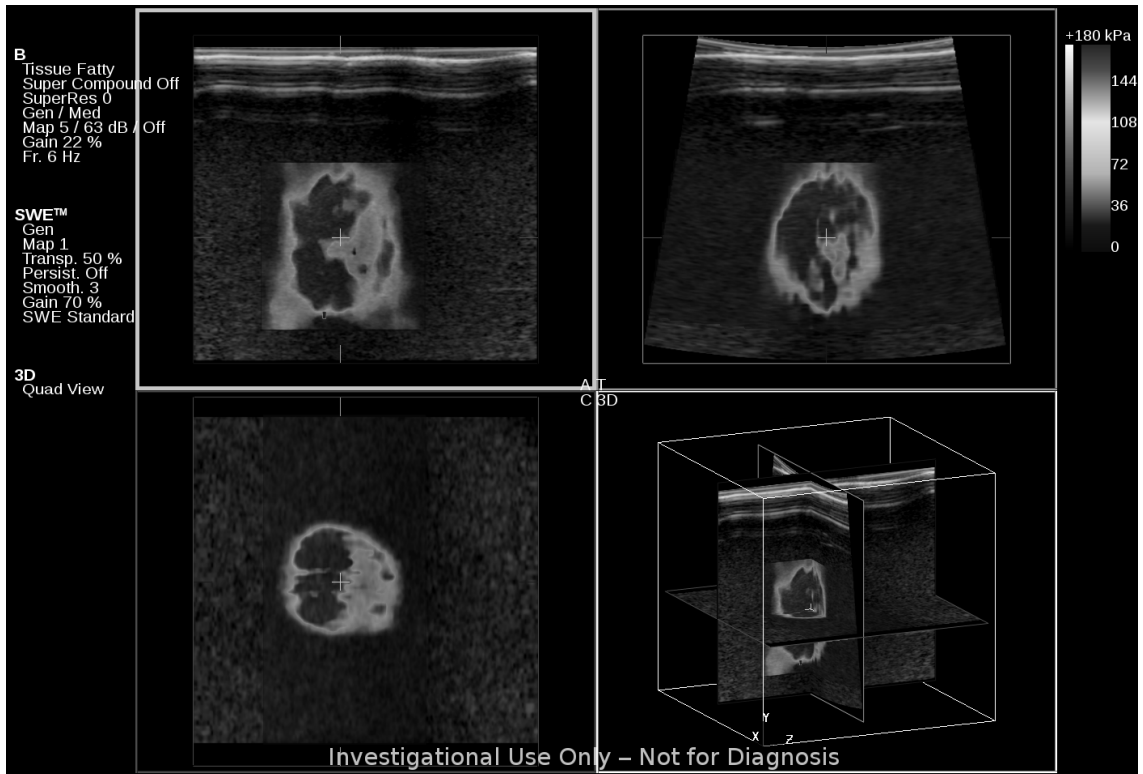


Figure 63 : SuperSonic Imagine Aixplorer image of a 1.5 cm lesion in the phantom. The elastography image is superposed with the ultrasound image

#### 5.1.2.2 Cone Production

We manufacture the first set of 5 cones at CERN. Considering the elevated cost of manufacturing TPX or RenShape cones and the fact, presented in figure 62b), that the US transducer hardly ever sees the opposite wall of the cone, we used Lexan Exell D produced by General Electric Structured Products [153], a polycarbonate known for its easy deformability at reasonably low temperatures, for the production of the cones.

We develop a method to produce cones. Figure 64 shows the process used to form cones of different sizes. In an oven, a flat Lexan plate is fixed to an outer ring that serves as a support. A

6 kg weight is attached to the centre of the plate with a screw. If the oven is heated to 160 degrees Celsius, the Lexan plate gets ductile and is pulled downwards by the weight. The inclination that later brings the patient's thorax closer to the PEM field of view is created by stopping the deformation of the cone's outer part with a second, inner ring. Then, only the part of the plate within the inner ring is pulled downwards until the weight comes into contact with a pedestal. Both the exact temperature as well as the respective heights of the inner cone and pedestal have direct influence on the final shape of the cone. The complete production process for one cone takes 90 minutes plus the time needed for the whole system to cool down.

Due to time constraints, the production of the final cones used in the ClearPEM-Sonic prototype is outsourced to a company, PLASTIQUA SA, Les Acacias (GE), Switzerland. They follow the same method but switch to PVC for the production. If more sophisticated cones are required, they have to be produced with a dedicated mould that defines the exact shape.

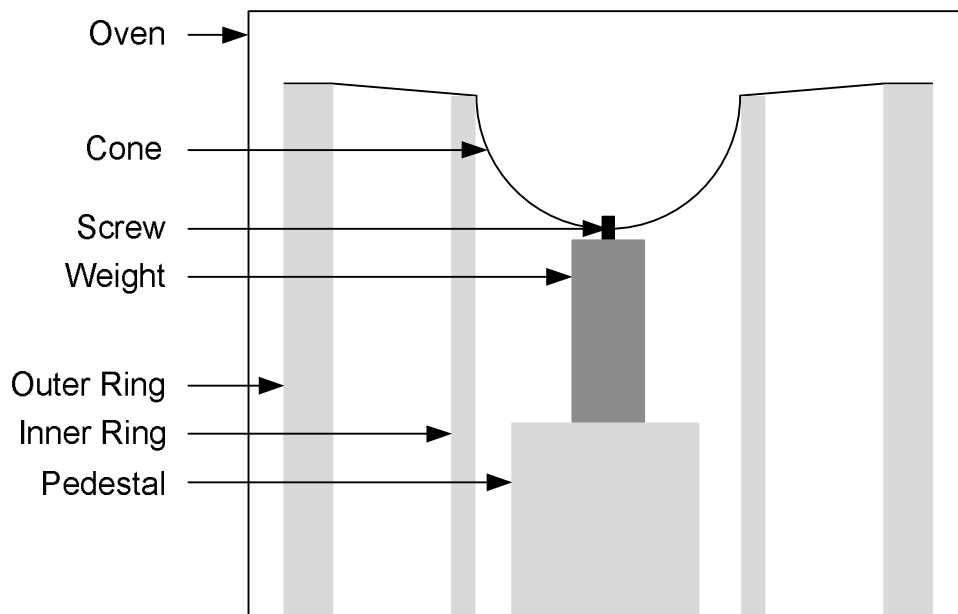


Figure 64 : Cone Production Setup

### 5.1.2.3 Conclusion

We select and develop the conical stabilization system for ClearPEM-Sonic: compared to compression paddles, it is more adapted to the medical requirement of anatomically correct imaging and more convenient to integrate into the final design.

A set of 7 cones with varying inner diameter and vertical elongation is produced to take varying breast sizes into account. The daily use of the system will show which corrections need to be made to the stabilization system to provide best comfort for the patient and optimum usability for the medical staff.



## 5.2 Image Co-registration

ClearPEM-Sonic shall deliver co-registered images to the user with good mapping precision. This requires proper, ideally partly or completely automated procedures for image co-registration. These can be substantially eased if either the exact position of each image with respect to the other one is known or common features in both images can be used as references. Both approaches are studied in the course of this thesis.

### 5.2.1 Fiducial Markers

The approach of using common features can be based on either natural or artificial characteristics. Unfortunately, PEM and US do not necessarily see the same object. Indeed, PEM is not able to properly show anatomical features whilst it might reveal cancerous lesions that are not visible with US.

Fiducial markers can however be used as artificial reference points visible with all involved modalities of an imaging system. In the case of ClearPEM-Sonic, such markers would need to be visible with ultrasound and PEM. We suggest the use of encapsulated  $^{22}\text{Na}$  positron emitting point sources in a cladding visible with US that can be fixed at different positions on the stabilization system.

#### 5.2.1.1 *Visibility of fiducial markers with US*

The visibility of fiducial markers has to be tested with an ultrasound transducer. These tests are carried out in collaboration with the LMA-CNRS in Marseille, with the setup presented in figure 65b). Marker mock-ups made of plexiglas in different sizes between 3 and 25 millimetres are fixed on a rear plate made out of RenShape (Figure 65a). The US transducer moves on the surface of the front plate. All candidate materials for the front plate of the stabilization system are tested. The most promising materials, Mylar 5  $\mu\text{m}$  and polyethylene 2 mm are also tested with a phantom, produced by Dang Jun from VUB [120], inserted between the front and the rear plate. A measurement without a front plate serves as the reference. All measurements are made once with the markers facing towards the transducer and once facing away to consider all possible cases of marker placement in the final design.

Figure 66 shows typical US images recorded during these tests, with a stretched Mylar foil of 50  $\mu\text{m}$  used as the front plate. The measurement of figure 66a) is made with all markers facing towards the US transducer. Each marker, including from left to right the 25 mm, 10 mm and 5 mm marker, leaves a clearly distinguishable echo. Indeed, the US wave is directly reflected by the markers and not attenuated by any additional material except the front plate.

If the fiducial markers face away from the transducer, as in figure 66b), they are much harder to distinguish. It is necessary to record an echo that shows first, with good contrast, the wave directly reflected by the RenShape rear plate. However, it lacks any information from the

fiducial markers. They will only reflect the wave that has already transited and been attenuated by the rear plate. This reflected wave then again transits through the RenShape plate, is once more attenuated and thus leaves a much fainter echo with lower contrast. On a high resolution screen, the echo from the 5 mm marker can still be distinguished. However, as shown in the summary of all measurements in table 14, a marker of 3 mm in diameter could not be distinguished anymore.

The result of this test is that if the markers face towards the transducer, even the smallest one of 3 mm can be seen. The presence of a phantom that simulates the influence of a breast does not change the result. If the markers face away from the breast, only a 5 mm marker can be distinguished. Again, the phantom only barely changes the result. Finally, the best results are obtained with either the stretched 50  $\mu$ m Mylar foil or the 2 mm polyethylene front plate.

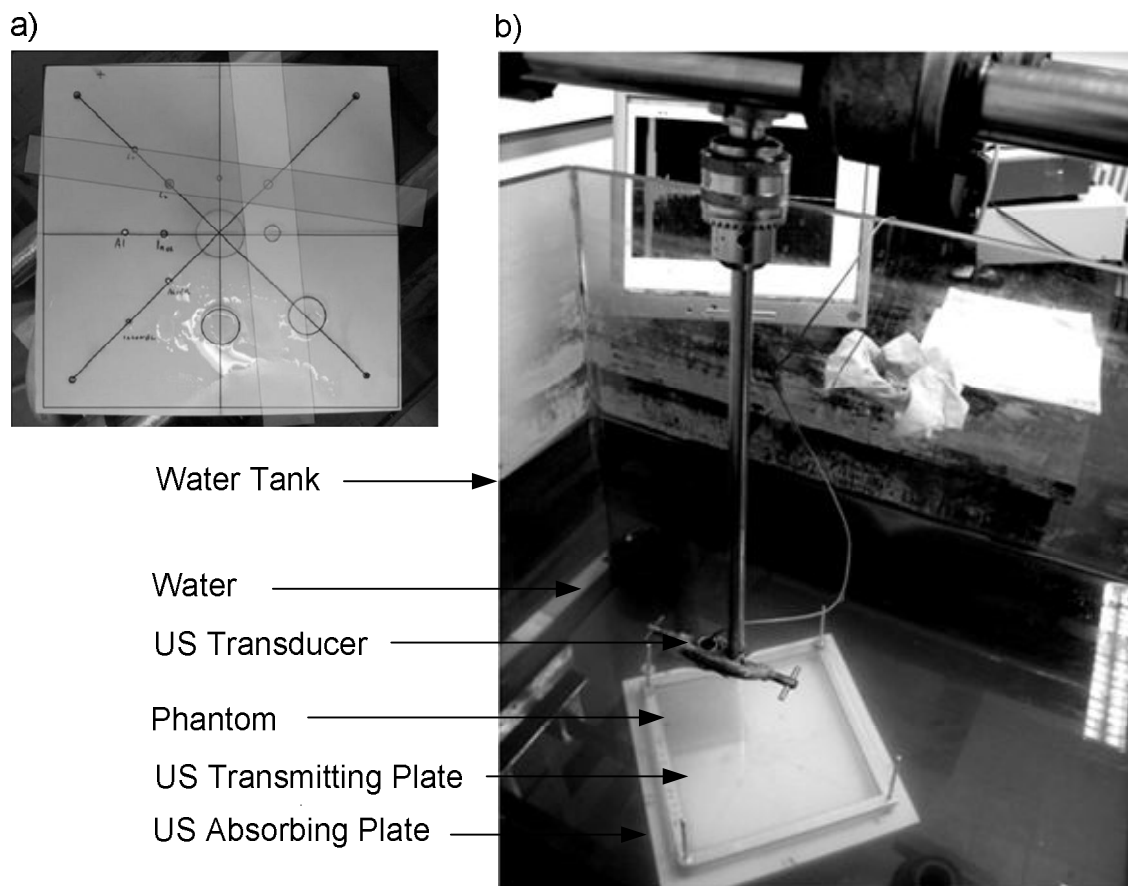


Figure 65 : a) Plate with different potential fiducial markers used for tests in b), the US test setup for fiducial markers

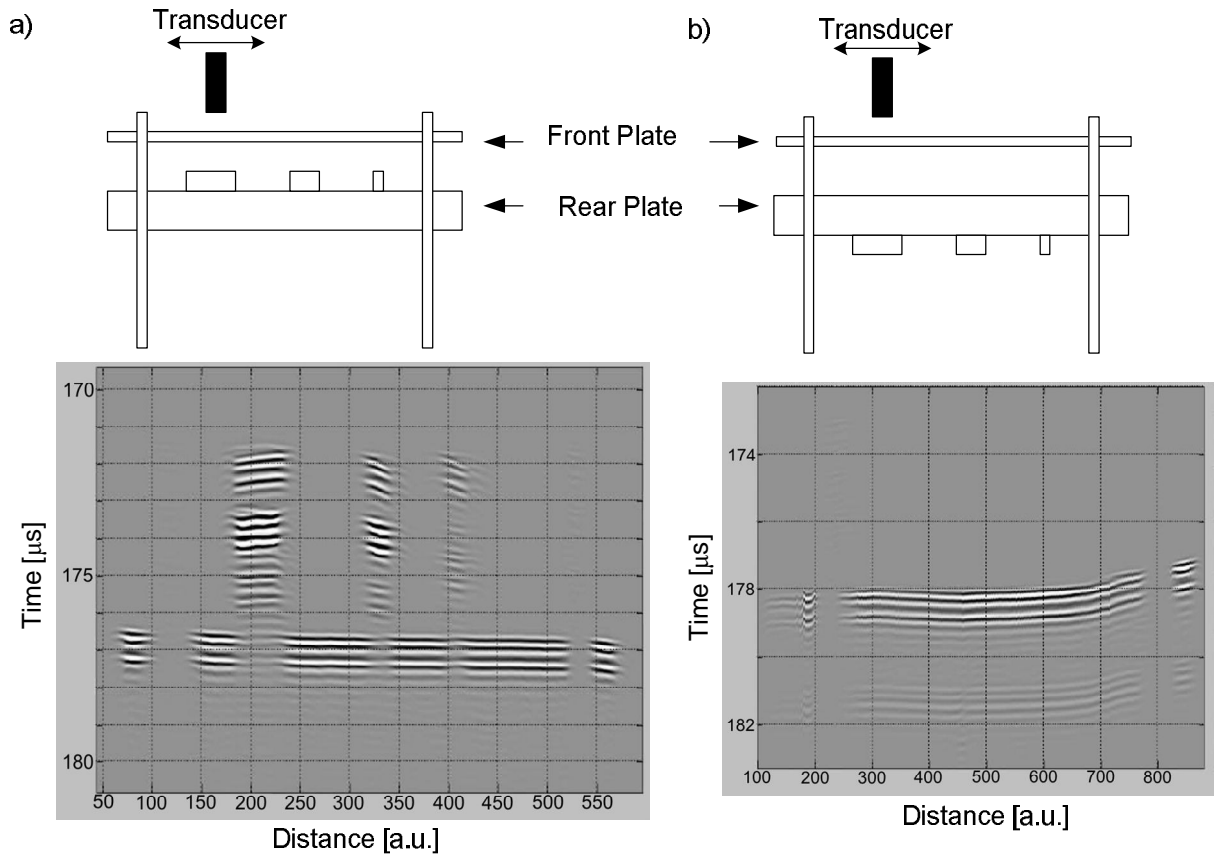


Figure 66 : Example for a US test with a) the fiducial markers facing towards and b) away from the transducer. A Mylar 50  $\mu\text{m}$  foil is used as the transmitting plate.

		Material	Thickness	Smallest visible marker [mm]	
			[cm]	Markers up	Markers down
WITHOUT PHANTOM	PLATES	none	n/a	3	5
		Mylar	0.005	3	5
			0.0125	5	5
			0.0175	5	25
	Kapton	0.0125	3	5	
	FOLDS	Plexiglas	0.1	5	25
		PVC	0.2	5	10
		Polyethylene	0.2	3	5
TPX		0.2	3	5	
WITH PHANTOM	Mylar	0.005	3	5	
	Polyethylene	0.2	3	10	

Table 14 : Fiducial marker visibility under ultrasound

### 5.2.1.2 Visibility of fiducial markers with PEM

The visibility of fiducial markers with ClearPEM is confirmed by both simulations and measurements made by LIP.

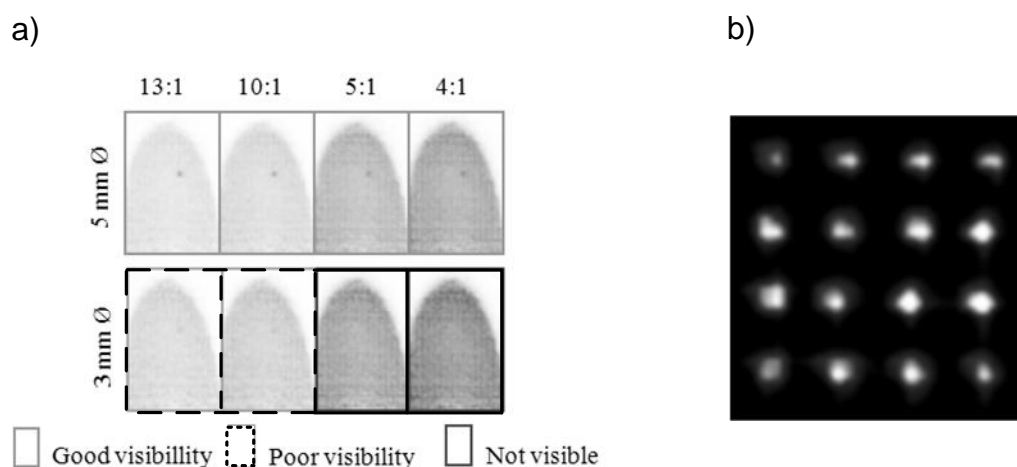


Figure 67 : a) Geant4 simulation of the visibility of 3 mm and 5 mm point sources with background radiation at varying source to background activity ratios [154] and b) measurement at 16 positions of a 1 mm point source without background radiation with ClearPEM [119]

Indeed figure 67a) shows a simulation by A. Trindade [154] of the visibility of 5 mm and 3 mm point sources in the presence of different background radioactivity levels: the 5 mm source is visible even if the background is rather high at a source-to-background activity level of 4:1. The 3 mm source is visible only if the ratio is better than 10:1. These simulations are experimentally verified with the measurement of a 1 mm point source in ClearPEM, presented in section 3.2.4 of this thesis.

It should therefore not be a problem to detect the presence of fiducial positron emitting markers with ClearPEM.

### 5.2.1.3 Discussion

The experiments and considerations presented above lead to the conclusion that it is possible to design fiducial markers that are visible by both ultrasound and PEM.

If compression paddles were chosen as a stabilization system for ClearPEM-Sonic, a sufficient number of unambiguously identifiable fiducial markers would have to be placed on the rear plate, facing towards the transducer. In the case of the stabilization cone however, the necessity of placing the window in front of an ROI defined by the prior PEM exam implies that the fiducial markers would also change their position during each US acquisition. This would thus require the parallel acquisition of an additional PEM image for each US image, extending the overall exam time as well as preventing the use of PEM tracer molecules with very short decay times.

Tests performed with the ultrasound transducer show that, due to its inclination when performing an exam, the transducer never images the wall on the opposite side of the window (Figure 62b). It would thus be necessary to place the fiducial markers on the window cut into

the cone. They would therefore be right in front of the region of interest in the breast that needs to be imaged. Figure 68 shows that this creates artefacts in the region of the phantom behind the fiducial marker, lowering global image quality.

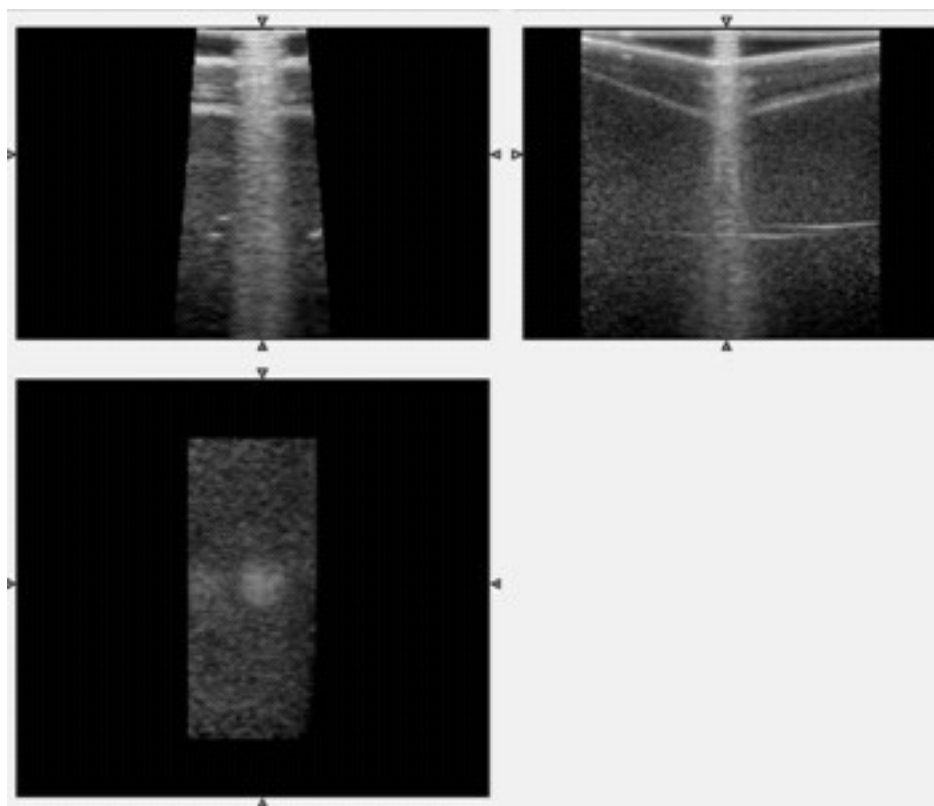


Figure 68 : Influence of a fiducial marker placed in front of the cone window on the ultrasound image quality

Since ClearPEM-Sonic will use stabilization cones and considering the disadvantages fiducial markers would have under this circumstance, we investigate alternative approaches to determine the position of the US image relative to the PEM image. Indeed, the information from a position tracking system that records the exact position and inclination of the US transducer in space can be used to calculate the exact position and inclination of the US image within the PEM spatial reference system.

## 5.2.2 Position Tracking Systems

### 5.2.2.1 Survey of Different Approaches

If the absolute position of the US transducer in space shall be recorded, mechanical, optical and magnetic tracking systems need to be studied. This fundamentally different approach leads to a certain number of advantages and disadvantages closely examined in the frame of ClearPEM-Sonic.

Mechanical tracking systems rely on a rotatable arm. One end of this arm – the base plate – is permanently fixed at a known position, in the case of ClearPEM for example the bed, the arm holding the PEM plates or an external table. This position is known within the ClearPEM reference system and thus relative to the position of the PEM image in space. The movement of the other end of the arm is recorded relative to the position of the base plate. By fixing the US transducer to the free extremity its exact position and therefore the exact position of the US image in space are known. This solution would deliver highest accuracy with precision better than a millimetre for the position and better than a degree for the angular information. Its main handicap is the prevention of any free-handed use of the US transducer because the tracking requires the presence of the arm. Besides that, commercially available arms are quite expensive and very bulky due to their size and weight. We rule out this solution due to its difficulty to handle. Avoiding an arm-based solution gives more freedom to a physician who wants to handle the US transducer in the traditional way by just holding it in his hand.

We retain the possibility of having a separate arm without incorporated tracking. As explained in section 5.3.2, it can be used to immobilize the arm in any given position if required.

Optical tracking is a wireless solution for position tracking. It is based on tracking an object with a set of cameras arranged around the region of interest where this object moves. In order to track the US transducer, it would be necessary to equip it with small, reflecting balls that could be seen by the cameras. The main disadvantage of this solution is, besides its cost, the necessity to cover the whole region of interest with cameras. Considering there are several obstacles like the breast, the stabilization system as well as the operator's hand in the region of interest, this solution requires a minimum number of cameras to be installed. A rapid survey of existing solution shows that four cameras placed on the PEM platform should cover the whole volume of interest in which the US transducer should be tracked. The optical tracking is ruled out during this phase of the project due to its high cost – over 15,000 EUR at the time of the survey – in comparison with the third tracking solution.

Another possibility of position tracking is a magnetic positioning system. It relies on a magnetic field generator whose exact position in space is well-known. This generator is made out of three orthogonal coils, one for each direction X, Y and Z. The maximum field strength does not exceed the strength of the earth field. The coils are fired at a regular interval. A Hall sensor measures the strength of the magnetic field at a synchronized rate and then determines its position in space with reference to the origin as well as its inclination with reference to the orientation of the reference axes. At the time of the survey, such systems are available from 3,000 EUR onwards. We therefore decide to acquire a magnetic tracking system to evaluate its compatibility with ClearPEM-Sonic.

#### *5.2.2.2 Magnetic Positioning System*

Ascension Technology trakSTAR is a high-precision magnetic tracking system rated for use in a medical environment outside of surgical interventions. It consists in an emitter box whose outer dimensions are around 10x10x10 cm<sup>3</sup> and sensors with 2 mm diameter and a length of 10 mm

(Figure 69). The emitter box sequentially fires three orthogonal coils, one per direction X, Y and Z. The coils are fired 20 times per second each, which provides an acceptable measurement rate. As further described in section 5.3, this emitter box will be placed on a removable bridge between the PEM plates and the sensors fixed to the ultrasound transducer.

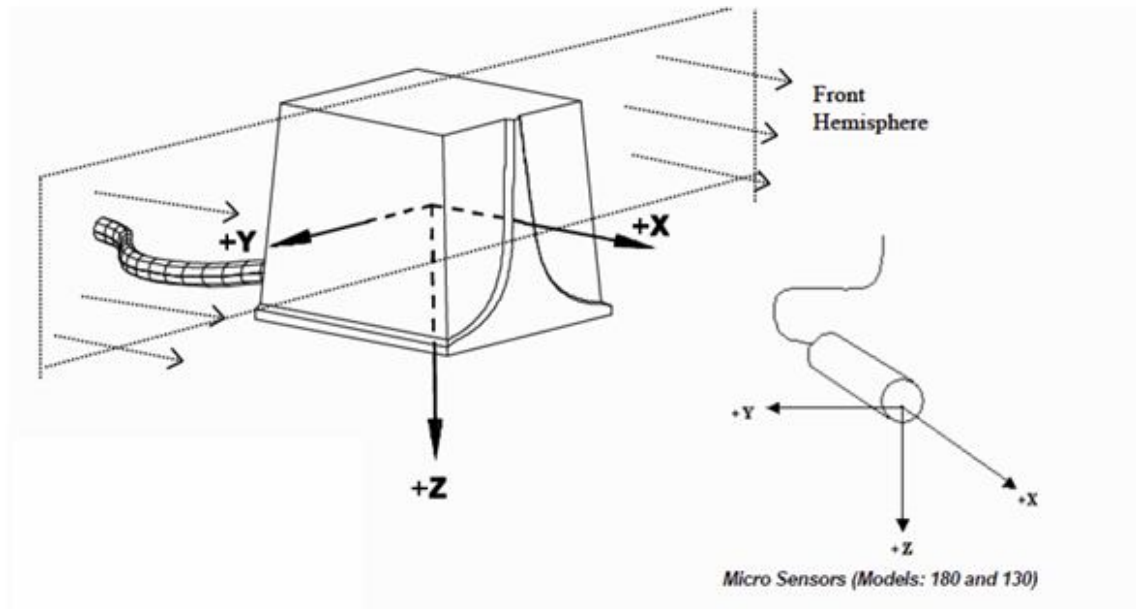


Figure 69 : Ascension trakSTAR, definition of the axes and coordinate system of the emitter and sensor [155]

According to the manufacturer, the combination of emitter and sensor we plan to use has a precision of 1.4 mm RMS for the absolute position of the sensor along X, Y and Z and a precision of 0.5 degrees RMS for the inclination along those three axes [155].

The positioning system can be connected by USB to any computer. Ascension Technology provides C++ libraries for use under Windows or Linux that allow communication with the system.

In order to verify this performance in ideal conditions, we use a grid drilled into a fibreglass plate, with holes every 25.4 mm along the X-axis and every 20.4 mm along the Y-axis (Figure 70). The accuracy along the Z-axis can be verified by modifying the height above ground at which the plate is fixed. The position sensor is enclosed in a Teflon housing for easier manipulation. The setup is installed at sufficient distance from any potentially disturbing source, including ferromagnetic metals and radiofrequency sources. Figure 71 shows that the measured position is in accordance with the theoretical value. This is confirmed by figure 73a) which shows a histogram of the deviation of each measurement from the theoretical value, along each of the three axis. The average deviation is 0.2 mm with a standard deviation of 0.28 mm. These values are better than the performance expected from the manufacturer's information.

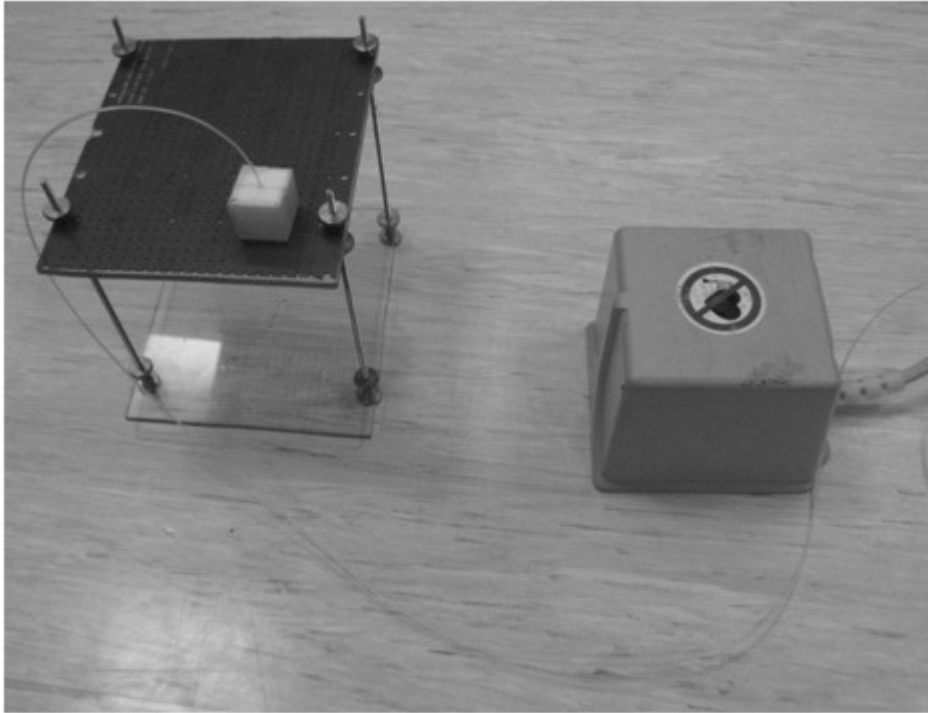


Figure 70 : Setup used to test the theoretical performance of the magnetic tracking system

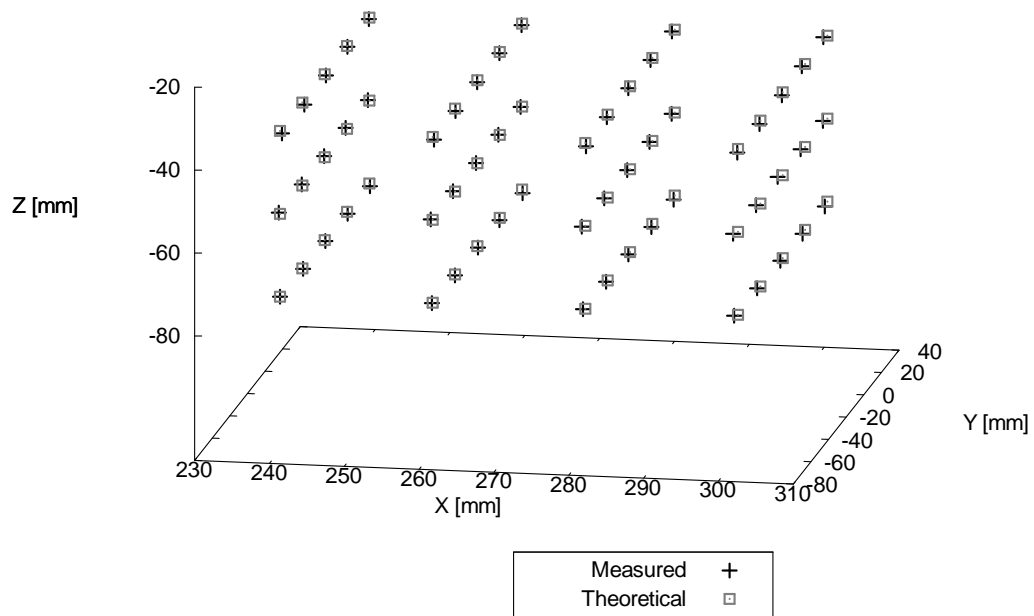


Figure 71 : Measured and theoretical position on the reference grid



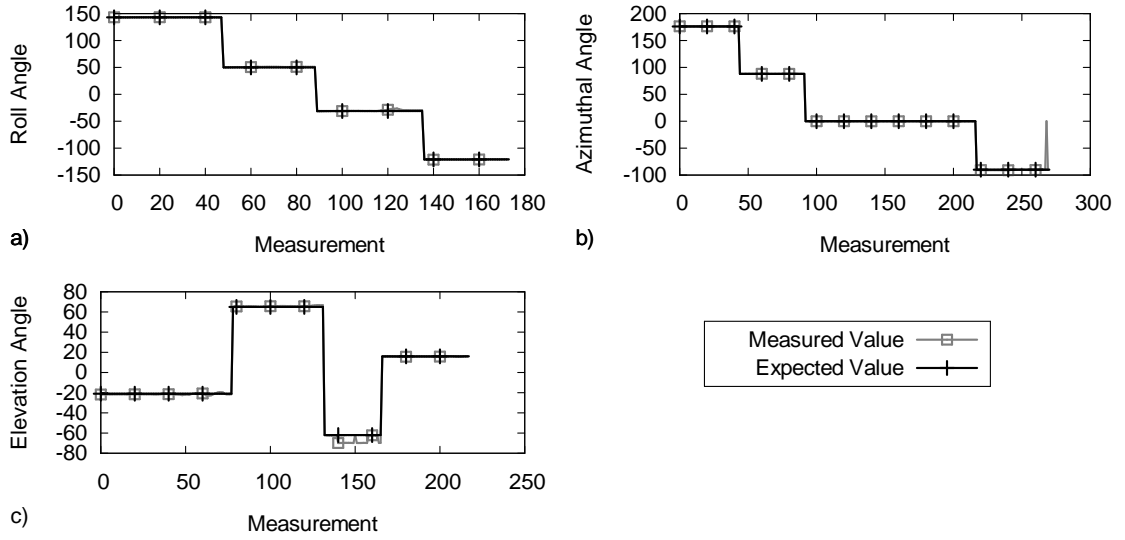


Figure 72 : Angular Precision under ideal conditions for a) roll, b) azimuth and c) elevation measurement

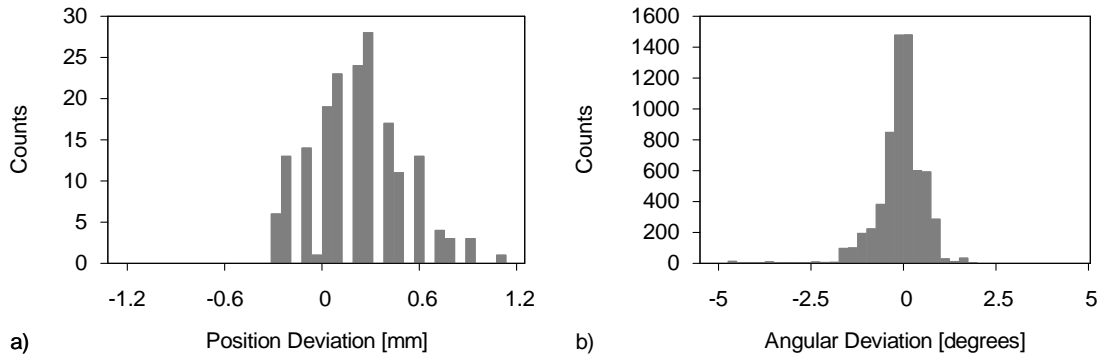


Figure 73 : Measured deviation under ideal conditions for a) the position and b) the angular measurement

We also test the angular measurement performance under ideal conditions. We evaluate the azimuth, elevation and roll which are defined to be the respective rotations about the Z, Y and X axis of the sensor. Figure 72 shows the result of this measurement. The sensor was rotated by steps of 90 degrees around each of its three axes. The measured values are in good agreement with the expected value. Figure 73b) shows a histogram of the measurement errors. The average error is 0.1 degrees, with a standard deviation of 2.1 degrees. This high standard deviation is probably due to alignment errors during the measurement rather than an imprecision of the tracking system.

These results indicate that the magnetic positioning system would have sufficient measurement precision if it was used in an ideal environment.

### 5.2.2.3 Tests in ClearPEM

ClearPEM was not designed to be combined with a second modality. It also has no provisions for the integration of a magnetic tracking system. The maximum distance at which the sensor is

expected to work properly is 760 mm above the emitter. Additionally, it is strongly recommended to avoid any disturbance to the magnetic field. The presence of a ferromagnetic steel table is expected to cause problems. Additionally, the presence of other metallic parts and electromagnetic motors might deteriorate the performance of the positioning system.

In order to test the tracking performance in realistic conditions, we designed a test setup similar to the one used to assess the performance under ideal conditions. We made tests on the first ClearPEM prototype installed in Porto, PT. The emitter is placed on a makeshift bridge between the PEM detectors. The sensor is enclosed in a Teflon housing for easier handling and moved along a grid with holes every 20 mm. The performance along the Z-axis is assessed by varying the height at which the plate is fixed.

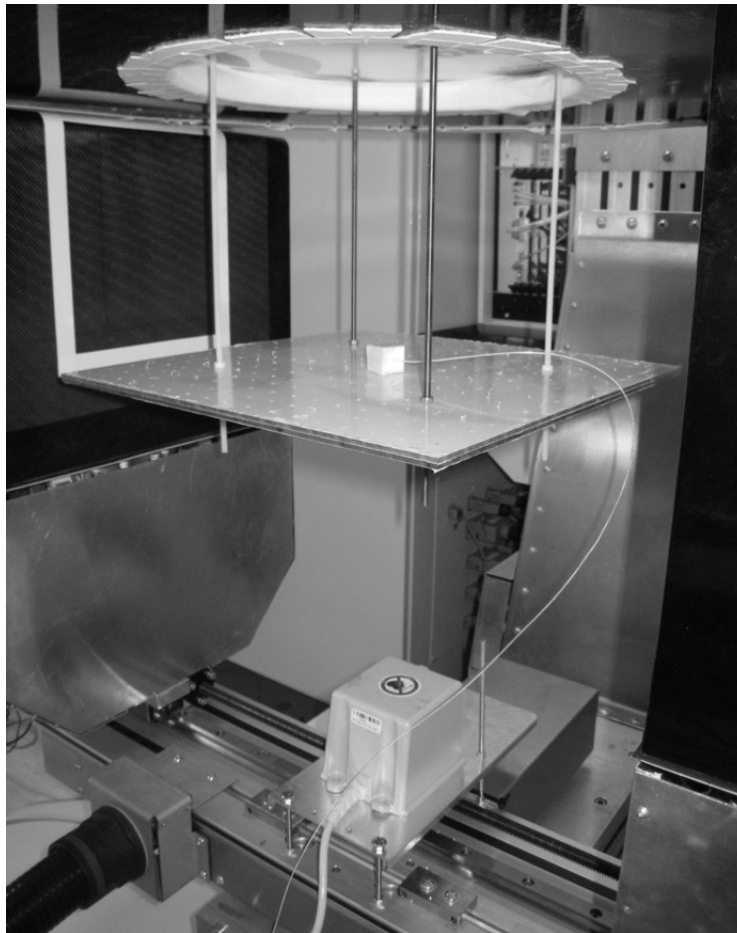


Figure 74 : Setup used to test the tracking performance in ClearPEM (Porto, PT)

In order to assess the distortions induced by the machine, we evaluate the position measured by the sensor on a grid of one centimetre by one centimetre. We move this grid in steps of one centimetre along the Z-axis and record the position information on each plane. Figure 75 shows four representative planes of such a measurement. If there were no distortions, one should see four perfect planes, measured at 6, 9, 12 and 15 cm below the bed. The Z coordinate indicates the position of the sensor above the magnetic emitter, along the negative Z-axis shown in figure 70.

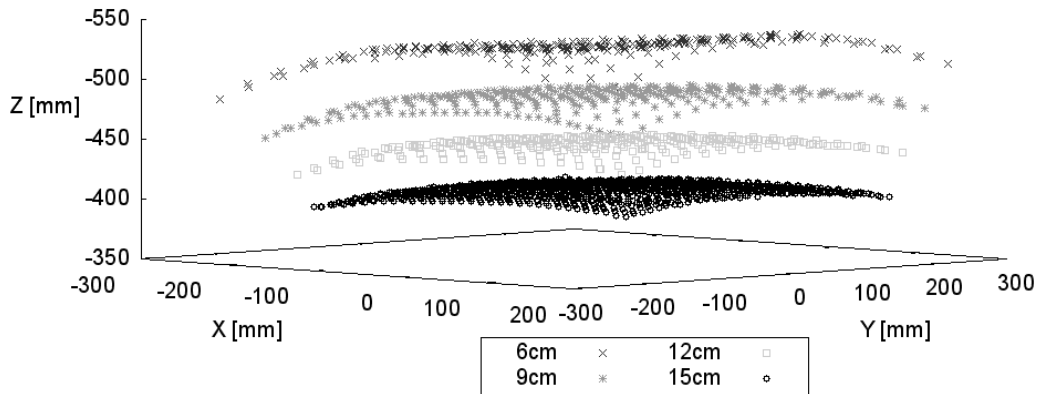


Figure 75 : Measured position on the reference grid in ClearPEM

There are parabolic distortions that get stronger close to the bed: the ferromagnetic bed and the hole definitely have an influence on the precision of the tracking system. It is therefore not possible to use the raw information provided by the magnetic tracker.

The measurement also shows that the distortion is fully bijective. Each point in the distorted measurement can be correlated to one and only one point in real space. In a sufficiently small volume, for instance between two measurement points, the distortion can be assumed to be linear. It is therefore possible to introduce a calibration procedure based on these assumptions.

The calibration requires measuring the distortion over the whole region of interest on a real grid, similar to the one used to evaluate the performance of the magnetic positioning system. This gives a set of measured points whose real position in space is well-known. This look-up-table can then be used during a position measurement.

The correction procedure of a measured value requires expressing this value in relation to its nearest neighbours in the distorted section of the look-up-table. Assuming a linear interpolation between neighbouring points, the measured value can be expressed relative to its neighbouring points. This relative value is then used to interpolate the real position in the real-space section of the look-up-table. Table 15 shows the result of applying this correction procedure. The corrected value has an error of up to 1 mm.

	Measured	Expected Value	Corrected	Error
<b>X</b>	125.5	127.2	127.76	0.56
<b>Y</b>	156	108.6	109.67	1.07
<b>Z</b>	-448.5	-435.6	-435.51	0.09

Table 15 : Testing the correction procedure for the magnetic tracking system (values in millimeters)

#### 5.2.2.4 Discussion

The evaluation of the magnetic tracking system shows that although it is the most competitive solution in matters of acquisition costs, it would only work properly if ClearPEM-Sonic was entirely redesigned with a focus on the use of such a device. In the current situation, using the magnetic tracking system might be possible to get an estimation of the position of the ultrasound image. However, it requires a heavy calibration procedure and cannot deliver as precise information as initially required. Manual adjustment by the operator is necessary in all cases.

Under these considerations, and keeping in mind that fiducial markers are not a solution either (section 5.2.1.3), optical tracking systems should undergo a close evaluation in a follow-up project.

### 5.2.3 Image Co-registration Software

The image acquisition processes as well as the respective image reconstruction algorithms and the storage of separate images are not part of this project. Indeed, they were subject of the separate technological developments of ClearPEM and Aixplorer.

We shall provide software dedicated to ClearPEM-Sonic that serves as a unique user-friendly interface for image processing. The software should allow the user of ClearPEM-Sonic to perform all necessary steps to visualize the pictures acquired with the two modalities.

This includes:

- data transfer from both modalities, ClearPEM and SuperSonic Imagine Aixplorer, to a common physical storage
- control of the tracking system and acquisition of the space coordinates used to locate the ultrasound transducer and transfer of this information to a common physical storage
- introduction of common, coordinated timestamps and patient IDs to unambiguously match acquired information during the image co-registration process
- monitoring of the PEM image reconstruction process
- proper image co-registration approaches, based on prior information from the tracking system and allowing the user to fine-tune the image co-registration
- a Graphic User Interface (GUI) for the user where the acquired information can be displayed and co-registered
- export to the Digital Imaging and Communications In Medicine (DICOM) format
- interaction with the hospital's Picture Archiving and Communication System (PACS).

The software development can be divided into two phases. Phase 1 groups all modules necessary for ClearPEM-Sonic to work: the initial image acquisition and transfer, the parallel display of images from the two modalities, the rigid image co-registration based on the image position information and manual adjustments made by the operator of the system. This software is developed in close collaboration with the University of Milano [156].

Phase 2, which is part of a future project, can include more complex image co-registration algorithms as well as a full set of data evaluation tools. It will also have to provide a direct interface for the hospital Picture Archiving and Communication System (PACS).

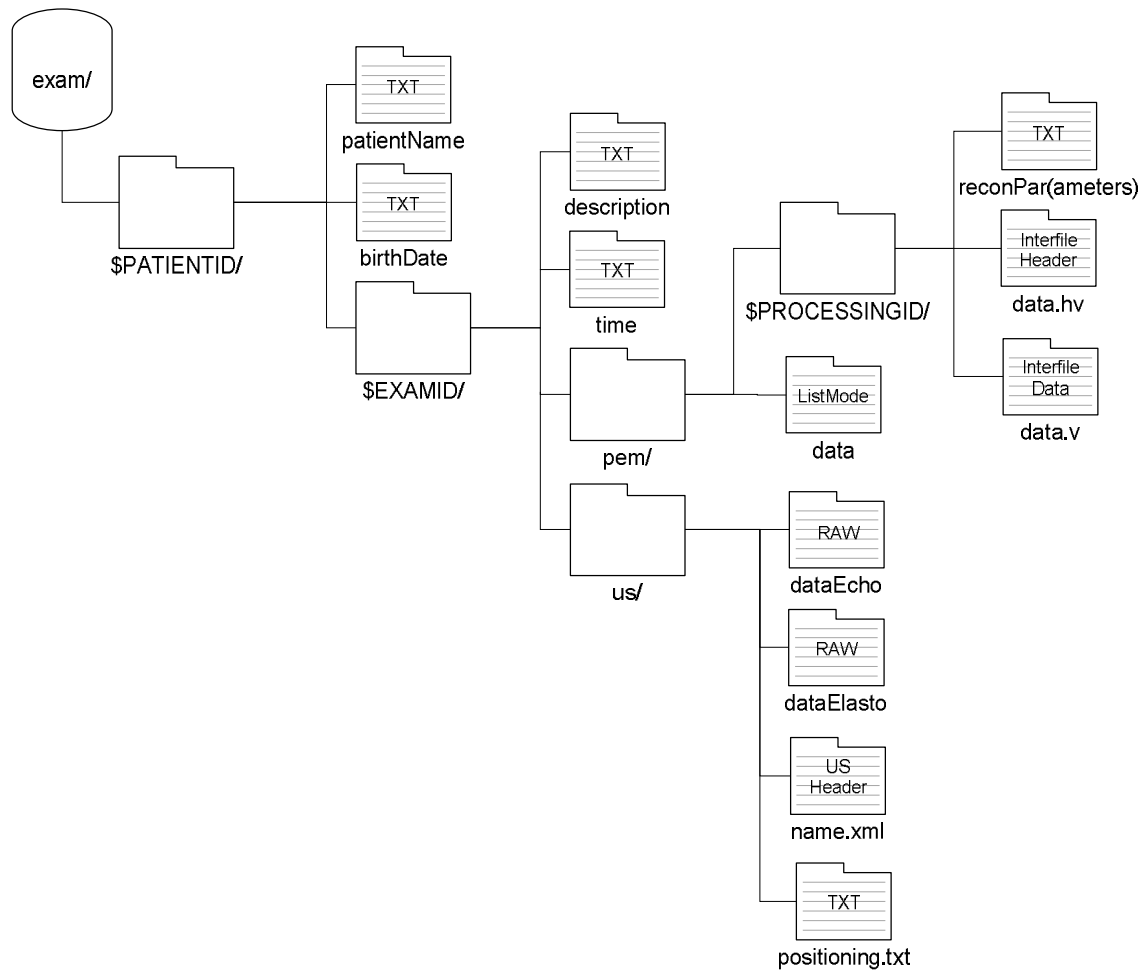


Figure 76 : Data storage structure

Figure 76 details the structure of the common data storage for ClearPEM-Sonic. All data is stored in the folder exam/ on the main server. Each patient has a unique patient ID with general information about himself and the exams attached to it. Each exam is identified by a unique exam ID and has general information about the exam as well as a PEM and a US exam. The raw listmode data from ClearPEM is kept in the same folder as the output of one or several image reconstructions. The binary outputs from the 3D B-mode echography and the elastography are stored together with general information about the ultrasound exam and the space coordinates provided by the tracking system.

3DSlicer is the main visualisation framework [157]. 3DSlicer is a multiplatform open-source software for image visualisation and manipulation. It is based on the Insight Segmentation and Registration Toolkit ITK [158] and the Visualisation Toolkit VTK [159]. It is easy to extend by implementing plug-ins, written in C++ or Python. 3DSlicer is expected to run in the background

during an exam. A plug-in monitors the acquisition of the space coordinates from the tracking system.

Once the acquisition is complete, it is possible to launch a stand-alone utility that monitors the PEM reconstruction. It is based on command-line reconstruction tools developed by the Laboratoria de Instrumentação e Física Experimental de Partículas (LIP), Lisbon, PT and Deutsches Krebsforschungszentrum (DKFZ), Heidelberg, DE. The user can define the parameters for the reconstruction process and monitor it. It is connected with the database and stores the output data in the proper place.

Then, the Image Loader module takes care of combining all data. Figure 77 summarizes the process of combining binary raw image data and positioning information into co-registered volumes. In 3DSlicer, it is possible to display separate PEM, B-mode and elastography images or the co-registered image. If the co-registration on the basis of the positioning information is not precise enough, it is possible to correct it.

Finally, the images can be converted into DICOM.

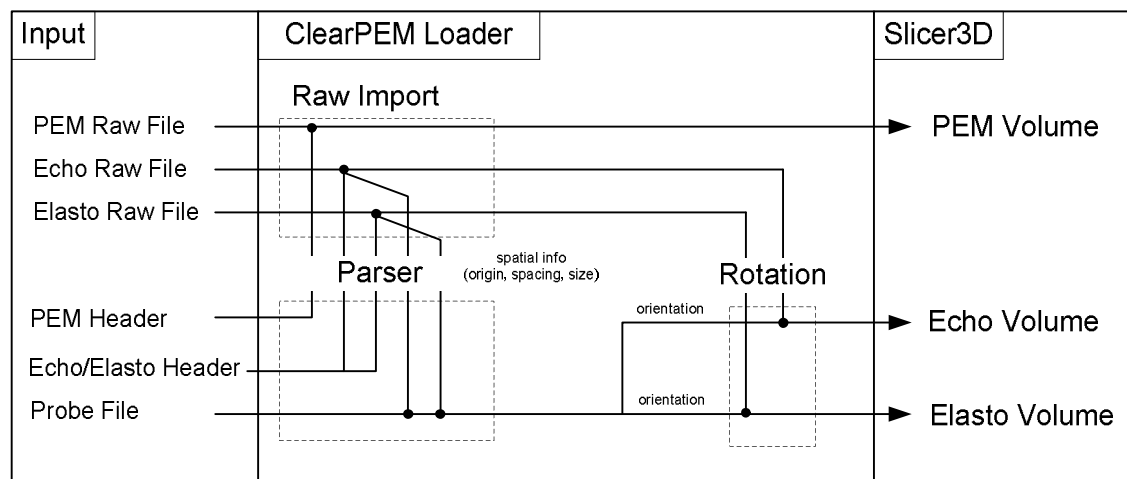


Figure 77 : The Image Loader module of the ClearPEM-Sonic software [156]

## 5.3 Mechanical Integration of both Modalities into a Single Machine

ClearPEM-Sonic is an integrated system for clinical trials expected to evolve into a commercial product. It thus requires the seamless mechanical integration of two completely different devices into a single modality under consideration of all constraints and user requirements.

One needs to bear in mind that ClearPEM was designed without any provision for the installation of a stabilization or an ultrasound system. As shown in figure 16, the ClearPEM bed and the PET plates are movable in three distinctive directions each, including a rotation by 180 degrees by the plates to cover the full region of interest. Any device added to ClearPEM must fully respect these degrees of freedom. In order to keep the distance between the PEM plates and the patient's chest wall, the bed thickness of 5 mm and maximum distance of 1 mm between the bed and the plates cannot be exceeded.

Based on these requirements, we looked for ways to include the stabilization system, ultrasound transducer and tracking systems in to ClearPEM. We developed, in close collaboration with mechanical engineers from INEGI - Instituto de Engenharia Mecânica e Gestão Industrial – in Porto and LMA-CNRS – Laboratoire de Mecanique et Acoustique – in Marseille, an integrated device where no modality impedes on the other one.

### 5.3.1 Conical Stabilization

The cone needs to be integrated into the existing ClearPEM system without impeding its functions. One major constraint is that the PEM plates shall be as close as possible to the chest wall to image as much as possible of the breast. The total thickness of the bed, cone, rail to position the cone and foam padding thus has to be as low as possible. Figure 78 shows the final solution that was designed in collaboration with INEGI – Instituto de Engenharia Mecânica e Gestão Industrial in Porto.

Avoiding an automatic positioning system for the cones reduces the overall thickness because no motors need to be incorporated. The cone will slide on a thin polyoxymethylene (POM, commercial name Delrin) rail and be manually positioned by the operator. The foam ring can be removed to allow easy exchange of the cone. It is narrower towards the centre: the chest of the patient is brought towards the hole and a bigger part of the breast is between the detector plates. If no stabilization is needed during an exam, the cone can be removed, without any further adjustments to be made.

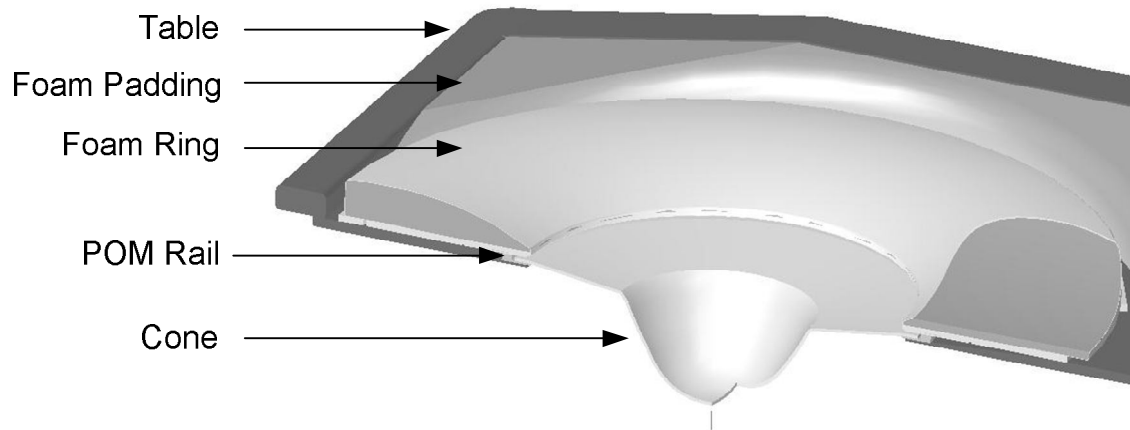


Figure 78 : Cutaway CAD model of the table with the breast cone

### 5.3.2 Ultrasonic Transducer

The simplest way of using the ultrasonic transducer would be fully free-hand. However, we were asked by our medical colleagues to provide a way of stabilizing the transducer position during the exam. Indeed, a full 3D B-mode and elastographic image acquisition of a given region of interest can take some time. Holding the ultrasound transducer in position on the breast, under the bed, for an extended period of time while manipulating the Aixplorer console could be rather uncomfortable.

We first suggested installing the ultrasound transducer on an arm mounted on a rail on the underside of the bed (Figure 79). This would allow sliding the arm around the hole to bring it in front of any ROI and then to adjust its exact position by changing the inclination of the arm. A blocking system would then immobilize the arm. The arm could be retracted during the PEM acquisition. This design soon proved to be incompatible with imaging constraints limiting the maximum thickness of the bed.

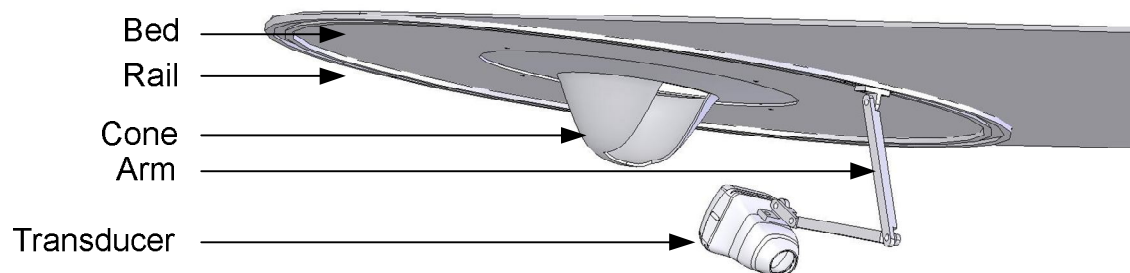


Figure 79 : Proposal for the US Integration, 12/2010

We therefore decided to decouple the arm from the bed. The ultrasound transducer is installed on an articulated arm (Figure 80). This arm is fixed on the PEM platform, at an angle of 90 degrees to the PET plates. There is no interference between the ultrasound installation and the mechanics of ClearPEM. The arm can place the ultrasound transducer in any position in front of any ROI. By using a quick-lock system, the arm can easily be removed from the PEM platform.



The arm can be placed on either side of the plates, depending on which side the physician prefers for the ultrasound exam.

If a magnetic tracking system is used, it can be placed on a bridge between the PEM plates. The arm holding the ultrasound transducer is then fixed to the bridge with the same quick-lock system (Figure 81).

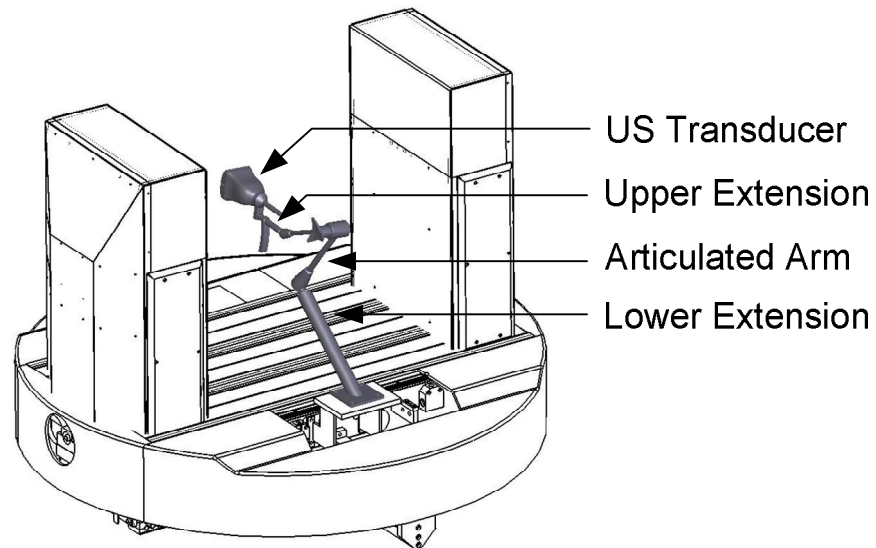


Figure 80 : Detail of the PEM platform. The transducer and its arm are highlighted in dark grey.



Figure 81 : Detail of the PEM platform as installed in Marseille, showing a mock-up of the US transducer on its arm and the bridge holding the magnetic emitter

### 5.3.3 Overall Design

The final solution respects the need of superposing both images and allows imaging of every region of interest with both modalities without interferences with the respective other one. Figure 82 shows the full design of ClearPEM-Sonic with all necessary modifications. Figure 83 is a photo showing the machine installed in December 2010 at Hôpital Nord, Marseille, with all modifications implemented.

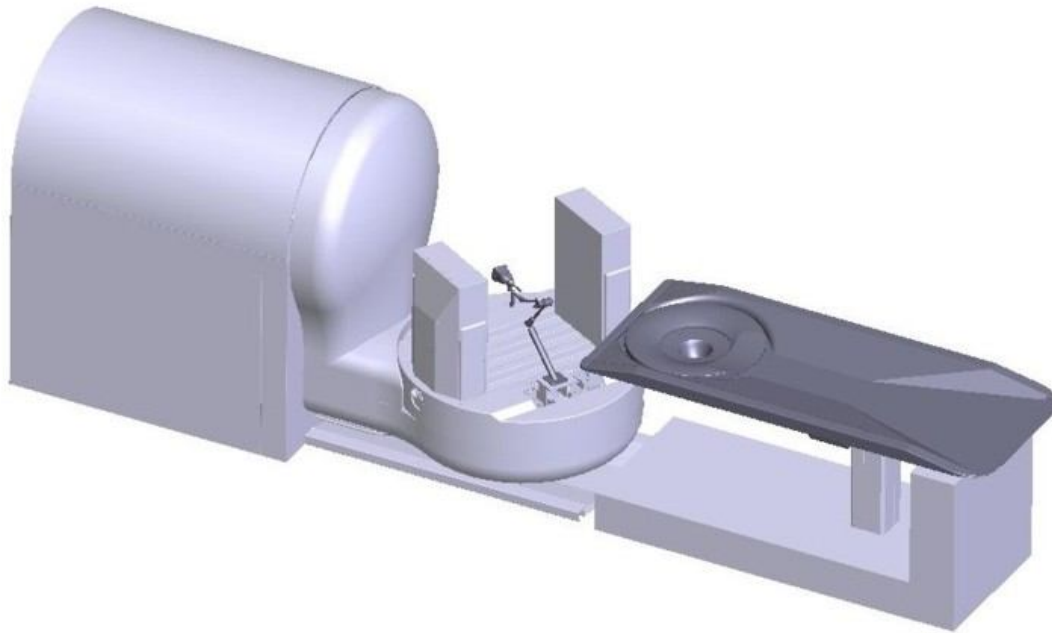


Figure 82 : Final Design of ClearPEM-Sonic: the new ClearPEM design is light grey, the dark grey parts were modified or developed as part of this thesis



Figure 83 : ClearPEM-Sonic as it is installed at Hopital Nord, Marseille. The SuperSonic Imagine Aixplorer is in the foreground, ClearPEM in the background.

L'usage d'un instrument savant n'a pas fait de toi un technicien sec. Il me semble qu'ils confondent but et moyen ceux qui s'effraient par trop de nos progrès techniques. Quiconque lutte dans l'unique espoir de biens matériels, en effet, ne récolte rien qui vaille vivre. Mais la machine n'est pas un but. L'avion n'est pas un but : c'est un outil. Un outil comme la charrue.

in Antoine de Saint-Exupéry, *Terre des Hommes*

## 6 System Evaluation

The ClearPEM used for the ClearPEM-Sonic project is assembled at Hôpital Nord, Marseille, FR in December 2010, by a team of engineers from LIP, Lisbon, PT and INEGI, Porto, PT. The commissioning of the machine starts at the beginning of 2011 and is finished by Summer 2011, when we start acquiring phantoms on ClearPEM. In September 2011, we submit an application for a clinical phase 1 trial, explained in more detail in section 6.4, to the competent French authorities. We receive the authorization for a trial on 20 patients in February 2012 and start the first medical study.

This chapter presents results from the commissioning and evaluation of the ClearPEM prototype installed at Hôpital Nord. It also provides a proof of concept for co-registering images from ClearPEM and the SuperSonic Imagine Aixplorer in the frame of the ClearPEM-Sonic project.

### 6.1 ClearPEM Detector Performance

During the commissioning of ClearPEM-Sonic at Hôpital Nord, we measure some key technical characteristics of the system during a standard acquisition sequence of 20 minutes with an Ultra Micro HotSpot Phantom – explained in section 6.2 – acquired with an initial filling of 1.5 MBq. The detector plates are at a distance of 160 mm from each other. This corresponds to usual plate distances during breast exams.

Figure 84a) shows the histogram of the energies of all events in the detector during that time span. The position and width of the photopeak are determined with a Gaussian fit:

$$y = a \cdot e^{-\frac{(x-\mu)^2}{2\sigma^2}} \quad (6.1)$$

where  $a$  is the amplitude,  $\mu$  the position and  $\sigma$  the Gaussian spreading of the peak.

The detectors had been calibrated by LIP before their shipment with a planar  $^{22}\text{Na}$  source to give correct energy measurements. The position of the photopeak at 511.3 keV confirms the proper calibration of the detectors. The average energy resolution of the complete detector system at 511 keV is 15.4 % FWHM. Figure 84b) shows the coincidence time spectrum of the same events. A Gaussian fit indicates that the coincidence time resolution of the system is 4.6 ns FWHM. These values confirm those published by Abrantes et al. on the ClearPEM prototype installed in Coimbra [16]. They found that the energy resolution is 13.3 % and the time resolution 4.5 ns FWHM.

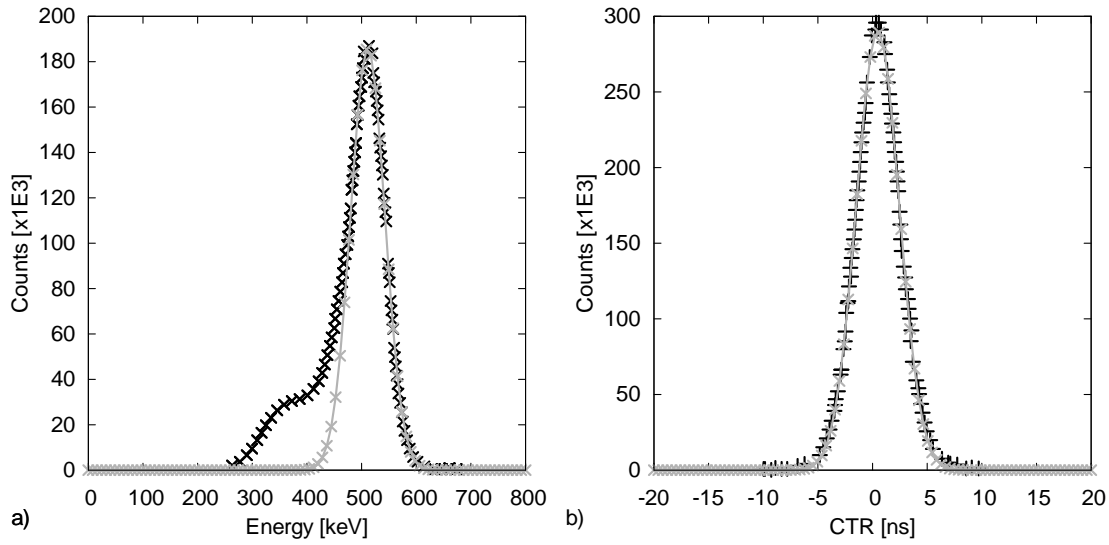


Figure 84 : a) Photospectrum measured over all events in the detector plates, b) coincidence time spectrum of the same events. Black crosses are real data points, the grey line represents the Gaussian fit.

## 6.2 ClearPEM Image Resolution

The image resolution describes how much detail the final reconstructed image holds. We use Derenzo-type phantoms to test the spatial resolution [160]. They quantify how close points can be to each other and still visibly be resolved as separate entities. The distance between the centres of two rods is equal to twice the rod diameter. The phantoms are filled with  $^{18}\text{F}$ -FluoroDeoxyGlucose (FDG) for the measurement.

In order to assess the image quality along a line of rods of similar diameter, we calculate the contrast according to Michelson [161]:

$$\text{contrast} = \frac{I_{\max} - I_{\min}}{I_{\max} + I_{\min}} \quad (6.2)$$

where  $I_{\max}$  and  $I_{\min}$  are the maximum and minimum pixel intensities along this line. This value is typically used to determine the contrast of a periodic pattern [161], [162]. A contrast of 100 % indicates a perfectly resolved pattern, a contrast of 0 % undistinguishable structures. We calculate an average contrast for each pattern by using the average intensity of the peaks and the average intensity of the valleys between adjacent peaks.

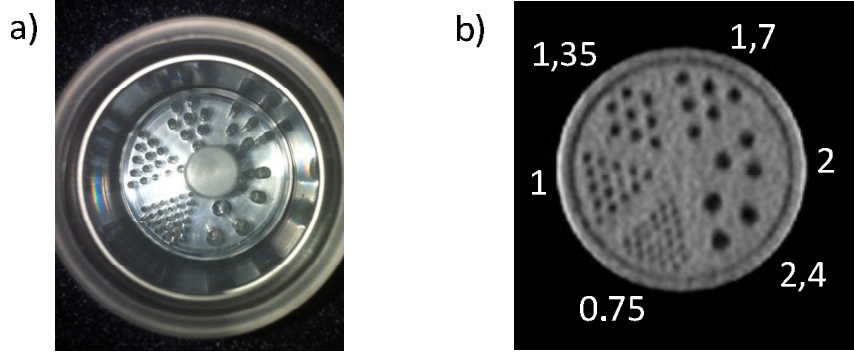


Figure 85 : a) Photography and b) CT image of the empty Ultra Micro Hotspot Phantom. The numbers are the rod diameters in millimetres.

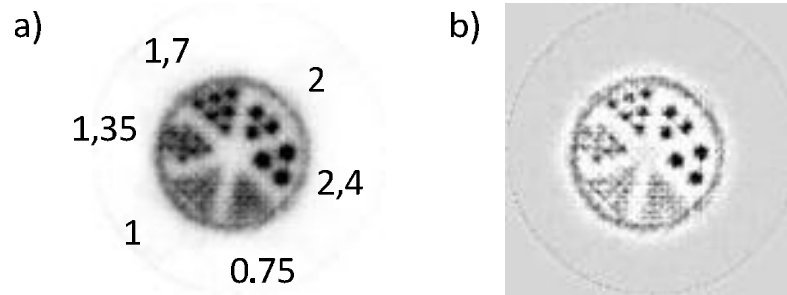


Figure 86 : a) ClearPEM image of the Ultra Micro Hotspot Phantom, filled with  $^{18}\text{F}$ -DG. The numbers are the rod diameters in millimetres. b) the same image with enhanced contrast

The first phantom is an Ultra Micro Hotspot Phantom produced by the Data Spectrum Corporation, Hillsborough, NC, USA. Figure 85 shows a photography and a CT image of this phantom. The rod diameters are 0.75, 1, 1.35, 1.7, 2 and 2.4 mm. It is used to get a first estimation of the image resolution. Figure 86a) shows the ClearPEM image of the same phantom, acquired during 20 minutes with an initial filling of 50 MBq. It is reconstructed with a list-mode file based OSEM algorithm with a voxel size of 0.5 mm and an energy window accepting events between 400 and 650 keV, arriving in a time window of 4 ns. Figure 86b) is the same image with enhanced contrast. It was modified by using a fast Fourier transformation (FFT) highpass filter. This filter first computes the discrete Fourier transform of the image. It then applies a cut-off for low spatial frequencies and finally computes the inverse Fourier transform, leading to a new image in the real space. The rods at 1.7 mm are the smallest clearly visible structure. Figure 89 shows the contrast calculated for different rod sizes for the original and the enhanced-contrast image. The contrast of 20.1 % in the original and 65.3 % in the enhanced image confirm the visual impression.

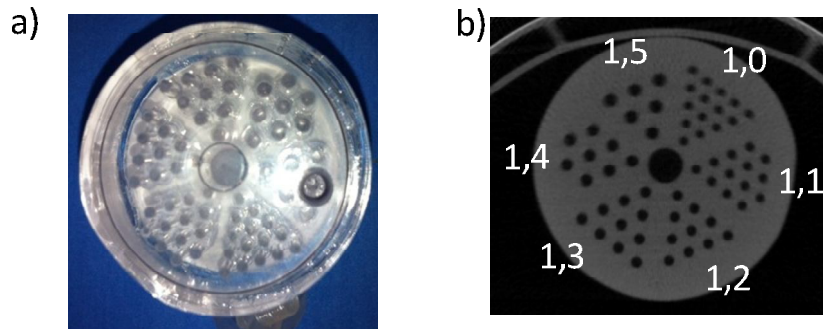


Figure 87 : a) Photography and b) CT image of the Bioscan mini-Jaszczak Phantom. The numbers are the rod diameters in millimetres.

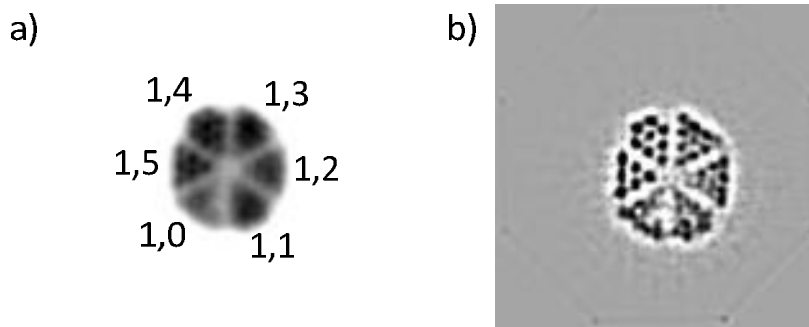


Figure 88 : a) Reconstructed ClearPEM image of the Bioscan mini-Jaszczak Phantom. The numbers are the rod diameters in millimetres. b) the same image with enhanced contrast

The second is a mini-Jaszczak phantom produced by Bioscan. Figure 87 shows a photo and a CT image of this phantom. The rod diameters are 1, 1.1, 1.2, 1.3, 1.4 and 1.5 mm. It is used to determine the exact image resolution. Figure 88a) shows the raw reconstructed image from a ClearPEM acquisition. It is reconstructed with the same parameters as the Ultra Micro Hotspot Phantom. Figure 88b) shows the same image after contrast enhancing with an FFT highpass filter. The rods at 1.5 mm are clearly visible in both images, the rods at 1.4 and 1.3 mm require contrast enhancing. The contrast according to Michelson is shown in figure 89. It is very low in the original reconstructed image. In the contrast-enhanced image, the contrast is 38.1 % for the rods at 1.4 mm and 18.8 % for the rod at 1.3 mm.

This confirms that the ClearPEM installed in Marseille has a resolution definitely better than 1.4 mm, with 1.3 mm possible after some image treatment. These results confirm those presented in [16], where a resolution better than 1.5 mm is presented on the ClearPEM prototype installed in Coimbra.

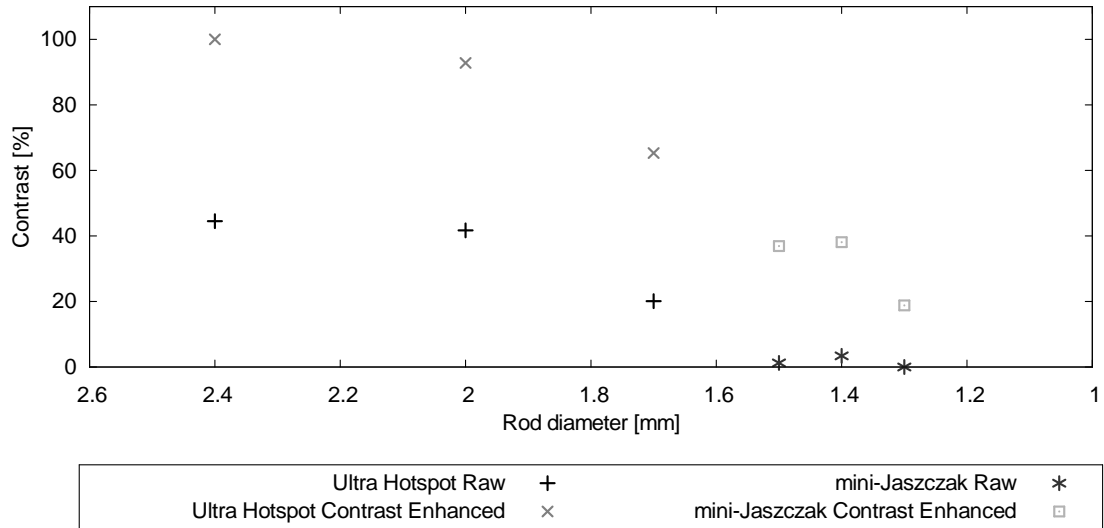


Figure 89 : Contrast according to Michelson of both phantoms

### 6.3 Image Co-registration

The performance of ClearPEM-Sonic as a multimodality system is tested by means of gelatine and Agar phantoms, developed by Dang Jun [120]. The phantoms are designed to imitate the behaviour of cancerous lesions surrounded by healthy breast tissue for an ultrasound, an elastography and a ClearPEM exam. Their acoustic and elastic properties are varied by changing the amount of gelatine and Agar during the preparation. Their radioactive properties are changed by preparing the gelatine-Agar mix with different concentrations of  $^{18}\text{F}$ FDG. All PET and PEM exams have to be done within a few hours after the preparation because of the relatively short lifetime of the positron emitter. Figure 90 is a photo of such a phantom being imaged on ClearPEM-Sonic.



Figure 90 : A gelatine-Agar phantom being imaged



Figure 91 presents a B-mode US, elastography and ClearPEM image acquired on a conical multimodality phantom, consisting of two hot spherical lesions with a diameter of 20 mm placed into radioactive background. The activity concentration in the spherical lesions is 8 times higher than in the background. Figures 92 and 93 show the co-registered US-ClearPEM and elastography-ClearPEM images. The position of the lesion seen on the ultrasound and elastography images matches the position of the lesion seen with ClearPEM.

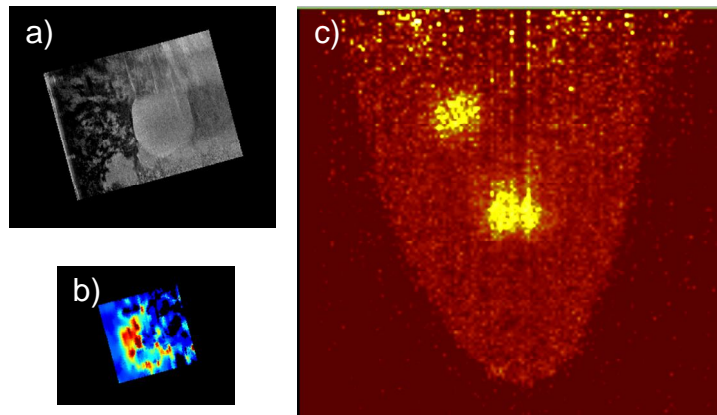


Figure 91 : a) US image, b) elastography image and c) ClearPEM image of a gelatine/Agar phantom

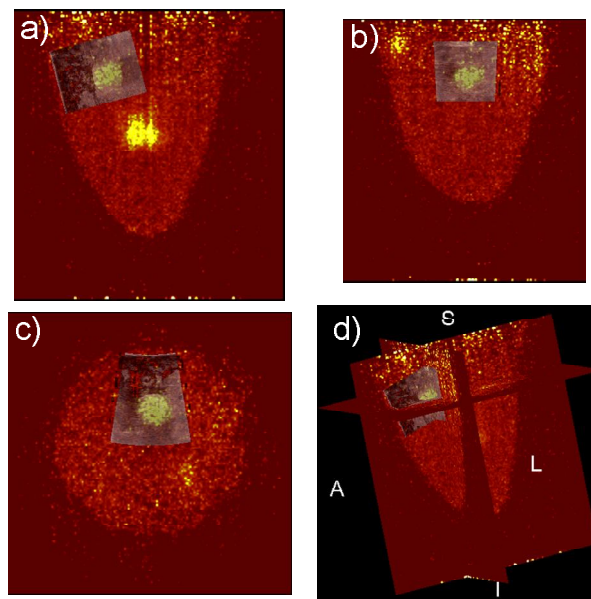


Figure 92 : a) Coronal, b) sagittal, c) transverse and d) 3D images of the co-registered US and ClearPEM acquisition

Due to the very limited availability of a SuperSonic Imagine Aixplorer with the 3D probe at Hôpital Nord, we performed a single co-registered ClearPEM-Sonic acquisition. It is the proof that co-registered ClearPEM and Aixplorer acquisitions are possible. Once the full SuperSonic Aixplorer with a 3D probe will be installed at Hôpital Nord, a more extensive evaluation will have to be performed. It will then be possible to apply this method to patient examinations.



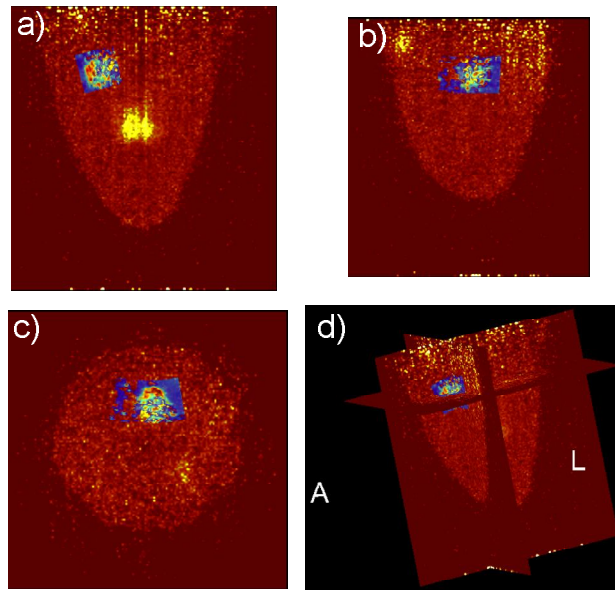


Figure 93 : a) Coronal, b) sagittal, c) transverse and d) 3D images of the co-registered elastography and ClearPEM acquisition

## 6.4 Patient Imaging Trial

The first step towards the clinical use of the multimodal imaging device ClearPEM-Sonic is to submit each modality to separate trials. The clinical assessments of the SuperSonic Aixplorer and the 3D probe used for ClearPEM-Sonic are not part of the ClearPEM-Sonic project. Section 3.3.4 of this thesis reviews the current status of clinical trials with the Aixplorer.

Both ClearPEM prototypes, installed in Coimbra and Marseille, are in the first phase of clinical trials. In analogy with drug trials, the main purpose of the phase 1 clinical trial of a medical device is to assess the feasibility of patient exams and the patient safety. It is usually conducted on a sample of 20 patients. It follows a preclinical study that demonstrated the proper functioning of the machine. Further steps in the clinical evaluation of a medical device will be a phase 2 and, if it is positive, a phase 3 trial [163]. The phase 2 trial, conducted on a sample of 100 to 300 patients, demonstrates that the diagnostic results obtained with the medical device are not worse than those obtained with established modalities. The third phase is a multicentre trial on several thousands of patients that establishes the added value of the medical device.

ClearPEM-Sonic has received approval from the competent French authority Agence Française de Sécurité Sanitaire des Produits de Santé (AFSSAPS) to conduct a first trial according to their guidelines [164]. This trial is also registered with United States National Institutes of Health (US NIH) clinical trial database [165]. The modalities of this trial are detailed in the protocol submitted by Dr. L. Tessonier [166]. The main goal of this trial is to study the feasibility and safety of ClearPEM exams. Secondary goals are:

- to compare the results with other modalities such as B-mode ultrasound, X-ray mammography, whole-body PET or MRI
- to study the feasibility of combined PEM and ultrasound

- to evaluate how the patient tolerates the exam
- to optimize the PEM acquisition protocol.

The gold standard that determines the final diagnosis is the histological assessment of a biopsy. All patients who participate in this trial will have preliminary reference exams, including X-ray mammography, ultrasound, MRI and whole-body PET/CT. The ClearPEM exam is done immediately after the whole-body PET/CT. This avoids a second injection of  $^{18}\text{F}$ FDG. The ClearPEM exam thus does not need any additional irradiation of the patient.

We plan to include 20 patients of at least 18 years who already have been diagnosed with breast cancer and comply with the following criteria:

- they need a whole-body PET/CT as part of their care
- they need to have a full conventional examination, including MRI, X-ray mammography and ultrasound
- they are informed about the trial and agree to it
- they are part of the French social security plan.

We exclude all other patients as well as patients who are pregnant, breast feeding, have a counter-indication to any of the mentioned diagnostic modalities or have another cancer. We also exclude patients whose follow-up is not guaranteed or who cannot give their written agreement to the exam.

The proposed clinical workflow for a ClearPEM exam is:

- a) The patient had prior exams. This includes a whole-body PET exam where a tracer is administered, immediately before the ClearPEM exam. Potential lesions should be known.
- b) The patient is installed on the ClearPEM-Sonic bed. In order to stabilize the breast for the exams, a breast stabilization system can be used.
- c) The breast is first imaged with ClearPEM. The US system is not used at this stage and retracted.
- d) The physician assesses the ClearPEM image immediately after the acquisition and compares it with the result of other examinations.

In the case of a multimodal ClearPEM-Sonic exam, the following steps would be added:

- e) In function of the assessment in (d), he defines regions of interest for the US examination.
- f) If necessary, the breast stabilization system is reconfigured for the US examination.
- g) The regions of interest are imaged with the US system, the ClearPEM plates are retracted at that moment.
- h) The images are superposed with suited software.
- i) A final diagnosis is established under consideration of these images.

During the whole exam, the patient does not change her position. This guarantees that the images from the separate modalities can be easily superposed for the final images.

This section presents three preliminary case-studies that illustrate the benefits and limitations of ClearPEM. They were acquired at Hôpital Nord in collaboration with Dr. Laurent Tessonier, Dr. Pascale Siles and Dr. Valérie Juhan.

#### 6.4.1 Case 1: infiltrating ductal carcinoma

This subject presents an infiltrating ductal carcinoma in her left breast. It is visible on the full-body PET/CT (Figure 94). Figure 95 shows the coronal and the sagittal views of ClearPEM images acquired on the same breast. The lesion is easy to spot on both images. This image confirms that a breast tumour of sufficient size that is seen with whole-body PET is also seen with ClearPEM. A closer examination of the image close to the chest wall shows that the tumour appears to be cut in the ClearPEM image. This indicates the major limitation in ClearPEM exams: due to the thickness of the bed and the minimum distance that needs to be kept between the bed and the detector plates, the detector cannot be brought sufficiently close to the chest wall and thus misses pathologies in this region. This will have to be assessed in further, more extensive trials.

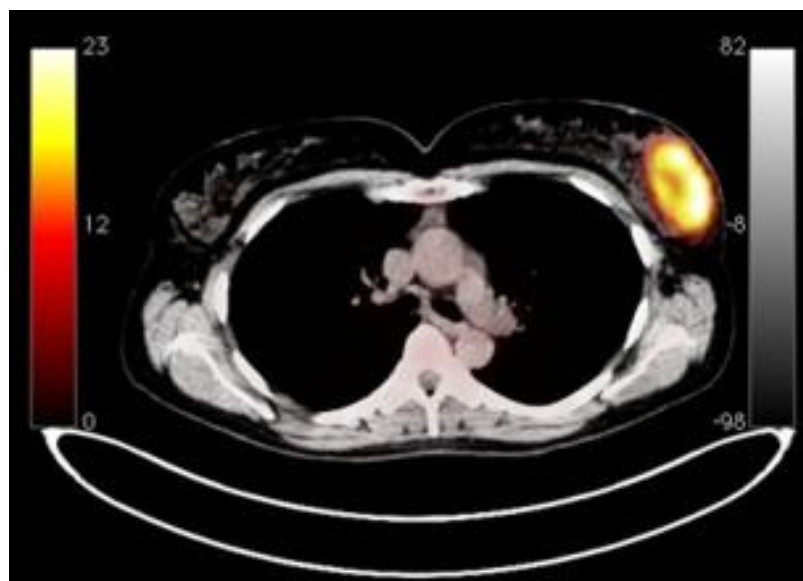


Figure 94 : a) Whole-body PET/CT of case 1

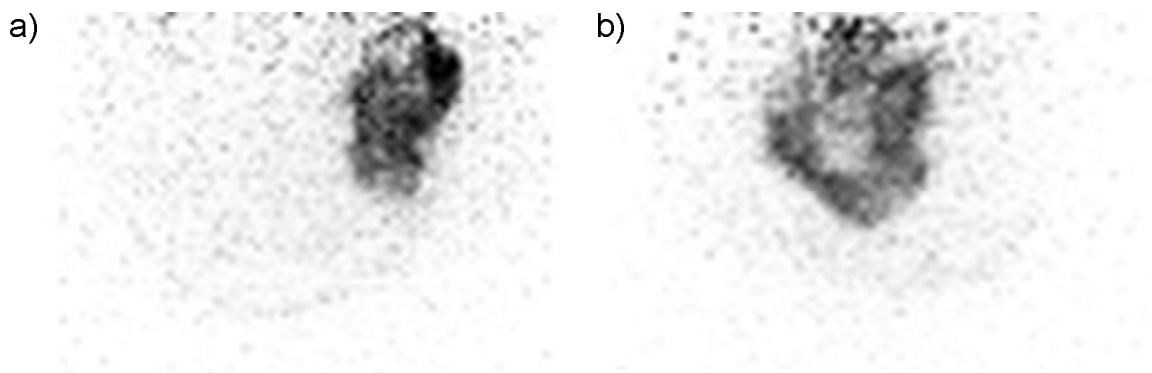


Figure 95 : a) coronal and b) sagittal ClearPEM images of case 1

#### 6.4.2 Case 2: bilateral breast cancer

Case 2 was diagnosed with a cancer in her right breast. Figure 96 compares the CT, MRI, whole-body PET and ClearPEM images of this lesion. It is clearly visible with every modality. The MRI exam also shows a small lesion in her left breast (Figure 97c). This lesion is not clearly visible with CT (Figure 97b) and invisible with whole-body PET (Figure 97a). The lesion is visible on the ClearPEM image (Figure 97d). This study shows that ClearPEM is able to detect additional lesions and increases the sensitivity of the exam. In combination with MRI it is also able to enhance the specificity of the exam as it confirms the suspicion seen with MRI.

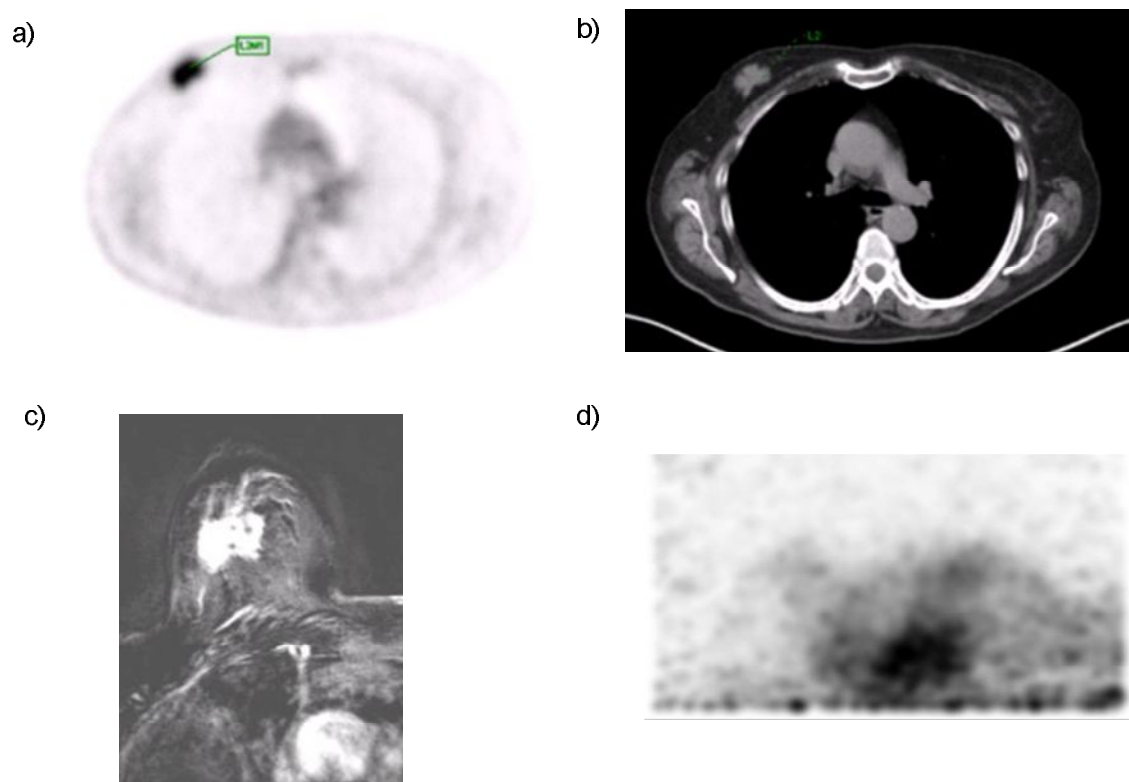


Figure 96 : a) whole-body PET, b) CT, c) MRI of and d) ClearPEM of the right breast of case 2

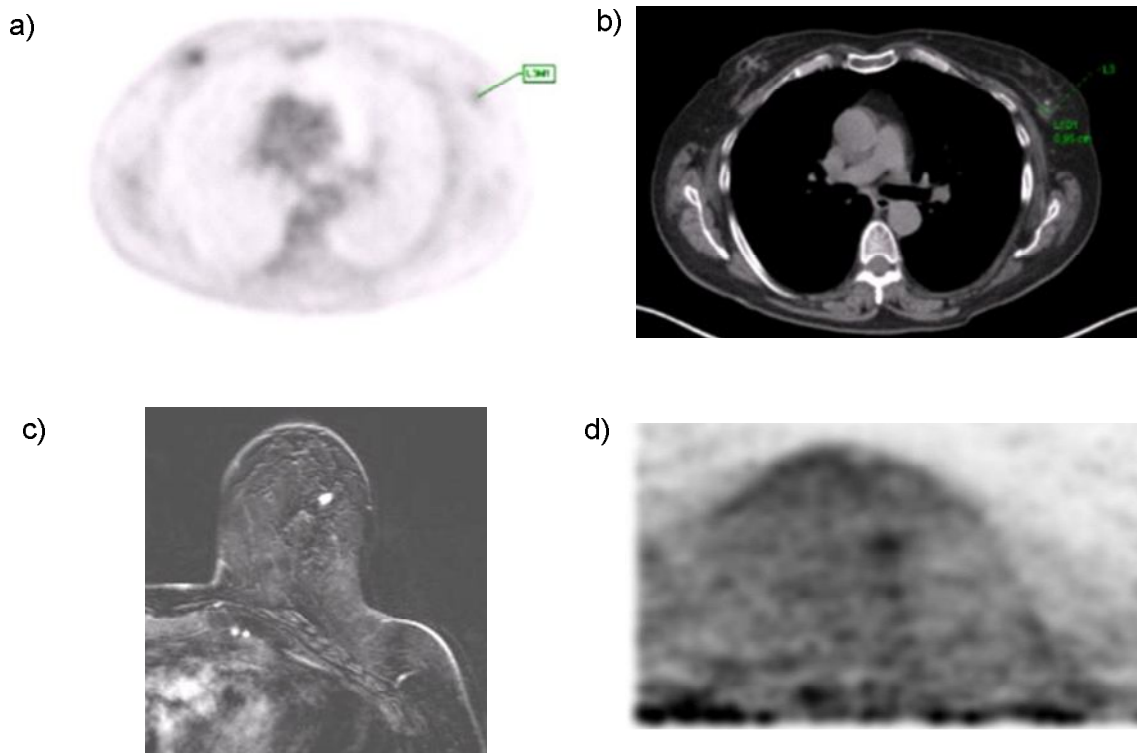


Figure 97 : a) whole-body PET, b) CT, c) MRI and d) ClearPEM of the left breast of case 2

#### 6.4.3 Case 3: multifocal breast cancer

Case 3 was diagnosed with a multifocal breast cancer during her initial exam. The whole-body PET/CT (Figure 98a) reveals a first lesion in the left breast and a second close to the axilla. The extended exam with MRI (Figure 98b) shows small lesions around the first one. The whole-body PET/CT (Figure 98a) however is not able to show the small lesions. Figure 99 shows the image acquired with ClearPEM. The small lesions around the main lesion are clearly visible. This case confirms that ClearPEM has higher sensitivity than a whole-body PET exam. The second focus is too close to the thoracic wall and cannot be imaged with ClearPEM.

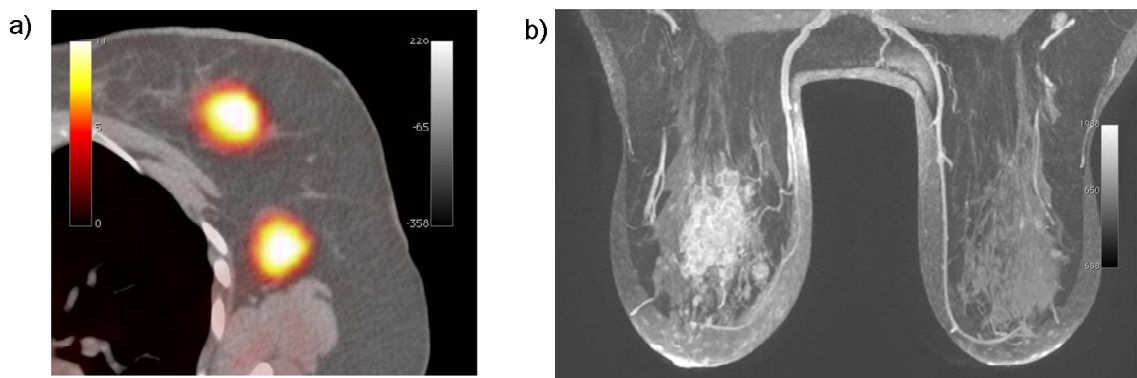


Figure 98 : a) Whole-body PET/CT of the left breast and b) MRI of case 3

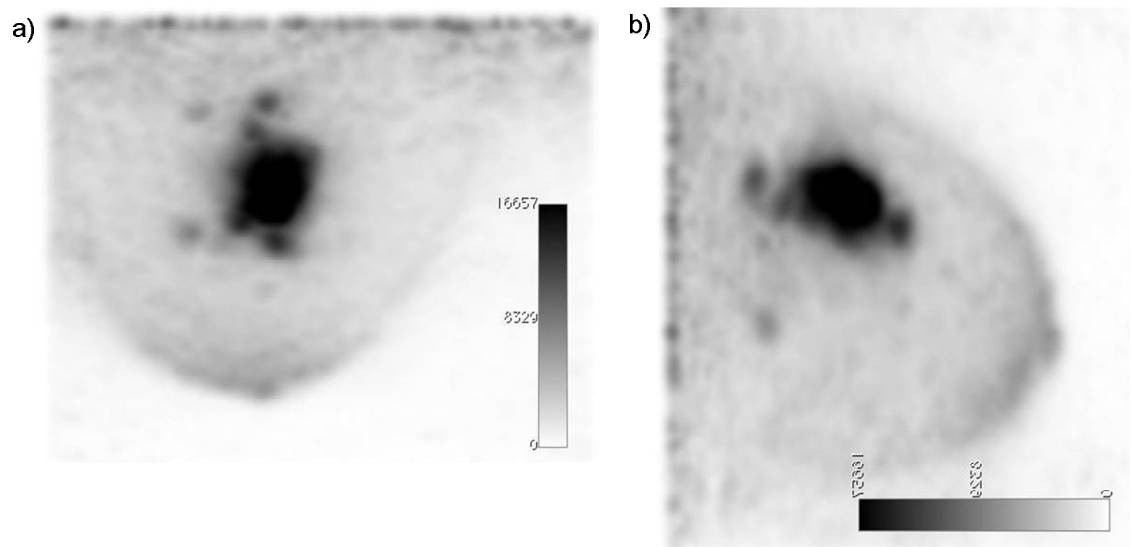


Figure 99 : a) coronal and b) sagittal ClearPEM images of case 3

Ô Mort, vieux capitaine, il est temps ! Levons l'ancre !  
Ce pays nous ennuie, ô Mort ! Appareillons !  
Si le ciel et la mer sont noirs comme de l'encre,  
Nos cœurs que tu connais sont remplis de rayons !

Verse-nous ton poison pour qu'il nous réconforte !  
Nous voulons, tant ce feu nous brûle le cerveau,  
Plonger au fond du gouffre, Enfer ou Ciel, qu'importe ?  
Au fond de l'inconnu trouver du *nouveau* !

in Charles Baudelaire, *Les Fleurs du Mal*

## 7 Summary and Outlook

Dedicated multimodality imaging is a discipline at the crossing points of radiology and nuclear medicine. It takes its upwind from the development of new technologies that allow building imaging devices targeted at certain organs. It also benefits from an increased awareness of the medical community about the possibilities interdisciplinary multimodality offers.

ClearPEM-Sonic aims at exactly this question by combining a high-resolution positron emission tomograph dedicated to breast exams with an advanced ultrasound elastography system. The aim of this thesis was to develop technological solutions for this system and to accompany its installation and commissioning in the clinical environment.

ClearPEM-Sonic uses the second ClearPEM that was built, learning from the first prototype currently installed at ICNAS, Coimbra. The improvement of the detector and thus the ongoing development of the scintillation crystals, that is part of this thesis, are among the technological improvements with respect to the first prototype. We investigate different crystal producers and develop a procedure to depolish the crystal surface. It produces crystals that comply with the design requirements relative to DOI, light yield and energy resolution without trade-offs on any of these quality factors. We develop a depolishing procedure for LYSO:Ce crystals. Their light output is around 17500 photons per MeV, with an energy resolution of 13 % and a depth of interaction resolution of 5.2 %/mm. This corresponds to an increase of 30 % of the light output and 2 percentage points in energy resolution in comparison with the crystals used in the first ClearPEM prototype.

The major result of this thesis is the development and installation of solutions that combine metabolic information from PEM with anatomical and elastographic information from the other modality, the SuperSonic Imagine Aixplorer. We have to master a certain number of challenges

to be able to image any region of interest of the breast with both modalities. We have developed a set of stabilization cones to stabilize the breast during the exam. The stabilization cone keeps the natural form of the breast: besides improved patient comfort due to the lack of compression, it allows anatomical correct imaging. A fully rotatable arm supports the US transducer and is able to immobilize it with any inclination in any position required by its operator.

While the PEM image position is known with reference to the PEM plates, the US transducer and therefore also the image it generates can be at any place in space. Since PEM and US do not necessarily see the same object, the precision when co-registering both images is enhanced if the spatial position and orientation of both images are known. The currently selected magnetic tracking solution is able to provide positioning information within the limitation of a distorted measurement. The operator uses this as primary information for co-registering both images.

ClearPEM-Sonic is installed with dedicated software that serves as a unique user-friendly interface. It controls the PEM image reconstruction, acquires the US image from Aixplorer as well as the corresponding space coordinates. It also provides all tools necessary for image co-registration as well as an interface to DICOM and the hospital's PACS.

ClearPEM-Sonic has been installed and commissioned at Hôpital Nord, Marseille, FR. We have proven its proper functioning as well as its imaging quality. The Marseille ClearPEM prototype has a PEM resolution close to 1.3 mm. We have also proven the concept of multimodal image acquisition with ClearPEM and Aixplorer. We can co-register images acquired with both modalities.

ClearPEM-Sonic entered its first clinical trial. The main goals of this trial on 20 patients are to determine the usability in a clinical environment and to prove that its use does not harm the patient. In this view, we only image patients who have been scheduled for whole-body PET/CT as part of their diagnostic follow-up. They also undergo classic imaging procedures including mammography, ultrasound, MRI. The comparison of ClearPEM-Sonic images with images from classic devices gives a first impression of its patient imaging performance. It also helps improving the clinical workflow in the view of further trials. The preliminary evaluation of patient data shows that if the lesion is within the field-of-view of the detector, it is visible with ClearPEM. The machine proves to be able to detect small lesions that are not visible with whole-body PET. The major limitation is its inability to image the part of the breast closest to the chest wall. A more extensive evaluation is required to assess the impact of this limitation on the global diagnostic value of ClearPEM-Sonic.

The ClearPEM and ClearPEM-Sonic projects, together with other breast PET systems, are heralds of a new generation of dedicated multimodality devices for nuclear medicine and radiology. Based on the lessons learned during the development and clinical trials of these prototypes, it is possible to imagine future devices.

In the field of dedicated breast imaging, compact detectors need to be developed. They would serve as an additional modality for patients where classical imaging is not able to provide a clear diagnosis. The metabolic information from a dedicated breast PET could be combined with anatomical information from CT and MRI, either by using a PEM insert or by combining images from separate acquisitions. Both provide an image showing the full breast as compared



to ultrasound which is always limited to a part of the breast. The main drawback of MRI is, despite its excellent sensitivity, its limited specificity. If an MRI image is refined with information from a PEM exam, the number of false positives could be reduced. The combination of PEM with MRI would provide excellent sensitivity paired with excellent specificity.

The histological analysis of a tissue specimen is the accepted way of confirming the diagnosis of cancer, based on indications from medical imaging. A dedicated breast imaging system thus benefits from the possibility of performing a biopsy under live monitoring. The combination of a PEM with a biopsy apparatus would fit into the future clinical workflow.



## Literature

- [1] H. Wagner, “A brief history of positron emission tomography (PET),” *Seminars in Nuclear Medicine*, vol. 28, no. 3, pp. 213–220, Jul. 1998
- [2] W. H. Sweet, “The uses of nuclear disintegration in the diagnosis and treatment of brain tumor,” *New England Journal of Medicine*, vol. 23, no. 245, pp. 875–878, Dec. 1951
- [3] M. M. Ter-Pogossian, M. E. Phelps, E. J. Hoffman, and N. A. Mullani, “A positron-emission transaxial tomograph for nuclear imaging (PETT),” *Radiology*, vol. 114, no. 1, pp. 89–98, Jan. 1975
- [4] R. Nutt, “The History of Positron Emission Tomography,” *Molecular Imaging & Biology*, vol. 4, no. 1, pp. 11–26, Jan. 2002
- [5] M. J. Weber and R. R. Monchamp, “Luminescence of Bi<sub>4</sub>Ge<sub>3</sub>O<sub>12</sub>: Spectral and decay properties,” *J. Appl. Phys.*, vol. 44, no. 12, pp. 5495–5499, Dec. 1973
- [6] O. H. Nestor and C. Y. Huang, “Bismuth Germanate: A High-Z Gamma-Ray and Charged Particle Detector,” *IEEE Transactions on Nuclear Science*, vol. 22, no. 1, pp. 68–71, Feb. 1975
- [7] C. L. Melcher, “Lutetium orthosilicate single crystal scintillator detector,” U.S. Patent 4958080, Sep. 1990
- [8] T. Ido et al., “Labeled 2-deoxy-D-glucose analogs. 18F-labeled 2-deoxy-2-fluoro-D-glucose, 2-deoxy-2-fluoro-D-mannose and 14C-2-deoxy-2-fluoro-D-glucose,” *Journal of Labelled Compounds and Radiopharmaceuticals*, vol. 14, no. 2, pp. 175–183, 1978
- [9] T. Beyer et al., “A Combined PET/CT Scanner for Clinical Oncology,” *J Nucl Med*, vol. 41, no. 8, pp. 1369–1379, Aug. 2000
- [10] H. Zaidi and A. Alavi, “Current trends in PET and combined (PET/CT and PET/MR) systems design,” *PET Clinics*, vol. 2, no. 2, pp. 109–123, 2007
- [11] A. Del Guerra and N. Belcari, “State-of-the-art of PET scanners for small animal and breast cancer imaging,” *Nuclear Instruments and Methods in Physics Research Section A: Accelerators, Spectrometers, Detectors and Associated Equipment*, vol. 580, no. 2, pp. 910–914, Oct. 2007
- [12] *Naviscan Data Sheet*. Naviscan (San Diego, CA), 2010
- [13] S. Majewski, A. Stolin, E. Delfino, P. Martone, and J. Proffitt, “High resolution fast stereotactic PET imager for prostate biopsy,” in *2011 IEEE Nuclear Science Symposium and Medical Imaging Conference (NSS/MIC)*, pp. 3406–3409, Oct. 2011
- [14] B. Frisch, “Development of ClearPEM-Sonic: A multimodal positron emission mammograph and ultrasound scanner,” in *2011 IEEE Nuclear Science Symposium and Medical Imaging Conference (NSS/MIC)*, pp. 2267–2272, Oct. 2011
- [15] P. Lecoq and J. Varela, “Clear-PEM, a dedicated PET camera for mammography,” *Nuclear Instruments and Methods in Physics Research Section A: Accelerators, Spectrometers, Detectors and Associated Equipment*, vol. 486, no. 1–2, pp. 1–6, 2002
- [16] M. Abrantes et al., “ClearPEM scanners: Performance results and studies in preclinical environment,” in *2011 IEEE Nuclear Science Symposium and Medical Imaging Conference (NSS/MIC)*, pp. 3291–3295, Oct. 2011
- [17] *Advancing the Art of Breast Ultrasound Imaging*. SuperSonic Imagine (Aix-en-Provence), 2010
- [18] *Convention for the establishment of a European organization for nuclear research*. CERN (Geneva), 1953
- [19] M. Barnier, M. Calmy-Rey, H. Curien, and R. Aymar, *Infinitely CERN, 1954-2004. Memories of Fifty Years of Research*. Hurter (Geneva), 2004
- [20] O. S. Brüning et al., *LHC Design Report*. CERN (Geneva), 2004
- [21] J.-L. Caron, “LHC Layout” CERN, LHC-PHO-1997-060, 1997
- [22] The CMS Collaboration, “Observation of a new boson at a mass of 125 GeV with the CMS experiment at the LHC,” *Physics Letters B*, vol. 716, no. 1, pp. 30–61, Sep. 2012

- [23] The ATLAS Collaboration, “Observation of a new particle in the search for the Standard Model Higgs boson with the ATLAS detector at the LHC,” *Physics Letters B*, vol. 716, no. 1, pp. 1–29, Sep. 2012
- [24] A. Hervé et al., *R & D proposal for the study of new fast and radiation hard scintillators for calorimetry at LHC*. The Crystal Clear Collaboration (CERN, Geneva), 1991
- [25] “Layout of CMS” CERN, CERN-DI-9803027, 1998
- [26] *A Study of New Fast and Radiation Hard Scintillators for Calorimetry at LHC*. The Crystal Clear Collaboration (CERN, Geneva), 2002
- [27] A. A. Annenkov, M. V. Korzhik, and P. Lecoq, “Lead tungstate scintillation material,” *Nuclear Instruments and Methods in Physics Research Section A: Accelerators, Spectrometers, Detectors and Associated Equipment*, vol. 490, no. 1–2, pp. 30–50, Sep. 2002
- [28] P. Lecoq et al., “Lead tungstate (PbWO<sub>4</sub>) scintillators for LHC EM calorimetry,” *Nuclear Instruments and Methods in Physics Research Section A: Accelerators, Spectrometers, Detectors and Associated Equipment*, vol. 365, no. 2–3, pp. 291–298, Nov. 1995
- [29] E. Auffray et al., “Cerium doped heavy metal fluoride glasses, a possible alternative for electromagnetic calorimetry,” *Nuclear Instruments and Methods in Physics Research Section A: Accelerators, Spectrometers, Detectors and Associated Equipment*, vol. 380, no. 3, pp. 524–536, Oct. 1996
- [30] A. G. Petrosyan et al., “Potential of existing growth methods of LuAP and related scintillators,” *Nuclear Instruments and Methods in Physics Research Section A: Accelerators, Spectrometers, Detectors and Associated Equipment*, vol. 486, no. 1–2, pp. 74–78, 2002
- [31] C. Kuntner, E. Auffray, P. Lecoq, C. Pizzolotto, and M. Schneegans, “Intrinsic energy resolution and light output of the Lu<sub>0.7</sub>Y<sub>0.3</sub>AP:Ce scintillator,” *Nuclear Instruments and Methods in Physics Research Section A: Accelerators, Spectrometers, Detectors and Associated Equipment*, vol. 493, no. 3, pp. 131–136, Nov. 2002
- [32] A. G. Petrosyan et al., “LuAP/LuYAP single crystals for PET scanners: effects of composition and growth history,” *Optical Materials*, vol. 24, no. 1–2, pp. 259–265, Oct. 2003
- [33] A. Petrosyan et al., “The melt growth of large LuAP single crystals for PET scanners,” *Nuclear Instruments and Methods in Physics Research Section A: Accelerators, Spectrometers, Detectors and Associated Equipment*, vol. 537, no. 1–2, pp. 168–172, Jan. 2005
- [34] A. Petrosyan et al., “Comparison of spectral and scintillation properties of LuAP: Ce and LuAP: Ce, Sc single crystals,” in *2008 IEEE Nuclear Science Symposium Conference Record*, pp. 4877–4882, 2008
- [35] J. Trummer, E. Auffray, P. Lecoq, A. Petrosyan, and P. Sempere-Roldan, “Comparison of LuAP and LuYAP crystal properties from statistically significant batches produced with two different growth methods,” *Nuclear Instruments and Methods in Physics Research Section A: Accelerators, Spectrometers, Detectors and Associated Equipment*, vol. 551, no. 2–3, pp. 339–351, 2005
- [36] E. Auffray et al., “The ClearPET project,” *Nuclear Instruments and Methods in Physics Research Section A: Accelerators, Spectrometers, Detectors and Associated Equipment*, vol. 527, no. 1–2, pp. 171–174, Jul. 2004
- [37] K. Ziemons et al., “The ClearPET(TM) project: development of a 2nd generation high-performance small animal PET scanner,” *Nuclear Instruments and Methods in Physics Research Section A: Accelerators, Spectrometers, Detectors and Associated Equipment*, vol. 537, no. 1–2, pp. 307–311, Jan. 2005
- [38] P. Sempere Roldan et al., “Raytest ClearPET(TM), a new generation small animal PET scanner,” *Nuclear Instruments and Methods in Physics Research Section A: Accelerators, Spectrometers, Detectors and Associated Equipment*, vol. 571, no. 1–2, pp. 498–501, Feb. 2007

- [39] M. C. Abreu et al., "Clear-PEM: A PET imaging system dedicated to breast cancer diagnostics," *Nuclear Inst. and Methods in Physics Research, A*, vol. 571, no. 1–2, pp. 81–84, 2007
- [40] *CERN technology transfers to industry and society*. CERN (Geneva), 2005
- [41] P. J. Bryant, *PIMMS Proton-ion medical machine study*. CERN (Geneva), 2000
- [42] U. Amaldi and M. Silari, *The TERA project and the Centre for Oncological Hadrontherapy*. INFN (Rome), 1994
- [43] T. Auberger, E. Griesmayer, and A. Wambersie, *Das Projekt MedAustron: Designstudie*, 2. Aufl. Fotec (Wiener Neustadt), 2007
- [44] O. Droessel, *Bildgebende Verfahren in der Medizin*. Springer, 2000
- [45] H. Morneburg, *Bildgebende Systeme für die medizinische Diagnostik*, 3rd ed. Publicis MCD Verlag, 1995
- [46] A. P. Dhawan, H. K. Huang, and D.-S. Kim, *Principles and advanced methods in medical imaging and image analysis*. World Scientific, 2008
- [47] M. H. Beers, *The Merck Manual of Diagnosis and Therapy, 18th Edition*, 18th ed. Merck, 2006
- [48] S. S. Gambhir et al., "A Tabulated Summary of the FDG PET Literature," *J Nucl Med*, vol. 42, no. 5 (suppl), p. 1S–93S, May 2001
- [49] *NCD for Positron Emission Tomography (PET) Scans*. U.S. Department of Health & Human Services, 2009
- [50] A. Selmin, A. Nuri, O. Ahmet, and O. Mehmet Ali, "Abnormal 18F-FDG Uptake Detected with Positron Emission Tomography in a Patient with Breast Cancer: A Case of Sarcoidosis and Review of the Literature," *Case Reports in Medicine*, vol. 2009, 2009
- [51] anypodetos, "Fludeoxyglucose 18-F skeletal." [Online]. Available: [http://upload.wikimedia.org/wikipedia/commons/4/4c/Fludeoxyglucose\\_18-F\\_skeletal.svg](http://upload.wikimedia.org/wikipedia/commons/4/4c/Fludeoxyglucose_18-F_skeletal.svg). [Accessed: 07-Oct-2012]
- [52] S. Yu, "Review of 18F-FDG synthesis and quality control," *Biomed. Imaging Interv. J.*, vol. 2, no. 4, Oct. 2006
- [53] *Molecular Imaging and Contrast Agent Database*. National Library of Medicine (US), NCBI (Bethesda (MD)), 2004
- [54] A. Oppelt, *Imaging Systems for Medical Diagnostics: Fundamentals, Technical Solutions and Applications for Systems Applying Ionizing Radiation, Nuclear Magnetic Resonance and Ultrasound*, 2. Auflage. Publicis Corporate Publishing, 2005
- [55] T. F. Budinger, K. M. Brennan, W. W. Moses, and S. E. Derenzo, "Advances in positron tomography for oncology," *Nuclear Medicine and Biology*, vol. 23, no. 6, pp. 659–667, Aug. 1996
- [56] P. Lecoq et al., *Inorganic Scintillators for Detector Systems Physical Principles and Crystal Engineering*. Springer (Berlin), 2006
- [57] D. Renker, "Geiger-mode avalanche photodiodes, history, properties and problems," *Nuclear Instruments and Methods in Physics Research Section A: Accelerators, Spectrometers, Detectors and Associated Equipment*, vol. 567, no. 1, pp. 48–56, Nov. 2006
- [58] M. E. Casey and R. Nutt, "A Multicrystal Two Dimensional BGO Detector System for Positron Emission Tomography," *IEEE Transactions on Nuclear Science*, vol. 33, no. 1, pp. 460–463, 1986
- [59] F. H. Fahey, "Data Acquisition in PET Imaging," *J Nucl Med Technol*, vol. 30, no. 2, pp. 39–49, Jun. 2002
- [60] J. L. Prince and J. M. Links, *Medical Imaging: Signals and Systems*. Pearson Education (Upper Saddle River, NJ), 2006
- [61] G. El Fakhri et al., "Impact of Acquisition Geometry, Image Processing, and Patient Size on Lesion Detection in Whole-Body 18F-FDG PET," *J Nucl Med*, vol. 48, no. 12, pp. 1951–1960, Dec. 2007

- [62] C. Lartizien et al., "Evaluating Image Reconstruction Methods for Tumor Detection in 3-Dimensional Whole-Body PET Oncology Imaging," *J Nucl Med*, vol. 44, no. 2, pp. 276–290, Feb. 2003
- [63] M. Lubberink, R. Boellaard, A. P. van der Weerd, F. C. Visser, and A. A. Lammertsma, "Quantitative Comparison of Analytic and Iterative Reconstruction Methods in 2- and 3-Dimensional Dynamic Cardiac 18F-FDG PET," *J Nucl Med*, vol. 45, no. 12, pp. 2008–2015, Dec. 2004
- [64] W. W. Moses, "Recent advances and future advances in time-of-flight PET," *Nuclear Inst. and Methods in Physics Research, A*, vol. 580, no. 2, pp. 919–924, 2007
- [65] C. Comtat, P. E. Kinahan, M. Defrise, C. Michel, and D. W. Townsend, "Fast reconstruction of 3D PET data with accurate statistical modeling," *IEEE Transactions on Nuclear Science*, vol. 45, no. 3, pp. 1083–1089, 1998
- [66] S. R. Cherry, J. A. Sorenson, and M. E. Phelps, *Physics in Nuclear Medicine*. Elsevier Health Sciences, 2012
- [67] H. Zaidi and M.-L. Montandon, "Scatter Compensation Techniques in PET," *PET Clinics*, vol. 2, no. 2, pp. 219–234, Apr. 2007
- [68] "Siemens plant Übernahme von US-Firma CTI Molecular Imaging," *Siemens Press*, 18. Mar. 2005
- [69] M. E. Casey, "Point spread function reconstruction in PET," *Siemens Medical Solution, Knoxville, USA*, 2007
- [70] M. Casey, "Improving PET With HD-PET + Time of Flight," *Siemens Medical Solution, Knoxville, USA*, 2008
- [71] B. W. Jakoby et al., "Physical and clinical performance of the mCT time-of-flight PET/CT scanner," *Physics in Medicine and Biology*, vol. 56, no. 8, pp. 2375–2389, Apr. 2011
- [72] *Discovery PET/CT 600*. General Electrics Healthcare, 2008
- [73] V. Bettinardi et al., "Physical Performance of the new hybrid PET/CT Discovery-690," *Medical Physics*, vol. 38, no. 10, pp. 5394–5411, 2011
- [74] S. Surti et al., "Performance of Philips Gemini TF PET/CT Scanner with Special Consideration for Its Time-of-Flight Imaging Capabilities," *J Nucl Med*, vol. 48, no. 3, pp. 471–480, Mar. 2007
- [75] N. Dartial et al., "Performance evaluation of the Siemens Inveon microPET system," *J Nucl Med Meeting Abstracts*, vol. 49, no. MeetingAbstracts\_1, p. 404P–c–, 2008
- [76] *Inveon - No Limits on Discovery*. Siemens Medical, 2006
- [77] A. Del Guerra and N. Belcari, "State-of-the-art of PET, SPECT and CT for small animal imaging," *Nuclear Instruments and Methods in Physics Research Section A: Accelerators, Spectrometers, Detectors and Associated Equipment*, vol. 583, no. 1, pp. 119–124, Dec. 2007
- [78] M. Bergeron, "Performance Evaluation of the LabPET<sup>TM</sup> APD-based Digital PET Scanner," *2007 IEEE Nuclear Science Symposium Conference Record*, p. 4185, 2007
- [79] *nanoScan Family*. mediso Medical Imaging Systems, 2012
- [80] M. Huisman, S. Reder, A. Weber, S. Ziegler, and M. Schwaiger, "Performance evaluation of the Philips MOSAIC small animal PET scanner," *European Journal of Nuclear Medicine and Molecular Imaging*, vol. 34, no. 4, pp. 532–540, Apr. 2007
- [81] A. P. Jeavons, R. A. Chandler, and C. A. R. Dettmar, "A 3D HIDAC-PET camera with sub-millimetre resolution for imaging small animals," *IEEE Trans. Nucl. Sci.*, vol. 46, no. 3, pp. 468–473, Jun. 1999
- [82] J. Missimer et al., "Performance evaluation of the 16-module quad-HIDAC small animal PET camera," *Phys. Med. Biol.*, vol. 49, no. 10, pp. 2069–2081, May 2004
- [83] Del Guerra A., Di Domenico G., Scandola M., and Zavattini G., "High spatial resolution small animal YAP-PET," *Nuclear Instruments and Methods in Physics Research Section A: Accelerators, Spectrometers, Detectors and Associated Equipment*, vol. 409, pp. 537–541, May 1998
- [84] Crystal Clear Collaboration, CERN, Geneva, "private communication"

- [85] Weidong Luo, E. Anashkin, and C. G. Matthews, "Performance Evaluation of a PEM Scanner Using the NEMA NU 4—2008 Small Animal PET Standards," *IEEE Transactions on Nuclear Science*, vol. 57, no. 1, pp. 94–103, 2010
- [86] L. MacDonald et al., "Clinical Imaging Characteristics of the Positron Emission Mammography Camera: PEM Flex Solo II," *Journal of Nuclear Medicine*, vol. 50, no. 10, pp. 1666–1675, Sep. 2009
- [87] W. A. Berg et al., "High-Resolution Fluorodeoxyglucose Positron Emission Tomography with Compression ('Positron Emission Mammography') is Highly Accurate in Depicting Primary Breast Cancer," *Breast Journal*, vol. 12, no. 4, pp. 309–323, Jul. 2006
- [88] A. M. Kavanagh, G. G. Giles, H. Mitchell, and J. N. Cawson, "The sensitivity, specificity, and positive predictive value of screening mammography and symptomatic status," *Journal of Medical Screening*, vol. 7, no. 2, p. 105, 2000
- [89] L. Moliner et al., "Performance characteristics of the MAMMI PEMT scanner based on NEMA NU 2," in *2010 IEEE Nuclear Science Symposium Conference Record (NSS/MIC)*, pp. 2591–2594, Nov. 2010
- [90] A. Karimian et al., "CYBPET: a cylindrical PET system for breast imaging," *Nuclear Inst. and Methods in Physics Research, A*, vol. 545, no. 1–2, pp. 427–435, 2005
- [91] G.-C. Wang, J. S. Huber, W. W. Moses, J. Qi, and W.-S. Choong, "Characterization of the LBNL PEM camera," *IEEE Transactions on Nuclear Science*, vol. 53, no. 3, pp. 1129–1135, Jun. 2006
- [92] "EndoTOFPET-US, 'Novel Multimodal Endoscopic Probes for Simultaneous PET/ultrasound Imaging for Image-guided Interventions,' European Union 7th Framework Program (FP7 /2007 -2013) under Grant Agreement No. 256984, HEALTH-20 10.1.2-1"
- [93] P. Lecoq, "Goals and challenges of the EndoTOFPET-US FP7 project," ICTR-PHE 2012 (Geneva), presentation given on 28. Feb. 2012
- [94] J. H. Breasted, *The Edwin Smith surgical papyrus, published in facsimile and hieroglyphic transliteration with translation and commentary in two volumes*. University of Chicago, Oriental Institute (Chicago, IL), 1930
- [95] J. F. Nunn, *Ancient Egyptian Medicine*. University of Oklahoma Press, 1996
- [96] O. E. Silva and S. Zurrida, *Breast Cancer: A Practical Guide*. Elsevier Health Sciences, 2005
- [97] O. E. Silva, *Brustkrebs: Diagnostik und Therapie*. Urban & Fischer in Elsevier (München [u.a.]), 2007
- [98] R. Tiling and N. Avril, *Mammakarzinom: nuklearmedizinische und radiologische Diagnostik*. Springer (Berlin [u.a.]), 1998
- [99] L. W. Bassett, V. Jackson, K. Fu, and Y. Fu, *Diagnosis of Diseases of the Breast*, 2nd ed. Saunders, 2004
- [100] W. H. Hindle, *Breast Disease for Gynecologists*. Appleton & Lange (London [u.a.]), 1990
- [101] J. Saglier, P. Beuzeboc, A. Pommeyrol, and A. Toledano, *Cancer du sein: Questions et réponses au quotidien*, 3e édition. Masson, 2009
- [102] "Types of Breast Cancer," 24. Jul. 2009. [Online]. Available: <http://www.bccancer.bc.ca/HPI/Nursing/Education/breastcancer/diagnosis/bcbasics.htm>. [Accessed: 11-Apr-2010]
- [103] I. Andersson et al., "Breast tomosynthesis and digital mammography: a comparison of breast cancer visibility and BIRADS classification in a population of cancers with subtle mammographic findings," *European Radiology*, vol. 18, no. 12, pp. 2817–2825, Dec. 2008
- [104] G. Gennaro et al., "Digital breast tomosynthesis versus digital mammography: a clinical performance study," *European Radiology*, Dec. 2009
- [105] H. Teertstra et al., "Breast tomosynthesis in clinical practice: initial results," *European Radiology*, vol. 20, no. 1, pp. 16–24, Jan. 2010

- [106] C. K. Kuhl, “New paradigms in breast imaging,” ECR 2008 (Vienna), presentation given on 10. Mar. 2008
- [107] G. Estrada-Sanchez, F. J. Ochoa-Carrillo, and J. Altamirano-Ley, “18 FDG PET/CT en linfoma primario de mama y cáncer de mama,” *Cir Ciruj*, vol. 76, no. 4, pp. 279–286, 2008
- [108] F. Benard and E. Turcotte, “Imaging in breast cancer: Single-photon computed tomography and positron-emission tomography,” *Breast Cancer Res*, vol. 7, no. 4, pp. 153–162, 2005
- [109] E. A. Levine et al., “Positron emission mammography: initial clinical results,” *Annals of Surgical Oncology*, vol. 10, no. 1, pp. 86–91, Feb. 2003
- [110] J. Santos and B. Frisch, “Solidworks Drawings” private communication from INEGI, 2010
- [111] E. Albuquerque et al., “The Clear-PEM Electronics System,” *Nuclear Science Symposium Conference Record*, vol. 53, no. 5, pp. 2704–2711, 2006
- [112] E. Albuquerque et al., “Experimental characterization of the 192 channel Clear-PEM frontend ASIC coupled to a multi-pixel APD readout of LYSO:Ce crystals,” *Nuclear Instruments and Methods in Physics Research Section A: Accelerators, Spectrometers, Detectors and Associated Equipment*, vol. 598, no. 3, pp. 802–814, Jan. 2009
- [113] P. Rodrigues, “First Results with ASIC V3,” Crystal Clear Collaboration Meeting, CERN, presentation given on Nov. 2007
- [114] J. Varela, “Status of the ClearPEM Project,” Crystal Clear Collaboration Meeting (Marseille), presentation given on Apr. 2009
- [115] J. Varela, “Status of ClearPEM Projects,” Crystal Clear Collaboration Meeting (CERN), presentation given on Nov. 2009
- [116] J. Trummer et al., “Scintillation Properties of LuYAP and LYSO Crystals Measured with MiniACCOS, an Automatic Crystal Quality Control System,” in *2005 IEEE Nuclear Science Symposium Conference Record*, Wyndham El Conquistador Resort, Puerto Rico, pp. 2807–2810
- [117] L. Cao et al., “List-Mode Maximum-Likelihood Reconstruction for the ClearPEM System,” in *2011 IEEE Nuclear Science Symposium Conference Record*, 2011
- [118] M. V. Martins et al., “Reconstruction of Clear-PEM data with STIR,” in *2005 IEEE Nuclear Science Symposium Conference Record*, vol. 4, Oct. 2005
- [119] E. Albuquerque et al., “Characterization of the Clear-PEM breast imaging scanner performance,” in *2009 IEEE Nuclear Science Symposium Conference Record (NSS/MIC)*, pp. 3487–3490, Nov. 2009
- [120] J. Dang et al., “Development of breast anthropomorphic phantoms for combined PET-Ultrasound elastography imaging,” *2009 IEEE Nuclear Science Symposium Conference Record*, vol. 1–5, pp. 3088–3092, 2009
- [121] G. Rizzatto, “Elastography: Clinical tool or toy?,” ECR 2010 (Vienna), presentation given on 06. Mar. 2010
- [122] J. Bercoff, M. Tanter, and M. Fink, “Supersonic shear imaging: a new technique for soft tissue elasticity mapping,” *IEEE Transactions on Ultrasonics Ferroelectrics and Frequency Control*, vol. 51, no. 4, pp. 396–409, 2004
- [123] R. Muthupillai et al., “Magnetic resonance elastography by direct visualization of propagating acoustic strain waves,” *Science*, vol. 269, no. 5232, pp. 1854–1857, Sep. 1995
- [124] A. Athanasiou, “Ultrasound elastography,” European Congress of Radiologists (Vienna), presentation given on 03. Mar. 2012
- [125] J. Bercoff, *ShearWave TM Elastography*. SuperSonic Imagine (Aix-en-Provence), 2008
- [126] N. Felix, “private communication”
- [127] C. Cohen-Bacrie, D. O. Cosgrove, C. J. Doré, and J.-P. Henry, “Preliminary assessment of ShearWave(TM) elastography features in predicting breast lesion malignancy,” presented at the ECR 2010, Vienna, Mar. 2010



- [128] W. A. Berg et al., "Shear-wave Elastography Improves the Specificity of Breast US: The BE1 Multinational Study of 939 Masses," *Radiology*, vol. 262, no. 2, pp. 435–449, Jan. 2012
- [129] D. Cosgrove et al., "Shear wave elastography for breast masses is highly reproducible," *European Radiology*, vol. 22, no. 5, pp. 1023–1032, 2012
- [130] H. S. Lim et al., "FDG PET/CT for the Detection and Evaluation of Breast Diseases: Usefulness and Limitations," *Radiographics*, vol. 27, no. Supplement 1, pp. S197–S213, Oct. 2007
- [131] S. Weber, S. Wojcinski, and K. Ertan, "Realtime Sonoelastography of 156 Breast Lesions in a Prospective Clinical Setting," presented at the Fourth International Conference on the Ultrasonic Measurement and Imaging of Tissue Elasticity (Austin, TX), Oct. 2005
- [132] W. R. Leo, *Techniques for nuclear and particle physics experiments a how-to approach*, 2nd ed. Springer (Berlin), 1994
- [133] J. B. Birks, *The Theory and Practice of Scintillation Counting*. Pergamon (Oxford), 1964
- [134] P. A. Rodnyi, *Physical Processes in Inorganic Scintillators*. CRC Press (Boca Raton, FL), 1997
- [135] A. Lempicki, A. Wojtowicz, and E. Berman, "Fundamental limits of scintillator performance," *Nuclear Instruments and Methods in Physics Research Section A: Accelerators, Spectrometers, Detectors and Associated Equipment*, vol. 333, no. 2–3, pp. 304–311, Sep. 1993
- [136] M. Kronberger, "Optimization of the light extraction from heavy inorganic scintillators," Thesis, Technische Universitaet Wien, Vienna, 2008
- [137] M. Moszynski, M. Kapusta, M. Mayhugh, D. Wolski, and S. O. Flyckt, "Absolute light output of scintillators," *IEEE Trans. Nucl. Sci.*, vol. 44, no. 3, pp. 1052–1061, Jun. 1997
- [138] B. Frisch, "Characterisation of Scintillation Crystal for a Mammography Positron Emission Tomograph," Diploma Thesis, Technische Universitaet Wien, Vienna, 2007
- [139] E. Breitenberger, "Scintillation Spectrometer Statistics," *Progress in nuclear physics*, vol. 4, p. 56, 1955
- [140] J. Trummer, "Study of a Positron Emission Mammograph," Thesis, Technische Universitaet Wien, Vienna, 2007
- [141] J. Trummer, E. Auffray, and P. Lecoq, "Depth of interaction resolution of LuAP and LYSO crystals," *Nuclear Instruments and Methods in Physics Research Section A: Accelerators, Spectrometers, Detectors and Associated Equipment*, vol. 599, no. 2–3, pp. 264–269, Feb. 2009
- [142] I. Vilardi et al., "Optimization of the effective light attenuation length of YAP:Ce and LYSO:Ce crystals for a novel geometrical PET concept," in *2004 IEEE Nuclear Science Symposium Conference Record*, vol. 5, pp. 2859–2863, Oct. 2004
- [143] E. Auffray et al., "Development of a Uniformisation Procedure for the PbW04 Crystals of the CMS Electromagnetic Calorimeter," *CMS Note*, 2001
- [144] *Surtronic 3+ - Operating Instructions*. Taylor-Hobson
- [145] I. Rolo, "Performance Evaluation of New Upgrades on ClearPEM Detector Modules," Universidade Tecnica de Lisboa, Lisbon, Portugal, 2009
- [146] *RenShape BM 5066 Datasheet*. Huntsman Switzerland (Switzerland), 2007
- [147] Kaye & Laby Online, "Tables of Physical & Chemical Constants," *Tables of Physical and Chemical Constants*, 1995. [Online]. Available: [www.kayelaby.npl.co.uk](http://www.kayelaby.npl.co.uk). [Accessed: 07-Oct-2012]
- [148] Ondo Corporation, "Tables of Acoustic Properties of Materials," *Tables of Acoustic Properties of Materials*, 2003. [Online]. Available: [http://www.ondacorp.com/tecref\\_acoustictable.shtml](http://www.ondacorp.com/tecref_acoustictable.shtml). [Accessed: 07-Oct-2012]
- [149] L. Pedersen, "List Of Material Properties" Apr. 2005
- [150] B. Hadimioglu and B. T. Khuri-Yakub, "Polymer films as acoustic matching layers," in *Ultrasonics Symposium, 1990. Proceedings., IEEE 1990*, pp. 1337–1340, 2002

- [151] Berger et al., “NIST XCOM: Photon Cross Sections Database,” *XCOM: Photon Cross Sections Database*, 1998. [Online]. Available: <http://www.nist.gov/pml/data/xcom/index.cfm>. [Accessed: 07-Oct-2012]
- [152] J. A. Shipley et al., “Automated quantitative volumetric breast ultrasound data-acquisition system,” *Ultrasound in medicine & biology*, vol. 31, no. 7, pp. 905–917, 2005
- [153] “Lexan Exell D FR Sheet” GE Structured Products, 2012
- [154] A. Trindade et al., “Breast cancer imaging studies by Monte Carlo simulation with ClearPEM,” in *2005 IEEE Nuclear Science Symposium Conference Record*, vol. 4, p. 5 pp., Oct. 2005
- [155] Ascension Technology Corporation, “3D Guidance trakSTAR - Installation and Operation Guide” 2008
- [156] M. Pizzichemi, “Image Fusion software on the ClearPEM-Sonic Project,” presentation given on 2011
- [157] S. Pieper, M. Halle, and R. Kikinis, “3D Slicer,” in *IEEE International Symposium on Biomedical Imaging: Nano to Macro, 2004*, pp. 632 – 635 Vol. 1, Apr. 2004
- [158] T. S. Yoo et al., “Engineering and algorithm design for an image processing Api: a technical report on ITK--the Insight Toolkit,” *Stud Health Technol Inform*, vol. 85, pp. 586–592, 2002
- [159] W. Schroeder, K. Martin, and B. Lorensen, *The Visualization Toolkit: An Object-oriented Approach to 3D Graphics*. Kitware, 2006
- [160] T. F. Budinger, S. E. Derenzo, G. T. Gullberg, W. L. Greenberg, and R. H. Huesman, “Emission computer assisted tomography with single-photon and positron annihilation photon emitters,” *J Comput Assist Tomogr*, vol. 1, no. 1, pp. 131–145, Jan. 1977
- [161] A. A. Michelson, *Studies in Optics*. Courier Dover Publications, 1926
- [162] E. Peli, “Contrast in complex images,” *J. Opt. Soc. Am. A*, vol. 7, no. 10, pp. 2032–2040, Oct. 1990
- [163] National Cancer Institute, “NCI FactSheet: Cancer Clinical Trials,” Apr. 2010. [Online]. Available: <http://www.cancer.gov/cancertopics/factsheet/Information/clinical-trials>. [Accessed: 26-Oct-2012]
- [164] “Mise en place et conduite en France d’essais cliniques portant sur des dispositifs médicaux et dispositifs médicaux de diagnostic in vitro” Agence nationale de sécurité du médicament et des produits de santé, May. 2012
- [165] Assistance Publique Hopitaux De Marseille, “Diagnosis of Breast Carcinoma: Characterization of Breast Lesions With CLEARPEMSONIC: Feasibility Study - ID NCT01569321” [clinicaltrials.gov](http://clinicaltrials.gov) - a service of the US National Institutes of Health, 20. Jun. 2012
- [166] L. Tessonnier, “Diagnostic du Cancer du Sein: Utilisation d Prototype ClearPEM-Sonic pour la Caracterisation des Lesions Mammaires, Etude de Faisabilite” Protocole de recherche, Nov. 2011